



Héliosismologie et Astrométrie solaire à haute résolution

Thierry Corbard

► To cite this version:

| Thierry Corbard. Héliosismologie et Astrométrie solaire à haute résolution. Astrophysique stellaire et solaire [astro-ph.SR]. Université Côte D'Azur, 2016. tel-02466222

HAL Id: tel-02466222

<https://theses.hal.science/tel-02466222>

Submitted on 4 Feb 2020

HAL is a multi-disciplinary open access archive for the deposit and dissemination of scientific research documents, whether they are published or not. The documents may come from teaching and research institutions in France or abroad, or from public or private research centers.

L'archive ouverte pluridisciplinaire **HAL**, est destinée au dépôt et à la diffusion de documents scientifiques de niveau recherche, publiés ou non, émanant des établissements d'enseignement et de recherche français ou étrangers, des laboratoires publics ou privés.



Travaux de Recherche

Présentés par

Thierry Corbard

Pour l'obtention de

L'Habilitation à Diriger des Recherches

Héliosismologie et Astrométrie solaire à haute résolution

Soutenue le 21 Octobre 2016 à Nice devant le jury composé de :

Thierry Appourchaux,	Institut d'Astrophysique Spatiale, Orsay	Rapporteur
Marianne Faurobert,	Université de Nice Sophia Antipolis, Nice	Rapporteur
Thierry Roudier,	Observatoire Midi-Pyrénées, Toulouse	Rapporteur
Bernard Gelly,	THEMIS, La Laguna, Tenerife	Examinateur
Jean-Marie Malherbe,	Observatoire de Paris, Meudon	Examinateur

" Je n'ai pas révélé la moitié de ce que j'ai vu, car je savais que l'on ne me croirait pas "

Marco Polo, 1324

Remerciements

Je tiens à remercier :

Messieurs Timothy Brown, Michael Thompson, Douglas Gough, John Leibacher, pour m'avoir accueilli respectivement à Boulder, Londres, Cambridge et Tucson dans les années qui ont suivi mon doctorat et précédé mon recrutement à l'Observatoire de la Côte d'Azur ;

Mesdames Janine Provost et Catherine Renaud avec qui j'ai eu de nombreux échanges toujours très fructueux et qui m'ont encouragés pour la rédaction de ce document;

Madame Marianne Faurobert et messieurs Thierry Appourchaux et Thierry Roudier pour avoir accepté d'être rapporteurs du présent travail ;

Messieurs Bernard Gelly et Jean-Marie Malherbe pour avoir accepté d'être membre du jury de ma soutenance d'habilitation.

Sommaire

Introduction.....	7
PARTIE I. L'héliosismologie à haute résolution	9
I.1 Introduction	9
I.1.1 L'activité solaire, un bref aperçu	9
I.1.2 Les modèles cinématiques de la dynamo solaire : une perspective d'héliosismologue.	
13	
I.2 Méthodes	16
I.2.1 Principes de l'héliosismologie globale et locale	16
I.2.2 L'analyse globale des modes f (article)	21
I.2.3 L'héliosismologie locale par l'analyse « ring-diagram ».....	41
I.2.3.1 La méthode.....	41
I.2.3.2 Les cartes et descripteurs de dynamique des fluides dérivés (article)	49
I.3 Résultats.....	65
I.3.1 Les gradients radiaux de la rotation sub-photosphérique et le siège de la dynamo...65	
I.3.1.1 Comparaison des résultats entre analyse des modes f et analyse locale	65
I.3.1.2 Application à un modèle dynamo (article)	67
I.3.2 La composante zonale : les oscillations de torsion, le lien avec l'activité magnétique et l'asymétrie nord-sud	73
I.3.3 La circulation méridienne.....	77
I.3.4 La circulation autour des zones actives	80
I.4 Conclusion.....	82
PARTIE II. L'astrométrie solaire à haute résolution.....	83
II.1 Introduction : objectifs et contexte historique	83
II.1.1 Les variations du rayon solaire à différentes échelles	83
II.1.1.1 L'échelle du cycle d'activité magnétique	83
II.1.1.2 Les échelles plus longues, évolution à long terme.....	84
II.1.2 Les observations de type astrolabe (article).....	89
II.2 Développements instrumentaux : PICARD-SOL	105
II.2.1 L'instrument SODISM-2	106
II.2.2 Effets atmosphériques sur la mesure du diamètre avec SODISM-2	107
II.2.2.1 Les principaux effets et leur importance relative	107
II.2.2.2 Comment traiter les effets de la turbulence optique ?.....	108
II.2.2.3 L'instrument MISOLFA (article).....	111

II.3	L'analyse des images	126
II.3.1	Calibrations radiométriques.....	126
II.3.2	Correction de la réfraction astronomique (article).....	131
II.4	Résultats (article).....	143
II.5	Conclusions	159
PARTIE III.	Perspectives.....	161
III.1	La dynamo solaire profonde et aux pôles.....	161
III.2	Le projet METEOSPACE.....	164
Bibliographie		171
Annexe 1 Curriculum Vitae.....		179
Annexe 2 Liste de Publications		183

Introduction

L'étude de notre étoile, le Soleil, est une branche particulière de l'astrophysique en ce sens qu'aucune étoile n'est à priori aussi accessible à l'observation. Même si la photométrie de précision, les techniques d'imagerie Doppler à haute résolution ou encore le développement l'interférométrie infrarouge et optique permettent maintenant de résoudre la surface d'autres étoiles (Zhao, et al. 2009), de mesurer précisément leurs tailles angulaires (Domiciano de Souza, et al. 2012) ou encore d'y observer les manifestations de leurs activités magnétiques (Carroll, et al. 2007), rien n'est encore comparable bien évidemment avec les résolutions spatiales et temporelles atteintes pour l'observation du Soleil.

Il reste en particulier un domaine, celui de l'héliosismologie, où la haute résolution n'est pas encore accessible pour d'autres étoiles que le Soleil. L'astérosismologie a en effet fait un bond de géant avec les satellites COROT puis Kepler, multipliant en quelques années le nombre d'étoiles dont l'intérieur peut être sondé par l'observation et l'analyse de leurs modes propres d'oscillation mais seuls les modes globaux de bas degrés restent accessibles pour les étoiles autres que le Soleil. Pour sonder avec une meilleure résolution la dynamique interne de ce dernier, des images Doppler à haute résolution sont produites depuis 2001 toutes les minutes (avec un taux de remplissage supérieur à 80%) par les instruments du réseau au sol GONG¹ (Harvey, Tucker et Britanik 1998) et, depuis 2010, l'instrument HMI² (Schou, et al. 2012) à bord du satellite SDO³ a pris la succession de MDI⁴ (Scherrer, et al. 1995) à bord de SoHO⁵ et fournit en continu, toutes les 45 secondes, des images Doppler et en intensité de la photosphère.

Mon travail de thèse portait sur une branche particulière de ce que l'on appelle aujourd'hui l'héliosismologie globale, c'est-à-dire l'observation et la modélisation des modes globaux d'oscillation du Soleil pour en déduire des propriétés globales sur sa structure ou sa dynamique interne. J'ai ainsi pu obtenir le profil de la rotation interne de notre étoile du cœur jusqu'à la surface et préciser notamment le profil dynamique d'une zone, nommée tachocline, située à l'interface entre les zones radiatives et convectives solaires soit 209 000 km sous la photosphère. Les forts gradients de vitesses angulaires qui caractérisent cette zone (d'où son nom) sont des éléments clefs de ce que l'on suppose être une 'dynamo solaire' à l'origine du cycle d'activité magnétique de 22 ans.

Mais cette vision globale de la dynamique de notre étoile restait incomplète. Tout d'abord l'héliosismologie globale ne donne pas accès aux composantes nord-sud, aussi

¹ Global Oscillation Network Group

² Heliospheric and Magnetic Imager

³ Solar Dynamics Observatory

⁴ Michelson Doppler Imager

⁵ Solar and Heliospheric Observatory

seul le profil de vitesse angulaire moyenné sur les deux hémisphères est accessible et la détection de la circulation méridienne reste inatteignable par cette méthode. Ensuite les extrêmes : le cœur nucléaire, les pôles mais aussi, paradoxalement, les zones les plus proches de la surface restent mal contraintes. Le cœur nucléaire reste insondable sans l'observation des modes de gravité qui seuls y pénètrent, les zones polaires restent intrinsèquement mal résolues à partir d'observations toujours menées depuis le plan de l'écliptique et enfin résoudre les zones proches de la photosphère nécessite d'observer les modes propres correspondants aux fréquences spatiales les plus grandes, c'est-à-dire les harmoniques sphériques les plus élevés, accessibles par l'observation Doppler de la surface à haute résolution spatiale. Et comme ce sont là les conditions aux limites de tout modèle de la dynamique interne ou de la dynamo solaire, nous comprenons l'importance de pouvoir apporter des contraintes observationnelles sur ces zones.

Dans la première partie de ce document je m'attache à montrer comment il a été possible avec notamment l'héliosismologie à haute résolution où « héliosismologie locale » de dépasser certaines de ces limitations et comment l'héliosismologie pourrait aussi à l'avenir contribuer à la météorologie de l'espace, c'est-à-dire la prévision des phénomènes solaires pouvant impacter l'environnement terrestre sur le court terme.

Dans la deuxième partie, je m'intéresse à la surveillance solaire à long terme à travers le programme d'astrométrie solaire au sol. J'expose tout d'abord pourquoi je pense qu'une surveillance à long terme des paramètres fondamentaux de notre étoile (éclairement, diamètre) est nécessaire et je présente ensuite les développements réalisés pour le programme PICARD-SOL dont l'objectif était d'une part d'assurer le suivi astrométrique depuis le sol simultanément aux observations du satellite PICARD pour comprendre et calibrer l'influence des effets atmosphériques, et d'autre part de continuer le suivi astrométrique sur le long terme après l'arrêt de la phase spatiale. L'influence éventuelle des variations à long terme de ces paramètres fondamentaux sur le climat terrestre fait partie de ce que l'on appelle parfois la climatologie de l'espace.

PARTIE I. L'héliosismologie à haute résolution

I.1 Introduction

Les paragraphes suivants présentent le contexte général dans lequel s'inscrivent plusieurs travaux que j'ai menés visant à apporter, par l'héliosismologie, des contraintes observationnelles utiles à l'élaboration de modèles visant à mieux comprendre les mécanismes à l'origine de l'activité solaire. Depuis une quinzaine d'années et l'avènement des observations continues à hautes résolutions temporelles, spatiales et spectrales, ces efforts de modélisations ont aussi clairement pour objectif la prévision non seulement des événements les plus violents susceptibles d'impacter directement l'environnement terrestre (c'est le domaine de la météorologie de l'espace) mais aussi de l'évolution générale du cycle d'activité.

I.1.1 L'activité solaire, un bref aperçu

La manifestation la plus visible et probablement la plus connue de l'activité solaire est la variation, avec un cycle d'environ 11 ans, du nombre de taches directement visibles sur la photosphère. Ces taches sont la simple signature de la présence, localement, d'un champ magnétique intense qui inhibe les mouvements de convection du plasma photosphérique qui apparaît donc, localement, plus sombre parce que plus froid que son environnement (Figure 1).

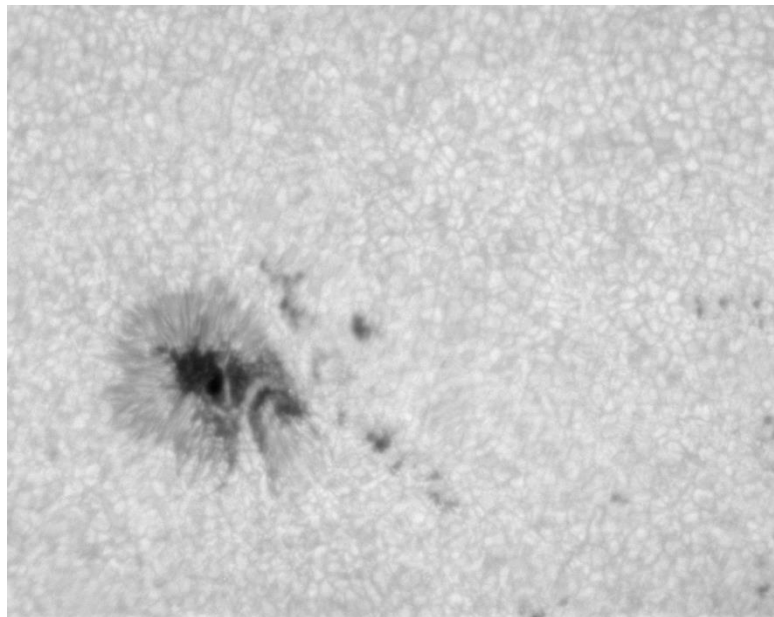


Figure 1. Exemple de tache solaire observée au Pic du Midi en 2003 lors d'une campagne de test des filtres pour la mission PICARD. Les cellules de convection constituant la granulation solaire sont clairement visibles tout autour de la tache. Le filtre utilisé est à 779 nm (bande passante 10.6 nm) et la résolution d'environ 0.2" (T. Corbard, J. Arnaud & R. Muller).

Le nombre de taches ou nombre de Wolf (Wolf 1859) est l'indice d'activité le plus populaire pour plusieurs raisons. C'est avant tout la série la plus longue d'un indice de

l'activité solaire, des moyennes mensuelles sont obtenues depuis 1750 et des observations moins régulières permettent aussi de remonter jusqu'à l'invention du télescope au début du 17^{ème} siècle assurant notamment une couverture complète de la période 1645-1715 dite du « Minimum de Maunder » durant laquelle très peu de taches furent observées (Figure 2). Il se trouve que cette période de la fin du 17^{ème} siècle correspond, au moins au nord de l'Europe, à ce qui a été appelé le petit âge glaciaire. Cette coïncidence entre les deux évènements a naturellement stimulé la recherche sur un possible lien entre l'activité solaire et le climat terrestre mais aussi, plus en amont, sur l'origine de l'activité solaire. Là encore la simple série des taches solaires est utile. En effet, la durée et la régularité exceptionnelle de ces observations astronomiques ne représentent pas leur seul intérêt. Le nombre de taches est aussi un indice riche dont l'interprétation précise reste un challenge. En effet, sans même parler des périodes singulières comme celles du minimum de Maunder, les cycles ont des durées et des amplitudes variables, ils présentent des phases ascendantes et descendantes et des composantes Nord-Sud asymétriques, les taches elles-mêmes ont des surfaces, des répartitions, des orientations et des polarités magnétiques variables mais qui semblent suivre certaines lois (la loi de Joy pour l'orientation relative d'une paire de tache, la loi de Hale pour leur polarité, le diagramme papillon pour la progression de leur répartition en latitude au cours du cycle (Figure 3)). Autant d'observations qui peuvent servir de contraintes pour la modélisation visant à comprendre la physique sous-jacente.

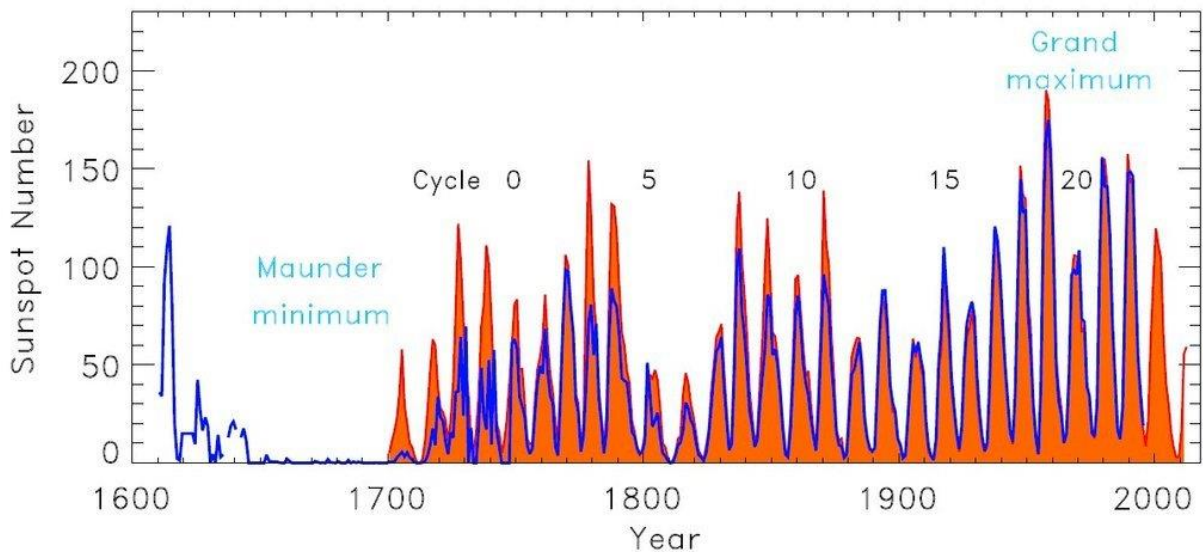


Figure 2. Moyennes mensuelles du nombre de tache solaire (orange, Solar Influence Data Center SIDC <http://www.sidc.be/>) et du nombre de groupes de taches solaires (bleue, (Hoyt et Schatten 1998))

DAILY SUNSPOT AREA AVERAGED OVER INDIVIDUAL SOLAR ROTATIONS

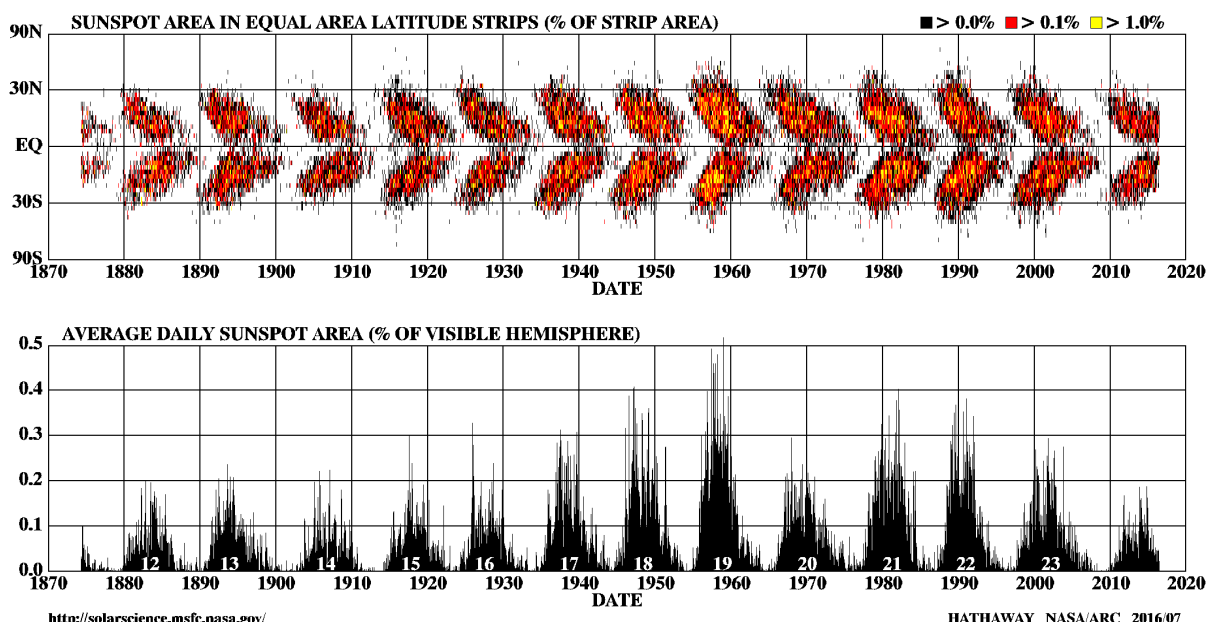


Figure 3. Le cycle solaire depuis 1875 représenté par l'évolution de la répartition en latitude des taches appelée « diagramme papillon » (haut). L'évolution journalière du pourcentage de la surface visible occupée par les taches est donnée depuis la fin du cycle 11 (bas).

Le cycle solaire est de toute évidence lié à l'existence d'un champ magnétique à grande échelle et produit par son évolution. Outre les manifestations localisées d'un magnétisme important dans les taches, une autre observation directe du magnétisme est très importante pour la modélisation globale du cycle : il s'agit de l'intensité du champ magnétique dans les zones polaires (latitudes supérieures à 75°). En effet, c'est au minimum d'activité que le flux magnétique accumulé aux pôles devient le plus important et, au maximum du cycle des taches que la polarité des pôles s'inverse (Figure 4). La dernière inversion a ainsi été enregistrée lors du maximum du cycle 24 fin 2014.

L'héliosismologie ne donne pas d'information directe sur le magnétisme mais plutôt sur tous les aspects de la dynamique interne. Un des objectifs que j'ai poursuivi est d'apporter des contraintes aux modèles de la dynamo solaire qui établissent un lien physique entre la dynamique interne et les manifestations de l'activité magnétique observable en surface.

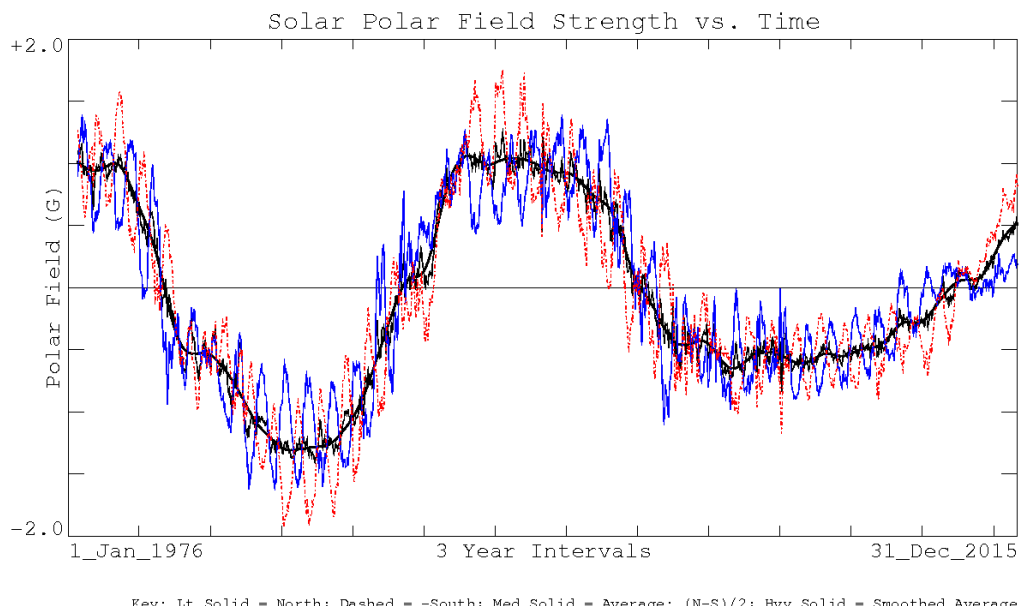


Figure 4. Variation de l'amplitude des champs magnétiques polaires d'après les observations du Wilcox Solar Observatory (Svalgaard, Duvall et Scherrer 1978). Les composantes nord (en bleue) et sud (avec le signe inversé en rouge) ont une évolution antisymétrique. Les extrema se produisent aux minima d'activité (minima du cycle des taches) alors que les changements de signe se produisent autour des maxima d'activité.

Mais les manifestations de l'activité solaire ne se limitent pas au cycle des taches et peuvent nous affecter plus directement de plusieurs façons. Les périodes de maximum d'activité se caractérisent aussi par des émissions ultraviolettes et des rayons X plus importantes qui affectent la haute atmosphère terrestre. L'augmentation de la densité et la température de l'atmosphère peut affecter la durée de vie ou le fonctionnement des satellites en basses altitudes. Les éruptions solaires et éjections de masses coronales (CME) sont également plus nombreuses en période de maximum d'activité et ces événements ont la capacité d'accélérer les particules (Solar Energetic Particules, SEP) qui viennent impacter l'environnement terrestre, les astronautes ou encore les passagers des lignes aériennes notamment au-dessus des pôles. Là encore l'héliosismologie ne donne pas des observables directes de ces manifestations violentes de l'activité mais les observations Doppler continues à haute résolution permettent de sonder localement la dynamique sub-photosphérique et d'y rechercher des indicateurs de changements dynamiques qui seraient des précurseurs aux événements éruptifs. En développant une technique particulière de l'héliosismologie locale pour le réseau GONG, j'ai contribué à la définition et à la production systématique de ces indicateurs locaux de la dynamique sub-photosphérique.

I.1.2 Les modèles cinématiques de la dynamo solaire : une perspective d'héliosismologie.

Une revue détaillée des différentes approches de la modélisation de la dynamo solaire peut être trouvée par exemple par Charbonneau (2010). Je veux juste ici replacer dans leur contexte les modèles qui vont directement utiliser les contraintes observationnelles que peut apporter l'héliosismologie.

Tous les modèles actuels de la dynamo solaire sont basés sur l'approche dite du « champ moyen » dans laquelle un système couplé d'équations aux dérivées partielles régit l'évolution des composantes poloïdales (selon les méridiens) et toroïdales (azimutales) d'un champ magnétique à grande échelle \mathbf{B} supposé à symétrie axiale. Le champ magnétique polaire de faible amplitude observé (Figure 4) est alors considéré comme une manifestation de la composante poloïdale du champ magnétique global alors que les taches solaires, sièges d'un champ magnétique beaucoup plus intense, sont une manifestation de la composante toroïdale du champ global.

Dans le cas le plus simple d'une turbulence homogène et isotrope, l'hypothèse de séparation des échelles pour laquelle l'échelle de la turbulence est petite par rapport à l'échelle des variables moyennes, l'équation de la dynamo est une modification de l'équation d'induction magnétohydrodynamique (MHD) liant l'évolution temporelle de \mathbf{B} au champ moyen de vitesse du plasma à grande échelle, \mathbf{U} par :

$$\frac{\partial \mathbf{B}}{\partial t} = \nabla \times (\mathbf{U} \times \mathbf{B} - \eta \nabla \times \mathbf{B}) \quad (1)$$

où η est la diffusivité magnétique turbulente. Dans certains modèles non linéaires le système est couplé avec une équation du mouvement régissant l'évolution de \mathbf{U} de type Navier-Stokes avec prise en compte des forces de Lorentz. Cependant, pour les modèles que l'on appelle « modèles cinématiques », le champ de vitesse est simplement imposé le plus souvent sous une forme analytique simple plus ou moins contrainte par l'héliosismologie.

En géométrie sphérique (Figure 5), on décompose typiquement le champ de vitesse par la somme d'une composante axisymétrique azimutale, la rotation interne $\Omega(r, \theta)$, et d'une composante poloïdale, la circulation méridienne $\mathbf{U}_p(r, \theta) = u_r(r, \theta) \vec{e}_r + u_\theta(r, \theta) \vec{e}_\theta$, soit :

$$\mathbf{U}(r, \theta) = \mathbf{U}_p(r, \theta) + r \sin \theta \Omega(r, \theta) \vec{e}_\phi \quad (2)$$

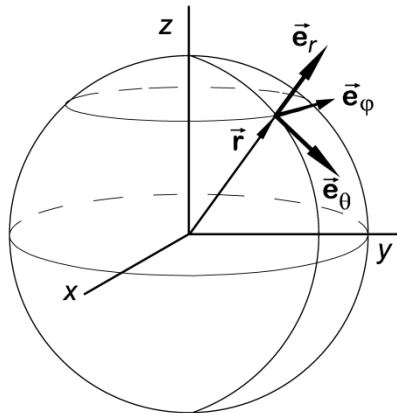


Figure 5. Représentation des vecteurs unités en coordonnées sphériques. L'axe z représente l'axe de rotation, r la distance radiale au centre, θ la co-latitude et φ la longitude. \vec{e}_r est perpendiculaire à la surface, alors que \vec{e}_θ et \vec{e}_φ sont tangents.

Un des tous premiers succès de l'héliosismologie a été de préciser la profondeur de la zone convective (jusqu'à 0.7 rayon solaire) et d'obtenir le profil 2D de la rotation interne $\Omega(r,\theta)$ montrant qu'il existe une zone de fort cisaillement nommée tachocline à l'interface. Ceci constituait mon travail de thèse en 1998 à partir des données Doppler de SoHO mais plus récemment j'ai également obtenu un tel profil à partir des données en intensité de la mission PICARD (Figure 6). En développant l'équation (1) en ses composantes poloïdales (\mathbf{B}_p) et toroïdales (\mathbf{B}_φ), on montre que le gradient $\nabla\Omega$ agit comme une source de génération du champ toroïdal à partir du champ poloïdal par conversion de l'énergie cinétique de rotation. Ce mécanisme est appelé « effet omega ». Ce gradient est d'amplitude maximale dans la tachocline. Comme il a été montré par ailleurs qu'il existe des mécanismes de pompage qui, dans des échelles de temps courtes par rapport au cycle, tendent à supprimer le flux magnétique de la zone convective pour le concentrer à sa base (Browning, et al. 2006), la tachocline a rapidement été considérée comme étant le « siège de la dynamo solaire » capable à la fois de générer et de stocker un champ toroïdal intense produisant les tubes de flux qui émergent ensuite à la surface en donnant naissance aux taches observées.

Pour établir un cycle il reste néanmoins à trouver un ou des mécanismes de conversion de la composante toroïdale en composante poloïdale du champ magnétique moyen. Ces mécanismes sont souvent appelés, d'une manière générique, « effet alpha ». L'équation (1) seule ne permet pas cette conversion. Il est nécessaire pour cela de trouver des mécanismes qui ne sont plus à symétrie axiale. Deux principales classes de mécanismes sont en général évoquées qui peuvent, selon les modèles, être invoquées séparément, agir de manière complémentaire ou encore être mis en compétition pour produire des cycles d'amplitudes variables sur le long terme (Sanchez, et al. 2014).

La première classe de mécanismes invoqués repose sur la production d'hélicité sous l'action de la force de Coriolis qui va être capable de déformer localement les lignes du champ toroïdal ou bien les tubes de flux émergeants pour produire une force

électromotrice moyenne proportionnelle au champ moyen ($\alpha\mathbf{B}$) incluant donc une composante poloïdale. La source d'hélicité peut se trouver dans la turbulence elle-même (Parker 1955) ou faire intervenir les instabilités hydrodynamiques ou MHD de la tachocline. Ce type de mécanismes est situé préférentiellement au niveau de la tachocline ce qui s'avère également nécessaire pour reproduire l'évolution antisymétrique observée des composantes nord et sud du champ magnétique (Dikpati et Gilman 2001).

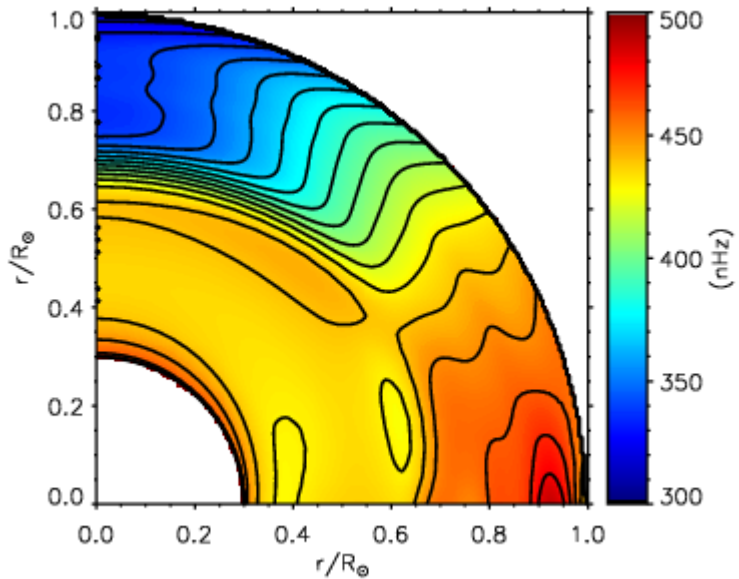


Figure 6. Profil de la rotation interne du Soleil déduite des données du programme d'héliosismologie de la mission PICARD. Les lignes de contours représentent le niveau de vitesse angulaire tous les 10 nHz entre 300 nHz et 480 nHz. La solution sous 0.3 rayon solaire n'est pas contrainte par les données. La tachocline est clairement visible à l'interface entre zone radiative et zone convective autour de 0.7 rayon solaire. Les régions les plus superficielles ($r>0.9 R_\odot$) sont mal résolues par les modes p observés (<100) (Corbard, Salabert, et al. 2013).

Le deuxième effet invoqué pour la régénération d'une composante poloïdale à partir du champ toroïdal est nommé mécanisme de Babcock-Leighton (Babcock (1961) ; Leighton (1969)). Il repose sur la dégénérescence des paires de taches de polarités magnétiques opposées qui, c'est la « loi de Joy », émergent préférentiellement avec un angle entre elles qui n'est pas nul par rapport à la direction est-ouest. Pour ces paires de taches il y a donc une tache « leader », plus proche de l'équateur et une tache « suiveuse » à une latitude légèrement supérieure. Le champ magnétique toroïdal étant antisymétrique (par rapport à l'équateur, c'est la « loi de Hale »), les taches leader vont voir leurs champs résiduels plus facilement annihilés par diffusion au travers de l'équateur alors que le champ résiduel des taches suiveuses va pouvoir être transporté par la circulation mérienne de surface vers les pôles en contribuant à former une composante poloïdale du champ moyen. Dans ces modèles, il faudra alors invoquer l'existence d'une circulation mérienne profonde pour transporter ce champ vers la tachocline où il pourra être transformé en champ toroïdal et amplifié jusqu'à générer à nouveau des tubes de flux

qui émergeront sous forme de nouvelles taches sur la photosphère. Ce type de modèles cinématiques de la dynamo dans lesquels la circulation méridienne est invoquée pour relier la surface source du champ poloïdal à la tachocline source du champ toroïdal est appelé « modèle de transport de flux » (e.g. Dikpati & Charbonneau (1999)). Le mécanisme de Babcock-Leighton génère une composante poloïdale à partir des taches qui sont la manifestation du champ toroïdal profond, il est donc modélisé en introduisant dans l'équation (1) un terme proportionnel au champ toroïdal ($S_{BL}B_\phi$). L'équation de la dynamo incluant les deux types de mécanismes sources de champ poloïdal peut donc s'écrire sous la forme générée :

$$\frac{\partial \mathbf{B}}{\partial t} = \nabla \times (\mathbf{U} \times \mathbf{B} - \eta \nabla \times \mathbf{B} + \alpha \mathbf{B} + S_{BL} B_\phi \hat{\mathbf{e}}_\phi). \quad (3)$$

Ceci représente donc l'équation principale des modèles cinématiques de la dynamo incluant une circulation méridienne et pour laquelle l'héliosismologie globale et locale va pouvoir apporter des contraintes.

I.2 Méthodes

I.2.1 Principes de l'héliosismologie globale et locale

En 2013 nous avons célébré à Tucson les 50 ans de l'héliosismologie (Jain, et al. 2013). Leighton et al. (1962) ont en effet découvert que la surface du Soleil était entièrement couverte d'éléments oscillant verticalement. La période de ces oscillations étant proche de cinq minutes, ce signal est depuis nommé « oscillations à 5 minutes du Soleil ». L'analyse locale de la propagation de ce champ d'ondes constitue ce que l'on appelle l'héliosismologie locale mais elle ne pourra être développée véritablement qu'avec l'avènement des observations à haute résolution spatiale à partir des années 1990. Au début des années 1970 l'interprétation en termes d'ondes acoustiques piégées dans l'enveloppe externe du Soleil a été suggérée par Ulrich (1970) et Leibacher & Stein (1971). Dès lors il devenait possible d'identifier les ondes observées aux modes propres d'oscillation du Soleil. Ces modes propres peuvent alors être décomposés sur la base des harmoniques sphériques $Y_l^m(\theta, \varphi)$ et décrit par leurs fréquences ν , leurs ordres radiaux n décrivant le nombre de nœuds de l'onde à l'intérieur, leurs degrés l et leurs ordres azimutaux m décrivant leur géométrie en surface (Figure 7). Cette hypothèse sur la nature globale des oscillations sera ensuite pleinement validée par l'acquisition d'observations résolues qui ont permis à Deubner (1975) d'établir un diagramme $k_h-\omega$ (où $k_h = \sqrt{l(l+1)}/r$ est le nombre d'onde horizontal et $\omega=2\pi\nu$ la pulsation) montrant que l'énergie des modes se concentre, sur ce diagramme, sur des lignes distinctes. La même année, Ando & Osaki (1975) obtiennent théoriquement, par un calcul non-adiabatique, les fréquences propres d'oscillations non-radiales du Soleil. La superposition des fréquences théoriques et du diagramme $k_h-\omega$ observé montrera un accord presque parfait. Le « presque » sera le véritable début de l'héliosismologie globale, c'est-à-dire le

processus par lequel l'observation et la caractérisation (fréquences, amplitudes, largeurs, etc..) des modes propres d'oscillations va permettre d'améliorer les modèles de la structure et de la dynamique interne du Soleil.

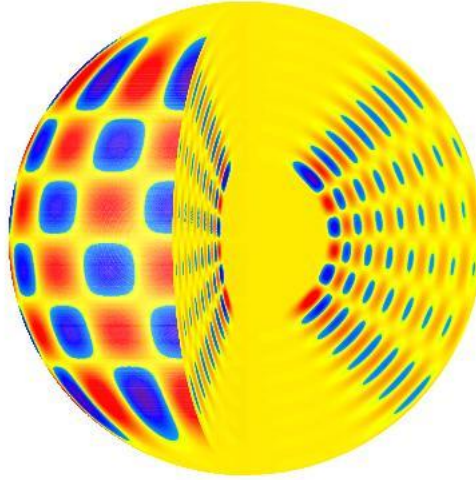


Figure 7. Illustration de la géométrie associée à un mode d'oscillation acoustique $l = 20, m = 15, n = 13$. Les zones en rouge représentent un mouvement vertical vers le haut alors que les zones en bleue se déplacent en sens opposé. L'ordre radial n donne le nombre de noeuds à l'intérieur. A la surface il y a $l - m$ lignes de noeuds selon des parallèles et m lignes de noeuds selon des longitudes. Les modes acoustiques n'ont pas d'amplitude dans le cœur nucléaire.

Sous l'approximation de Cowling dans laquelle on néglige la perturbation du potentiel gravitationnel, l'équation de dispersion des modes d'oscillation peut s'écrire sous la forme :

$$k_r^2 + k_h^2 \left(1 - \frac{N^2}{\omega^2} \right) = \frac{\omega - \omega_c^2}{c^2} \quad (4)$$

où c est la vitesse du son, k_r la composante radiale du vecteur d'onde, N la fréquence de Brunt-Väisälä et ω_c la fréquence de coupure acoustique. Les modes oscillent en fonction de r dans le domaine où k_r est réel et sont évanescents dans les régions où k_r est imaginaire. Cela définit deux types de modes : les modes de pression (modes p où modes à 5 mn) pour lesquels $\omega > c k_h$ et $\omega > \omega_c$ et, à plus basses fréquences, les modes de gravité (modes g) confinés dans l'intérieur radiatif dans une région où $\omega < N$. En fait il est possible de montrer, toujours sous l'approximation de Cowling, que, pour ces modes (p et g) c'est la quantité $\psi = c^2 \rho^{\frac{1}{2}} \operatorname{div} \delta \mathbf{r}$ où ρ est la densité et $\delta \mathbf{r}$ le vecteur déplacement, qui obéit à l'équation d'oscillation sous la simple forme $\frac{d^2 \psi}{dr^2} = -k_r^2 \psi$. Il existe cependant une troisième catégorie de modes qui ne peuvent être décrit par cette équation : ce sont les modes fondamentaux (ou modes f) incompressibles pour lesquels $\operatorname{div} \delta \mathbf{r} \approx 0$ et $n=0$. Quand la surface est considérée comme une simple discontinuité de densité, ces modes se comportent comme des ondes de surface suivant une relation de dispersion ne

dépendant que de la gravité de surface $g_s = \frac{GM}{R^2}$ où M et R sont respectivement la masse et le rayon du modèle :

$$\omega^2 = g_s k_h = \frac{GM}{R^3} l(l + 1) \quad (5)$$

Dans le diagramme l - ν ces modes sont à l'interface entre modes p et modes g (Figure 8). Les modes f de degrés intermédiaires et élevés ($l > 110$) sont observés. D'après l'équation (5), la fréquence de ces modes est, en première approximation, indépendante de la stratification interne et ils sont donc un diagnostic intéressant et robuste pour les effets les plus superficiels et notamment la circulation photosphérique et sub-photosphérique. Avec M. Thompson nous avons développé une méthode spécifique pour exploiter les splittings des modes f observés par MDI sur SoHO ce qui nous a permis pour la première fois d'obtenir une mesure robuste du gradient radial de la rotation sub-photosphérique là où l'analyse des modes p de degrés intermédiaires ne permettait pas d'obtenir une résolution spatiale suffisante.

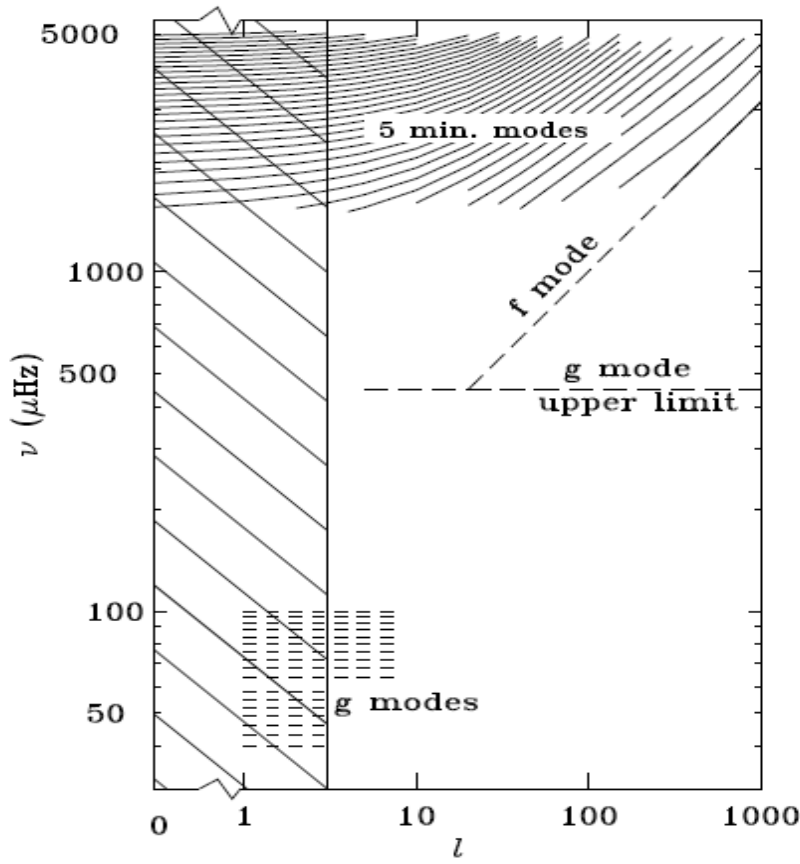


Figure 8. Représentation schématique des domaines des modes p, g et f dans un diagramme l - ν théorique. Dans le domaine des oscillations à 5 minutes chaque ligne représente un ordre radial n différent. Les modes f ont des fréquences inférieures aux modes p et correspondent à $n=0$. Ils sont observés pour $l > 120$. Les modes g ont des fréquences inférieures à 0.5 mHz et n'ont pas été détectés avec certitude pour le Soleil. La zone hachurée montre la zone des modes détectables par intégration du signal sur la Soleil entier ou sur une étoile non résolue (Christensen-Dalsgaard 2014).

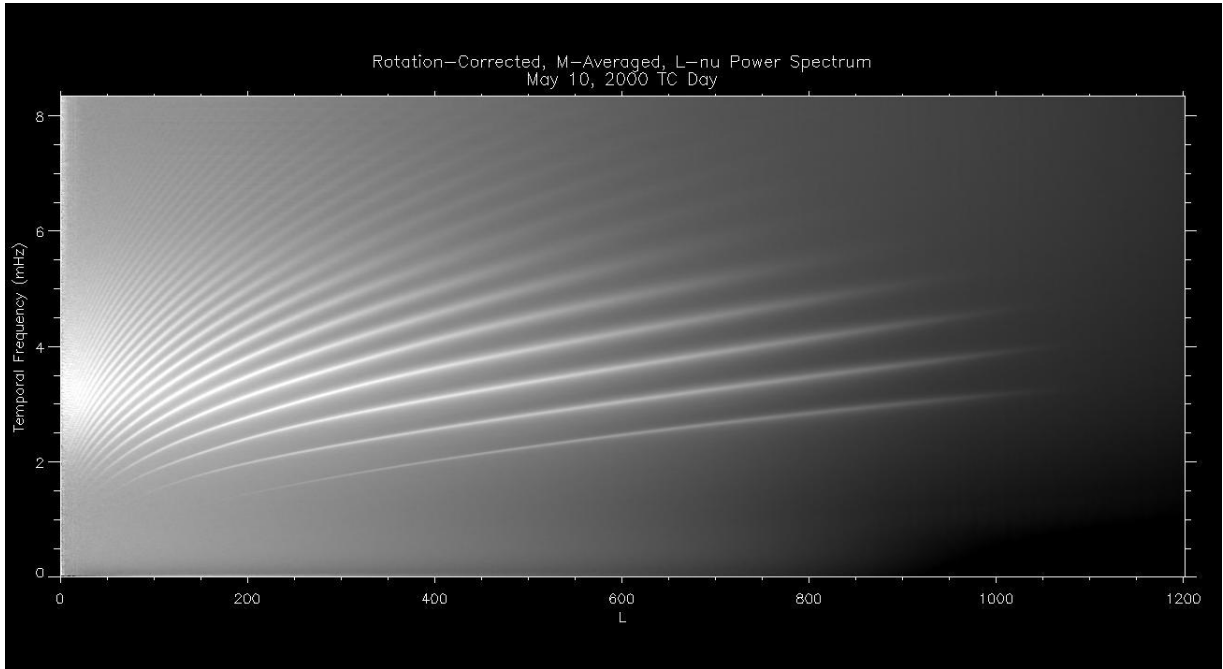


Figure 9. Exemple d'un diagramme $\mathbf{l}-\nu$ obtenu à partir des données du réseau GONG. Chaque ligne représente un ordre radial n différent. Les modes f ($n=0$) sont visibles pour $l>200$ sur la ligne la plus basse en fréquence.

Pour l'héliosismologie locale, c'est-à-dire l'analyse locale de la propagation du champ d'onde observé soit en soleil calme soit autour de régions actives, on utilise les modes de degrés élevés. La longueur d'onde de ces modes étant petite par rapport à l'échelle typique à laquelle la structure d'équilibre change, il est possible de faire une simple approximation en onde plane et d'utiliser la géométrie Cartésienne (x,y,z) , où (x,y) représente le plan sur la photosphère et z la profondeur, au lieu des coordonnées sphériques. Le nombre d'onde horizontal se décompose alors selon ses composantes suivant x et y et l'équation de dispersion en l'absence de champ de vitesse ou de champ magnétique serait simplement:

$$k^2 = k_z^2 + k_h^2 = \frac{\omega^2}{c^2} \quad k_h^2 = k_x^2 + k_y^2 \quad (6)$$

En héliosismologie globale k_h étant simplement lié au degré \mathbf{l} , les diagrammes $\mathbf{l} - \nu$ où $\mathbf{k}_h - \omega$ sont équivalents. Pour l'héliosismologie locale l'équivalent est une représentation 3D $(\mathbf{k}_x, \mathbf{k}_y, \omega)$ du spectre de puissance obtenu sur un domaine restreint de la surface.

Une autre différence entre l'héliosismologie locale et globale est que pour cette dernière, c'est-à-dire l'analyse des modes propres d'oscillation, on utilise des séries temporelles qui sont d'une durée bien supérieure à la durée de vie des modes (typiquement deux ou trois « mois GONG » de 36 jours soit des séries de 72 ou 108 jours). Ceci permet de mesurer très précisément toutes les caractéristiques des modes (fréquences, amplitudes, largeurs, splittings) dans le spectre de puissance. Mais cette longue intégration dans le temps ne

permet pas d'étudier l'évolution rapide du magnétisme ou de la dynamique. Seule l'étude locale du champ d'onde sur des temps beaucoup plus court permet ces investigations.

I.2.2 L'analyse globale des modes f (article)

ARTICLE : The subsurface radial gradient of solar angular velocity from MDI f-mode observations

(Corbard et Thompson 2002)

L'instrument MDI sur SoHO nous a offert pour la première fois la possibilité de mesurer précisément les propriétés des modes fondamentaux du Soleil et notamment leur dégénérescence par la rotation ainsi que leur évolution dans le temps. La méthode d'analyse que nous avons développée dans Corbard & Thompson (2002) est une adaptation des méthodes classiques de l'héliosismologie globale au cas particulier de ces modes. Non seulement les modes f sont très peu sensibles à la stratification interne mais, en plus, leur fonctions propres se présentent sous la forme d'un pic unique d'énergie bien localisé sous la surface. Le maximum de ce pic sera d'autant plus profond que le mode a un degré faible allant de $r/R=0.990$ pour $l = 117$ à $r/R=0.995$ pour $l = 300$ (cf. Figure 1 de Corbard & Thompson (2002)) L'information apportée par chaque mode observé est donc très bien définie et localisée sous la photosphère et, contrairement aux modes p, il n'est pas nécessaire de combiner plusieurs modes par inversion pour obtenir une information radiale localisée. Cependant, pour obtenir une information localisée en latitude, il faut décomposer la dépendance latitudinale de la rotation sur une certaine base polynomiale. Nous avons montré que les coefficients de Clebsch-Gordan utilisés pour exprimer la dépendance en fréquence des différentes composantes du splitting rotationnel peuvent être directement reliés à un développement de la rotation sur les polynômes de Gegenbauer et que les observations de MDI permettent d'atteindre une résolution d'environ 10° de l'équateur jusqu'aux hautes latitudes. En faisant une simple hypothèse de linéarité dans le domaine entre 3 et 10 Mm sous la photosphère sondé par ces modes, il devient alors possible d'étudier le gradient radial de rotation dans cette zone pour chaque latitude et ce d'une manière très robuste qui évite en grande partie le processus d'inversion qui, habituellement, introduit une part d'incertitude par l'introduction de la régularisation nécessaire pour rendre le système numériquement stable.

THE SUBSURFACE RADIAL GRADIENT OF SOLAR ANGULAR VELOCITY FROM MDI *f*-MODE OBSERVATIONS

T. CORBARD and M. J. THOMPSON

*Space and Atmospheric Physics Group, The Blackett Laboratory, Imperial College,
London SW7 2BW, U.K.*

(Received 6 September 2001; accepted 12 October 2001)

Abstract. We report quantitative analysis of the radial gradient of solar angular velocity at depths down to about 15 Mm below the solar surface for latitudes up to 75° using the Michelson Doppler Imager (MDI) observations of surface gravity waves (*f* modes) from the Solar and Heliospheric Observatory (SOHO). A negative outward gradient of around $-400 \text{ nHz}/R_\odot$, equivalent to a logarithmic gradient of the rotation frequency with respect to radius which is very close to -1 , is found to be remarkably constant between the equator and 30° latitude. Above 30° it decreases in absolute magnitude to a very small value at around 50° . At higher latitudes the gradient may reverse its sign: if so, this reversal takes place in a thin layer extending only 5 Mm beneath the visible surface, as evidenced by the most superficial modes (with degrees $l > 250$). The signature of the torsional oscillations is seen in this layer, but no other significant temporal variations of the gradient and value of the rotation rate there are found.

1. Introduction

The velocity field of the rotational flow in the Sun's near-surface layers may play a significant role in small-scale dynamo action in that region and in the dynamics of supergranular convection. Surface observations over decades and even centuries have shown that the latitudinal variation of the surface rotation is rather smooth, being rather well described by a three-term (i.e., second-order) polynomial in μ^2 where $\mu = \cos \theta$ and θ is the colatitude. Recent analyses of high-resolution data, in particular those utilizing solar *f*-mode observations by the Michelson Doppler Imager (MDI) on board the Solar and Heliospheric Observatory (SOHO), have highlighted important departures from such a description of the rotation of the near-surface layers. The polar subsurface layers (i.e., $\theta < 20^\circ$ and depths down to 28 Mm below the surface) have been shown to be approximately 10 nHz slower than expected from a simple three-term extrapolation from lower latitudes (Birch and Kosovichev, 1998; Schou *et al.*, 1998; Schou, 1999) and Kosovichev and Schou (1997) have shown that, at a depth of 2 to 9 Mm beneath the surface, there exist zonal bands of alternate faster and slower rotation rate of $\sim \pm 5 \text{ m s}^{-1}$ superimposed on the general trend described by the second order polynomial. This latter feature, inferred from the first observations of MDI in 1996, was found to be similar to the surface 'torsional oscillations' (Howard and Labonte, 1980) and



Solar Physics **205**: 211–229, 2002.

© 2002 Kluwer Academic Publishers. Printed in the Netherlands.

also observed in 1995 in Doppler measurements using the first GONG observations (Hathaway *et al.*, 1996.) More recently still, analysis of both p and f modes from the GONG network and MDI instrument have further led to the conclusion that these banded structures extend at least down to 60 Mm below the surface (Howe *et al.*, 2000).

The observed f modes, being confined to the outer layers of the Sun, provide a relatively clean and straightforward measure of conditions there. But those results above that were obtained just from the f modes assumed at least implicitly that the angular velocity is not varying significantly with depth within the layer sensed by those modes. It is, however, well known that another important property of the subsurface layers is that they present a radial gradient of angular velocity. This was first suggested by the fact that different indicators such as Doppler shifts of photospheric Fraunhofer lines, various magnetic field features of different ages and sizes (sunspots, faculae, network elements, H α filaments) or the supergranular network, present different rotation rates (see the review of Howard, 1984; Schroeter, 1985; Snodgrass, 1992). This has been interpreted by assuming that the different magnetic features are anchored at different depths (e.g., Foukal, 1972; Collin *et al.* 1995), their different rotation rate being therefore interpreted as an indication of the existence of radial gradients of angular velocity in the subsurface layers. More specifically, noticing that the supergranular network rotation rate (~ 473 nHz) was found to be $\sim 4\%$ faster than the upper photospheric plasma rate obtained from spectroscopic methods and also $\sim 2\%$ faster than various magnetic indicators thought to be rooted under the supergranulation layer, Snodgrass and Ulrich (1990) inferred that a maximum of angular velocity should exist somewhere between $0.95 R_{\odot}$ and the surface.

From the theoretical point of view, it has been suggested that the angular momentum per unit mass $\Omega r^2 \sin^2 \theta$ could be conserved in the supergranular flow (Foukal and Jokipii, 1975; Foukal, 1977; Gilman and Foukal, 1979). From $\partial \Omega / \Omega = -2\partial r / r$, at fixed latitude, this simple argument leads effectively to a negative gradient below the surface, and the 4% difference in rotation rates would be explained if the supergranulation network velocity observed at the surface were reflecting the rotation rate at a depth of $2\% R_{\odot} \simeq 15$ Mm, which turns out to correspond to the depth expected for the supergranular convection (Foukal, 1977; Duvall, 1980) (but see also Beck and Schou, 2000, for a more recent estimate). In order to reproduce the observed patterns of solar activity such as the equatorward migration of sunspots, early dynamo models based on a positive surface α -effect indicated also that the angular velocity must decrease outwards, i.e., $\partial \Omega / \partial r < 0$ (e.g., Leighton, 1969; Roberts and Stix, 1972). One of the first goals of helioseismology was therefore to test the assumptions about the negative gradient of angular velocity below the surface suspected from different surface observations. This was indeed first attempted by Deubner, Ulrich, and Rhodes (1979): although they did not resolve individual modes, they were able, from ridge-fitting separately the eastward- and westward-propagating near-equatorial waves in the

(k, w) diagram, to detect such a negative gradient close to the surface. Subsequent helioseismic work using resolved mode frequencies has shifted much theoretical focus to the base of the convection zone by showing that the radial gradient of angular velocity in the bulk of the convection zone is weak and that a strong radial shear, the so-called tachocline, occurs at its base. The gradient $\partial\Omega/\partial r$ is positive in the tachocline at sunspot (i.e., low) latitudes (Brown *et al.*, 1989). This has led various dynamo theories to locate the dynamo action below the convection zone, with a negative α -effect operating there (e.g., Gilman, Morrow, and Deluca, 1989; Parker, 1993) though some recent work has revisited the idea of a positive surface α -effect but invoking the action of a meridional circulation, equatorward below the convection zone and poleward at the surface, to produce the observed equatorward migration of sunspots by advective transport of flux (Dikpati and Charbonneau, 1999; Küker, Rüdiger, and Schultz, 2001). The lack until recently of precise determinations of high-degree mode parameters made it difficult to obtain very localized inferences about the subsurface layers. But, because all the observed modes have large amplitude close to the surface, inverters again got hints about the existence of a radial shear close to the surface (especially using methods such as regularized least-squares which readily extrapolate into regions where the data provide no localized information) though without being able to quantify precisely its extent and amplitude (e.g., Thompson *et al.*, 1996; Corbard *et al.*, 1997).

We show in this work that f -mode observations allow us to make quantitative inferences about the surface radial shear. These should be taken into account when modeling near-surface dynamo action or the dynamics of the supergranulation layer.

2. Observations

The data used here are 23 independent time series of 72 days obtained from the so-called MDI medium- l program. These cover the period from 1 May 1996 to 4 April 2001 with interruptions during the summer 1998 (23 June to 23 October) and between 4 December 1998 and 4 February 1999 due to SOHO spacecraft problems. More details on the production of these time series from the observations can be found in Schou (1999).

A given f -mode multiplet in the spectra comprises $2l+1$ frequencies ν_{lm} , where l and m are the degree and azimuthal order of the spherical harmonic $Y_l^m(\theta, \phi)$ describing the angular dependence of the modes. The so-called a coefficients for the multiplet are defined by the polynomial expansion:

$$\nu_{lm} = \nu_{l0} + \sum_{j=1}^{2l} a_j^l \mathcal{P}_j^{(l)}(m) \quad m = \pm 1, \pm 2 \dots \pm l, \quad (1)$$

where \mathcal{P} are orthogonal polynomials normalized such that $\mathcal{P}_j^{(l)}(l) = l$ (Schou, Christensen-Dalsgaard, and Thompson, 1994). All f modes considered here have

degrees between $l = 117$ and $l = 300$ but the total number of multiplets observed is between 112 and 143, depending on the 72-day interval considered. For each observed mode, the central frequencies ν_{l0} and the first 36 a coefficients have been estimated using the method described in Schou (1992). Odd-indexed a coefficients, which describe the dependence of the frequencies that is an odd function of m , arise from the north-south symmetric part of the solar rotation. Even-indexed coefficients arise from latitudinal structural variation, centrifugal distortion and magnetic fields.

3. Data Analysis

Following Ritzwoller and Lavelle (1991), we identify the north-south symmetric part of the angular velocity $\Omega(r, \mu)$ with the odd-degree, zonal part of the toroidal component of a general stationary and laminar velocity field and write

$$\Omega(r, \mu) = \sum_{j=0}^{\infty} \Omega_{2j+1}(r) \bar{T}_{2j}^1(\mu) , \quad (2)$$

where r is fractional radius and $\bar{T}_{2j}^1 = T_{2j}^1(\mu)/T_{2j}^1(0)$ are Gegenbauer polynomials (see Appendix) normalized such that the equatorial rate is given by the straight sum of the $\Omega_{2j+1}(r)$.

Assuming slow rotation, we can use a linear perturbation theory to predict the effect of rotation on the oscillation modes (e.g., Hansen, Cox, and Van-Horn, 1977). Moreover, with the polynomials \mathcal{P} and expansion Equation (2) as chosen, there is a one-to-one relation between odd a coefficients and the components $\Omega_{2j+1}(r)$ (Ritzwoller and Lavelle, 1991), thereby reducing the full 2D problem to a set of 1D integral equations often referred to as the 1.5D problem. In the particular case of the f modes, we obtain

$$2\pi a_{2j+1}^l = u_{2j+1}^l \int_0^1 K_h^l(r) \Omega_{2j+1}(r) dr , \quad (3)$$

where the expression for the kernels $K_h^l(r)$ and u_{2j+1}^l are derived in the Appendix.

The 36 a coefficients extracted from observation do not provide information about the terms above $j = 17$ in the summation in Equation (2) and that corresponds to a limitation in the latitudinal resolution we can reach. Defining

$$b_{2j+1}^l \equiv \frac{2\pi a_{2j+1}^l}{u_{2j+1}^l} , \quad (4)$$

from Equations (2)–(4) we obtain

$$\sum_{j=0}^{17} b_{2j+1}^l \bar{T}_{2j}^1(\mu_0) \approx \int_0^1 K_h^l(r) \bar{\Omega}(r, \mu_0) dr , \quad (5)$$

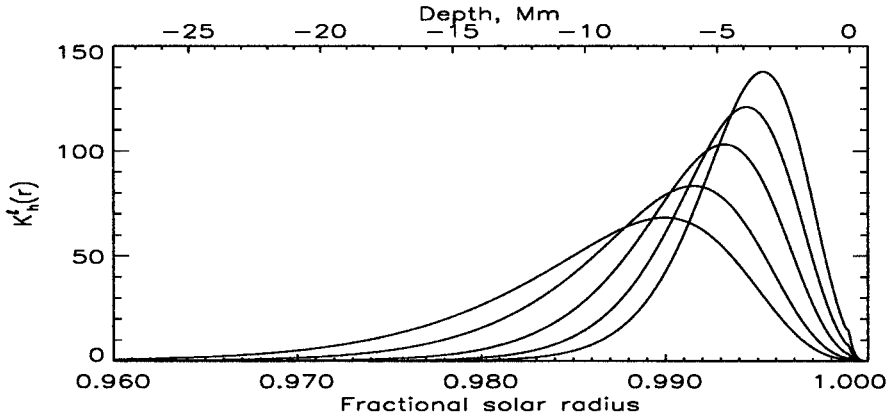


Figure 1. f -modes rotational kernels $K_h^l(r)$ for $l = 117, 150, 200, 250, 300$ from left to right.

where $\bar{\Omega}(r, \mu)$ refers to the part of the rotation profile corresponding to the sum Equation (2) truncated at $j = 17$. We can also show (Pijpers, 1997) that the above linear combination of b coefficients is such that

$$\sum_{j=0}^{17} b_{2j+1}^l \bar{T}_{2j}^1(\mu_0) = \int_0^1 \int_0^1 K_h^l(r) \kappa(\mu_0, \mu) \Omega(r, \mu) dr d\mu , \quad (6)$$

where $\kappa(\mu_0, \mu)$ are the so-called latitudinal averaging kernels which show what latitudinal average of the true rotation rate is made at each latitude. Figure 2(a) shows that these kernels have their main peak centered at μ_0 but present an oscillatory behavior which may lead to systematic errors if some small-scale features (corresponding to terms with $j > 17$) exist in the true rotation rate. In order to avoid this, one may try to find instead the combination of b coefficients that leads to kernels that are optimally localized around a given latitude. This can be achieved following for instance the method of Backus and Gilbert (1968), but we notice here that a similar result can be obtained simply by introducing, in the sum of Equation (6), a correcting factor $e^{-j(j+3/2)/l_0}$ where $l_0 \equiv 117$ corresponds to the lowest degree of the observed f modes (see also Equation (15)). Doing this, the latitudinal averaging kernels are found better peaked (Figure 2(b)) and the formal errors associated with the linear combination of the b coefficients is lowered. Following the definition of Corbard *et al.* (2001), the latitudinal resolution obtained is about 10° at all latitudes.

The kernels $K_h^l(r)$ associated with each f mode have a simple shape with only one maximum located at slightly different radial positions depending on the degree l (Figure 1). If we define $r_0^l \equiv \int_0^1 K_h^l(r) r dr$, the radial location of the center of gravity of these kernels, and assume a linear behavior of the rotation rate at each latitude in the radial domain where the f modes considered have appreciable amplitude, i.e.,

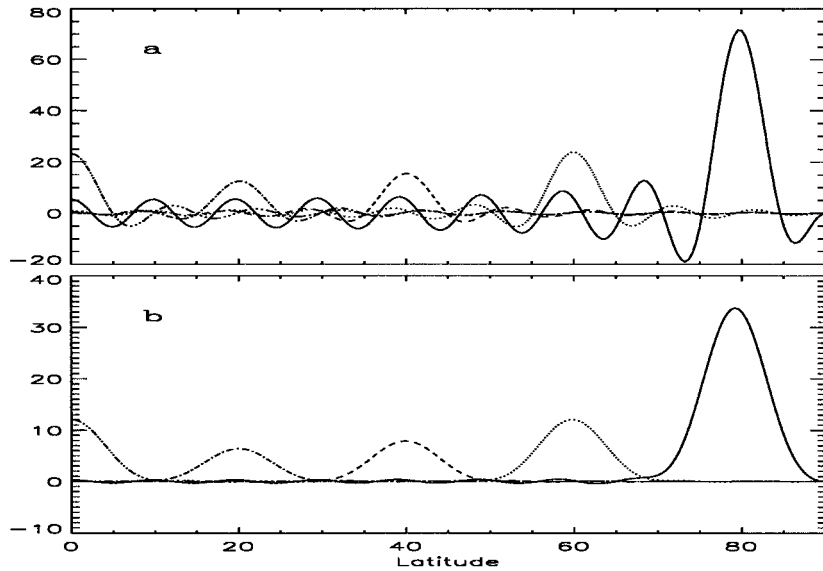


Figure 2. Latitudinal averaging kernels at 0, 20, 40, 60, 80° of latitude (double-dot-dash, dot-dash, dash, dot, and full lines, respectively) corresponding to the combination (a) Equation (8), (b) Equation (9).

$$\Omega(r, \mu_0) = \alpha(\mu_0) - \beta(\mu_0)(r - 1) \quad (7)$$

in $r > 0.97$, say, we simply obtain

$$\sum_{j=0}^{17} b_{2j+1}^l \bar{T}_{2j}^1(\mu_0) \approx \bar{\Omega}(r_0^l, \mu_0) , \quad (8)$$

where the meaning of $\bar{\Omega}$ is the same as in Equation (5). Alternatively, a slightly modified choice of weights yields

$$\sum_{j=0}^{17} b_{2j+1}^l \bar{T}_{2j}^1(\mu_0) e^{-[j(j+3/2)]/117} \approx \langle \Omega(r_0^l, \mu) \rangle_{\mu_0} \approx \Omega(r_0^l, \bar{\mu}_0) , \quad (9)$$

where the brackets denote the weighted average around μ_0 , the weighting function being the kernels of Figure 2(b). The second approximate equality in Equation (9) would be exact if the rotation profile were a linear function of μ^2 in the domain covered by the averaging kernels (i.e., $\pm 10^\circ$), with $\bar{\mu}_0^2 \equiv \int_0^1 \kappa(\mu_0, \mu) \mu^2 d\mu$; the approximation is less good, however, at high solar latitudes.

The parameters α and β can then be estimated at each latitude from a linear least-squares fit, yielding not only an estimate of the value of the rotation rate at, e.g., the surface, but also an estimate of the average gradient $\partial \Omega / \partial r$ in the region sampled by the f modes. Finally we note that the dependence of Ω as a function of radius in the near-surface layers may sometimes conveniently be described by

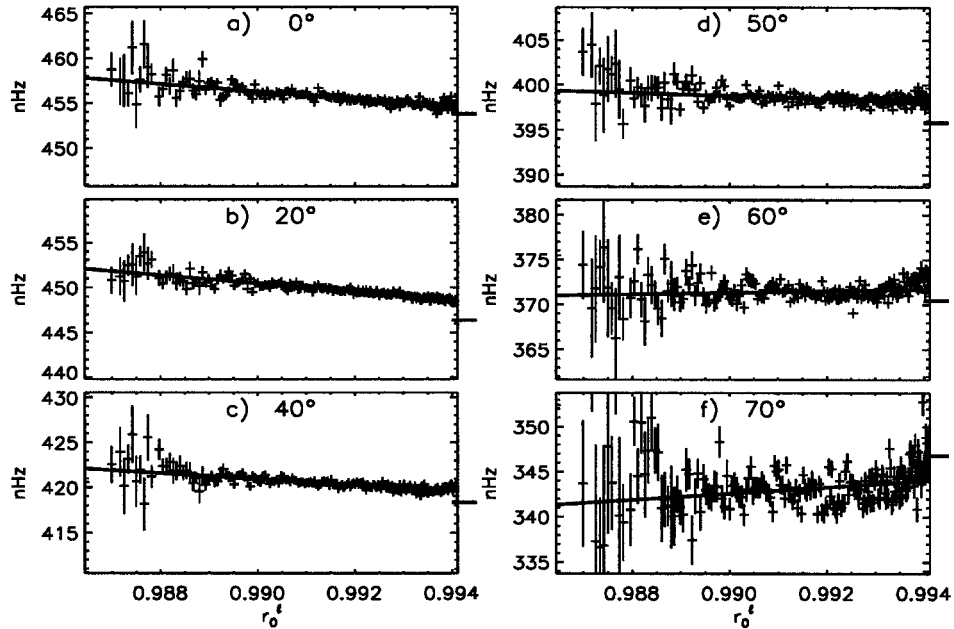


Figure 3. Time average of $\bar{\Omega}(r_0^l, \mu_0)/2\pi$ (Equation (8)) for values of μ_0 corresponding to the latitudes indicated in each panel. The result of the linear fits (Equation (7)) are shown by the straight lines. The error bars are the standard deviation associated with the weighted temporal mean. The mark on the right of each panel indicate the surface plasma rate obtained by Snodgrass, Howard, and Webster (1984). Note that the surface spectroscopic value indicated on panel f is essentially an extrapolation from observations at lower latitudes.

a power of r : we note that this description is immediately derivable from our α and β , since for small values of $1 - r$ the right-hand side of Equation (7) is well approximated by $\alpha(\mu_0)r^{-\alpha(\mu_0)/\beta(\mu_0)}$.

4. Results

By combining the frequency splittings within each f -mode multiplet in the manner given by Equation (8), for different choices of target latitude, we obtain measures of the near-surface rotation which are reasonably well localized in latitude and which correspond to different weightings in the depth direction. The latitudinal sensitivity is illustrated in Figure 2 and the depth sensitivity in Figure 1. Figure 3 shows the results of combining the data using Equation (8), averaged in time over all the datasets under study. In depth, the points are plotted at the center of gravity ($r = r_0^l$) of the corresponding kernels (cf., Figure 1). It is evident from these results that, at low latitudes, the weighted rotation increases with depth. If at each latitude separately we fit these results to a rotation profile that is linear in depth, we obtain the linear fits overplotted in Figure 3. These provide an average rotational gradient

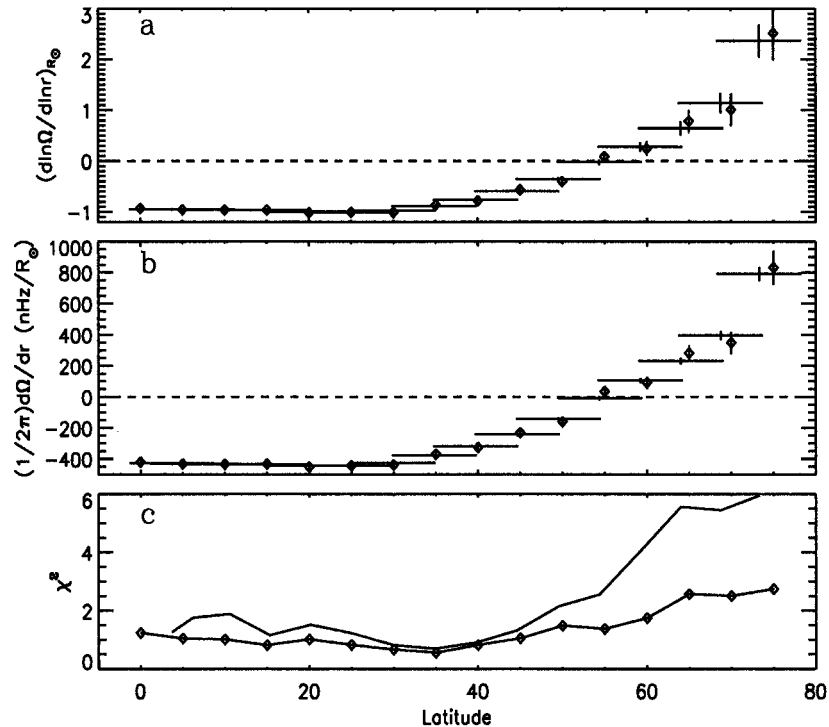


Figure 4. (a) Logarithmic derivative of angular velocity as a function of latitude. This corresponds to the ratio β/α of Equation (7). (b) Radial gradient of angular velocity β as a function of latitude. (c) Normalized χ^2 value of the linear fit. The *diamond symbols* are for the results obtained using Equation (8) while the other points are obtained using Equation (9). The *horizontal error bars* indicate the angular resolution as deduced from Figure 2(b). The *vertical error bars* are formal errors deduced from the linear fit. The *dashed horizontal lines* correspond to no radial gradient of angular velocity.

$\beta(\mu_0)$ in the outer 15 Mm or so of the solar interior, and an extrapolated surface rotation rate $\alpha(\mu_0)$. The gradient, as a function of latitude, is presented in Figure 4, both in terms of its dimensional value and in terms of the logarithmic derivative $\partial \ln \Omega / \partial \ln r$. It may be seen that for latitudes below 50° the gradient of rotation with depth is negative; at about 50° it is close to zero; and for higher latitudes the average rotational gradient becomes positive. We note that the radial gradient is remarkably constant at latitudes up to 30°, and the value of the logarithmic derivative at these latitudes is close to -1 . We return to this in Section 5.

Another way to visualize the changing gradient with latitude is that in Figure 5, where we show the rotation rate extrapolated both to the surface ($r = 1$) and to $r = 0.97$. The deeper rotation is faster than the surface rotation at low- and mid-latitudes, but slower at high latitudes. At low- and mid-latitudes the extrapolated surface rate agrees well with the spectroscopic surface measurements, given the approximately 1.5% spread in recent such determinations (see the review by Beck,

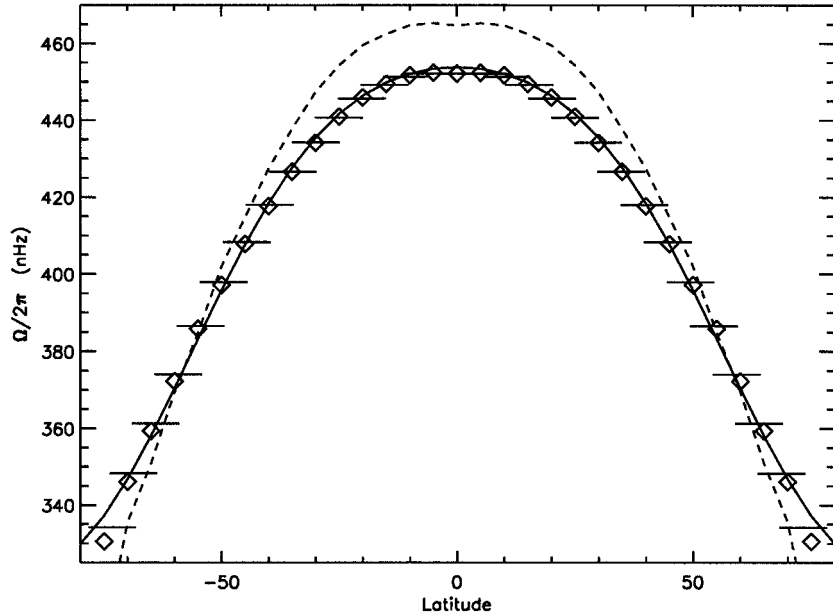


Figure 5. The full line gives the photospheric plasma rotation rate inferred by Snodgrass, Howard, and Webster (1984); the diamond symbols and horizontal bars corresponds to α , the intercept of the linear fit respectively in the case of Equations (8) and (9) and the dashed line corresponds to an extrapolation of the rotation rate at $0.97 R_{\odot}$ using Equation (7) in the case of Equation (8).

2000). For comparison, we have made a fit to our inferred surface rate below 60° latitude and present our fitting coefficients with the spectroscopic coefficients of Snodgrass, Howard, and Webster (1984) in Table I. Similarly to what has been found previously, our inferred rotation rate above 70° is markedly slower than what would be expected from a 3-term fit at low- and mid-latitudes: we return to this issue of the so-called ‘slow pole’ later.

Figure 4(c) shows the chi-squared for the least-squares fits at each latitude. The large chi-squared values at higher latitudes are striking. The difference between the chi-squared values when using Equations (8) and (9) is also very noticeable: this arises largely because the error bars on the fitted points are reduced by the exponential factor in Equation (9), which results in an increased chi-squared. Thus the interpretation of the absolute value of the chi-squared may be a little uncertain, but the trend with latitude for the two cases is similar. The larger values of chi-squared at higher latitudes is consistent with the greater deviation from a linear fit in the high-latitude panels of Figure 3. The systematic deviation of the near-surface points contributes most to the chi-squared: these correspond to the high-degree modes and so motivates taking a closer look at those data. (The scatter of the deepest points is large but less significant because of the large error bars on those points.)

TABLE I

Comparison between the surface plasma rate and our results from f -mode analysis.

Method	$\Omega_1/2\pi$ (nHz)	$\Omega_3/2\pi$ (nHz)	$\Omega_5/2\pi$ (nHz)
Snodgrass, Howard, and Webster (1984) ¹	436.4	21.0	-3.6
f modes (l -averaged) ²			
($117 \leq l \leq 300$) $\langle r_0^l \rangle = 0.991$ ³	438.8	21.0	-3.9
($160 \leq l \leq 250$) $\langle r_0^l \rangle = 0.991$	438.9	21.2	-4.0
f modes (surface extrapolation) ⁴			
($117 \leq l \leq 300$)	435.8	20.2	-3.2
($160 \leq l \leq 250$)	435.7	20.5	-3.6

¹Spectroscopic measurements made at the Mount Wilson 150-foot Tower between 1967 and 1982.

²Average of the first 3 b coefficients (cf., Equations (4) and (8)).

³Center of gravity of the corresponding l averaged radial kernels.

⁴Obtained by fitting the intercept $\alpha(\mu)$ to the expansion equation (2) for latitudes below 60° .

We have therefore repeated our analysis but excluding those modes of degree $l > 250$ and $l < 160$. The resulting gradient and chi-squared are shown in Figure 6. Compared with the previous result (Figure 4) the gradient is similar for latitudes lower than 50° . Now it is evident from Figure 3 that, at high latitudes, excluding the high-degree modes will tend to make the fitted gradient less positive. Indeed, we find that the gradient without the $l > 250$ data remains slightly negative up to about 75° . Also, the values of chi-squared have been more than halved at high latitude, compared with our previous linear fit to all the f -mode data (Figure 6(b)). The inferred low- and mid-latitude surface rate is barely affected (compare the last two lines of Table I).

It is interesting also to compare the linear fit to the $l < 250$ data with a fit of a constant function to the same data: the constant fit is equivalent averaging the f -mode splittings over l (see Table I). It is evident from Figure 6(b) (dotted line) that this provides a very poor fit below about 55° : the data strongly favor the model with a linear depth-dependence there. At high latitudes, the linear fit selects only a very small gradient and so the two chi-squared functions are very similar: the data for $l < 250$ indicate that at high latitudes the gradient is small, in the range of depths spanned by their lower turning points.

If the data for $l > 250$ are indeed reliable, then the discrepancy between the results in Figures 4(a) and 6(a) implies that the model of rotation varying linearly with depth is not appropriate at high latitudes and the extrapolation to the surface at those latitudes will be unreliable. An alternative approach is to attempt to construct

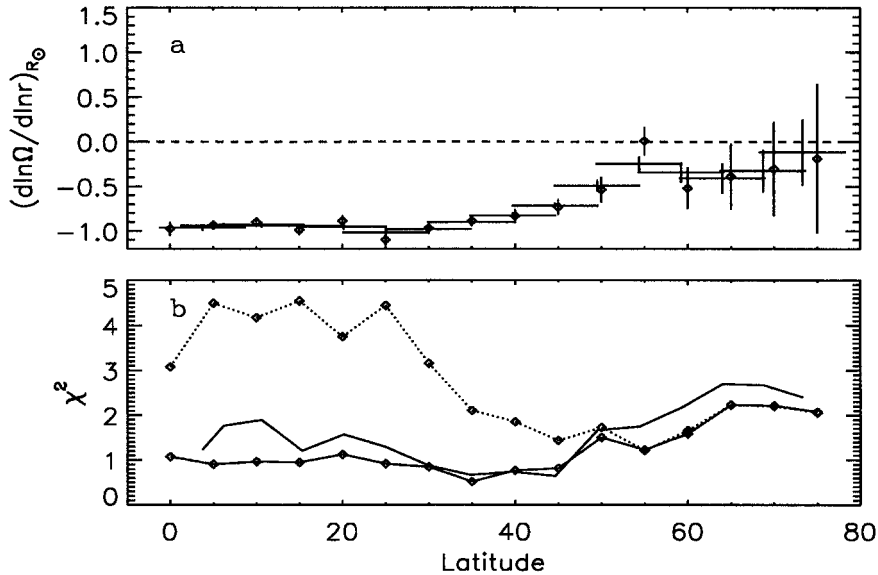


Figure 6. Similar to Figure 4 but using only modes $160 \leq l \leq 250$. The radial gradient of angular velocity remains negative even at latitudes above 55° . The dotted line on panel b shows, in the case of Equation (8), the χ^2 values corresponding to a fit by a constant which is equivalent of taking an average over l .

kernels that are localized in depth using the Optimally Localized Averaging (OLA) kernel in depth (cf., Christensen-Dalsgaard, Schou, and Thompson, 1990) in the manner of Backus and Gilbert (1968). Such kernels at two selected depths are shown in Figure 7: they were constructed using all the available f modes. It should be noted that the method succeeds in producing kernels which are reasonably localized and which have their center of gravity outside the range of abscissa values in Figure 3, that is, the method uses the mode sensitivities to extrapolate to greater depths and closer to the surface. In particular, in the latter case one expects that the increasing trend of values for the near-surface points in Figures 3(e) and 3(f) means that the near-surface Backus–Gilbert inversion at those latitudes will have values higher than those seen in Figure 3. This is exactly what is found (Figure 7): the Backus–Gilbert inversion at high latitudes for $r = 0.986$ interestingly falls below the 3-term spectroscopic surface rate, but even more strikingly the corresponding near-surface result at $r = 0.997$ lies above it by 2–4 standard deviations. This is another way of demonstrating that the increasing values of the combined splittings for $l > 250$, if they are reliable, indicate a strongly positive gradient of rotation with radius in the rather superficial subsurface layers at high latitudes.

To look for possible temporal variations of the subsurface shear, we have analyzed each one of the 23 72-day datasets individually in exactly the same manner as we analyzed the time-averaged set (e.g., Figure 3), and derived an intercept value $\alpha(\mu_0; t)$ (corresponding to the surface rate at that location and epoch) and slope

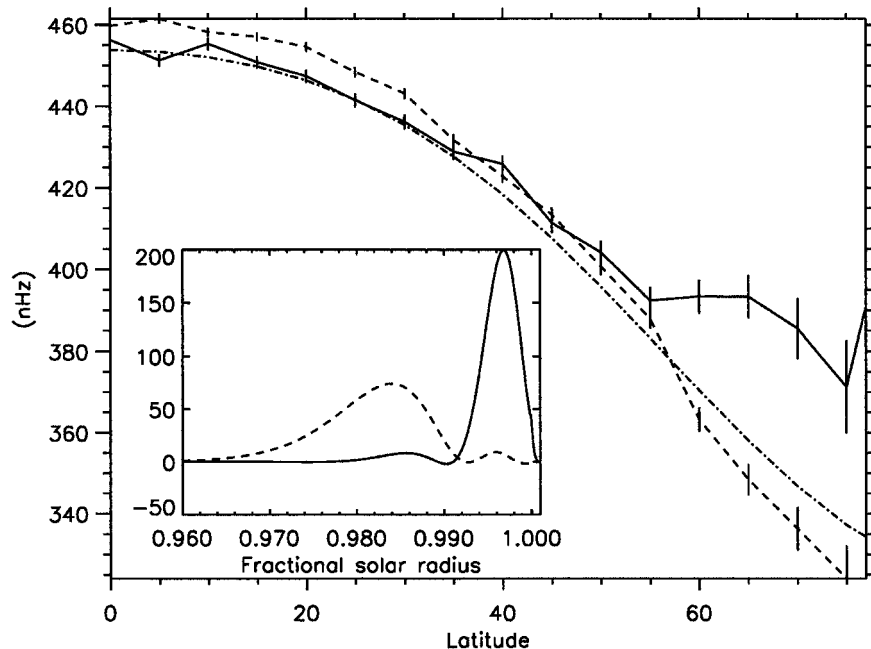


Figure 7. Rotation profiles as a function of latitude corresponding to depth averaged shown in the sub panel. The *dashed* and *full lines* correspond, respectively, to the shallower and deeper kernels which have respectively $0.986 R_{\odot}$ and $0.997 R_{\odot}$ as center of gravity. The *dot-dashed line* corresponds to the Snodgrass, Howard, and Webster (1984) plasma rotation rate. These results are obtained by using all modes from $l = 117$ to $l = 300$.

$\beta(\mu_0; t)$ from a linear fit to the combined splittings for each latitudinal location μ_0 and time t . The resulting estimated surface rates and slopes at three latitudes (equator, 30° , 60°) are shown in Figure 8. The large-scale variations in the surface rate correspond very well to the migrating banded zonal flows (torsional oscillations) measured by Schou (1999) and by Howe *et al.* (2000): the equatorial surface rate starts high because of the tail-end of one migrating band of faster flow, then drops down and rises again towards solar maximum as another band of faster flow reaches the equator: the latter was at 30° at the beginning of the cycle, hence the rate at that location starts high and drops as the band migrates closer to the equator. The 60° rate rises as the high-latitude banded flow reported by, e.g., Schou (1999) strengthens towards solar maximum. The slope shows no significant corresponding variations, implying that the torsional oscillations raise and lower the rotation rate across the whole depth of the layer without changing the shear gradient. There are indications of annual variations in the inferred values of the slope (most strikingly at 30°), which are almost certainly an artifact: such artifacts can conceivably arise from annual variations in SOHO's orbit. Other evidence for one-year artifacts in the f -mode data is presented by Antia *et al.* (2001). These should not affect the time-

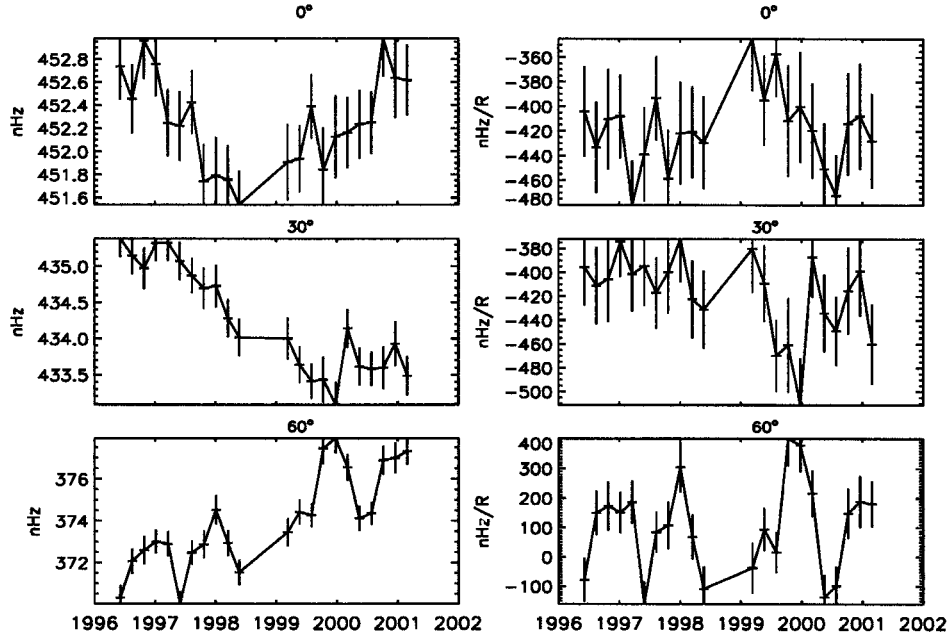


Figure 8. Intercept (left column) and slope (right column) of the linear fit Equation (7) at the equator, 30° and 60° of latitude (from top to bottom).

averaged values, however. There is no noticeable annual variation in our inferred values of the surface rotation rate.

5. Discussion

We have used the depth and latitude variation in the sensitivities of the solar f modes to deduce the rotation profile in the subsurface shear layer of the Sun in the outer 15 Mm of the solar interior. Our work differs from earlier seismic investigations. These were either based on the f modes but implicitly assumed a depth-independent model of the rotation (e.g., Schou, 1999), or used global inversions of p - and f -mode splittings and consequently may suffer from any systematic difference between the p - and f -mode data (e.g., Schou *et al.*, 1998), or used local helioseismic ring analysis (e.g., Basu, Antia, and Tripathy, 1999; Haber *et al.*, 2000), which promises to be a powerful diagnostic of near-surface flows and stratification but the sensitivity and systematics of which are still under investigation (Hindman *et al.*, 2001, in preparation). By using just the splittings of the f modes, which are arguably the most straightforward helioseismic modes to interpret, we believe we are able to obtain not only a simple but also a clean measure of the near-surface shear. As with all inferences about rotation from global splittings, we

note that only that component of rotation which is symmetric about the equator is recovered.

The most robust results concern the low-latitude shear. The average gradient $\partial \ln \Omega / \partial \ln r$ (at constant latitude) in the outer 15 Mm is close to -1 and remarkably constant from the equator to 30° latitude. Between 30° and 55° latitude, the gradient is still negative but makes a steady transition to a small (absolute) value. All our analyses show this. The variation of rotation at these latitudes appears to be well described by a linear function of depth, within the outer 15 Mm.

As discussed in the Introduction, if moving parcels of fluid were to conserve their specific angular momentum as they moved towards or away from the rotation axis, one would find that the rotation rate varied as the inverse square of the distance from the axis of rotation, so at low latitudes one would have that $\partial \ln \Omega / \partial \ln r \approx -2$. In reality other effects such as diffusion will cause exchange of angular momentum between parcels, so we may expect a logarithmic gradient somewhat smaller in magnitude than -2 . A precise measurement of this value in the Sun provides information about the relative effectiveness of competing mechanisms transporting angular momentum. Our finding is that at latitudes below 30° the value of the logarithmic gradient is much closer to -1 than to -2 . In fact, this seems in reasonable agreement with the equatorial value found by DeRosa in numerical simulations of rotating compressible convective fluid in a thin shell representing the Sun between about $0.94R_\odot$ and $0.98R_\odot$ (DeRosa, 2001; DeRosa, Gilman, and Toomre, 2001). Also these simulations show a tendency for the gradient to decrease in magnitude as one moves from equator to mid-latitudes, albeit at lower latitudes than we find for the Sun. Although these simulations exclude for numerical reasons the near-surface layers that we are probing, the qualitative agreement is nonetheless encouraging.

At latitudes above $\sim 55^\circ$, the depth-averaged gradient over the layer appears to change sign with respect to the low-latitude shear, though this is largely a consequence of the behavior in the very near-surface layers (outer 5 Mm) which in turn is deduced from the splittings of the highest-degree f modes. The gradient in the range of depths 5–15 Mm is small at these high latitudes; and such significant gradient $\partial \Omega / \partial r$ as does exist at high latitude (if any) is in the outer 5 Mm and predominantly positive. We note that, using a ring-analysis technique, Basu, Antia, and Tripathy (1999) deduced a similar behavior at high latitudes, finding a reversal of gradient in a zone above $0.994 R_\odot$.

Concerning the surface rotation rate itself, below 55° our extrapolation of the rotation rate to the surface is in satisfactory agreement with the directly measured spectroscopic surface rotation rate (cf., Table I). Our inferred surface rate should be more accurate than one simply inferred from the averaged f -mode splittings, because we take out the linear gradient with depth which undoubtedly exists at these latitudes: this can make a difference of ~ 5 nHz, even over the fairly small range of depths sampled by the observed f modes.

The seismically inferred surface rate at high latitudes is considerably less secure. It has previously been reported from helioseismic investigations that the high-latitude surface rate is lower what one would expect from a simple three-term extrapolation from lower latitudes (Schou, Christensen-Dalsgaard, and Thompson, 1998; Schou, 1999). Indeed it can be seen from Figure 3(f) that many of the points fall below the extrapolated spectroscopic rate for that latitude, implying that the rotation rate at *some* depth is lower than the spectroscopic surface rate one would infer from the values in Table I. The rather flat plateau of values in those panels strongly suggests that the rotation rate at about 10–15 Mm depth is slower than the extrapolated spectroscopic rate, which is confirmed by our OLA inversion result at those depths. However, the combined splittings at high degree are *increasing* with l and if taken at face value, as is done in our OLA inversion result for $r = 0.997R$, this behavior implies that the very near-surface rotation rate is actually higher than the spectroscopic rate. Thus the matter is still open. Since the quoted spectroscopic rate is principally an extrapolation of surface observations at low- and mid-latitudes, the true rotation rate that would be determined by spectroscopy at high latitudes is uncertain. Direct spectroscopic determinations at high latitude would resolve the question. The very high-degree splittings could contain some systematic errors, and if these affect the low- m data the most (some evidence for such an effect for p modes at lower degrees is offered by the comparison of GONG and MDI splittings by Schou *et al.* (2001)), then the near-surface, high-latitude rotation rates inferred here could be erroneously high. We hope that this possibility will shortly be addressed by independent determinations of these splittings by the GONG experiment using the new higher-resolution GONG+ observations.

6. Conclusion

Finally, to return again to our principal focus which is the shear gradient of the near-surface rotation, we find that at low and mid-latitudes the gradient $\partial\Omega/\partial r$ in the outer 15 Mm or so is close to -1 and is quite independent of latitude below 30° ; between 30° and $\sim 50^\circ$ latitude, it is still negative but makes a transition to small absolute value. At higher latitudes, the gradient in the bulk of the outer 15 Mm is probably small, but if the highest-degree ($l > 250$) data are to be believed there is a region of positive gradient in the outer 5 Mm at high latitudes, similar to what (Basu, Antia, and Tripathy (1999) found from ring analysis. We find no evidence for the gradient to vary with time: the torsional oscillation seems to pass through without changing the shear gradient in the outer 15 Mm.

Interestingly, the most recent circulation-dominated dynamo models (Dikpati and Charbonneau, 1999; Küker, Rüdiger, and Schultz, 2001) are able to reproduce to some extent the equatorward migration patterns without invoking any radial gradient of angular velocity at the surface. Such negative gradient at low latitude should however probably be taken into account because if it is associated with

a positive surface α -effect, it will compete against the surface poleward circulation and contribute to producing the equatorward migration of magnetic patterns observed at the surface of the Sun.

Acknowledgements

We thank Jesper Schou for providing the data and Marc DeRosa, Mausumi Dikpati, François Lignières, and Peter Gilman for useful discussions. Juri Toomre and Steve Tomczyk are thanked for hospitality at JILA and HAO, respectively, where part of this work was carried out. The work was supported by the UK Particle Physics and Astronomy Research Council through the award of grant PPA/A/S/2000/00171.

Appendix. Derivation of f -Mode 1.5D Kernels

The polynomial \mathcal{P} used to describe the frequency splittings can be expressed in terms of the Clebsch-Gordan coefficients $C_{j_1 m_1 j_2 m_2}^{jm}$ (e.g., Edmonds, 1960) by

$$\mathcal{P}_j^{(l)}(m) = \beta_j^l C_{lmj_0}^{lm}, \quad \beta_j^l \equiv \frac{l\sqrt{(2l-j)!(2l+j+1)!}}{(2l)!\sqrt{2l+1}}. \quad (10)$$

The Gegenbauer polynomials used in Equation (2) are defined by (e.g., Morse and Feshbach, 1953)

$$T_{2j}^1(\mu) = \sqrt{\frac{4\pi}{4j+3}} \frac{\partial Y_{2j+1}^0(\theta, \phi)}{\partial \mu}. \quad (11)$$

From Ritzwoller and Lavelle (1991) we can deduce that

$$2\pi a_{2j+1}^l = \frac{v_{2j+1}^l}{T_{2j}^1(0)} \int_0^1 K_j^l(r) \Omega_{2j+1}(r) dr, \quad (12)$$

where $v_{2j+1}^l \equiv L^2 C_{l1(2j+1)0}^{l1}/\beta_{2j+1}^l$, $L^2 \equiv l(l+1)$ and

$$K_j^l(r) = \frac{(\xi_l^2 + (L^2 - 1 - j(2j+3))\eta_l^2 - 2\xi_l\eta_l) \rho r^2}{\int_0^1 (\xi_l^2 + L^2 \eta_l^2) \rho r^2 dr}, \quad (13)$$

ξ_l and η_l being respectively the radial and horizontal displacement eigenfunctions which are determined by solving the differential equations describing the motion of a self-gravitating fluid body in a standard solar model (e.g., Unno *et al.*, 1989) and ρ is the density profile given by the model, all these being functions of the fractional solar radius r .

Other expressions of practical interest can be found for v_{2j+1}^l that are recalled here for completeness. Pijpers (1997) established the recurrence relation

$$v_{2j+1}^l = \frac{(j-l)(2j+1)}{j(2l+2j+1)} v_{2j-1}^l \quad (14)$$

and Schou (1999) noticed that to a very good approximation

$$v_{2j+1}^l / T_{2j}^1(0) \approx e^{-j(j+3/2)/l}. \quad (15)$$

The f modes are horizontally propagating surface gravity waves for which the displacement eigenfunctions satisfy the following surface boundary condition under the Cowling approximation (e.g., Berthomieu and Christensen-Dalsgaard, 1991):

$$\eta_l(r) \approx \frac{g_s}{R_\odot w_l^2} \xi_l(r), \quad (16)$$

where $g_s = GM_\odot/R_\odot^2$ is the surface gravitational acceleration. Moreover, the angular frequencies $w_l = 2\pi\nu_{l0}$ of the f modes follow asymptotically (for $l \rightarrow \infty$) the dispersion relation $w_l^2 \approx g_s L/R_\odot$. Therefore we have $\xi_l \approx L\eta_l$ and, from Equation (13), the rotational kernels associated with the f modes can be written as a function of the horizontal displacement only:

$$K_j^l(r) \approx k_j^l K_h^l(r) \quad \begin{cases} K_h^l(r) \equiv \frac{\eta_l(r)^2 \rho(r) r^2}{\int_0^1 \eta_l(r)^2 \rho(r) r^2 dr} \\ k_j^l \equiv 1 - \frac{1}{L} - \frac{1}{2L^2}(1 + j(2j+3)) \end{cases}. \quad (17)$$

Finally, Equation (3) is obtained by taking

$$u_{2j+1}^l \approx k_j^l e^{-j(j+3/2)/l}. \quad (18)$$

We note that Equation (5) is obtained by using the fact that, in the approximation Equation (17) valid for f modes, the rotational kernels depend on j only by a multiplicative factor. Taking instead $K_j^l \approx K_0^l$ for all j as usually done for high degree modes would also allow us to write Equation (5) but the integrated difference $\int(K_j^l - K_0^l) dr$ would reach 2.2% for $l = 117$, $j = 17$ whereas it remains negligible for all l and j in the case of the approximation used here.

References

- Antia, H. M., Basu, S., Pintar, J., and Schou, J.: 2001, in A. Wilson (ed.), *Helio- and Asteroseismology at the Dawn of the Millennium*, ESA Publications Division, Noordwijk, The Netherlands, SP-464, p. 27.
 Backus, G. E. and Gilbert, J. F.: 1968, *Geophys. J. Roy. Astron. Soc.* **16**, 169.
 Basu, S., Antia, H. M., and Tripathy, S. C.: 1999, *Astrophys. J.* **512**, 458.
 Beck, J. G.: 2000, *Solar Phys.* **191**, 47.
 Beck, J. G. and Schou, J.: 2000, *Solar Phys.* **193**, 333.

- Berthomieu, G. and Christensen-Dalsgaard, J.: 1991, in A. N. Cox, W. C. Livingston, and M. Matthews (eds.), *Solar Interior and Atmosphere*, The University of Arizona Press, Tucson, p. 412.
- Birch, A. C. and Kosovichev, A. G.: 1998, *Astrophys. J.* **503**, L187.
- Brown, T. M., Christensen-Dalsgaard, J., Dziembowski, W. A., Goode, P., Gough, D. O., and Morrow, C. A.: 1989, *Astrophys. J.* **343**, 526.
- Christensen-Dalsgaard, J., Schou, J., and Thompson, M. J.: 1990, *Monthly Notices Royal Astron. Soc.* **242**, 353.
- Collin, B., Nesme-Ribes, E., Leroy, B., Meunier, N., and Sokoloff, D.: 1995, *C.R. Acad. Sci. Paris* **321**, 111.
- Corbard, T., Berthomieu, G., Morel, P., Provost, J., Schou, J., and Tomczyk, S.: 1997, *Astron. Astrophys.* **324**, 298.
- Corbard, T., Jiménez-Reyes, S. J., Tomczyk, S., Dikpati, M., and Gilman P.: 2001, in A. Wilson (ed.), *Helio- and Asteroseismology at the Dawn of the Millennium*, ESA Publications Division, Noordwijk, The Netherlands, SP-464, p. 265.
- DeRosa, M. L.: 2001, Ph.D. Thesis, University of Colorado, Boulder, USA.
- DeRosa, M. L., Gilman, P., and Toomre, J.: 2001, *Astrophys. J.* (submitted).
- Deubner, F.-L., Ulrich, R. K., and Rhodes, E. J.: 1979, *Astron. Astrophys.* **72**, 177.
- Dikpati, M. and Charbonneau, P.: 1999, *Astrophys. J.* **518**, 508.
- Duvall, T. L.: 1980, *Solar Phys.* **66**, 213.
- Edmonds, A. R.: 1960, *Angular Momentum in Quantum Mechanics*. Princeton University Press, Princeton, New Jersey.
- Foukal, P.: 1972, *Astrophys. J.* **173**, 439.
- Foukal, P.: 1977, *Astrophys. J.* **218**, 539.
- Foukal, P. and Jokipii, J. R.: 1975, *Astrophys. J.* **199**, L71.
- Gilman, P. A. and Foukal, P. V.: 1979, *Astrophys. J.* **229**, 1179.
- Gilman, P. A., Morrow, C. A., and Deluca, E. E.: 1989, *Astrophys. J.* **338**, 528.
- Haber, D. A., Hindman, B. W., Toomre, J., Bogart, R. S., Thompson, M. J., and Hill, F.: 2000, *Solar Phys.* **192**, 335.
- Hansen, C. J., Cox, J. P., and Van-Horn, H. M.: 1977, *Astrophys. J.* **217**, 151.
- Hathaway, D. H. et al.: 1996, *Science* **272**, 1306.
- Howard, R.: 1984, *Ann. Rev. Astron. Astrophys.* **22**, 131.
- Howard, R. and Labonte, B. J.: 1980, *Astrophys. J.* **239**, L33.
- Howe, R., Christensen-Dalsgaard, J. et al.: 2000, *Astrophys. J.* **533**, L163.
- Kosovichev, A. G. and Schou, J.: 1997, *Astrophys. J.* **482**, L207.
- Küker, M., Rüdiger, G., and Schultz, M.: 2001, *Astron. Astrophys.* **374**, 301.
- Leighton, R. B.: 1969, *Astrophys. J.* **156**, 1.
- Morse, P. and Feshbach, H.: 1953, *Methods of Theoretical Physics*, Vol. 1, McGraw-Hill, New York, USA.
- Parker, E. N.: 1993, *Astrophys. J.* **408**, 707.
- Pijpers, F. P.: 1997, *Astron. Astrophys.* **326**, 1235.
- Ritzwoller, M. H. and Lavelle, E. M.: 1991, *Astrophys. J.* **369**, 557.
- Roberts, P. H. and Stix, M.: 1972, *Astron. Astrophys.* **18**, 453.
- Schou, J.: 1992, Ph.D. Thesis, Aarhus University, Aarhus, Denmark.
- Schou, J.: 1999, *Astrophys. J.* **523**, L181.
- Schou, J., Christensen-Dalsgaard, J., and Thompson, M. J.: 1994, *Astrophys. J.* **433**, 389.
- Schou, J. et al.: 1998, *Astrophys. J.* **505**.
- Schou, J., Howe, R. et al.: 2001, *Astrophys. J.* (submitted).
- Schroeter, E. H.: 1985, *Solar Phys.* **100**, 141.
- Snodgrass, H. B.: 1992, in K. L. Harvey (ed.), *ASP Conf. Ser. 27: The Solar Cycle*, ASP, San Francisco, p. 205.

- Snodgrass, H. B. and Ulrich, R. K.: 1990, *Astrophys. J.* **351**, 309.
Snodgrass, H. B., Howard, R., and Webster, L.: 1984, *Solar Phys.* **90**, 199.
Thompson, M. J., Toomre, J. *et al.*: 1996, *Science* **272**, 1300.
Unno, W., Osaki, Y., Ando, H., Saio, H., and Shibahashi, H.: 1989, *Nonradial Oscillations of Stars*, 2nd ed., University of Tokyo Press, Tokyo.

I.2.3 L'héliosismologie locale par l'analyse « ring-diagram »

Tous les instruments du réseau GONG ont été revus et les capteurs remplacés pour conduire en 2001 au réseau GONG+ permettant d'atteindre des résolutions spatiales de l'ordre de l'arc-seconde et les analyses locales des oscillations. En 2002 j'étais au sein du groupe GONG chargé de développer les outils pour la mise en œuvre de l'une des approches de l'héliosismologie locale appelée analyse « ring-diagram » initialement développée par F. Hill (1988). Le réseau GONG+ augmenté des outils de l'analyse locale constitue aujourd'hui ce que l'on appelle le réseau GONG++.

I.2.3.1 La méthode

Les détails de l'analyse sont décrits dans plusieurs documents (Corbard et al. (2003), Corbard (2003)) mais je résume ici les grandes étapes de cette analyse « ring-diagram » en soulignant les éléments nouveaux que j'ai été amené à introduire. La procédure d'analyse « ring-diagram » peut se décomposer en quatre grandes étapes :

1) La construction de plusieurs cubes de données à partir de la série temporelle des images Doppler.

a. Définition de la zone d'intérêt sur le Soleil

L'analyse étant locale, nous devons définir une région localisée de la surface solaire sur laquelle va porter l'analyse. Cependant les coordonnées (x,y) du capteur ne sont pas appropriées pour définir la zone d'intérêt. Une simple grille (hélio-) latitude-longitude ne conviendrait pas non plus. En effet, nous voulons suivre dans le temps les ondes, assimilées à des ondes planes, qui, localement vont se propager sur des grands cercles de la sphère solaire (distance la plus courte entre deux points). De plus, dans une étape ultérieure, nous allons utiliser une transformée de Fourier spatio-temporelle qui suppose donc l'équidistance entre les points à la fois dans le temps et l'espace. Il nous faudrait donc idéalement construire une carte pour laquelle chaque ligne et chaque colonne représenterait un grand cercle et pour laquelle les distances seraient préservées dans les deux directions. Une telle projection n'existant pas, il faut trouver un compromis. L'équipe MDI avait choisi la projection de Postel (ou azimutale équidistante) qui préserve les distances dans toutes les directions à partir du point central mais pour laquelle ni les lignes horizontales ni les lignes verticales de la grille ne représentent des grands cercles (exceptées les lignes passant par le centre). Une légère distorsion est donc introduite dans les deux directions de manière symétrique. J'ai introduit une autre classe de projections, cylindrique équidistante et cylindrique équidistante transverse, pour lesquelles soit les lignes soit les colonnes représentent toutes des grands cercles selon lesquels les distances sont préservées. Une légère distorsion est alors introduite dans l'autre direction seulement. Ceci présente un avantage lorsque nous voulons privilégier spécifiquement l'analyse de la circulation dans une direction particulière telle que la

circulation méridienne par exemple. La différence entre les deux types de projections devient notable seulement lorsque l'on analyse une zone loin du centre de l'image (proche du limbe) ou lorsque la zone analysée couvre une fraction importante du disque solaire mettant à mal l'hypothèse 'onde plane' (Corbard (2003) ; Zaatri, Corbard et al. (2008))

b. Projection sur l'image et interpolation

Chaque point de la zone d'intérêt ainsi définie sur le Soleil est ensuite projeté sur notre image et les vitesses Doppler pour chaque point de grille sont trouvées par interpolation. L'introduction d'une interpolation par produit tensoriel de B-splines m'a permis à ce stade de rendre la chaîne de traitement beaucoup plus rapide tout en préservant les qualités spectrales d'une interpolation idéale (sinc).

c. Propagation temporelle

La grille est ensuite propagée c'est-à-dire recalculée pour l'instant suivant en supposant la rotation synodique (vue depuis la Terre) connue pour chaque hélio-latITUDE observée. Les vitesses Doppler associées sont alors trouvées par projection de la grille propagée sur l'image suivante et interpolation. Il est à noter ici que la vitesse synodique est légèrement variable au cours de l'année de par l'ellipticité de l'orbite terrestre et l'inclinaison de l'axe de rotation solaire par rapport au plan de l'écliptique. Les séries temporelles analysées étant relativement courtes (de l'ordre de la journée), il convient de prendre en compte cet effet.

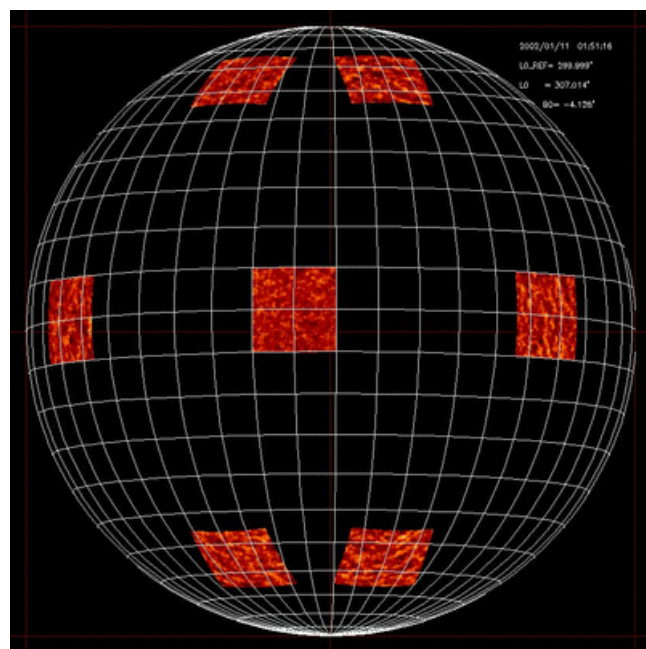


Figure 10 Exemple de 7 zones analysées par « Ring-Diagram ». Chaque zone est définie sur une projection équidistante cylindrique transverse de la sphère solaire puis retranscrite sur le plan du capteur CCD. Les lignes blanches représentent les lignes d'hélio-latitudes et d'hélio-longitudes constantes avec une séparation de 7.5° . Nous

voyons que la zone définie sur la projection correspond à 15°x15° d'hélio longitudes-latitudes au centre à l'équateur mais que cela n'est plus vrai pour les zones plus éloignées. Chaque zone est suivie à la vitesse de rotation correspondant à la latitude de son centre, pour former un cube spatio-temporel de données Doppler.

Une analyse typique définit ainsi 189 zones d'environ 15°x15° sur la projection équidistante cylindrique du Soleil, zones qui sont suivies sur des séquences de 1664 minutes à raison d'une image par minute (Figure 10).

2) La transformée de Fourier 3D de chacun de ces cubes de données.

La transformée de Fourier 3D des cubes de données est une transformée classique mais il est nécessaire de prendre en compte le caractère fini du signal dans les 3 dimensions. Pour les deux dimensions spatiales, une apodisation en cloche (cosine bell) est appliquée. Pour la dimension spatiale, la fenêtre d'observation de GONG n'étant pas parfaite même si le taux de remplissage est souvent supérieur à 90%, j'ai été amené à introduire une technique dite 'multi-taper' qui consiste à appliquer une série de fonctions d'apodisation prises orthogonales sur la fenêtre d'observation, à calculer les FFT temporelles pour chaque série apodisée puis à faire la moyenne des spectres de puissance. Cela permet d'éviter la perte de données qui serait associée à l'utilisation d'une seule fonction d'apodisation et réduit les effets d'aliasing induit par la fenêtre d'observation. Cela conduit à une meilleure répartition de la puissance le long des anneaux dans un spectre de puissance qui est beaucoup plus lissé. L'utilisation d'un nombre de fonctions d'apodisations (taper) trop important conduirait à un spectre de puissance trop lissé. Le choix de ce nombre résulte donc d'un compromis et il a été l'objet de tests pour optimiser les nombres d'anneaux et donc les nombres de modes qui peuvent être ajustés à l'étape suivante (Figure 11).

3) L'ajustement des spectres de puissance pour en déduire les décalages en fréquences (distorsion des « rings »).

La présence d'un champ de vitesse \mathbf{U} perturbe la fréquence du mode par advection du front d'onde et produit un décalage Doppler apparent $\Delta\omega$ donné par :

$$\Delta\omega = \vec{k} \cdot \vec{U} = k_x U_x + k_y U_y \quad (7)$$

Dans un domaine autour de chaque fréquence angulaire ω_0 et de chaque fréquence spatiale k_h le spectre de puissance est ajusté par une méthode de maximum de vraisemblance avec un profil du type :

$$P_{\omega_0, k_h}(\omega) = \frac{A}{(\omega - \omega_0 + k_x U_x + k_y U_y)^2 + \Gamma^2} + \frac{b}{k_h^3} \quad (8)$$

dans lequel le premier terme représente un profil Lorentzien de largeur Γ et d'amplitude A et le second terme modélise le bruit. Un terme d'asymétrie a ensuite été ajouté à cette équation conduisant à un meilleur ajustement des spectres calculés. Le terme modélisant le bruit peut également être cherché sous une forme polynomiale moins contrainte.

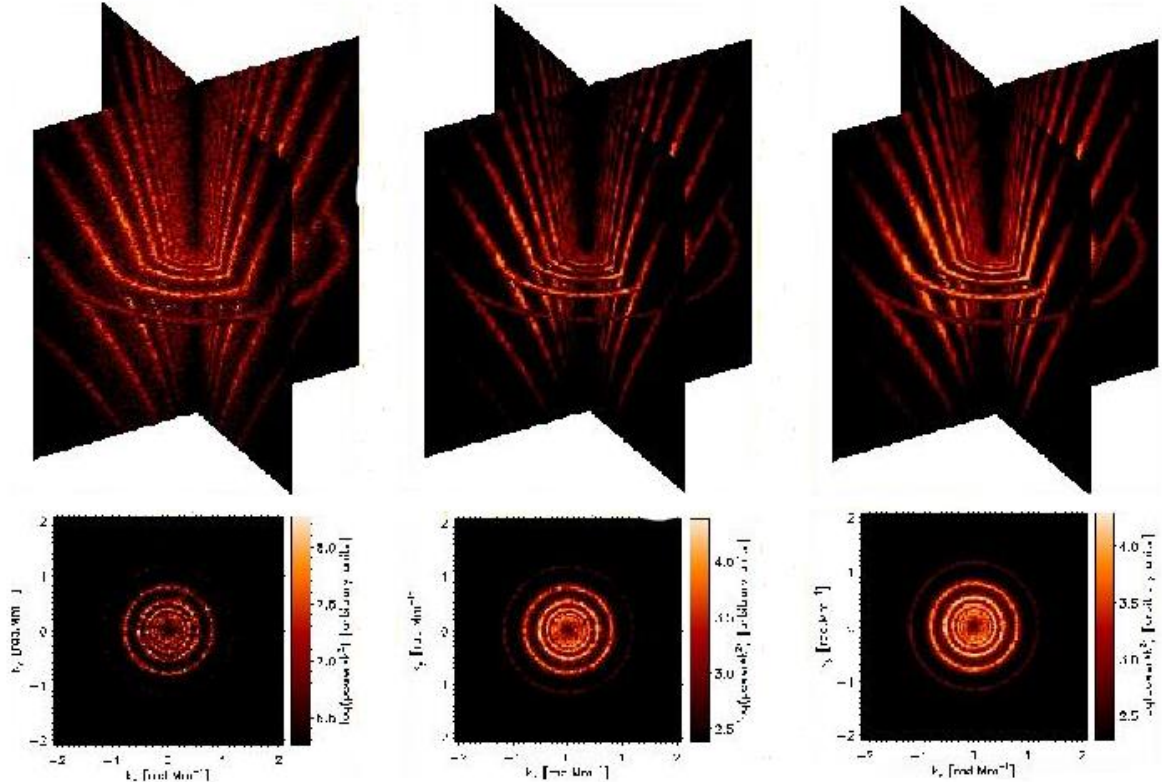


Figure 11 Exemple de spectres de puissance 3D obtenus par transformations FFT 3D des cubes de données Doppler spatio-temporelles avec une technique multi-taper dans la dimension temporelle. La ligne du bas représente une coupe horizontale des spectres 3D c'est-à-dire à fréquence temporelle fixe. Les deux axes sont les fréquences spatiales. La colonne de gauche n'utilise pas d'apodisation spatiale, la colonne du milieu utilise 3 tapers et la colonne de droite utilise 6 tapers (T. Corbard 2003).

4) L'inversion des décalages en fréquence pour en déduire les deux composantes de la vitesse horizontale en fonction de la profondeur.

En fait, la quantité \mathbf{U} directement déduite de l'ajustement des spectres de puissance est une moyenne sur une certaine profondeur de la vitesse \mathbf{V} avec une fonction de pondération qui est donnée par une moyenne des noyaux des modes qui contribuent aux anneaux observés dans le spectre de puissance. Ainsi, pour en déduire les composantes x et y du vecteur vitesse et leur dépendance en fonction de la profondeur z, il faut inverser pour chaque composante une équation intégrale 1D :

$$U_{x,y}(\omega_0, k_h) = \int K(\omega_0, k_h, z) V_{x,y}(z) dz + \varepsilon_{x,y}(\omega_0, k_h) \quad (9)$$

Les noyaux $K(\omega_0, k_h, z)$ sont calculés à partir des fonctions propres d'oscillation obtenues à partir d'un modèle solaire et d'un code d'oscillation. A chaque observable U_x et U_y est associée une certaine incertitude ε que l'on suppose distribuée selon une loi normale dont on estime la variance. Tous les ajustements autour de bandes de fréquences différentes sont supposés indépendants. C'est-à-dire que les observables déduites de l'ajustement dans des bandes (ω_0, k_h) différentes sont supposées non corrélées. Ainsi la matrice de covariance B_ε est prise diagonale.

Ma principale contribution pour cette étape de l'analyse a été d'introduire une méthode de type « noyaux localisés optimaux» pour résoudre ces équations intégrales. En effet les méthodes de type moindre carrés régularisés qui étaient jusqu'alors utilisées sont plus rapides et faciles à mettre en œuvre mais elles offrent beaucoup moins de contrôle sur le résultat. Plutôt que de minimiser globalement la somme du carré des résidus entre les quantités observées et celles que produit la solution via l'équation (9), la méthode des noyaux localisés cherche localement, pour chaque profondeur z_0 , à trouver une combinaison linéaire des observables de telle sorte que le noyau qui en résulte dans l'équation (9) se rapproche le plus possible d'une fonction de Dirac. Ainsi la solution trouvée en z_0 est bien une mesure locale de $V_{x,y}(z_0)$.

Deux types de diagnostics peuvent être examinés pour illustrer et comprendre la différence entre les deux approches de l'inversion. Il y a d'une part les noyaux de résolution qui représentent le domaine (en profondeur) sur lequel la fonction recherchée est moyennée pour chaque profondeur z . De même que la valeur estimée des vitesses est une combinaison linéaire des observables, les noyaux de résolution sont la même combinaison linéaire des noyaux $K(\omega_0, k_h, z)$. Idéalement, ces noyaux de résolution seraient des fonctions de Dirac pour chaque z . L'autre outil de diagnostic est la matrice de covariance ou la matrice de corrélation associée. Les éléments non diagonaux de cette matrice montrent comment la vitesse estimée à une certaine profondeur est corrélée statistiquement aux vitesses estimées aux autres profondeurs (toujours sous l'hypothèse, dans notre cas, d'observables considérées comme indépendantes). Là encore, l'interprétation du résultat est facilitée si les termes diagonaux sont dominants. Une illustration de ces diagnostics est donnée Figure 12 pour la méthode des moindres carrés et Figure 13 pour la méthode des noyaux localisés. La méthode des noyaux localisés visant à optimiser le compromis entre ces deux diagnostics pour chaque profondeur, il est naturel que l'interprétation des résultats ainsi obtenus soit facilitée. L'application de cette méthode d'inversion a donc représenté un progrès pour l'interprétation des résultats de l'analyse ring-diagram et pour les efforts d'inter-comparaisons avec d'autres méthodes ou des jeux de données différents.

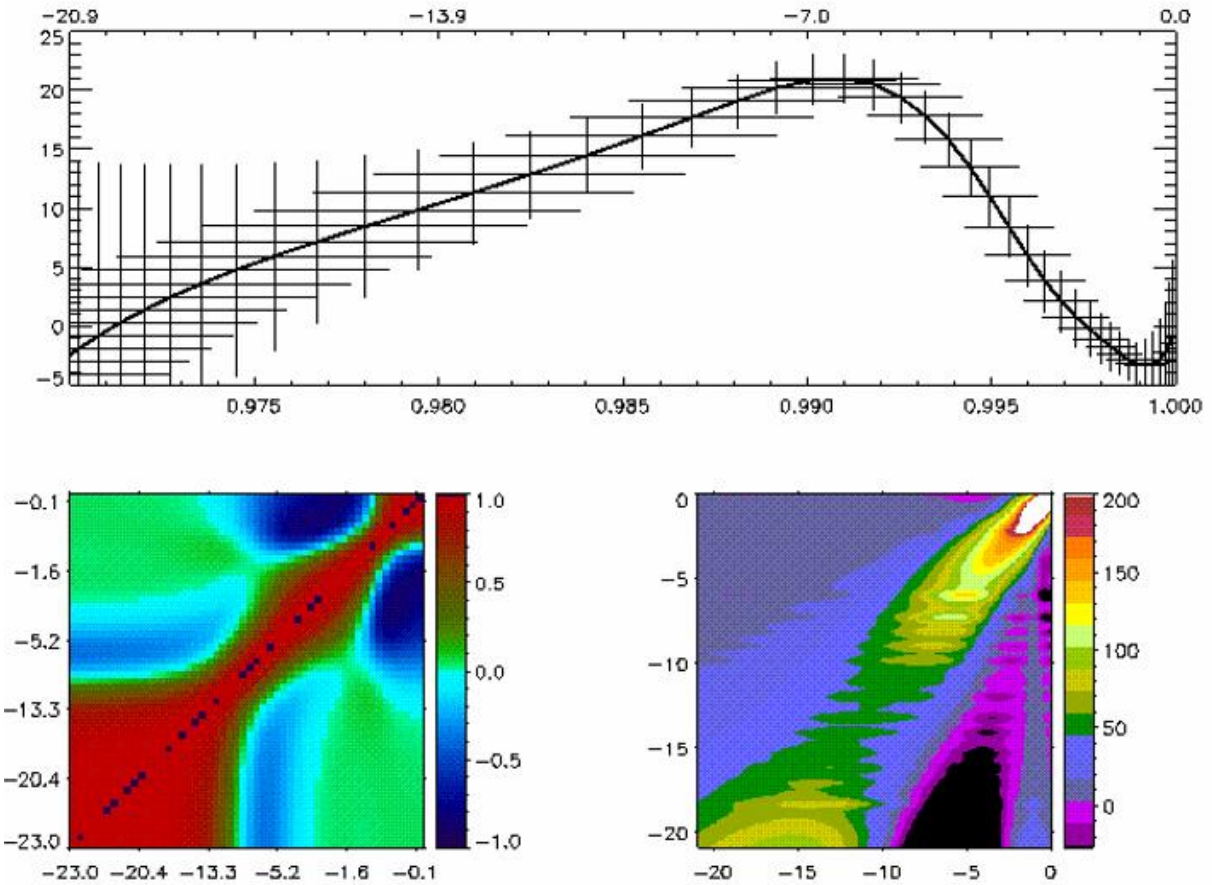


Figure 12 Exemple de résultat d'une inversion par moindre carrés régularisés et diagnostics associés. La figure du haut montre la fonction $V_x(z)$ obtenue en fonction de la profondeur sous la photosphère donnée en fraction de rayon solaire en bas et en Mm en haut. La figure en bas à gauche montre la matrice de corrélation. Les éléments diagonaux de cette matrice produisent les barres verticales d'incertitudes sur le graphique du haut. La figure en bas à droite montre les noyaux de résolution en fonction de la profondeur (en Mm sur les deux axes). Les noyaux de résolution sont relativement bien localisés proche de la surface mais, plus en profondeur, des contributions importantes venant de la surface demeurent (lobes négatifs en violet et noir). Les barres horizontales sur le graphique du haut représentent seulement la largeur du pic central des noyaux de résolution et ne sont dans ce cas qu'une représentation tronquée de la réalité.

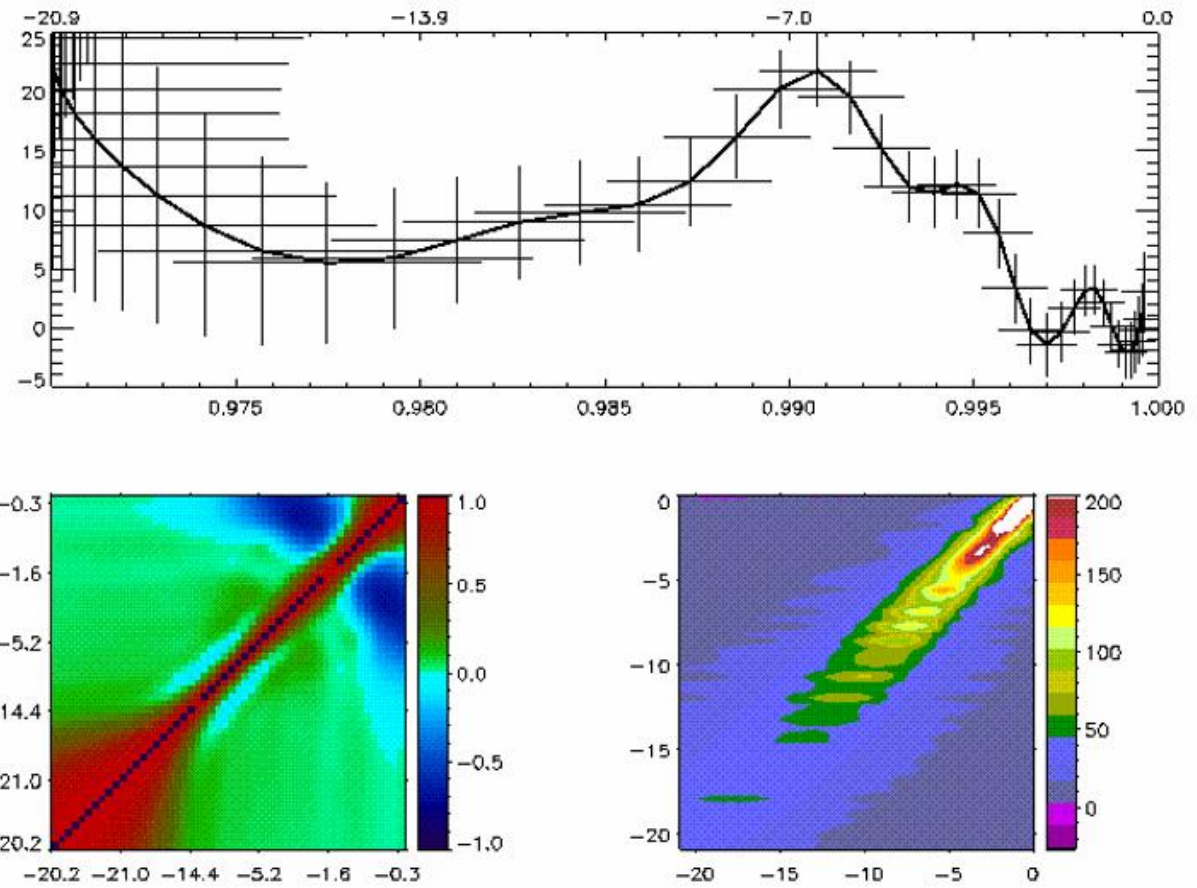


Figure 13. Même chose que sur la figure précédente mais pour une inversion de type « noyaux localisés ». Les termes non diagonaux des matrices de corrélation (en bas à gauche) et des noyaux de résolution (en bas à droite) sont réduits. Les noyaux de résolution étant constitués d'un seul pic localisé, l'interprétation des barres horizontales en termes de résolution est plus intuitive.

I.2.3.2 Les cartes et descripteurs de dynamique des fluides dérivés (article)

ARTICLE : Solar subsurface fluid dynamics descriptors derived from Global Oscillation Network Group and Michelson Doppler Imager data (Komm, Corbard et al. (2004))

Dans le premier article (Komm, Corbard et al. (2004)) exploitant cette chaîne de traitements, nous avons analysé les données GONG et MDI pour l'ensemble d'une rotation solaire (rotation de Carrington n° 1988, 30 mars-26 Avril 2002). Cela nous a permis d'obtenir notamment les premières cartes synoptiques des vitesses horizontales jusqu'à 15 Mm de profondeur à partir du nouveau réseau GONG+. Les cartes de la composante zonale (dans la direction azimutale) V_x donnent le résidu par rapport à la rotation différentielle dans lequel nous retrouvons notamment la signature des oscillations de torsion. Les cartes de la composante méridionale V_y donnent directement une estimation de la circulation méridienne sub-photosphérique. A partir de ces cartes nous avons pu estimer de nouveaux paramètres tels que la divergence horizontale $\text{div } V_h = \frac{\partial V_x}{\partial x} + \frac{\partial V_y}{\partial y}$, la vorticité horizontale $\text{vort } V_h = \frac{\partial V_y}{\partial x} - \frac{\partial V_x}{\partial y}$ et les gradients verticaux $\frac{\partial V_x}{\partial z}$ et $\frac{\partial V_y}{\partial z}$ sur toute la surface du Soleil et en profondeur. A partir de la divergence du flux horizontal et avec une hypothèse de conservation de la masse, nous avons par ailleurs obtenu un estimateur de la vitesse horizontale V_z . A partir des estimateurs des trois composantes de la vitesse nous pouvons calculer les cartes de densité moyenne d'hélicité cinétique $H = \langle V \cdot \nabla \times V \rangle$ et les comparer notamment aux cartes du champ magnétique de surface données par les magnétogrammes. Cette première étude couvrant une rotation de Carrington nous a notamment permis de mettre en évidence pour la première fois avec ce type d'analyse que les zones de forte activité magnétique sont associées à :

- un excès de vorticité
- un important gradient vertical de la vitesse azimutale

La comparaison entre les données GONG+ et MDI ont permis d'inter-calibrer l'analyse sur cette rotation. Les résultats divergent cependant concernant la circulation méridienne à haute latitude, les données MDI montrant une cellule de circulation méridienne vers l'équateur qui n'est pas trouvée dans les données GONG+. Dans les deux cas cependant le gradient vertical de circulation méridienne change de signe à environ 7 Mm sous la surface.

SOLAR SUBSURFACE FLUID DYNAMICS DESCRIPTORS DERIVED FROM GLOBAL OSCILLATION NETWORK GROUP AND MICHELSON DOPPLER IMAGER DATA

R. KOMM

National Solar Observatory,¹ 950 North Cherry Avenue, Tucson, AZ 85719; komm@noao.edu

T. CORBARD

Observatoire de la Côte d'Azur, F-06304 Nice Cedex 4, France

AND

B. R. DURNEY,² I. GONZÁLEZ HERNÁNDEZ, F. HILL, R. HOWE, AND C. TONER

National Solar Observatory, 950 North Cherry Avenue, Tucson, AZ 85719

Received 2003 November 11; accepted 2003 December 19

ABSTRACT

We analyze Global Oscillation Network Group (GONG) and Michelson Doppler Imager (MDI) observations obtained during Carrington rotation 1988 (2002 March 30–April 26) with a ring-diagram technique in order to measure the zonal and meridional flow components in the upper solar convection zone. We derive daily flow maps over a range of depths up to 16 Mm on a spatial grid of 7.5° in latitude and longitude covering ±60° in latitude and central meridian distance and combine them to make synoptic flow maps. We begin exploring the dynamics of the near-surface layers and the interaction between flows and magnetic flux by deriving fluid dynamics descriptors such as divergence and vorticity from these flow maps. Using these descriptors, we derive the vertical velocity component and the kinetic helicity density. For this particular Carrington rotation, we find that the vertical velocity component is anticorrelated with the unsigned magnetic flux. Strong downflows are more likely associated with locations of strong magnetic activity. The vertical vorticity is positive in the northern hemisphere and negative in the southern hemisphere. At locations of magnetic activity, we find an excess vorticity of the same sign as that introduced by differential rotation. The vertical gradient of the zonal flow is mainly negative except within 2 Mm of the surface at latitudes poleward of about 20°. The zonal-flow gradient appears to be related to the unsigned magnetic flux in the sense that locations of strong activity are also locations of large negative gradients. The vertical gradient of the meridional flow changes sign near about 7 Mm, marking a clear distinction between near-surface and deeper layers. GONG and MDI data show very similar results. Differences occur mainly at high latitudes, especially in the northern hemisphere, where MDI data show a counter cell in the meridional flow that is not present in the corresponding GONG data.

Subject headings: convection — Sun: activity — Sun: helioseismology — Sun: interior — Sun: magnetic fields — Sun: oscillations

On-line material: color figures

1. INTRODUCTION

We study horizontal flows in the outer 2% of the Sun near the solar surface derived from Global Oscillation Network Group (GONG) and Michelson Doppler Imager (MDI) Doppler images using a ring-diagram analysis. The ring-diagram technique has been used with great success by Haber et al. (2000, 2002) to analyze MDI Dynamics-run data. They found that large-scale solar flows such as zonal and meridional flows are more complex in the presence of strong magnetic activity than during times of low activity. The most important results to come out of that analysis to date are the discovery and characterization of flow concentrations around active regions and the structure of the near-surface global meridional circulation pattern, including a very surprising turnover at depths below about 7 Mm (counter cell) in the northern hemisphere only during the peak years of the solar activity cycle.

We begin exploring the dynamics of the near-surface layers of the convection zone by deriving fluid dynamics descrip-

tors such as divergence ($\text{div } \mathbf{v}$) and vorticity ($\text{curl } \mathbf{v}$) from the measured horizontal flows. These descriptors allow us to estimate other quantities such as, for example, the vertical velocity component and the mean kinetic helicity. The kinetic helicity together with the magnetic helicity play an important role in solar dynamo models (Steenbeck & Krause 1966; Krause 1967; Dikpati & Gilman 2001; Kleeorin & Rogachevskii 2003). In addition, we derive the vertical gradients of the zonal flow (rotation) and the meridional flow, which is not only of interest for the understanding of the dynamics of the near-surface layers but might also provide evidence for the existence of a near-surface dynamo. In this study, we focus on the relationship between these fluid dynamics descriptors and the magnetic flux to begin exploring more quantitatively the relation between dynamics and magnetic activity.

We show results from GONG and MDI observations covering Carrington rotation 1988 (2002 March 30–April 26) analyzed with the GONG ring-diagram analysis pipeline (Corbard et al. 2003). The ring-diagram technique uses three-dimensional power spectra from small patches of the solar disk to follow zonal and meridional flows below the surface and monitor local near-surface changes in high-degree modes.

¹ Operated by the Association of Universities for Research in Astronomy, Inc. under cooperative agreement with the National Science Foundation.

² University of Arizona, Physics Department, Tucson, AZ 85721.

Such analysis (Hill 1988) has previously been extensively used on the “Dynamics” (full-field, 1024×1024 pixel) data from the MDI instrument on board the *Solar and Heliospheric Observatory (SOHO)* (e.g., Haber et al. 2000, 2002). Upgraded cameras now allow similar data to be taken year-round from the six stations of the GONG network. Howe et al. (2004) show the results of an analysis of mode width and amplitudes obtained from such GONG data in addition to MDI data, while we focus on the derived horizontal flows.

2. DATA AND METHOD

We analyze observations obtained during Carrington rotation 1988 (2002 March 30–April 26), for which we have full-disk Doppler data from both the MDI instrument on *SOHO* and the GONG network. This data set was selected for the purposes of a detailed comparison of results obtained through multiple paths, from observation through each of the analysis steps. Such comparisons can provide a certain degree of validation of the implementations of the analysis procedures, hints of systematic errors, and better characterization of the observations, possibly leading to improved calibrations.³ Bogart et al. (2003) discuss the initial results of the ongoing comparison with regard to the ring-diagram technique; a more detailed comparison is in preparation. In this study, we analyze both data sets with the GONG pipeline and compare the results to check their consistency and thus their reliability.

We determine the horizontal components of solar subsurface flows with a ring-diagram analysis. The underlying principle is that a local velocity field changes the frequencies of acoustic waves through the advection of the wave pattern (Gough & Toomre 1983). This shift can be measured by obtaining a time series of a localized area on the solar surface and then calculating a three-dimensional power spectrum from this image cube as a function of temporal frequency ω and spatial frequencies k_x and k_y (Hill 1988). A two-dimensional cut at a given temporal frequency shows a set of rings in which each one corresponds to a ridge in the $\ell-\nu$ diagram. These rings are shifted by the horizontal flow field in k_x and k_y . The rings are fitted with a Lorentzian profile to measure the frequency shift of each mode as a function of mode order n and horizontal spatial frequency k (Bogart et al. 1995; Haber et al. 2002). These inferred shifts are then inverted to determine the horizontal velocity components as a function of depth.

We use the same technique as described by Haber et al. (2002) for their dense-pack analysis of MDI Dynamics Program data. We analyze the data in “days” of 1664 minutes, which means that consecutive day images are shifted by $15^\circ 25'$ in Carrington longitude. For each day, the full-disk Doppler images are divided into 189 overlapping regions covering the solar disk within $\pm 60^\circ$ in latitude and central meridian distance (CMD), and each region covers a $16^\circ \times 16^\circ$ domain in the transverse cylindrical projection of the solar sphere around the region center. The centers of the regions are spaced by $7^\circ 5'$, ranging from $\pm 52^\circ 5'$ in latitude and CMD. Each of these regions is tracked throughout the sequence of images using the surface rotation rate (Snodgrass 1984) appropriate for the center of each region as tracking rate and remapped in latitude and longitude. The tracking rate in terms of linear velocity is of the form $\cos(\theta)[a_0 + a_2 \sin^2(\theta) + a_4 \sin^4(\theta)]$, where θ is the

latitude ($a_0 = 451.43$, $a_2 = -54.77$, and $a_4 = -80.17$ nHz). Each of the resulting image cubes has a size of 128×128 pixels in the spatial directions and 1664 pixels in the temporal direction. The tracked image cubes are apodized with a circular function, reducing the effective size to 15° before being Fourier transformed. The analysis is described in detail in Corbard et al. (2003), and its implementation as the GONG ring-diagram pipeline is described in Hill et al. (2003). For GONG data, simultaneous images from different sites are merged (Toner et al. 2003) and the time series of merged images is analyzed. MDI and GONG data are processed in the same way, with the exception of the image-merge step.

In this way, we derive 189 pairs of zonal and meridional velocity at 52 grid points in depth for each 1664 minute day. Since the inversion grid points are not all independent and the errors increase rapidly at greater depth, we use 16 depths ranging from 0.6 to 15.8 Mm. We combine these daily flow maps to calculate synoptic flow maps for each depth. In merging the various daily flow maps together, a weighting factor of cosine CMD to the fourth power is used, as in the low-resolution maps of magnetic activity created at the National Solar Observatory (NSO, Kitt Peak). For a given Carrington longitude, 7 or 8 days can contribute to a synoptic map value at the equator (depending on its even or odd position on the longitude grid) compared to 3 or 4 days at 52.5° latitude. Together with the CMD weighting, the values at 52.5° latitude are averaged over about 70% of the amount of data used for regions from the equator to 37.5° latitude.

In addition, we calculate a residual synoptic flow map in order to focus on the flows near active regions. To remove the large-scale component from the flows, we subtract a low-order polynomial fit in latitude of the longitudinal average of the flows. For the zonal flows, we subtract a fit of sine latitude to the fourth power to reduce the effect of the difference between the differential rotation rate at a given depth and the surface tracking rate. We also subtract a linear trend to remove any north-south asymmetry that might be caused by image distortion or a potential error in the P -angle estimate. For the meridional flows, we remove a function in latitude that is zero at the equator and at the poles. We choose the derivatives in latitude of the first two even Legendre polynomials ($\partial P_2/\partial\theta$ and $\partial P_4/\partial\theta$) to represent the average meridional flow.

From the daily flow maps, we calculate the divergence of the horizontal flow components and the vertical vorticity component

$$\text{div } v_h = \frac{\partial v_x}{\partial x} + \frac{\partial v_y}{\partial y}, \quad (1)$$

$$\text{vort } v_h = \frac{\partial v_y}{\partial x} - \frac{\partial v_x}{\partial y}, \quad (2)$$

where v_x is the zonal component and v_y is the meridional flow component. We identify the horizontal component of the velocity by v_h and use $\text{div} v_h$ and $\text{vort} v_h$ to distinguish the components from the complete divergence ($\nabla \cdot \mathbf{v}$) and vorticity ($\nabla \times \mathbf{v}$). We then calculate synoptic maps of these quantities in the same way as for the velocities. We also calculate the vertical gradients, $\partial v_x/\partial z$ and $\partial v_y/\partial z$, of the horizontal flow components and the corresponding synoptic maps. All quantities are functions of latitude, longitude, and depth.

Using the continuity equation (representing mass conservation), we estimate the vertical velocity component from the

³ For more information see the Web site of the Local Helioseismology Comparison Group at <http://gong.nso.edu/lohc>.

measured divergence of the horizontal flow (Scorer 1978; Holton 1979). The continuity equation can be written

$$\frac{\partial \rho}{\partial t} + \nabla \rho \cdot \mathbf{v} + \rho \nabla \cdot \mathbf{v} = 0, \quad (3)$$

where ρ is the density and \mathbf{v} is the three-dimensional velocity vector. Since each data point represents an average over 1664 minutes, we neglect the term of the temporal density fluctuations. In addition, we assume that any horizontal density variations average out over the area of a dense-pack patch. The density is simply a function of radius. The continuity equation can then be simplified to

$$\frac{\partial v_z}{\partial z} + \left(\frac{1}{\rho} \frac{\partial \rho}{\partial z} \right) v_z + \text{div } v_h = 0, \quad (4)$$

where $\text{div } v_h$ is the horizontal flow divergence (eq. [1]). This equation has the solution

$$v_z(d) = - \frac{1}{\rho(d)} \int_0^d \rho \text{ div } v_h dz + v_z(0) \frac{\rho(0)}{\rho(d)} \quad (5)$$

at a depth d , where $v_z(0)$ and $\rho(0)$ are vertical velocity and density at the solar surface. To calculate the vertical velocity component, we use the density from a solar model by Christensen-Dalsgaard et al. (1996) and use as a boundary condition that the vertical velocity is zero at the surface [$v_z(0) = 0.0$]. (For future work, we will try to include surface measurements to check the validity of the boundary condition.) From the error in the divergence measurements, we estimate the error of the vertical velocity by repeating the calculation after adding or subtracting the divergence error to the differential equation. To estimate the numerical accuracy, we calculate $\partial v_z(d)/\partial z$ from the derived vertical velocity $v_z(d)$ and calculate the left-hand side of equation (4). This residual value of the left-hand side can be interpreted as the difference between the calculated gradient $\partial v_z(d)/\partial z$ and the gradient necessary to fulfill the continuity equation. The solution is then acceptable as long as the residual is smaller than the error of the calculated velocity gradient. We find that the residual-to-error ratio is 0.01 ± 0.02 on average for GONG data and 0.02 ± 0.04 for MDI data. We choose the gradient for this quality check and not the divergence or the velocity itself because the error of the observed divergence leads to the error in the vertical velocity, which in turn leads to the error in the gradient.

For a weakly stratified atmosphere, the continuity equation can be further simplified and the vertical velocity is defined as

$$v_z(d) = - \int_0^d \text{div } v_h dz. \quad (6)$$

In § 3 we find that the divergence of the horizontal flow components is of the order of 10^{-7} s^{-1} . The density gradient term, $(1/\rho)(\partial \rho / \partial z)$, is about 10^{-7} m^{-1} at a depth of 15.8 Mm and increases to $2 \times 10^{-6} \text{ m}^{-1}$ at a depth of 0.6 Mm near the surface. Multiplied by a vertical velocity of the order of 1 m s^{-1} or less, this term is comparable to the divergence and not negligible. However, we can use this estimate and its difference from the value calculated using equation (4) to judge the influence of the density stratification on the vertical velocity component.

The kinetic helicity of a fluid flow is the integrated scalar product of the velocity field, \mathbf{v} , and the vorticity field, $\nabla \times \mathbf{v}$ (Moffatt & Tsinober 1992),

$$H = \int \mathbf{v} \cdot \nabla \times \mathbf{v} dV, \quad (7)$$

where $\mathbf{v} \cdot \nabla \times \mathbf{v}$ is called the helicity density of the flow. The kinetic helicity and its density are pseudoscalar quantities. If the vorticity is a stationary random quantity (e.g., homogeneous turbulence), one can define the mean helicity

$$\mathcal{H} = \langle \mathbf{v} \cdot \nabla \times \mathbf{v} \rangle, \quad (8)$$

where the angle brackets indicate either an ensemble average or a space average. We can estimate the kinetic helicity using the measured horizontal flow components and the vertical component derived from the divergence of the horizontal flows. Since the horizontal flow components represent the average flow in a volume element defined by the horizontal size of each dense pack and the depth extent of the inversion kernels, the resulting scalar product $\mathbf{v} \cdot \nabla \times \mathbf{v}$ is already a “mean” quantity. To avoid confusion, we will call this scalar product the mean kinetic helicity density. The mean kinetic helicity density is dominated by the effect of the differential rotation. To emphasize the influence of magnetic activity, we calculate it from the residual velocities in which the large-scale component of the flows has been removed. The kinetic helicity density is the only quantity derived in this study in which the separation of the flow into an average and a residual component leads to two cross terms between these flow components in addition to the average and residual component.

3. RESULTS

3.1. Synoptic Flows

We derive daily flow maps of the horizontal flow components, which are then combined to synoptic flow maps. Figure 1 shows two examples of synoptic flow maps at 2 and 7 Mm below the solar surface derived from MDI data, superposed on a synoptic map of magnetic activity derived from GONG magnetograms. The flows at 2 Mm swirl around the active regions with strong zonal and meridional components. The flows at 7 Mm show mainly a strong east-west trend; the rotation rate at this depth is faster than the surface tracking rate. The error bars given for the depth values represent the widths of the inversion kernels.

From these synoptic flow maps, we calculate zonal and meridional flows averaged over 1 Carrington rotation at different depths ranging from 0.6 to 15.8 Mm. Figure 2 shows the average zonal flow component derived from GONG and MDI data. To emphasize the change in the differential rotation with depth, we subtract the constant term of the low-order fit at each depth. This value increases almost linearly from -5 m s^{-1} at 0.6 Mm to $+40 \text{ m s}^{-1}$ at 15.8 Mm for GONG data and from -8 to 33 m s^{-1} for MDI data with a zero crossing between 2 and 3 Mm. The increase of the constant term with increasing depth reflects the well-known increase of the rotation rate near the outer shear layer.

At high latitudes there is a strong variation with depth of the differential rotation profile. The $\sin^4 \theta$ term, which represents the difference between the differential rotation rate at high latitude and the surface tracking rate, changes from 54 m s^{-1}

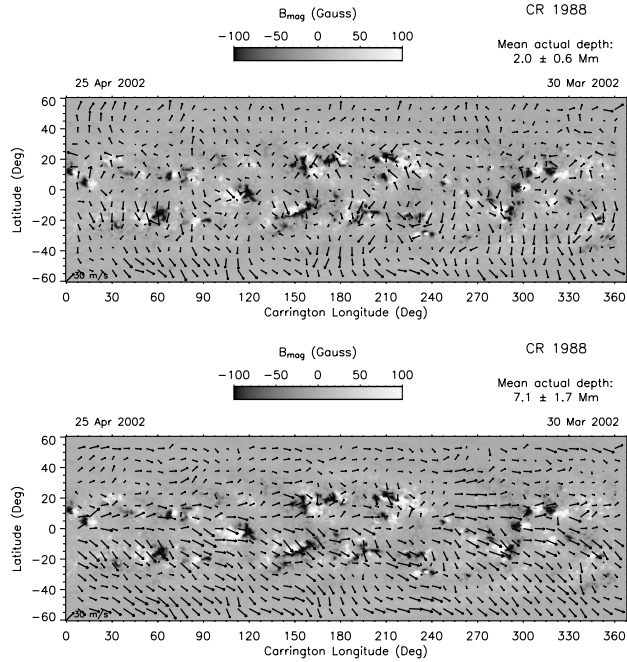


FIG. 1.—*Top:* Synoptic flow map at 2 Mm below the solar surface derived from MDI Dynamics data, superposed on synoptic magnetic data derived from GONG magnetograms. *Bottom:* Same for 7 Mm below the solar surface. [See the electronic edition of the Journal for a color version of this figure.]

at 0.6 Mm to -48 m s^{-1} at 15.8 Mm for GONG data and ranges from 36 m s^{-1} at 0.6 Mm to -49 m s^{-1} at 15.8 Mm for MDI data with a zero crossing between 6 and 7 Mm. With the a_4 -coefficient of the tracking rate being negative, this means that the latitudinal dependence of the zonal flow is increasingly more “differential” with increasing depth. The MDI data show a north-south asymmetry that might be caused by an insufficient P -angle correction.

The panel of Figure 2 showing zonal flows at a depth of 7.1 Mm includes the zonal flow at $r = 0.99 R_\odot$ derived from a global rotation inversion (*thick curve*) of GONG data for the corresponding time period. The local method distinguishes between the hemispheres, while the global analysis leads to a better resolution in latitude. The flows derived from the ring-diagram analysis are similar to the one at $r = 0.99 R_\odot$ derived from a global rotation inversion (*thick curve*) with faster flows near the equator and slower flows at mid-latitude, which is the signature of the so-called torsional oscillations. At this depth, the zonal flow derived from the ring-diagram analysis is quite symmetrical with regard to the equator, while near the surface it is almost antisymmetrical at latitudes equatorward of about 40° .

Figure 3 shows the meridional flows at the same depths as in Figure 2. Positive/negative values imply a flow in a northern/southern direction. The meridional flows are mainly poleward in each hemisphere. Exceptions are the equatorward flow at high latitudes in the northern hemisphere at depths of 7–12 Mm (counter cell) found in the MDI data and near the surface in the GONG data. GONG and MDI data lead to similar flows at other latitudes and depths. The constant terms of the low-order polynomial fits range from -3 to -7 m s^{-1} for GONG and -4 to -8 m s^{-1} for MDI data. The coefficients of the even Legendre derivatives are different for GONG and MDI data, as expected from Figure 3. For GONG data, the

$\partial P_2 / \partial \theta$ term is about -20 m s^{-1} at depths greater than 3 Mm and approaches 0 m s^{-1} near the surface, while for MDI data it is about -25 m s^{-1} near the surface and about -10 m s^{-1} at depths below about 5 Mm. The coefficients of $\partial P_4 / \partial \theta$ range between -30 and 0 m s^{-1} , reaching the smallest magnitude near 6 Mm for GONG and near 4 Mm for MDI data.

The counter cell seen in the MDI data at depths of 7–12 Mm in the northern hemisphere agrees with previous results by Haber et al. (2002), but it is not seen in the GONG data. The reason for this difference might be that the GONG observations have less high spatial frequency coverage than the MDI observations (Howe et al. 2004) because of the influence of the Earth’s atmosphere. We attempted to correct the GONG images with the observed modulation transfer function, as described in Toner et al. (2003). When the image restoration is applied, the counter cell at 7–12 Mm is present in the flows derived from GONG data and the near-surface counter flow disappears. However, the current version of image restoration introduces artifacts in frequency shifts and mode amplitudes. At the time of this study, we did not know the reason for these artifacts and thus cannot rule out that the procedure introduces artifacts in the flows as well. Therefore, we present in this study only GONG results without image restoration applied.

3.2. Divergence and Vertical Velocity

From the daily flow maps, we calculate daily maps of the divergence of the horizontal flow components and combine them to create synoptic maps. Figure 4 shows a synoptic map of the divergence of the horizontal flow components at 7 Mm (see Fig. 1b) for MDI and GONG as a function of latitude and Carrington longitude. The divergence maps derived from MDI and GONG data are very similar, with differences occurring mainly at high latitudes as expected from differences especially in the meridional flow component (see Fig. 3). The equatorial region shows predominantly source terms representing upflows, while the region near 20° latitude shows sink terms or downflows associated with active regions.

Figure 5 shows the longitudinal average of the divergence as a function of latitude and depth. GONG and MDI show positive values (source term) near the equator representing upflows and negative values (sink term) near 20° latitude representing downflows. As in the synoptic maps, the downflows appear at locations of large magnetic flux. At high latitudes in the northern hemisphere, the counter flow seen in MDI data results in large negative values at depths greater than 6 Mm that are not seen in GONG data. However, flows are more difficult to measure at high latitudes, and as a consequence, the derived values are less reliable. To emphasize the influence of magnetic activity, we reduce the effect of large-scale flows by fitting and removing a low-order polynomial in latitude (see Figs. 2 and 3) and calculate the divergence of the residual flows. The resulting divergence leads to the same pattern, but it is shifted toward more negative values. We point out that the divergence is a linear combination of the derivatives in latitude and longitude of the horizontal flow components and that its longitudinal average can thus be calculated as the sum of the contribution of the derivative in longitude and that of the derivative in latitude. The longitudinal average of the contribution of the derivative in longitude reduces essentially to the difference between the zonal flow at the beginning and the one at the end of the averaging interval. Assuming that the interval is short enough

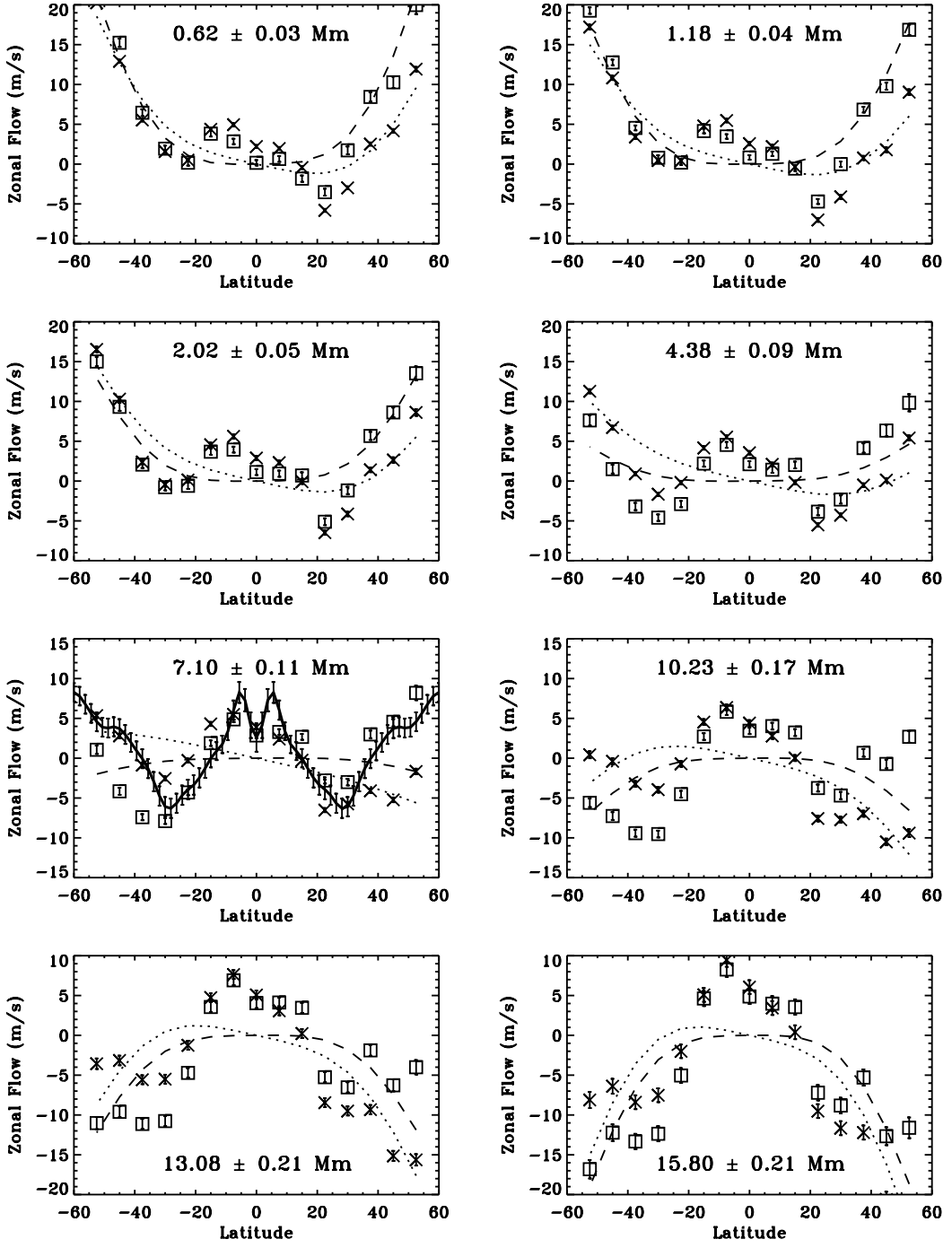


FIG. 2.—Zonal component of the flows averaged in longitude over Carrington rotation CR 1988 (squares: GONG data; crosses: MDI data) at several depths (0.6, 1.2, 2.0, 4.4, 7.1, 10.2, 13.1, and 15.8 Mm). The error bars associated with the depths represent the width of the inversion kernels. The surface rotation rate (tracking rate) has been subtracted. The low-order polynomial fits are included for comparison (dashed line: GONG data; dotted line: MDI data). The fitted equatorial value has been subtracted. The thick curve in the panel at depth 7.1 Mm represents the zonal flow at 0.99 R_{\odot} derived from a global rotation inversion.

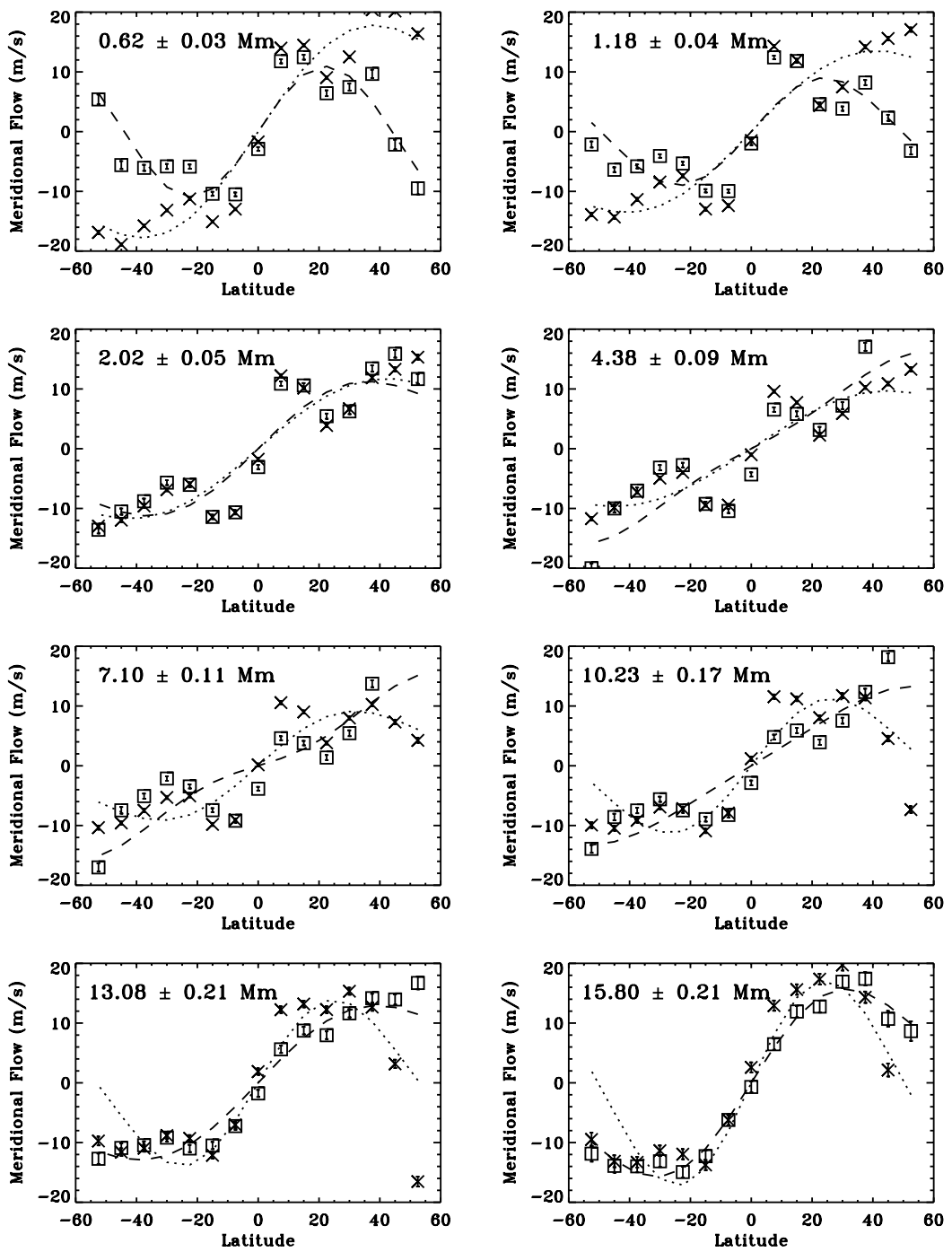


FIG. 3.—Same as Fig. 2, for the meridional flow component

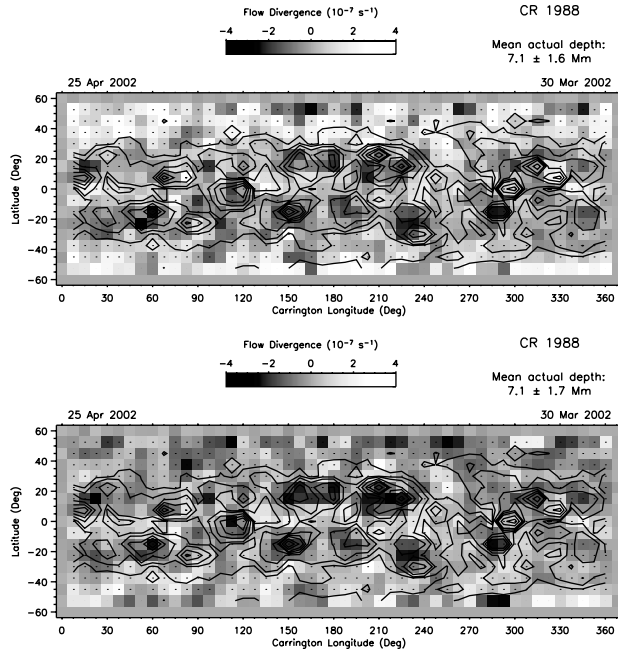


FIG. 4.—*Top:* Divergence of the horizontal flow components at a depth of 7 Mm derived from GONG data. The contour lines indicate the magnetic flux (5, 10, 20, 40, 60, 80, 120, and 160 G). *Bottom:* Same for MDI data. [See the electronic edition of the Journal for a color version of this figure.]

that the zonal flow does not change much, the longitudinal average of the divergence is dominated by the derivative in latitude of the average meridional flow.

With the continuity equation (eq. [4]) and the divergence values of the measured horizontal flow components, we calculate the vertical velocity component for each daily map and combine them to synoptic maps. Figure 6 shows, as examples, the vertical velocity at a depth of 7 and 13 Mm derived from GONG data in which the large-scale component of the flows has been removed. At a given depth, the vertical flow component shows upflows and downflows at the same horizontal locations where sources and sinks are present in the corresponding divergence map. Locations of strong magnetic activity are more likely associated with downflows at a depth of 7 Mm (*top panel*), while they show up- or downflows with a slight dominance of upflows at greater depth (*bottom panel*). Downflows are present at medium flux levels near 20° latitude at all depths.

The MDI data lead to the same results. The correlation between vertical velocities derived from GONG and MDI data is 0.78 ± 0.04 on average for depths up to 3 Mm and 0.48 ± 0.10 for depths greater than 8 Mm. The reduced correlation at greater depth is due to the presence of the counter cell in the northern hemisphere in the MDI data. By excluding latitudes poleward of 30° in the northern hemisphere, the correlation nearly doubles to 0.80 ± 0.01 below 8 Mm. Even near the surface, the correlation increases to 0.87 ± 0.05 , indicating that the values at poleward latitudes are more uncertain than values at equatorward ones.

Figure 7 shows the longitudinal average of the vertical velocity. It is qualitatively very similar to the average divergence shown in the third panel of Figure 5. However, the vertical velocity shows large values at greater depth, while the divergence shows large values also near the surface. This difference is especially noticeable near the equator.

Figure 8 shows examples of the vertical velocity as a function of depth at four different latitude-longitude positions. Velocities derived from GONG and MDI data show the same depth dependence but differ quantitatively at depths greater than about 10 Mm. The four cases are representative of the different depth dependences present in the data. To judge the influence of the density stratification, we include the vertical velocity component (*dashed line*) derived from MDI data without including the density gradient term in the continuity equation (eq. [6]). The consequence of neglecting the density stratification is a vertical velocity that is qualitatively similar but by a factor of 2–3 too large.

To explore the relationship between vertical velocity and magnetic flux, we group the data into ranges of different magnetic flux and calculate the average vertical velocity for a given range of flux values. Figure 9 shows the average vertical velocity for locations with less than the median flux, 6 times the median flux, and the range in between as a function of

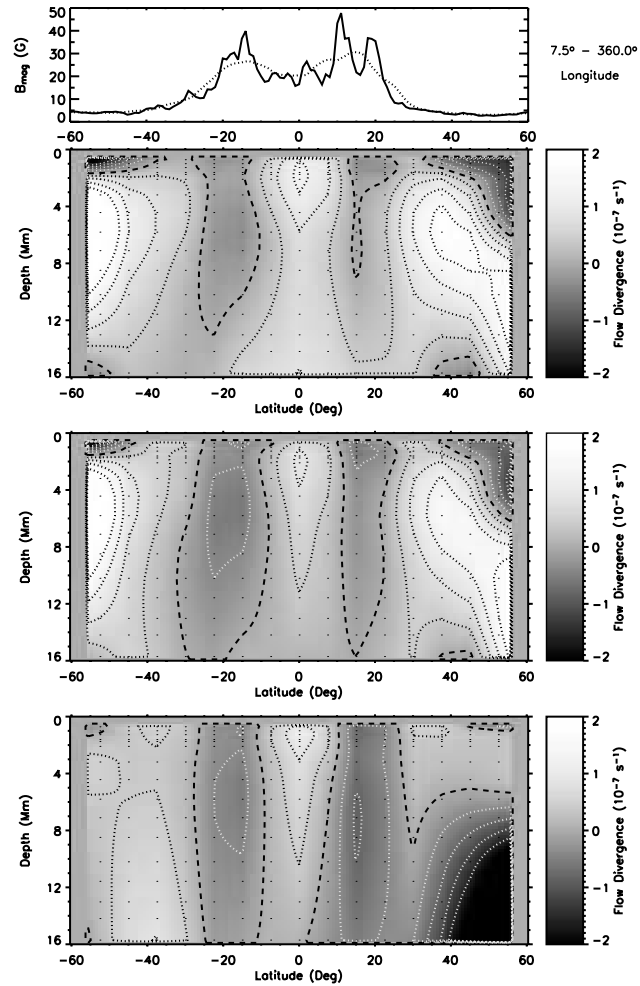


FIG. 5.—Divergence of the horizontal flow components averaged over Carrington rotation CR 1988 (2002 March 30–April 25) as a function of latitude and depth. *Top:* Surface magnetic flux as a function of latitude (*solid line*) and averaged over 15° (*dotted curve*). *Second panel:* Flow divergence derived from GONG data. The dashed line indicates the zero contour; the dotted lines indicate 20%, 40%, 60%, and 80% of the minimum and the maximum of the color scale. The dots indicate the depth-latitude grid. *Third panel:* Flow divergence derived from GONG data after removing the large-scale flow components. *Bottom:* Same as third panel, but for MDI data. [See the electronic edition of the Journal for a color version of this figure.]

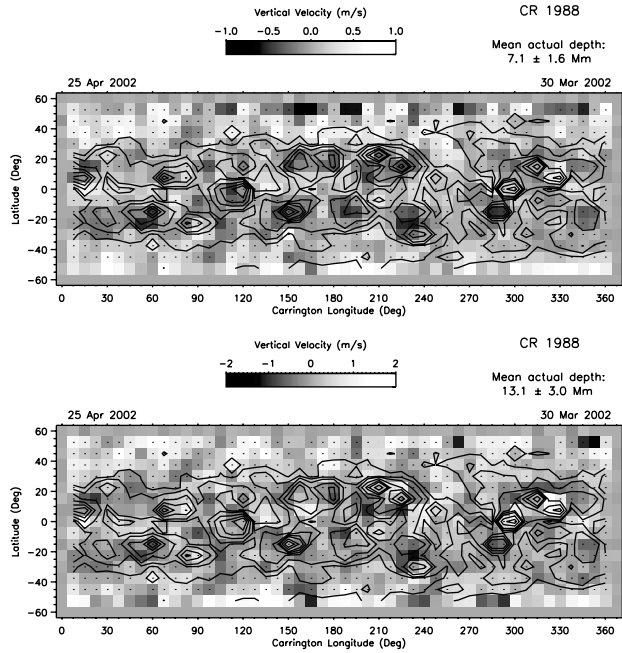


FIG. 6.—*Top:* Vertical velocity at a depth of 7.1 Mm derived from GONG data with the low-order polynomial fit removed. The contour lines indicate the magnetic flux (5, 10, 20, 40, 60, 80, 120, and 160 G). *Bottom:* Same, but at a depth of 13.1 Mm. [See the electronic edition of the Journal for a color version of this figure.]

depth averaged over all latitudes within $\pm 37.5^\circ$ and all Carrington longitudes. Locations of low magnetic flux (*dashed line*) show upflows on average, while locations of medium magnetic activity (*dotted line*) show downflows. Locations of very high activity (*solid line*) show even larger downflows at depths of less than about 8 Mm. The vertical velocity is anticorrelated with the magnetic flux with a correlation coefficient of -0.33 ± 0.04 for GONG data and -0.37 ± 0.04 for MDI data at depths of less than 8 Mm.

However, at depths greater than about 10 Mm, large upflows occur at some locations with magnetic flux greater than 6 times the median flux (see Fig. 8), which results in an average upflow in GONG data and a greatly reduced downflow in MDI data. The correlation coefficient is $+0.11$ for GONG and -0.05 for MDI data at a depth of 15.8 Mm. This seems to imply that the vertical flow can change direction at locations of strong activity. However, at the same locations, there is a surprisingly strong correlation between the magnetic activity and the error of the horizontal flow components. For MDI data, the average correlation is 0.68 ± 0.10 for high-activity data compared to -0.09 ± 0.09 for low- and medium-activity data. For GONG data, the average correlation is 0.48 ± 0.14 for high-activity data at depths greater than 9 Mm and 0.12 ± 0.09 closer to the surface compared to -0.25 ± 0.08 for low- and medium-activity data. This correlation is most likely a side effect of the reduced power of the ring spectra in the presence of strong magnetic flux. The power is reduced by about 20%–30% (Howe et al. 2004), which amounts to a reduced signal-to-noise ratio. The presence of magnetic fields can also distort the shape of the rings (Hill, Haber, & Zweibel 1996). For example, it can change the contrast along outer rings and the radii of inner rings. While effects such as the varying contrast along a ring are taken into

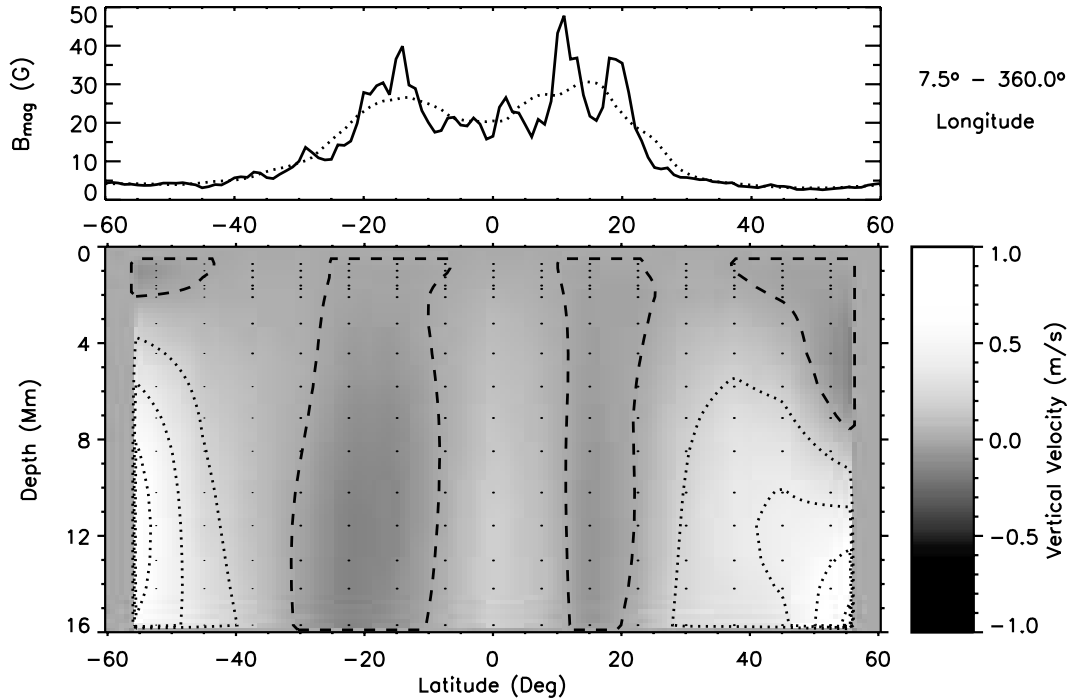


FIG. 7.—Vertical velocity component averaged over Carrington rotation CR 1988 (2002 March 30–April 25) as a function of latitude and depth. *Top:* Surface magnetic flux as a function of latitude (*solid line*) and averaged over 15° (*dotted curve*). *Bottom:* Vertical velocity derived from GONG data after removing the large-scale flow components. The dashed line indicates the zero contour; the dotted lines indicate 20%, 40%, 60%, and 80% of the minimum and the maximum of the color scale. The dots indicate the depth-latitude grid. [See the electronic edition of the Journal for a color version of this figure.]

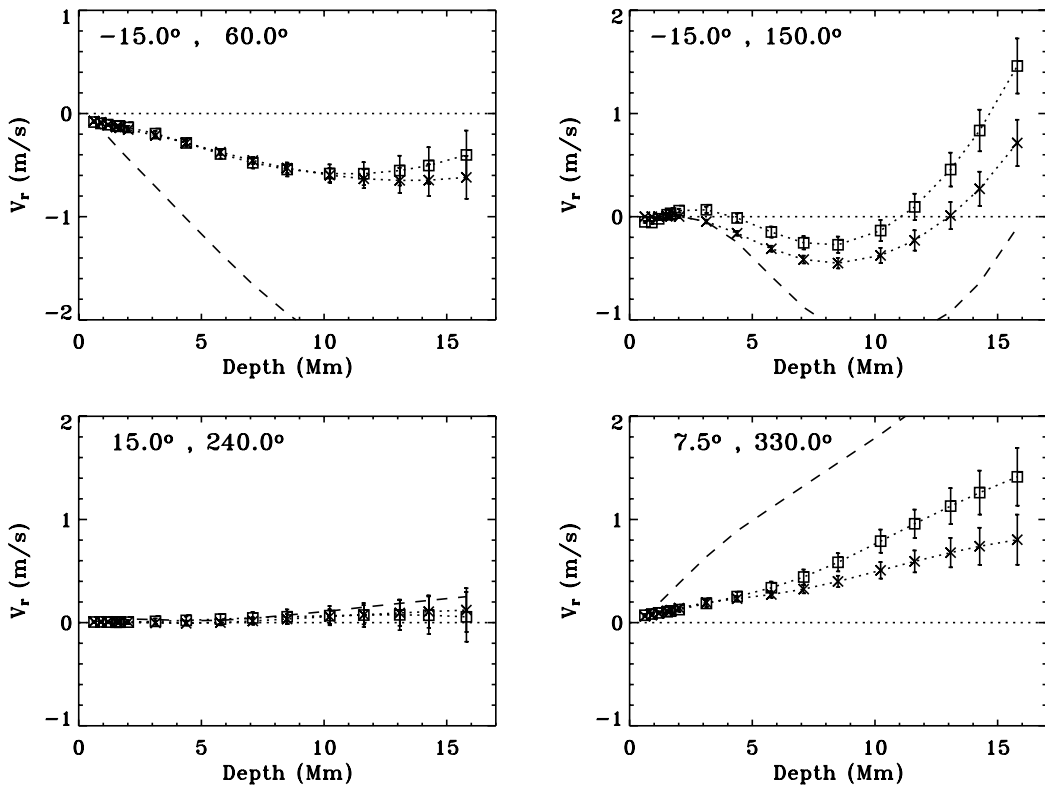


FIG. 8.—Vertical velocity as a function of depth at four different positions in latitude and longitude (squares: GONG data; crosses: MDI data). The large-scale flow component was removed. The dashed line indicates the vertical velocity derived from MDI data without including the density gradient.

account in the fitting procedure, it is possible that other distortions of the ring shape caused by magnetic fields contribute to the error correlation. Therefore, it is possible that this reversal of the vertical flow at locations of very high activity is an artifact due to the large error correlation at greater depth. It is also possible that this is an artifact due to the statistically

small sample and that this reversal will be less apparent when we have more data sets analyzed.

3.3. Vorticity and Kinetic Helicity

From the daily flow maps, we also calculate daily maps of the vertical vorticity component and combine them to synoptic maps. An eddy rotating counterclockwise would have a positive local vorticity, and similarly, the vorticity of differential rotation is positive in the northern hemisphere and negative in the southern hemisphere. The vertical vorticity due to differential rotation changes sign at the equator. Since we focus on the relation between magnetic activity and the horizontal flows, we use the residual flows after subtracting the large-scale components to derive the vorticity component.

Figure 10 shows the synoptic map of the vertical vorticity component averaged over depth. The maps constructed from GONG and MDI data are again very similar; differences occur mainly at high latitudes. The correlation between vorticity values derived from GONG and MDI synoptic maps for each depth is 0.78 ± 0.05 on average. It increases to 0.89 ± 0.35 when the correlation is restricted to regions equatorward of 45° latitude. At locations of strong activity, there is a slight preference for the vorticity to be positive in the northern hemisphere and negative in the southern hemisphere. The correlation between magnetic flux and vorticity is only 0.12 ± 0.01 on average for all depths. To calculate the correlation, we changed the sign of vorticity in the southern hemisphere. The correlation changes to 0.17 ± 0.01 at depths less than 3 Mm when the calculation is restricted to regions equatorward of 45° latitude but remains at 0.11 ± 0.004 at depths greater than 8 Mm. In the synoptic maps, the correlation between magnetic flux and vorticity is much smaller in magnitude than the

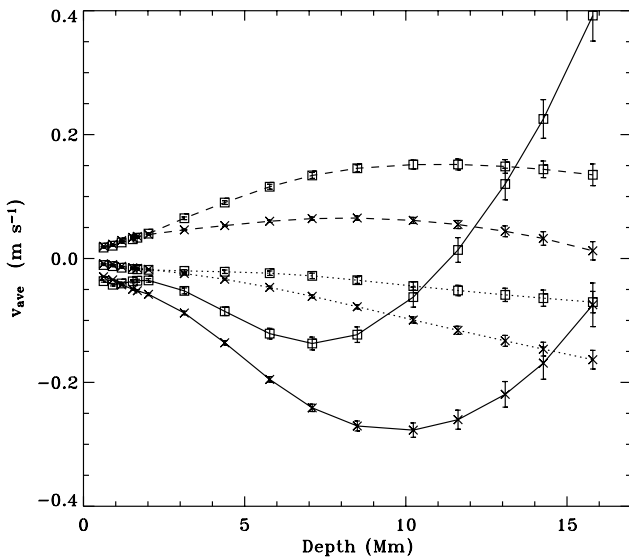


FIG. 9.—Vertical velocity averaged over three different ranges of surface magnetic flux (dashed line: less than median flux of 8.9 G; dotted line: between 1 and 6 times the median flux; solid line: greater than 6 times the median flux) for all longitudes and $\pm 37.5^\circ$ latitude for both data sets (squares: GONG data; crosses: MDI data).

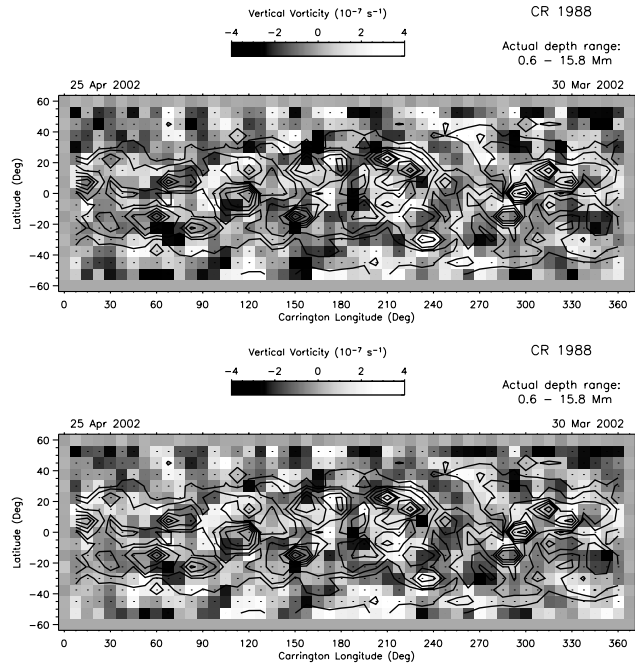


FIG. 10.—Same as Fig. 4, for the vertical vorticity component averaged over all depths. Top: GONG data. Bottom: MDI data. [See the electronic edition of the Journal for a color version of this figure.]

corresponding correlation between flux and divergence or vertical velocity.

As shown in Figure 11, the longitudinal average of the vertical vorticity component derived from MDI data shows hardly any variation with depth. Near 20° latitude the vorticity

is positive on average in the northern hemisphere and negative in the southern hemisphere, while the sign is reversed near 40° latitude. The corresponding plot of GONG data (not included) shows the same behavior. The contribution to the longitudinal average by the derivative in longitude reduces essentially to the difference between the meridional flow at the beginning and the end of the averaging interval. The longitudinal average of the vorticity is thus mainly determined by the derivative in latitude of the zonal flow.

The vertical vorticity calculated from the average flow (including differential rotation) is negative throughout the southern hemisphere and positive in the northern one at all depths with values ranging from -1.1×10^{-6} to $1.0 \times 10^{-6} \text{ s}^{-1}$. The vorticity of the mean flow is about 1 order of magnitude larger than the vorticity of the residual flow. In each hemisphere, its sign is the same as the one of the residual vorticity near 20° latitude. At locations of magnetic activity, there is an excess vorticity of the same sign as the one introduced by the rotation. The torsional oscillation pattern, which is known to show a strong gradient at the mean latitude of magnetic activity, and the circulation of the horizontal flows around active regions are the most likely contributors to the residual vorticity. The vorticity of opposite sign at high latitudes in Figure 11 might simply indicate that we need to remove an additional trend in latitude to completely separate the vorticity into average and residual components.

Figure 12 shows a synoptic map of the kinetic helicity density of the residual flow at a depth of 7 Mm derived from MDI data. The GONG data (not shown here) lead to a similar synoptic map. As throughout this study, differences between GONG and MDI data occur mainly at high latitudes. Locations of strong activity show large positive or negative values of helicity density. The unsigned helicity density is correlated

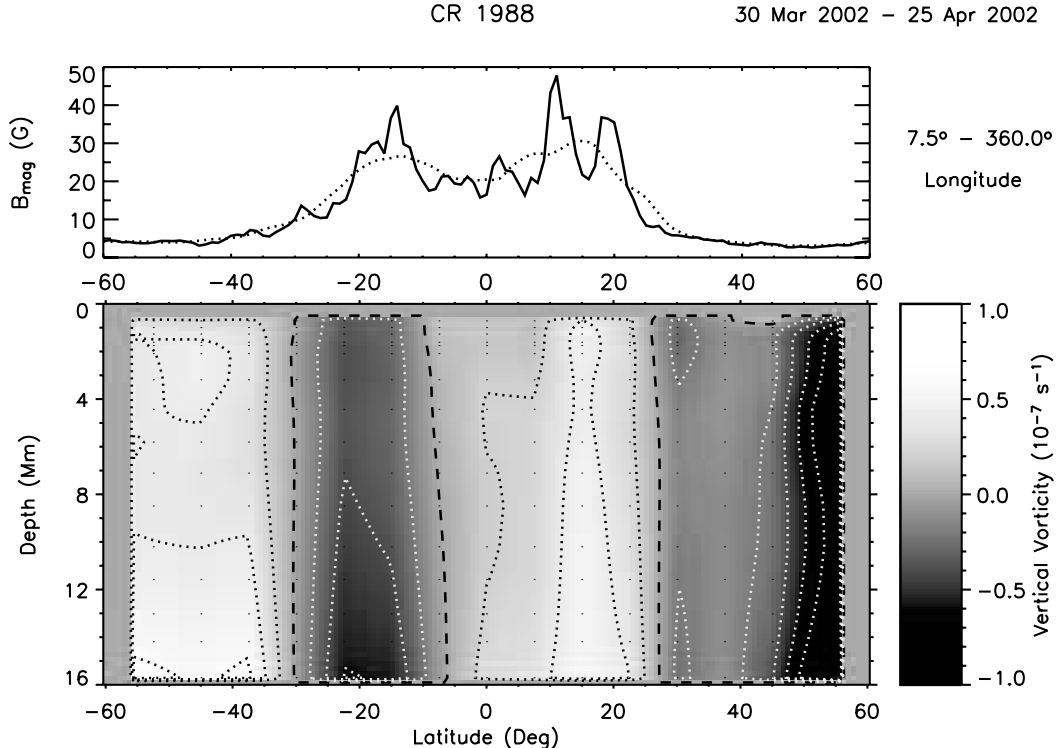


FIG. 11.—Same as Fig. 7 (Carrington rotation CR 1988: 2002 March 30–April 25), for the vertical vorticity component derived from MDI data after removing the large-scale flow components. [See the electronic edition of the Journal for a color version of this figure.]

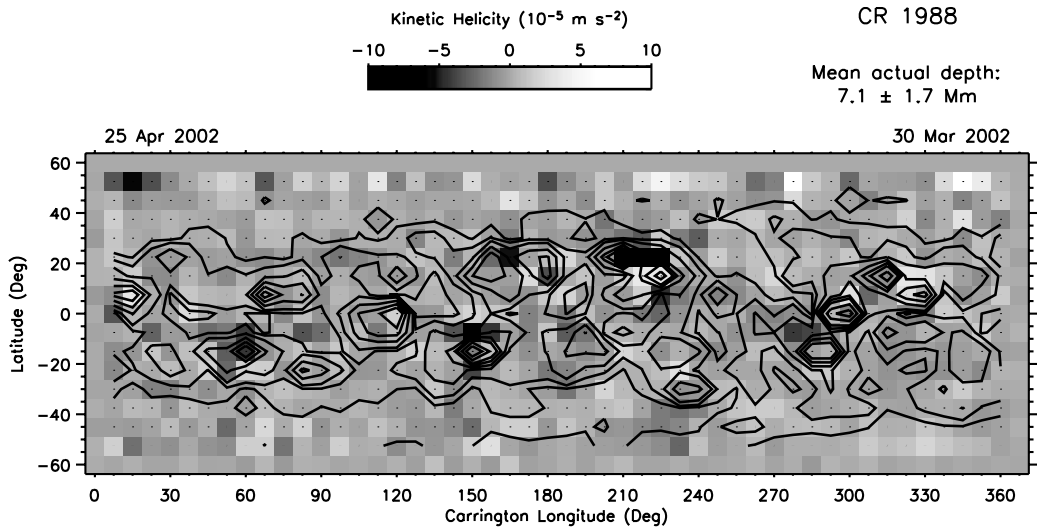


FIG. 12.—Kinetic helicity density at a depth of 7 Mm derived from MDI data. The contour lines indicate the magnetic flux (5, 10, 20, 40, 60, 80, 120, and 160 G). [See the electronic edition of the Journal for a color version of this figure.]

with the unsigned magnetic flux with an average coefficient of 0.28 ± 0.03 for MDI and 0.24 ± 0.05 for GONG data at depths greater than 2 Mm.

3.4. Vertical Gradients of Horizontal Flows

From global helioseismology, it is well-known that the rotation rate decreases from the location of the shear layer near $0.95 R_{\odot}$ toward the solar surface. For this reason, we expect the vertical gradient of rotation to be negative at depths observable with this study. As seen in Figure 13, the vertical gradient of the zonal flow averaged over longitude shows the expected behavior at depths greater than 2 Mm. The negative

gradient is stronger at latitudes equatorward of about 25° than at higher latitudes. Within 2 Mm of the surface at latitudes poleward of about 20° the gradient reverses its sign, indicating an increase of the rotation rate toward the surface. The sign reversal of the gradient at high latitudes agrees with previous observations (Basu, Antia, & Tripathy 1999; Corbard & Thompson 2002).

To study this sign reversal in more detail, we calculate synoptic maps of the gradient at different depths. Figure 14 shows synoptic maps of the vertical gradient of the zonal flows averaged over three different depth ranges. Near the surface (*top panel*) locations with positive gradient alternate with

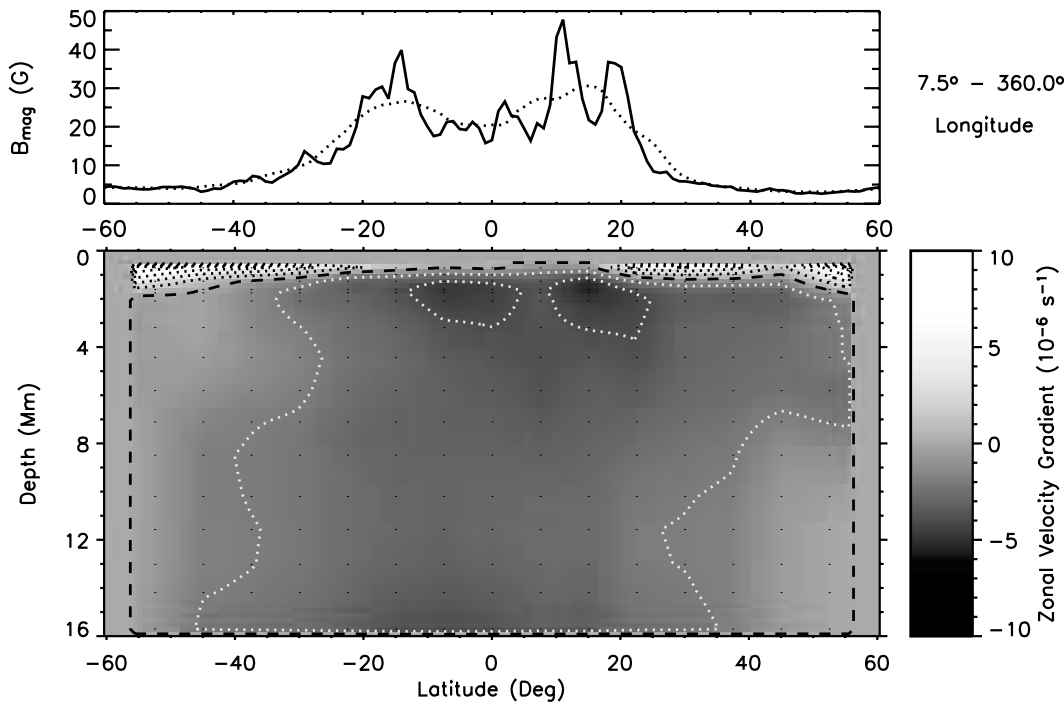


FIG. 13.—Same as Fig. 11 (Carrington rotation CR 1988: 2002 March 30–April 25), for the vertical gradient of the zonal flow derived from GONG data. [See the electronic edition of the Journal for a color version of this figure.]

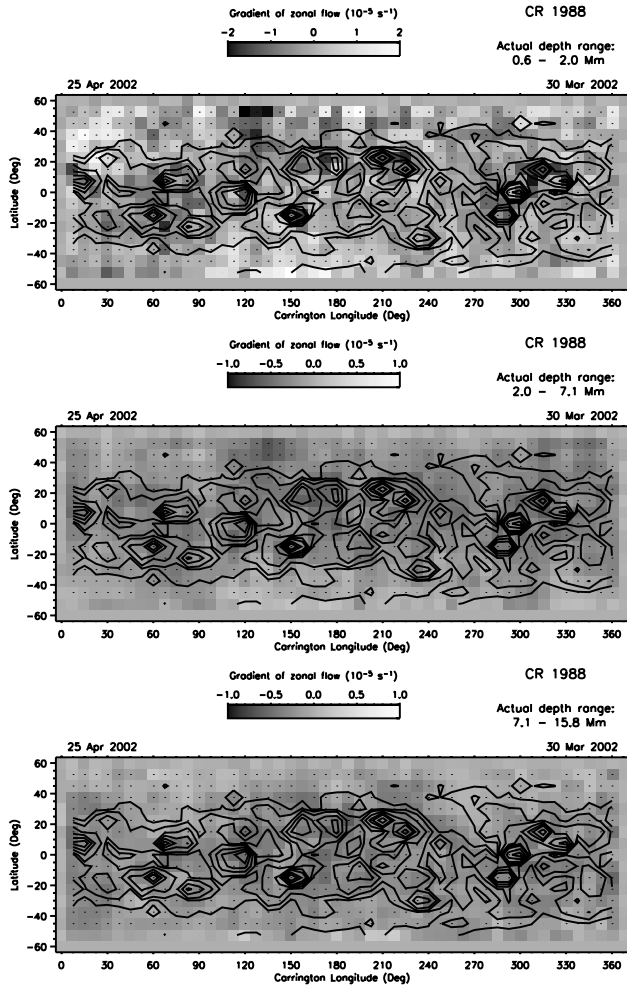


FIG. 14.—Gradient of zonal flows averaged over three depth ranges derived from GONG data. The contour lines indicate the magnetic flux (5, 10, 20, 40, 60, 80, 120, and 160 G). Top: 0.6–2.0 Mm. Middle: 2.0–7.1 Mm. Bottom: 7.1–15.8 Mm. [See the electronic edition of the Journal for a color version of this figure.]

locations with negative gradient at a given latitude. The positive gradient seen in the longitudinal average is a net result and does not reflect a uniform distribution. At greater depths (*middle and bottom panels*), the vertical gradient is predominantly negative. However, there are some locations at high latitudes that show a positive gradient. The most surprising feature is that the vertical gradient appears to track the distribution of magnetic activity. The correlation between magnetic flux and vertical gradient is on average -0.24 ± 0.07 for MDI and -0.24 ± 0.02 for GONG data over all depths, which makes it significant almost at the 99.9% level.

Figure 15 shows the vertical gradient of the meridional flow averaged over Carrington longitude derived from MDI data. We calculate this gradient from the absolute values to ensure that it reflects the change in magnitude and not a change in direction. At depths greater than about 7 Mm, the gradient is mainly negative except near the equator and near about 25° latitude in the northern hemisphere. Large negative gradients occur near 20°–30° latitude below about 12 Mm. The large negative values at latitudes poleward of about 45° are due to the counter cell. Closer to the surface, the gradient is mainly positive except very close to the surface near the equator and

at high latitudes. The GONG data show a similar behavior with the same clear distinction between near-surface and deeper layers.

4. SUMMARY AND DISCUSSION

Flow maps are the basic product of a ring-diagram analysis. While they show the complex behavior of the horizontal flows, other tools might be necessary to eventually quantify the dynamics of the flows and their interaction with magnetic activity. For this purpose, we begin exploring the use of fluid dynamics descriptors. These descriptors involve, in general, derivatives of the velocity field and not just the velocity itself. We show that we can derive such quantities from flow maps created from MDI and GONG data.

We derive the vertical velocity component of the flow field by assuming mass conservation, as stated in the continuity equation. This is an important step, since the ring-diagram analysis so far measures only the horizontal flow components. It would be of great interest if it were possible to derive the vertical velocity directly from the ring-diagram analysis. We find that during the Carrington rotation analyzed in this study, the vertical velocity is anticorrelated with magnetic activity. Locations of weak magnetic flux show mainly upflows, while locations of strong magnetic activity show downflows. This agrees with Zhao & Kosovichev (2003), who found downflows near a sunspot from a time-distance analysis of MDI data. We also find that the vertical velocity can change direction near a depth of about 8 Mm when the magnetic flux is very strong. This might be an artifact introduced by error correlation, as discussed in § 3.2. However, it is interesting that Zhao & Kosovichev (2003) find a similar reversal of the vertical flow in their time-distance analysis of a sunspot.

The small-scale component of the vertical vorticity shows a correlation with magnetic flux. The presence of magnetic activity leads to an excess vorticity of the same sign as that introduced by the differential rotation. The small-scale component of helicity density is large at locations of strong magnetic activity. This agrees with Zhao & Kosovichev (2004), who found that the residual vorticity peaks in the activity belts and is of opposite sign in each hemisphere from a time-distance analysis of MDI data. Since magnetic activity occurs mainly between 10° and 20° latitude in the analyzed time period, this result also agrees with the latitudinal distribution of helicity derived from sunspot observations by Pevtsov, Canfield, & Metcalf (1995), who used magnetograms covering a much longer time period, from 1988 to 1994. We will study the kinetic helicity in greater detail when we have more than 1 Carrington rotation analyzed.

The vertical gradient of the zonal flow shows, as expected, that the rotation rate decreases with increasing radius near the solar surface. We also confirm the sign reversal near the surface at high latitudes previously observed by Basu et al. (1999) and Corbard & Thompson (2002). To our surprise, we find that the negative gradient is stronger at locations of large magnetic flux. The vertical gradient of the absolute value of the meridional flow is mainly negative at depths greater than about 7 Mm and mainly positive closer to the surface.

The results shown in this paper are promising, but they should not be overinterpreted since the observations cover only 1 Carrington rotation. From this limited sample, we cannot distinguish whether a result is due to flow dynamics or magnetic activity. For example, the correlation between magnetic flux and the vertical gradient of the zonal flow could just be a

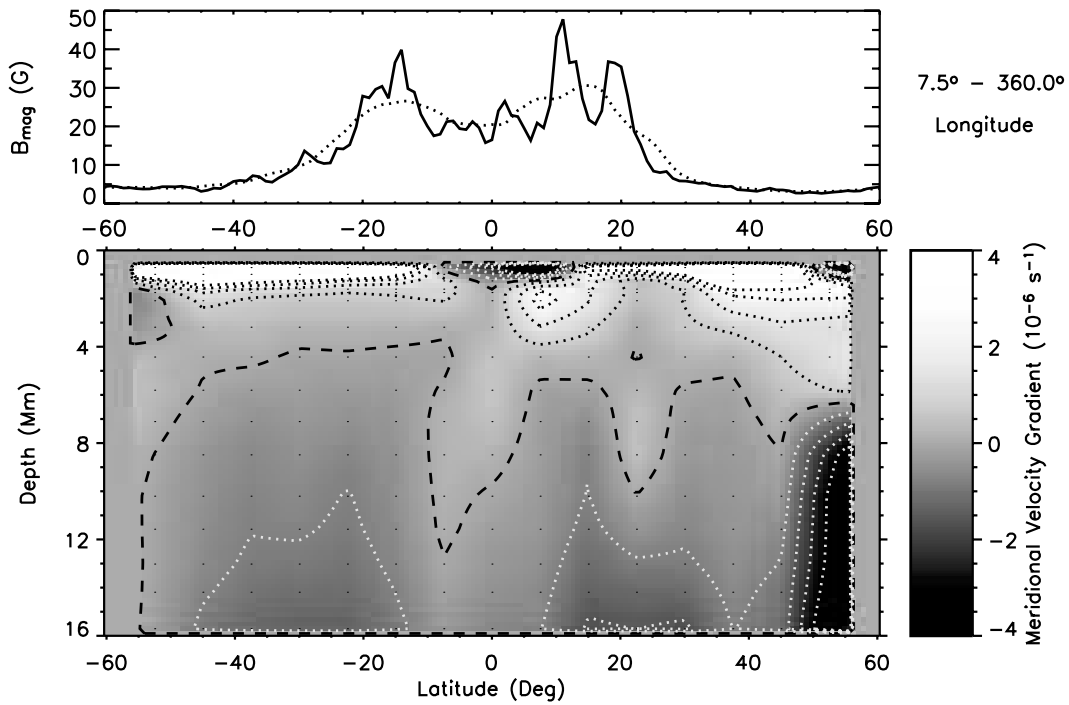


FIG. 15.—Same as Fig. 11 (Carrington rotation CR 1988: 2002 March 30–April 25), for the vertical gradient of the absolute value of the meridional flow derived from MDI data. [See the electronic edition of the Journal for a color version of this figure.]

coincidence. The latitudinal distribution of the gradient could be time-independent, and we happen to observe during a phase of the solar cycle when magnetic activity is present at low latitudes. The similarity of the results derived from GONG and MDI data gives some confidence in the results since the two different data sets have different systematics. However, both data sets were analyzed with the same ring-diagram pipeline, and the GONG pipeline is still being improved. Systematic effects caused by the analysis pipeline would be present in either data set.

As a next step, we intend to analyze data covering a range of activity levels in order to distinguish between the effect of flow dynamics and magnetic activity. For this purpose, we plan to analyze more MDI Dynamics Program data, which cover the solar cycle from the previous minimum to the current maximum and declining phase. When the GONG data taken with the upgraded system become available, we will have a continuous data set to analyze covering 2001 July to the present.

This work was supported by NASA grants S-92698-F and NAG 5-11703. This work utilizes data obtained by the Global Oscillation Network Group (GONG) project, managed by the National Solar Observatory, which is operated by AURA, Inc. under a cooperative agreement with the National Science Foundation. The data were acquired by instruments operated by the Big Bear Solar Observatory, High Altitude Observatory, Learmonth Solar Observatory, Udaipur Solar Observatory, Instituto de Astrofísico de Canarias, and Cerro Tololo Inter-American Observatory. The SOI-MDI project is supported by NASA grant NAG 5-3077 to Stanford University, with subcontracts to Lockheed Martin, to the University of Colorado, and to Harvard University. *SOHO* is a mission of international cooperation between ESA and NASA. NSO/Kitt Peak data used here are produced cooperatively by NSF/NOAO, NASA/GSFC, and NOAA/SEL. The ring-fitting analysis is based on algorithms developed by D. A. Haber, B. W. Hindman, and R. M. Larsen with support from NASA and Stanford University. We thank the referee for his valuable comments.

REFERENCES

- Basu, S., Antia, H. M., & Tripathy, S. C. 1999, *ApJ*, 512, 458
- Bogart, R. S., Sá, L. A. D., Duvall, T. L., Jr., Haber, D. A., Toomre, J., & Hill, F. 1995, in Proc. 4th *SOHO* Workshop: Helioseismology, Vol. 2, ed. J. T. Hoeksema (ESA SP-376; Noordwijk: ESA), 147
- Bogart, R. S., et al. 2003, SPD Meeting, 34, 08.04
- Christensen-Dalsgaard, J., et al. 1996, *Science*, 272, 1286
- Corbard, T., & Thompson, M. 2002, *Sol. Phys.*, 205, 211
- Corbard, T., Toner, C., Hill, F., Hanna, K. D., Haber, D. A., Hindman, B. W., & Bogart, R. S. 2003, in Local and Global Helioseismology: The Present and Future, ed. H. Sawaya-Lacoste (ESA SP-517; Noordwijk: ESA), 255
- Dikpati, M., & Gilman, P. 2001, *ApJ*, 559, 428
- Gough, D. O., & Toomre, J. 1983, *Sol. Phys.*, 82, 401
- Haber, D. A., Hindman, B. W., Toomre, J., Bogart, R. S., Larsen, R. M., & Hill, F. 2002, *ApJ*, 570, 885
- Haber, D. A., Hindman, B. W., Toomre, J., Bogart, R. S., Thompson, M. J., & Hill, F. 2000, *Sol. Phys.*, 192, 335
- Hill, F. 1988, *ApJ*, 339, 996
- Hill, F., Haber, D. A., & Zweibel, E. G. 1996, in Proc. IAU Symp. 181, Sounding Solar and Stellar Interiors, ed. J. Provost & F.-X. Schmider (Poster Vol.; Nice: Nice Obs.), 181
- Hill, F., et al. 2003, in Local and Global Helioseismology: The Present and Future, ed. H. Sawaya-Lacoste (ESA SP-517; Noordwijk: ESA), 295
- Holton, J. R. 1979, An Introduction to Dynamic Meteorology (New York: Academic)
- Howe, R., Komm, R. W., Hill, F., Haber, D. A., & Hindman, B. W. 2004, *ApJ*, in press
- Kleeorin, N., & Rogachevskii, I. 2003, *Phys. Rev. E*, 67, 026321
- Krause, F. 1967, Habilitationsschrift, Univ. Jena

- Moffatt, H. K., & Tsinober, A. 1992, *Annu. Rev. Fluid Mech.*, 24, 281
Pevtsov, A. A., Canfield, R. C., & Metcalf, T. R. 1995, *ApJ*, 440, L109
Scorer, R. S. 1978, *Environmental Aerodynamics* (Chichester: E. Horwood)
Snodgrass, H. B. 1984, *Sol. Phys.*, 94, 13
Steenbeck, M., & Krause, F. 1966, *Z. Naturforschung*, 21a, 1285
Toner, C., Haber, D. A., Corbard, T., Bogart, R. S., & Hindman, B. W.
2003, in *Local and Global Helioseismology: The Present and Future*, ed.
H. Sawaya-Lacoste (ESA SP-517; Noordwijk: ESA), 405
Zhao, J., & Kosovichev, A. G. 2003, *ApJ*, 591, 446
———. 2004, *ApJ*, 603, 776

I.3 Résultats

I.3.1 Les gradients radiaux de la rotation sub-photosphérique et le siège de la dynamo

I.3.1.1 Comparaison des résultats entre analyse des modes *f* et analyse locale

Le gradient radial de rotation jusqu'à 15 Mm sous la photosphère a été étudié précisément pour la première fois à partir des modes *f* de MDI (Corbard et Thompson 2002). Nous avons trouvé une pente du taux de rotation proche de la surface et à basse latitude d'environ -400 nHz/R. Ce gradient est remarquablement constant entre 0 et 30° de latitude puis décroît en amplitude pour devenir positif aux alentours de 60° de latitude. L'inversion du gradient n'est cependant observée que dans les couches les plus superficielles, jusqu'à 5 Mm sous la photosphère, vues par les modes $l \geq 250$. Cette valeur du gradient est tout à fait remarquable. En effet elle conduit à une valeur de la dérivée logarithmique $(\delta\Omega/\Omega)/(\delta r/r) \approx -1$ alors que si les parcelles de plasma conservaient leur moment angulaire spécifique, $\Omega r^2 \sin^2 \theta$, quand elles s'éloignent de l'axe de rotation, la dérivée logarithmique devrait être proche de -2. En fait les simulations numériques d'un fluide compressible en rotation et soumis à la convection montrent que d'autres effets tel que la diffusion vont introduire des échanges de moment angulaire si bien qu'une dérivée logarithmique du gradient de rotation plus proche de -1 est effectivement attendue (De Rosa, Gilman et Toomre 2002).

Le gradient radial de rotation proche juste sous la photosphère est également accessible par l'héliosismologie locale pour les latitudes inférieures à 55°. La Figure 14 montre une comparaison entre les résultats obtenus à partir des modes *f* de MDI et deux résultats obtenus en moyennant le gradient radial de la composante zonale V_x obtenue par analyse ring-diagram de deux jeux de données MDI et GONG+. Le profil global est en bon accord. Les valeurs trouvées aux basses latitudes diffèrent légèrement mais restent compatibles avec une dérivée logarithmique plus proche de -1 que de -2. L'analyse locale est trop incertaine au-dessus de 55° de latitude pour confirmer l'inversion du gradient. La tendance à la baisse de l'amplitude du gradient entre 30° et 50° est cependant la même pour toutes les analyses et données.

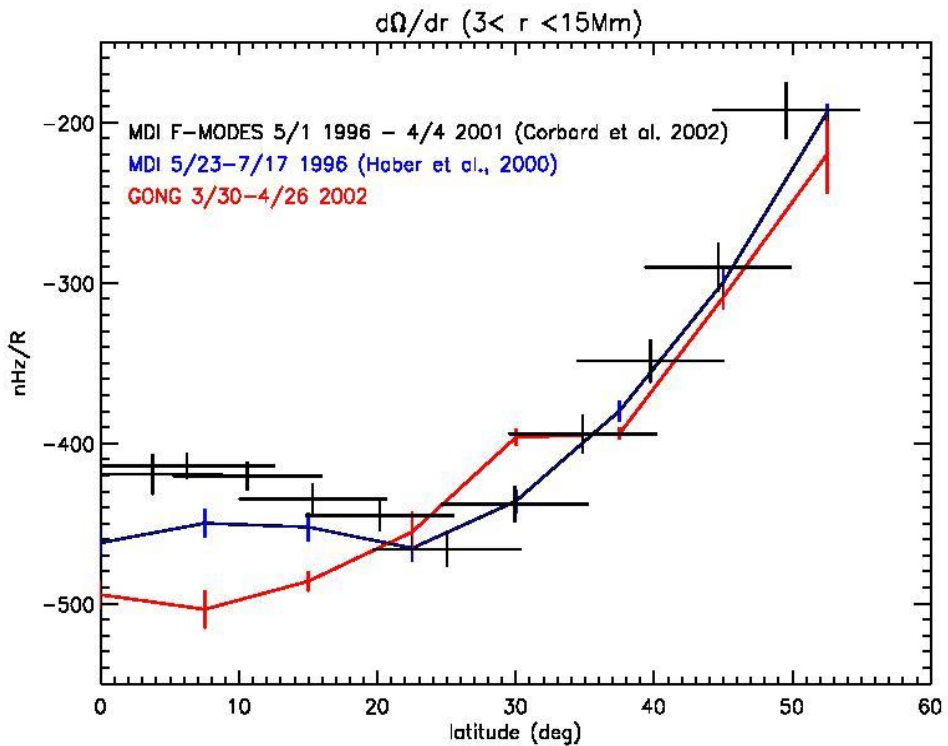


Figure 14 Gradient radial de la rotation en fonction de la latitude. Les trois courbes comparent des méthodes d'analyse et des données différentes : analyse des modes f de MDI en noir, analyses ring-diagram de données MDI en bleu et de données GONG+ en rouge.

Historiquement l'une des principales motivations pour obtenir le signe et l'amplitude de ce gradient sous la surface a été de pouvoir contraindre les premiers modèles de la dynamo Solaire. En effet, avant l'avènement de l'héliosismologie, les observations Doppler de surface montraient une rotation plus lente que la rotation des traceurs magnétiques. Ceux-ci étant ancrés plus profondément un gradient négatif avait été déduit mais la profondeur d'ancrage des traceurs magnétiques étant incertaine, l'amplitude du gradient restait également incertaine. Ainsi les premiers modèles de la dynamo opéraient juste sous la surface avec un effet alpha positif et un effet omega, lié au gradient de rotation, négatif. Avec l'héliosismologie et la découverte de la tachocline, il a été réalisé que la zone de gradients les plus forts étaient en fait à la base de la zone convective mais avec un signe positif aux basses latitudes. De ce fait la plupart des modèles de la dynamo considère maintenant que l'effet oméga opère dans la tachocline ou un effet alpha, cette fois négatif est également introduit. Mais du coup, beaucoup de ces modèles développés après la découverte de la tachocline, ignorent complètement l'existence du gradient de surface.

I.3.1.2 Application à un modèle dynamo (article)

ARTICLE : [Flux Transport Solar Dynamos with Near-Surface Radial Shear](#) (Dikpati, Corbard, et al. 2002)

Avec M. Dikpati au HAO à Boulder nous avons voulu vérifier contribution potentielle du gradient sub-photosphérique à la dynamo solaire ((Cobard, Dikpati, et al. 2002) (Dikpati, Cobard, et al. 2002)). Nous avons montré que sa contribution à la génération du champ toroïdal reste faible et ne pourrait pas expliquer seule la formation des taches avec un champ magnétique dépassant le KG et que les polarités des taches ainsi formées ne respecteraient pas la répartition observée. Le champ toroïdal formé en surface, s'il ne permet pas de générer les taches, peut par contre contribuer par diffusion à la réduction du champ polaire, le rapprochant, dans les modèles, de la valeur observée. Globalement cette étude renforce le schéma généralement admis dans lequel l'effet omega doit prendre place essentiellement dans la tachocline alors que des effets alpha doivent être invoqués à la fois en surface et dans la tachocline. La génération d'un champ toroïdal par l'action du gradient radial de rotation à la surface peut toutefois contribuer à affaiblir par diffusion le champ polaire.

FLUX TRANSPORT SOLAR DYNAMOS WITH NEAR-SURFACE RADIAL SHEAR

MAUSUMI DIKPATI

High Altitude Observatory, National Center for Atmospheric Research,¹ 3450 Mitchell Lane, P.O. Box 3000, Boulder, CO 80301-3000; dikpati@ucar.edu

THIERRY CORBARD

National Optical Astronomy Observatory, National Solar Observatory, 950 North Cherry Avenue, Tucson, AZ 85726-6732; corbard@noao.edu

MICHAEL J. THOMPSON

Space and Atmospheric Physics, Blackett Laboratory, Imperial College, Prince Consort Road, London SW7 2BW, England, UK; michael.thompson@ic.ac.uk

AND

PETER A. GILMAN

High Altitude Observatory, National Center for Atmospheric Research,¹ 3450 Mitchell Lane, P.O. Box 3000, Boulder, CO 80301-3000; gilman@ucar.edu

Received 2002 May 15; accepted 2002 June 28; published 2002 July 17

ABSTRACT

Corbard & Thompson analyzed quantitatively the strong radial differential rotation that exists in a thin layer near the solar surface. We investigate the role of this radial shear in driving a flux transport dynamo operating with such a rotation profile. We show that despite being strong, near-surface radial shear effectively contributes only ~ 1 kG ($\sim 30\%$ of the total) to the toroidal fields produced there unless an abnormally high, surface α -effect is included. While 3 kG spot formation from ~ 1 –2 kG toroidal fields by convective collapse cannot be ruled out, the evolutionary pattern of these model fields indicates that the polarities of spots formed from the near-surface toroidal field would violate the observed polarity relationship with polar fields. This supports previous results that large-scale solar dynamos generate intense toroidal fields in the tachocline, from which buoyant magnetic loops rise to the photosphere to produce spots. Polar fields generated in flux transport models are commonly much higher than observed. We show here that by adding enhanced diffusion in the supergranulation layer (originally proposed by Leighton), near-surface toroidal fields undergo large diffusive decay preventing spot formation from them, as well as reducing polar fields closer to the observed values. However, the weaker polar fields lead to the regeneration of a toroidal field of less than ~ 10 kG at the convection zone base, too weak to produce spots that emerge in low latitudes, unless an additional poloidal field is produced at the tachocline. This is achieved by a tachocline α -effect, previously shown to be necessary for coupling the north and south hemispheres to ensure toroidal and poloidal fields that are antisymmetric about the equator.

Subject headings: magnetic fields — MHD — Sun: activity — Sun: interior — Sun: magnetic fields — Sun: rotation

1. INTRODUCTION

It is widely believed that a magnetohydrodynamic dynamo produces the 11 yr activity cycle by generating a magnetic field within the Sun. Extensive studies over the past decade (Wang, Sheeley, & Nash 1991; Choudhuri, Schüssler, & Dikpati 1995; Dikpati & Charbonneau 1999, hereafter DC99; Küker, Rüdiger, & Schultz 2001; Dikpati & Gilman 2001) reveal that flux transport dynamos are successful in reproducing many large-scale solar cycle features, including a difficult one, the phase relationship between the toroidal and poloidal components. These models can also produce the correct dynamo cycle period when the amplitude of the meridional flow that is observed near the surface is used. These models invoked solar-like differential rotation that contains a strong radial gradient in the tachocline and showed that the strong toroidal fields are generated in the tachocline. The surface eruption of these fields as bipolar spots is believed to be due to their buoyant rise through the convection zone.

Recently, Corbard & Thompson (2002) reported a quantitative analysis of the radial gradient of angular velocity in the subphotospheric layer using Michelson Doppler Imager (MDI) observations of surface gravity waves from the *Solar and Heliospheric Observatory*. Their analysis infers that a strong radial shear resides in a thin layer just below the solar surface for

depths down to about 15 Mm. Foukal (1972) first proposed such a shear layer with angular velocity increasing inward as an explanation for differences in rotation rates of large and small sunspots. Foukal & Jokipii (1975) argued that radially moving fluid elements in convection could produce the inward increase if they tended to conserve their angular momentum. Gilman & Foukal (1979) verified this effect with a Boussinesq spherical shell convection model, and De Rosa (2002) has recently shown that it happens in (anelastic) compressible convection as well. Kosovichev (1996), while estimating the tachocline thickness, also noted that a subsurface shear layer results when the helioseismically obtained internal rotation is matched with the surface rotation (Snodgrass 1992).

The observational as well as theoretical inferences for the existence of this subphotospheric radial shear layer immediately raise several questions. Is the α - Ω solar dynamo operating primarily near the surface? Do the toroidal fields manifest directly after they are generated there? Are the poloidal fields also generated there by the decay of active regions? Is there no longer a need for flux storage in the subadiabatically stratified overshoot layer and radiative zone? To answer these questions, we simulate a flux transport dynamo incorporating this newly estimated rotation profile.

In flux transport dynamos, meridional circulation takes the primary role in transporting magnetic flux. Thus, if the toroidal fields are generated by the near-surface radial shear (Ω -effect) in such models, they would be transported toward the pole. On the

¹ The National Center for Atmospheric Research is sponsored by the National Science Foundation.

TABLE 1
PARAMETER VALUES

Ω_0 (nHz)	$\Omega_{\text{eq}}(R)$ (nHz)	r_{tac}/R	r_{cz}/R	a_2 (nHz)	a_4 (nHz)
435	452.5	0.69	0.71	-61	-73.5

NOTE.—Parameter values kept the same as in Kosovichev 1996.

other hand, a strong, negative radial shear, in conjunction with a positive poloidal source term (such as a Babcock-Leighton-type source) near the surface would give rise to an equatorward, classical dynamo speed, since $\alpha \partial \Omega / \partial r < 0$. This speed can potentially compete with the poleward advective speed. One aim of this Letter is to investigate the evolutionary pattern of the magnetic fields in the subphotospheric shear layer, specifically to explore the feasibility of closing an α - Ω dynamo loop directly in the near-surface shear layer, ignoring any tachocline Ω -effect (Brown et al. 1989).

2. ANALYTICAL PRESCRIPTION FOR THE OBSERVED NEAR-SURFACE SHEAR

In order to infer the radial gradient of angular velocity close to the surface, Corbard & Thompson used a small, but significant, radial dependence of the f -modes with degrees between $l = 117$ and 300 observed by MDI between 1996 May and 2001 April (Schou 1999). The outward gradient is found to be negative with a value of about 400 nHz R_{\odot}^{-1} , remarkably constant up to 30° latitude, before decreasing to a small value approaching zero at about 50° latitude. At higher latitudes, the inference is much less certain, but the high degree modes $l > 250$ seem to indicate that the gradient may reverse its sign and become strongly positive.

To incorporate the near-surface radial shear in the dynamo simulation, we derive an analytical form for the solar internal rotation as a function of latitude and depth. This model can be described as follows (from the core to the surface): (1) the rotation rate is taken to be constant in the radiative interior (Ω_0); (2) the location (r_{tac}) and the width (ω_{tac}) of the tachocline are assumed independent of latitude; (3) the rotation rate at the top of the tachocline (r_{cz}) and at the surface are given by $\Omega(r, \mu) = \Omega_{\text{eq}}(r) + a_2\mu^2 + a_4\mu^4$, where (a_2, a_4) describe the latitudinal differential rotation, $\Omega_{\text{eq}}(r_{\text{cz}}) = \Omega_0 - a_2/5 - 3a_4/35$, assuming no net torque across the tachocline, and ($\Omega_{\text{eq}}[R]$) is taken from surface plasma observations (Snodgrass 1992);

TABLE 2
NONCOMMON PARAMETER VALUES

Model	ω_{tac}/R	ω_{cz}/R	ω_s/R	r_s/R	β_0 (nHz R^{-1})	β_6 (nHz R^{-1})
A	0.1	0	0	0.983	891.5	0
B	0.05	0.05	0.05	0.97	437	-1445

(4) the near-surface radial gradient is assumed to be constant at a given latitude down to a radius (r_s), and its latitudinal dependence is given by (β_0, β_6), obtained by fitting the results of Corbard & Thompson (2002) with $\beta(\mu) = \beta_0 + \beta_6\mu^6$, which gives the very flat part at low latitude corresponding to the constant negative gradient and allows for a strong positive gradient above 50° .

The transitions between different gradients are constructed by using error functions centered at $r_{\text{tac}}, r_{\text{cz}}$, and r_s and widths $\omega_{\text{tac}}, \omega_{\text{cz}}, \omega_s$: $\phi_x(r) = 0.5 \{1 + \text{erf}[2(r - r_x)/\omega_x]\}$, where x stands for tac, cz, or s. This introduces two new parameters ($\omega_{\text{cz}}, \omega_s$), leading to a total of 12 parameters (see parentheses in the description above) for the final expression of the solar internal rotation, given by

$$\Omega(r, \mu) = A_1(r, \mu) + \phi_{\text{tac}}(r)(\Omega_{\text{cz}} - \Omega_0 + a_2\mu^2 + a_4\mu^4), \quad (1)$$

with

$$A_1(r, \mu) = \Omega_0 + \phi_{\text{cz}}[\alpha(\mu)(r - r_{\text{cz}})] + \phi_s(r) \times [\Omega_{\text{eq}} - \Omega_{\text{cz}} - \beta(\mu)(r - R) - \alpha(\mu)(r - r_{\text{cz}})], \quad (2)$$

$$\alpha(\mu) = \frac{\Omega_{\text{eq}} - \Omega_{\text{cz}} + \beta(\mu)(R - r_s)}{r_s - r_{\text{cz}}}. \quad (3)$$

This form can be related to Kosovichev's (1996) profile, where the parameters were fixed by fitting the tachocline parameters from the Big Bear Solar Observatory observations and assuming the conservation of angular momentum in the supergranulation layer. Here we keep the values of those parameters the same as in Kosovichev's model except for considering a thinner tachocline (see the review from Corbard et al. 2001) and assuming nonzero widths of the transitions at r_{cz} and r_s in order to avoid discontinuities in the derivative. We take the position of the near-surface maximum arbitrarily at the base of the layer

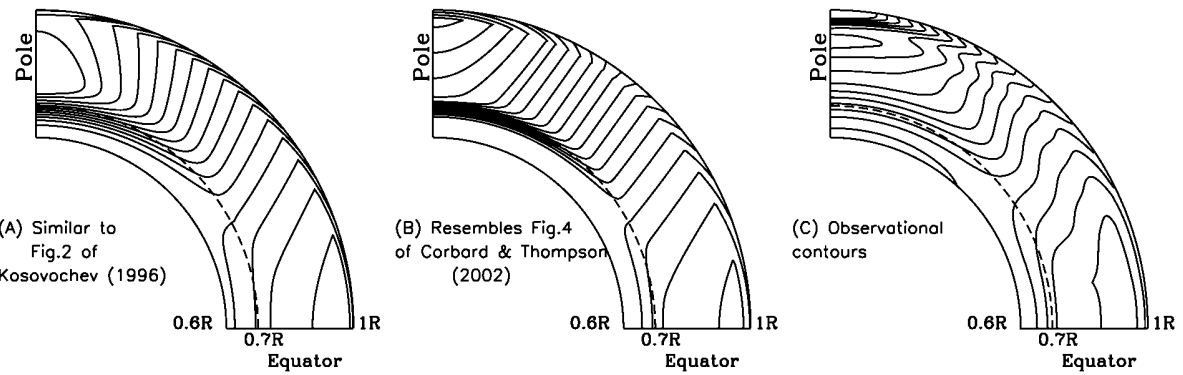


FIG. 1.—Isocontours of solar rotation profile plotted in the meridional cut. (a) Kosovichev's (1996) profile, (b) profiles from eq. (1) taking into account the subsurface gradients inferred by Corbard & Thompson (2002), and (c) the result of inverting 72 days of MDI data. Lowest contour corresponds to 301 nHz and highest to 452 nHz.

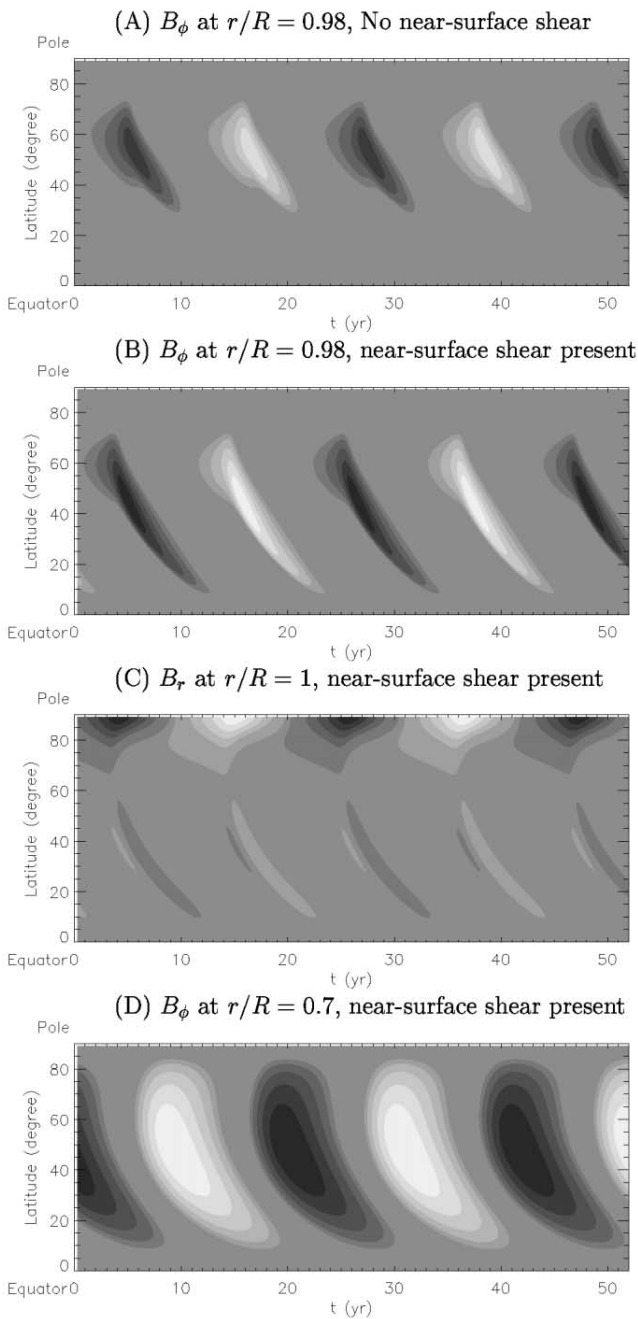


FIG. 2.—Time-latitude diagrams obtained from a Babcock-Leighton flux transport dynamo: near-surface toroidal field produced (a) without near-surface shear and (b) with near-surface shear; (c) surface radial field and (d) tachocline toroidal field. In (a), white shading represents 1.2 kG positive toroidal field, in (b) 1.7 kG toroidal field, and in (c) 68 kG toroidal field (see Table 1). Dark shading represents negative fields. Negative toroidal fields in a time-latitude diagram denote the negative polarity of the following spots in the bipolar spot groups.

sensed by the observed f -modes and fit the f -mode observation as discussed above in order to get the subsurface shear parameter, instead of assuming angular momentum conservation (see Tables 1 and 2).

Figure 1 shows the solar rotation contours. Figure 1a corresponds to Kosovichev's (1996) profile (see his Fig. 2); Figure 2b shows the profile from the new model based on the observed surface gradient. For comparison, we include in Fig-

TABLE 3
DYNAMO-GENERATED FIELD STRENGTHS AT DIFFERENT DEPTHS

$\eta_p/\eta_{\text{core}}$	$\partial\Omega/\partial r _{r=0.98R}$	$B_\phi _{r=0.98R}$ (kG)	$B_\phi _{r=0.7R}$ (kG)
1000	Present	1.7	68
1000	Absent	1.2	68
1	Present	5.7	28

ure 1c a profile obtained by RLS inversion of 72 days of MDI frequency-splitting observations. This last profile exhibits much more complicated structures, especially at high latitudes. The result of such a global inversion involving global regularization is however not good for providing precise and localized information about the shear layers. Since the purpose of this work is to study the influence of such shear layers in dynamo models, we believe it is more important at this stage to use the best observational inference of the radial shear, while keeping a simple description of the differential rotation in the bulk of the convection zone rather than attempting to include all details of differential rotation deduced from a global inversion.

3. WHERE IS THE SOLAR DYNAMO LOCATED?

To focus primarily on the question of whether the major toroidal fields are generated near the surface or at the tachocline, we select the framework of a Babcock-Leighton-type flux transport dynamo of DC99. The reason is that the poloidal fields in Babcock-Leighton models are also generated near the surface, and therefore they can be available immediately after they are born for further generation of toroidal fields by the action of strong, surface radial shear. Prescribing our newly parameterized solar rotation profile (eq. [1]), we solve the dynamo equations (3a) and (3b) of DC99. We keep the other ingredients—the meridional flow pattern, a Babcock-Leighton-type poloidal source term that depends on latitude and magnetic field strength, and a depth-dependent diffusivity profile—the same as in DC99. We apply the similar boundary conditions and employ the same numerical technique of DC99. We plot time-latitude diagrams of solutions for the evolution of $B_\phi|_{r=0.7R}$, $B_\phi|_{r=0.98R}$, and $B_r|_{r=R}$ in Figure 2. Note that $B_\phi = 0$ at the top boundary; therefore, we extract the solution at $r = 0.98R$, at the center of the near-surface shear layer.

In panels *a* and *b*, we see an equatorward migration of the near-surface toroidal fields (produced, respectively, without and with near-surface shear) suggesting a solar-type butterfly diagram in both cases. Panels *b* and *c* of Figure 2 reveal that B_r leads $B_\phi|_{r=0.98R}$ by 90° in phase rather than lagging by 90° as is observed. In other words, polar fields would have the polarity of follower spots early in a sunspot cycle and that of leader spots late in the cycle, exactly the opposite of what is observed. If the spots are generated from the buoyantly rising toroidal flux tubes from the base of the convection zone, then they would appear with a correct phase with respect to their vector counterparts at the surface. Note that the polar fields (in Fig. 2c) reverse their sign from positive (*white*) to negative (*black*) when the subsurface toroidal field (in Fig. 2d) is already negative (*black*). The same thing is true without near-surface shear, which can be seen by comparing Figure 2a with its corresponding polar field in a time-latitude diagram (not shown). Therefore, the near-surface shear as the source of spots can be ruled out as it produces a 180° phase error.

Table 3 below presents the field strength generated at the convection zone base and near the surface when the near-surface

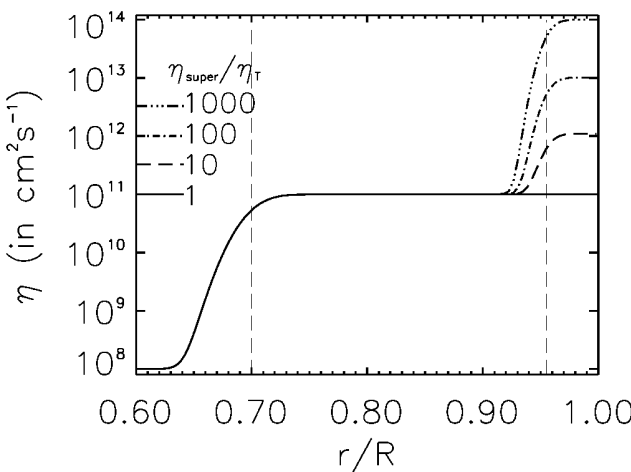


FIG. 3.—Diffusivity profile as a function of depth for four different ratios of supergranular diffusion (η_{super}) to turbulent diffusion (η_T). Depth of the supergranulation layer ($\sim 0.05R$ in which η_{super} works) is chosen assuming that supergranular cells have an aspect ratio (width to depth) of approximately unity.

radial shear is present and also when it is absent. We find that the presence of the near-surface radial shear hardly contributes to B_ϕ at $0.98R$, increasing the strength by 0.5 kG only. $B_\phi|_{r=0.7R}$ undergoes much less decay than $B_\phi|_{r=0.98R}$ because our choice of diffusion coefficient is $3 \times 10^8 \text{ cm}^2 \text{ s}^{-1}$ at the bottom boundary, while it varies as an error function to reach a value of $3 \times 10^{11} \text{ cm}^2 \text{ s}^{-1}$ in the main bulk of the convection zone. We ensure, by running a case with constant diffusivity ($10^{11} \text{ cm}^2 \text{ s}^{-1}$) throughout our computation domain ($0.6R$ – $1R$ in the northern meridional cut) that the ratio of $B_\phi|_{r=0.7R}$ and $B_\phi|_{r=0.98R}$ reduces to 5 : 1 from 40 : 1 (see the third row in Table 3).

The possibility of flux concentration by convective collapse near the surface and hence the 3 kG spot formation even from ~ 1 – 2 kG toroidal field cannot be ruled out. But the polarities of spots that would be formed from the peak toroidal field near the surface, rather than from the buoyantly rising flux loop originating in the peak toroidal field at the convection zone base, would violate the observed polarity relationship with the polar fields.

The near-surface toroidal fields are not weak in this model because the poloidal fields themselves are not weak (> 100 G). Such strong poloidal fields near the surface eventually result in producing the strong (> 500 G) polar fields owing to the poleward convergence of the meridional flow. This has been noted as one of the drawbacks in Babcock-Leighton flux trans-

port models (Durney 1995; Dikpati & Charbonneau 1999; Küker et al. 2001). A turbulent diffusion (η_T) of 10^{11} – $10^{12} \text{ cm}^2 \text{ s}^{-1}$ is not enough to reduce them. There is no direct measurement for η_T other than the mixing-length-type arguments. Increasing the value of η_T to greater than $10^{12} \text{ cm}^2 \text{ s}^{-1}$ in the bulk of the convection zone would lead to a reduced polar field due to large diffusive decay of the large-scale poloidal fields in the upper convection zone, but it would also lead to an incorrect dynamo speed and an incorrect phase relationship between the sunspot fields and the surface radial fields (not shown here) because the mode of operation of the dynamo no longer remains the advective conveyor belt type; rather, it shifts to the diffusion-dominated regime.

However, we can remedy this problem of large polar field production in the Babcock-Leighton flux transport models if we include a second diffusivity contrast, across the thin supergranulation layer near the surface, in addition to one across the core-envelope interface. While a supergranular diffusion coefficient ($\eta_{\text{super}} \sim 10^{12}$ – $10^{14} \text{ cm}^2 \text{ s}^{-1}$) near the surface will destroy much of the poloidal flux before the polar concentration takes place, a somewhat reduced, turbulent diffusivity ($\eta_T \sim 10^{11} \text{ cm}^2 \text{ s}^{-1}$) in the bulk of the convection zone will help the dynamo remain in the advection-dominated regime. Leighton (1964) first proposed such an enhanced diffusion of $\sim 10^{13} \text{ cm}^2 \text{ s}^{-1}$ in the supergranulation layer to explain the observed dispersal rate of the unipolar magnetic regions. Later, slightly lower values [$\sim (2$ – $4) \times 10^{12} \text{ cm}^2 \text{ s}^{-1}$] were estimated and used by various authors (e.g., Mosher 1977; Wang, Nash, & Sheeley 1989; Schrijver 2001) to model the observed dispersal of bipolar and unipolar regions. We have chosen here a broader range of supergranular diffusion that is consistent with the full range of estimates from analysis of surface magnetic field and supergranular patterns.

Incorporating such diffusivity contrast as shown in Figure 3, we first solve the Babcock-Leighton flux transport dynamo. Then, we also explore how the polar field strength is affected in a flux transport dynamo driven by a tachocline α -effect (Dikpati & Gilman 2001) and operating with this supergranular diffusion. We compare the results in Table 4. We fix η_{core} at $10^8 \text{ cm}^2 \text{ s}^{-1}$, η_T at $10^{11} \text{ cm}^2 \text{ s}^{-1}$, and poloidal source amplitude at 1 ms^{-1} , and we vary η_{super} from 10^{12} to $5 \times 10^{13} \text{ cm}^2 \text{ s}^{-1}$.

We see that with the increase in supergranular diffusion in the Babcock-Leighton model, $B_\phi|_{r=0.98R}$ decreases much faster than $B_\phi|_{r=0.7R}$, but the polar field decreases at the same rate as $B_\phi|_{r=0.7R}$. This is because the surface poloidal fields act as the seed for further toroidal field production, so B_{pole} reduction leads to reduction of the toroidal fields at the convection zone base. Beyond a certain high supergranular diffusion, the polar fields are reduced to the solar-like value, but that, in turn, reduces

TABLE 4
EFFECT OF η_{super} ON DYNAMO-GENERATED FIELD STRENGTHS

Dynamo Driven by	η_{super}	$B_\phi _{r=0.7R}$ (kG)	$B_\phi _{r=0.98R}$ (G)	$B_r _{\text{pole}}$ (G)
Babcock-Leighton poloidal source	1×10^{12}	100.1	965	1198
	2×10^{12}	65.8	405	736
	5×10^{12}	31.1	92	293
Tachocline α -effect	1×10^{13}	3.2	6	25
	1×10^{12}	157.5	527	555
	2×10^{12}	154.5	323	482
	5×10^{12}	147.2	149	346
	1×10^{13}	134.3	80	278
	5×10^{13}	61.5	7	69

$B_\phi|_{r=0.7R}$ below the strength necessary (5×10^4 – 10^5 G; Choudhuri & Gilman 1987) for spot emergence at low latitudes at the surface.

By contrast, in the flux transport dynamo driven by a tachocline α -effect, $B_r|_{\text{pole}}$ decreases much faster than $B_\phi|_{r=0.7R}$. Therefore, this model, operating with a supergranular diffusion of 5×10^{13} cm 2 s $^{-1}$, leads to a solar-like polar field of a few tens of gauss, without reducing the $B_\phi|_{r=0.7R}$ below the required

amplitude for low-latitude spot emergence. All the above simulations fail as dynamos if the tachocline shear is removed.

We thank Matthias Rempel for reviewing the manuscript and for his helpful comments. We extend our thanks to an anonymous referee whose insightful suggestions have helped us improve the Letter. This work is supported by NASA grants W-19752 and S-10145-X.

REFERENCES

- Brown, T. M., Christensen-Dalsgaard, J., Dziembowski, W. A., Goode, P. R., Gough, D. O., & Morrow, C. A. 1989, ApJ, 343, 526
 Choudhuri, A. R., & Gilman, P. A. 1987, ApJ, 316, 788
 Choudhuri, A. R., Schüssler, M., & Dikpati, M. 1995, A&A, 303, L29
 Corbard, T., Jiménez-Reyes, S. J., Tomczyk, S., Dikpati, M., & Gilman, P. 2001, in Proc. SOHO 10/GONG 2000 Workshop, Helio- and Asteroseismology at the Dawn of the Millennium, ed. A. Eff-Darwich & A. Wilson (ESA SP-464; Noordwijk: ESA), 265
 Corbard, T., & Thompson, M. 2002, Sol. Phys., 205, 211
 De Rosa, M. 2002, Ph.D. thesis, Univ. Colorado, Boulder
 Dikpati, M., & Charbonneau, P. 1999, ApJ, 518, 508 (DC99)
 Dikpati, M., & Gilman, P. A. 2001, ApJ, 559, 428
 Durney, B. R. 1995, Sol. Phys., 160, 213
 Foukal, P. 1972, ApJ, 173, 439
 Foukal, P., & Jokipii, J. R. 1975, ApJ, 199, L71
 Gilman, P. A., & Foukal, P. 1979, ApJ, 229, 1179
 Kosovichev, A. G. 1996, ApJ, 469, L61
 Küker, M., Rüdiger, G., & Schultz, M. 2001, A&A, 374, 301
 Leighton, R. B. 1964, ApJ, 140, 1547
 Mosher, J. M. 1977, Ph.D. thesis, Caltech
 Schou, J. 1999, ApJ, 523, L181
 Schrijver, C. J. 2001, ApJ, 547, 475
 Snodgrass, H. B. 1992, in ASP Conf. Ser. 27, The Solar Cycle, ed. K. L. Harvey (San Francisco: ASP), 205
 Wang, Y.-M., Nash, A. G., & Sheeley, N. R., Jr. 1989, Science, 245, 712
 Wang, Y.-M., Sheeley, N. R., Jr., & Nash, A. G. 1991, ApJ, 383, 431

I.3.2 La composante zonale : les oscillations de torsion, le lien avec l'activité magnétique et l'asymétrie nord-sud

La rotation différentielle du Soleil n'est pas constante dans le temps, elle subit des variations qui sont fortement corrélées avec l'activité magnétique observée en surface. Ces variations temporelles de la rotation différentielle sont appelées « oscillations de torsion ». Elles ont été mises en évidence pour la première fois à partir des observations Doppler de la surface obtenues au Mont Wilson (Howard et Labonte 1980). Une bande de rotation plus rapide que la moyenne apparaît aux latitudes moyennes (45°) puis se propage vers l'équateur en suivant un schéma qui s'apparente au « diagramme papillon » lié à la progression des taches au cours du cycle (Figure 3). C'est l'exemple le plus flagrant de lien observé entre le magnétisme et la dynamique globale du Soleil. L'observation d'une forte corrélation entre ces deux observables globales suggère que les oscillations de torsion sont une signature de la dynamo solaire couplant la dynamique au magnétisme. Le ou les processus précis qui produisent cette variation de la composante zonale de la vitesse reste cependant très débattu. Les candidats évoqués sont la rétroaction des forces de Lorentz sur la rotation (Schussler 1981), une rétroaction thermique (Spruit, Origin of the torsional oscillation pattern of solar rotation 2003) ou encore un blocage magnétique du transport du moment angulaire (Kitchatinov, et al. 1999).

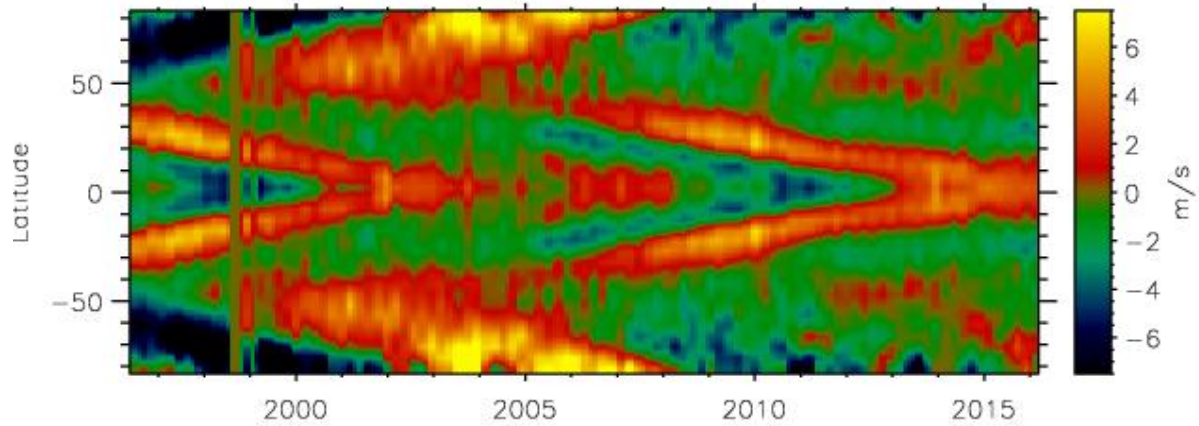


Figure 15 Oscillation de torsion obtenue par l'analyse des splittings des modes f observés par SoHO/MDI (1996-2011) et SDO/HMI (2011-2016) selon la procédure développée par Corbard & Thompson (2002). Ce diagramme donne, en fonction du temps et de la latitude héliographique, l'écart à la vitesse de rotation différentielle moyenne calculée par une moyenne glissante sur ± 5 ans. Pour les 5 premières et dernières années, la moyenne de référence est prise sur les 10 premières et 10 dernières années respectivement. L'analyse globale des modes f ne donne accès qu'à la composante symétrique par rapport à l'équateur de la rotation. C'est cette composante, symétrique, qui est montrée ici.

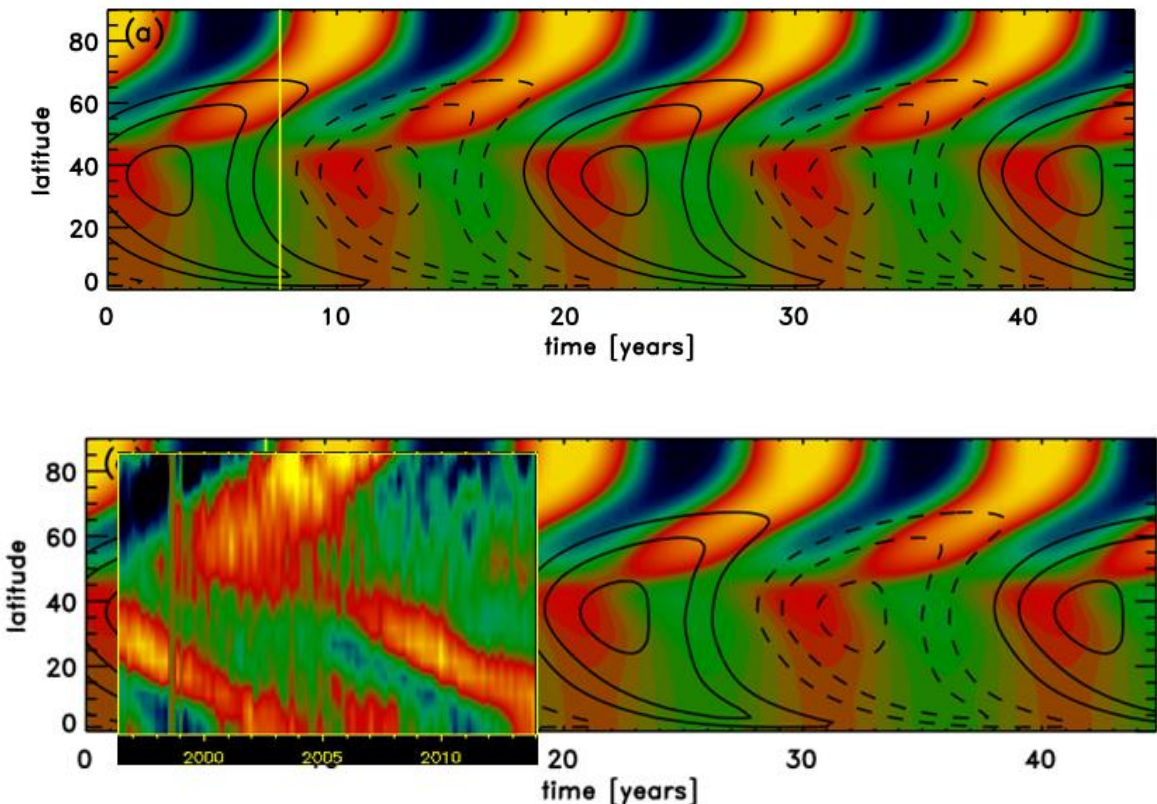


Figure 16 En haut : simulation de la branche polaire ($>45^\circ$) des oscillations de torsion basé sur une Dynamo de type Babcock–Leighton avec transport de flux. Les lignes de contours donnent le champ magnétique à la base de la zone convective comme proxy du diagramme papillon magnétique (Rempel 2012). En bas : un extrait de la Figure 15 mise à l'échelle est superposée à la simulation montrant l'excellent accord entre théorie et observation entre 1996 et 2007. Au-delà de 2007 cependant la nouvelle branche polaire attendue n'est pas observée.

Deux branches distinctes de rotations plus rapides que la moyenne apparaissent sur ce diagramme : une branche équatoriale et une branche polaire, les deux partant aux environs de 50° de latitude et migrant vers l'équateur et les pôles respectivement. Un modèle dynamo de type Babcock–Leighton a été développé (Rempel 2006) dans lequel la rotation différentielle et la circulation méridienne sont obtenues de façon auto-consistante par la modélisation de l'équation de transport turbulent des contraintes de Reynolds. Dans ce modèle la branche polaire résulte de la rétroaction des forces de Lorentz alors que la branche équatoriale fait intervenir les aspects thermiques proposés par Spruit (2003). Des simulations de la branche polaire des oscillations de torsion utilisant ce modèle (Rempel 2012) donnent un très bon accord avec l'observation entre 1996 et 2007 (Figure 16).

A partir de 2007 une différence notable avec le cycle précédent est apparue sur ce diagramme : alors que la branche équatoriale est bien présente, la signature de la branche polaire est quasi absente jusqu'en 2014 et demeure faible ensuite. Il a été suggéré en 2013 que la signature d'une branche polaire peut être mise en évidence si au lieu de prendre comme référence une rotation moyenne sur 10 ans, nous prenions la rotation moyenne sur la seule phase ascendante de chaque cycle (Howe, et al. 2013).

Cette procédure fait effectivement apparaître une zone de rotation plus rapide que la moyenne au-dessus de 45° à partir de 2012 mais, je montre sur la Figure 17 que si nous l'appliquons également au cycle précédent, elle conduit à partir de 1999 à une branche dont le contraste pour le cycle 23 est toujours beaucoup plus important que celui observé pour le cycle 24. De plus le très bon accord obtenu entre 1997 et 2007 entre l'observation de la branche polaire et ce qui est attendu à partir d'un modèle dynamo incluant la rétroaction des forces de Lorentz n'est plus obtenu si l'on applique la procédure de Howe et al. (2013).

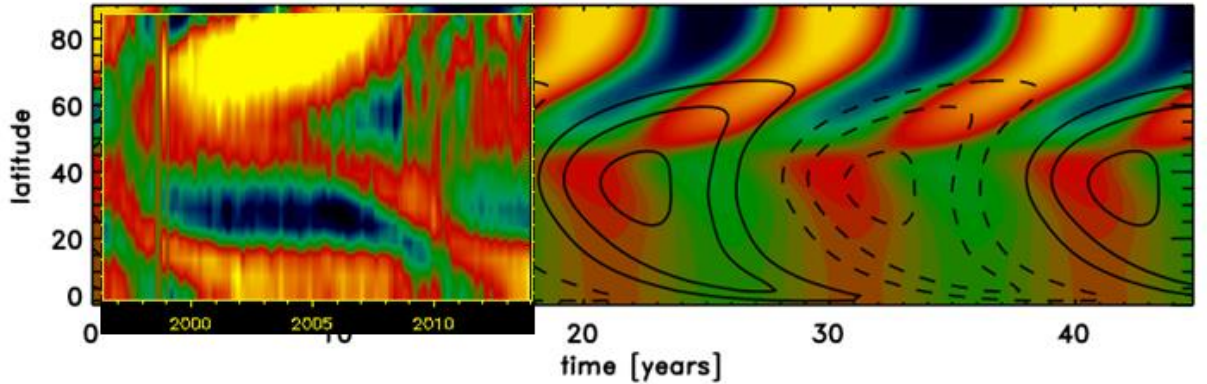


Figure 17 Comme la Figure 16 (bas) mais en utilisant la procédure de Howe et al. (2013) pour les observations. Un signal de branche polaire apparaît en 2011 mais au détriment de l'accord avec la courbe théorique sur le cycle précédent.

En fait la Figure 15 montre que des indications de l'existence d'une branche polaire apparaissent bien à partir de 2014 en gardant une moyenne sur 10 ans comme référence. Le fait qu'elle soit plus faible qu'au cycle précédent peut être lié au fait que le champ polaire observé (Figure 4) est plus faible qu'au cycle précédent ce qui peut être la signature d'un effet alpha moins important. Les simulations de Rempel (2012) ont en fait montré qu'une diminution progressive de l'effet alpha peut conduire à une perte de contraste apparent sur la branche polaire des oscillations de torsion. La réduction de l'action des forces de Lorentz entraîne une rotation différentielle accrue avec une rotation polaire dont l'amplitude moyenne est réduite. Au cours de la phase d'ajustement du taux de rotation moyen, qui dans les simulations peut prendre 20 ans, les oscillations de torsion deviennent plus difficiles à mettre en évidence. Il semble donc que la faible branche polaire observée pour le cycle 23 soit la signature d'un cycle de faible amplitude sans que l'action dynamo ne soit interrompue. Des spéculations sur l'entrée dans une phase étendue de minimum d'activité du type minimum de Maunder (c.f. Figure 2) ont en effet été formulées dès 2011 mais l'observation d'une signature de la branche polaire depuis 2014 et les simulations ne permettent pas de confirmer cette hypothèse : la perte de contraste observée peut s'expliquer par une réduction temporaire du taux de rotation et du champ magnétique sans que cette phase soit nécessairement prolongée pour conduire à une période de grand minimum. Compte tenu de l'importance de suivre l'évolution de ce diagramme des oscillations de torsion, j'ai mis en place une procédure

automatique qui transfert tous les 72 jours depuis le serveur de la mission SDO/HMI les splittings des modes f observés et met à jour la Figure 15 en suivant la procédure développée dans (Corbard et Thompson 2002)⁶.

Finalement il est à noter que l'héliosismologie locale et notamment l'analyse « ring-diagram » donne également accès à la composante zonale de la vitesse en faisant simplement des moyennes en longitude de la composante V_x pour les différentes latitudes observées. Ces analyses permettent essentiellement d'apporter deux informations supplémentaires par rapport aux analyses globales : la possibilité d'étudier séparément les zones de forte activité magnétique et celles associées à un magnétisme faible, et la possibilité d'accéder à la composante non symétrique de la rotation par rapport à l'équateur.

Dans notre travail exploitant la chaîne de traitement « ring diagram » sur une année complète de données GONG+ (Komm et al. (2005)) nous avons pu montrer que la composante zonale moyenne de la vitesse n'est pas affectée par les vitesses convergentes ou divergentes observées autour des zones actives. En effet lorsque les zones actives sont exclues de l'analyse, ce que seule l'héliosismologie locale permet, l'aspect moyen de la rotation et donc des oscillations de torsion n'est pas modifié. Cela montre qu'il s'agit bien d'une propriété qui affecte globalement la rotation et non pas d'un effet qui serait la somme des vitesses de circulations particulières observées autour des zones actives.

Par ailleurs, avec mon étudiante nous avons analysé l'asymétrie nord-sud des deux composantes horizontales de la vitesse et donc de la rotation et des oscillations de torsion associées (Zaatri et al. (2006)). Cette analyse portait sur 44 rotations de Carrington couvrant la phase descendante du cycle 23 (2001-2004). Des effets systématiques ont été mis en évidence résultant d'incertitudes sur l'angle B_0 de l'inclinaison de l'axe de rotation solaire par rapport à l'observateur. Une fois cette correction apportée, les variations temporelles de la rotation dans les deux hémisphères ont été trouvées très bien corrélées pour les latitudes inférieures à 20° . Le taux de rotation est trouvé supérieur dans l'hémisphère sud et cette asymétrie nord-sud augmente avec la profondeur. Les détails de cette asymétrie nord-sud sont en concordance avec l'asymétrie du champ magnétique observé en surface et comme cette dernière, elle évolue avec le cycle.

⁶ <https://solar-physics.oca.eu/spip.php?article417>

I.3.3 La circulation mérienne

La circulation mérienne est comme nous l'avons vu un élément clef des modèles de la dynamo avec transport de flux. Une circulation mérienne entre 10 et 20 mètres par seconde et dirigée vers les pôles est observée en surface par les mesures Doppler (Hathaway, et al. 1996) ou encore le suivi des traceurs magnétiques (Komm, Howard et Harvey 1993). En invoquant la conservation de la masse, une circulation inverse est supposée exister en profondeur. De plus, afin de pouvoir transporter le champ poloïdal dans la tachocline où il peut être amplifié et transformé en champ toroïdal par l'effet omega, la circulation retour est généralement considérée comme devant avoir lieu au niveau de la tachocline. Avant le développement de l'héliosismologie locale nous n'avions cependant aucun moyen de vérifier ces hypothèses par l'observation.

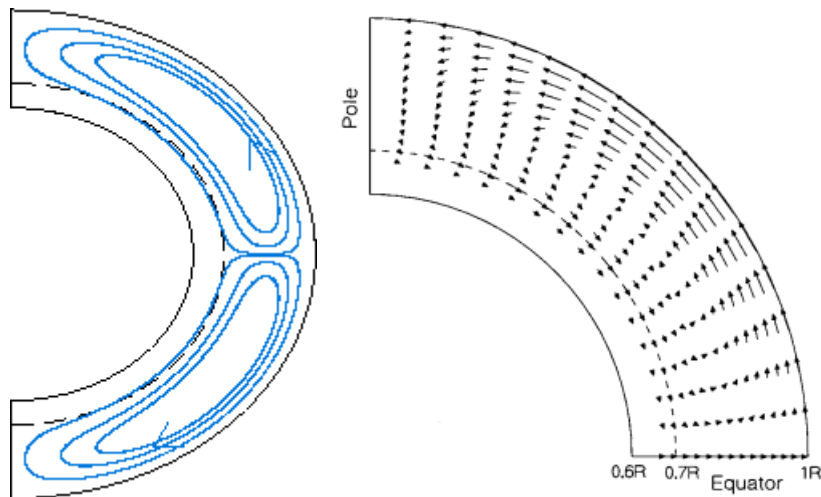


Figure 18 Exemple de profil de la circulation mérienne utilisé dans un modèle dynamo avec transport de flux. Ce profil permet la migration vers les pôles du champ magnétique diffus à grande échelle et son transport vers la tachocline où il peut être amplifié et transformé en champ toroïdal. Dans ce modèle, l'amplitude de la circulation vers le pôle est maximale en surface à mi-latitude et la circulation vers l'équateur est d'amplitude maximale à 0.7 R (Dikpati et Charbonneau 1999)

Un des premiers enjeux de l'héliosismologie locale a été de chercher à obtenir des contraintes observationnelles sur cette circulation mérienne : son profil en profondeur et en latitude avec l'existence ou non de plusieurs cellules dans chaque hémisphère et sa variabilité avec le cycle. Une analyse temps-distance de données MDI a initialement trouvé la signature d'une cellule de circulation mérienne inverse à haute latitude (Giles 2000). Une étude ‘ring-diagram’ menée sur la même période, toujours avec les données MDI a également trouvé la signature d'une cellule à haute latitude dans l'hémisphère nord avec une circulation mérienne dirigée vers l'équateur en surface (Haber, et al. 2002). La présence à hautes latitudes de telles cellules de circulation mérienne vers l'équateur pourrait influencer le transport du flux magnétique vers le pôle et réduire l'amplitude du champ polaire. C'est donc une question essentielle sur laquelle l'héliosismologie locale essaye d'apporter des contraintes.

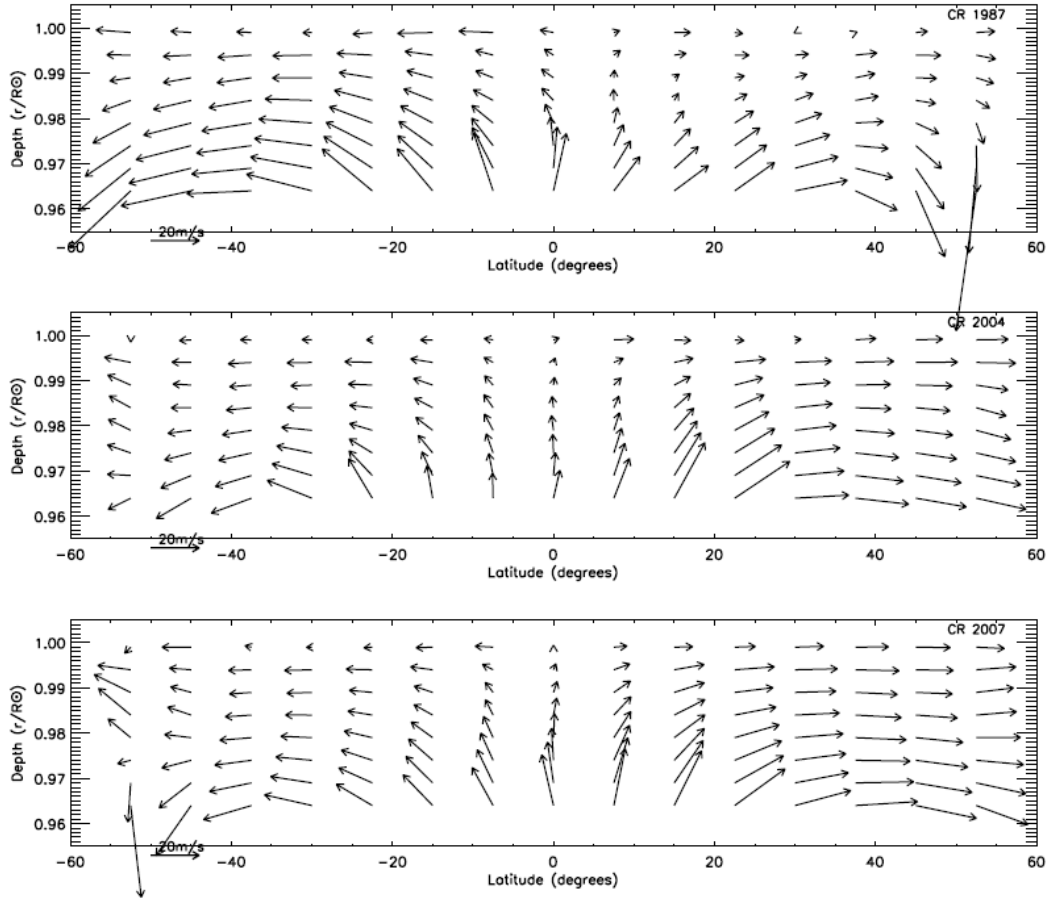


Figure 19 Circulation méridienne obtenue en combinant la composante V_y de la vitesse horizontale avec la vitesse radiale déduite de la divergence de la vitesse horizontale et de l'équation de continuité. Le résultat moyen est donné pour les rotations de Carrington 1987 (haut), 2004 (milieu) et 2007 (bas). Sur les figures de haut et du bas, la signature d'une circulation inversée est trouvée sous 0.97 R dans les hémisphères nord et sud respectivement. (González Hernández, et al. 2006)

Nous avons mené ce travail avec l'équipe GONG en exploitant notamment une version modifiée de la chaîne de traitement mise en place pour l'analyse ring-diagram. En effet pour essayer de sonder les couches plus profondes que les 15 Mm habituellement accessibles par l'analyse, nous avons élargi les surfaces d'analyse à $30^\circ \times 30^\circ$ au lieu des $15^\circ \times 15^\circ$ habituellement utilisés. Cela permet de capturer le signal de modes de degrés plus faibles pénétrant plus profondément. L'approximation en ondes planes utilisée par la méthode locale est toutefois d'autant plus mise en défaut que la surface analysée est grande. Cette extension nous a néanmoins permis d'obtenir des résultats jusqu'à 26 Mm sous la photosphère, soit 0.96 rayon solaire (González Hernández, et al. 2006).

La Figure 19 montre la circulation méridienne que nous avons obtenue par l'analyse de données GONG+ pour trois rotations de Carrington différentes. La solution est obtenue pour les latitudes inférieures à 55° . Il est à noter que, habituellement, seule la composante V_y de la vitesse horizontale est donnée comme estimation de la circulation méridienne. Cependant la composante méridienne de la circulation est fonction non seulement de la latitude mais aussi de la profondeur (c.f. Equation (2)). Nous avons donc utilisé la vitesse verticale estimée à partir de la divergence de la vitesse horizontale et de

l'équation de continuité (Komm, Corbard, et al. 2004) pour en déduire pour la première fois les deux composantes du vecteur vitesse correspondant à la circulation méridienne. Le premier résultat visible sur ces figures est que, contrairement à ce qui est généralement imposé dans les modèles de la dynamo, l'amplitude de la circulation méridienne croît avec la profondeur dans la zone superficielle explorée. La densité croissant avec la profondeur, l'amplitude de la circulation méridienne ne peut pas croître indéfiniment avec la profondeur. Nous nous attendons donc à ce qu'une zone de transition existe au-delà de la zone accessible à notre analyse. Nous voyons clairement dans chaque hémisphère une cellule principale de circulation vers les pôles. Pour les rotations de Carrington 1987 et 2007, une circulation inversée apparaît aux plus grandes profondeurs sondées ($0.965 R$) dans les hémisphères nord et sud respectivement. Nous avons cependant remarqué que, aux plus hautes latitudes analysées, l'apparition de circulation vers l'équateur se produit lorsque la valeur de l'angle B_0 est la plus forte (Figure 20). Il est donc probable que l'apparition sporadique de ces cellules de circulations inverses aux hautes latitudes parfois dans l'hémisphère nord, parfois dans l'hémisphère sud soit la conséquence d'un effet géométrique. L'analyse étant limitée aux latitudes inférieures à 55° nous ne pouvons pas exclure l'existence de cellules de circulation vers l'équateur aux hautes latitudes mais ce travail utilisant les données GONG et la comparaison avec les données MDI nous a permis de mieux comprendre l'importance des effets de projection pour l'analyse des hautes latitudes.

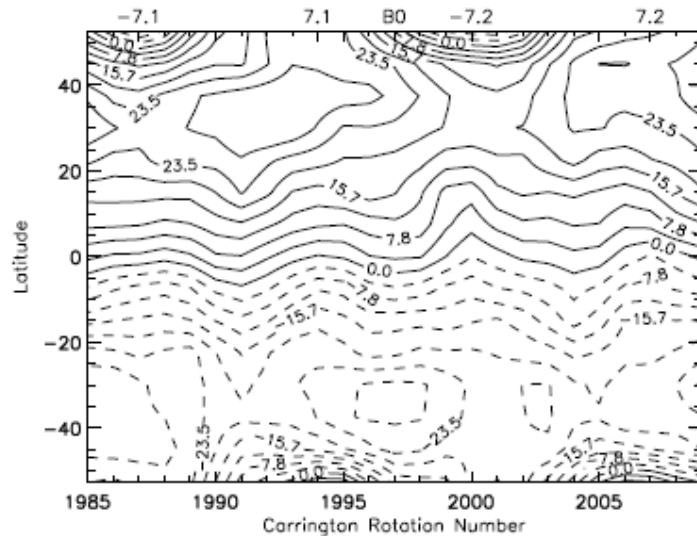


Figure 20 Amplitude de la circulation méridienne à $0.96 R$ (26 Mm) en fonction de la latitude et du temps. Les valeurs de l'angle B_0 au centre des rotations de Carrington 1987, 1994, 2000 et 2007 sont données sur l'axe supérieur. Les circulations inverses observées aux latitudes supérieures à 50° se produisent autour des maxima de B_0 , pour les valeurs négatives de B_0 dans l'hémisphère nord et les valeurs positives dans l'hémisphère sud (González Hernández, et al. 2006).

A la suite de ce travail une correction systématique des effets de projection dû à la variation annuelle de l'angle B_0 a été introduite ce qui a par la suite, avec les données SDO/HMI, permis de confirmer que la circulation méridienne demeure dirigée vers les

pôles à toutes les profondeurs (jusqu'à 16 Mm) pour les latitudes inférieures à $\pm 67.5^\circ$. Cependant cet effet que nous avons mis en évidence avec les données GONG demeure problématique au-delà de 75° pour l'analyse des données HMI (Komm, Gonzalez Hernandez, et al. 2013).

I.3.4 La circulation autour des zones actives

L'analyse ring-diagram avec des zones d'analyse de $15^\circ \times 15^\circ$ ne permet pas à proprement parler de résoudre spatialement la circulation autour des zones actives. Cependant, en s'aidant des magnétogrammes, il est possible de classer chaque zone en fonction du flux magnétique moyen qu'elle contient et de séparer l'analyse des zones de faible activité de celles contenant des zones actives. C'est ce que nous avons fait en moyennant les résultats sur une période couvrant 14 rotations de Carrington (R. Komm, R. Howe, et al. 2005). La Figure 21 montre que d'une manière générale les latitudes actives (autour de $\pm 20^\circ$ pour la période considérée) correspondent à des mouvements vers l'intérieur jusqu'à 16 Mm alors que pour les latitudes calmes nous trouvons plutôt des mouvements vers la surface. Lorsque nous isolons seulement les zones les plus magnétisées, une zone de transition apparaît vers 11 Mm avec un flux vers la surface sous cette limite et vers l'intérieur au-dessus. Concernant la circulation méridienne, nous pouvons soustraire la circulation moyenne et regarder la circulation résiduelle. Sur la Figure 22, nous voyons qu'un flot convergent vers les zones actives est mis en évidence. Si nous isolons les zones les plus actives nous trouvons à nouveau une zone de transition vers 8 Mm en dessous de laquelle la circulation s'inverse. D'une manière générale nous avons ainsi mis en évidence qu'au profil moyen de la circulation s'ajoute une composante associée aux zones actives avec un flot convergent dans les couches les plus superficielles et qui devient divergent entre 10 et 16 Mm. Le profil de la circulation moyenne reste sensiblement le même au cours du cycle mais son amplitude varie et une circulation localisée liée aux zones actives vient se superposer.

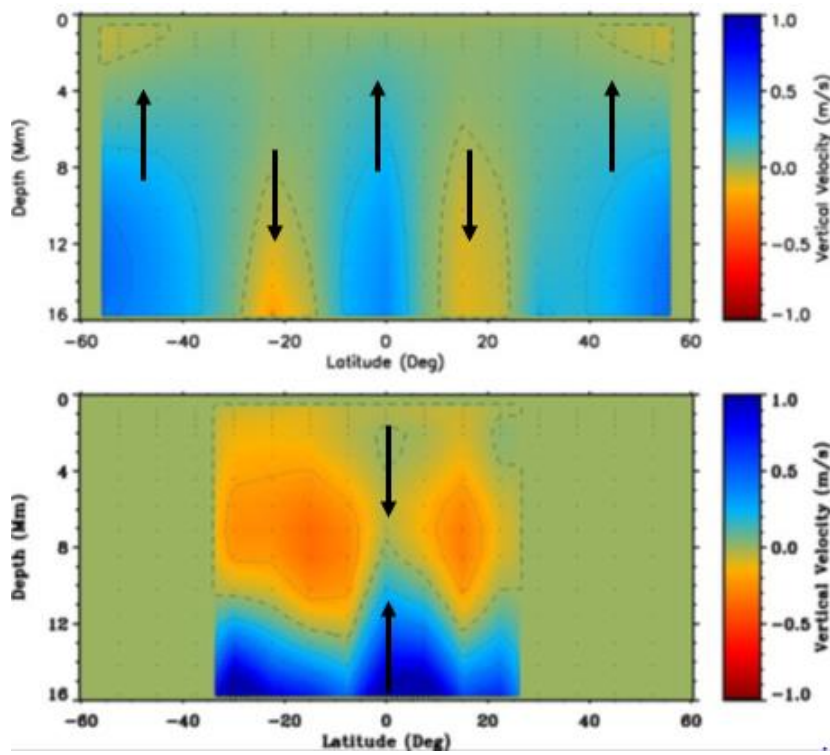


Figure 21. Vitesse verticale résiduelle moyennée sur les zones de faible activité (haut) et sur les zones avec des flux moyens supérieurs à 71 G. Les flèches indiquent la direction de circulation

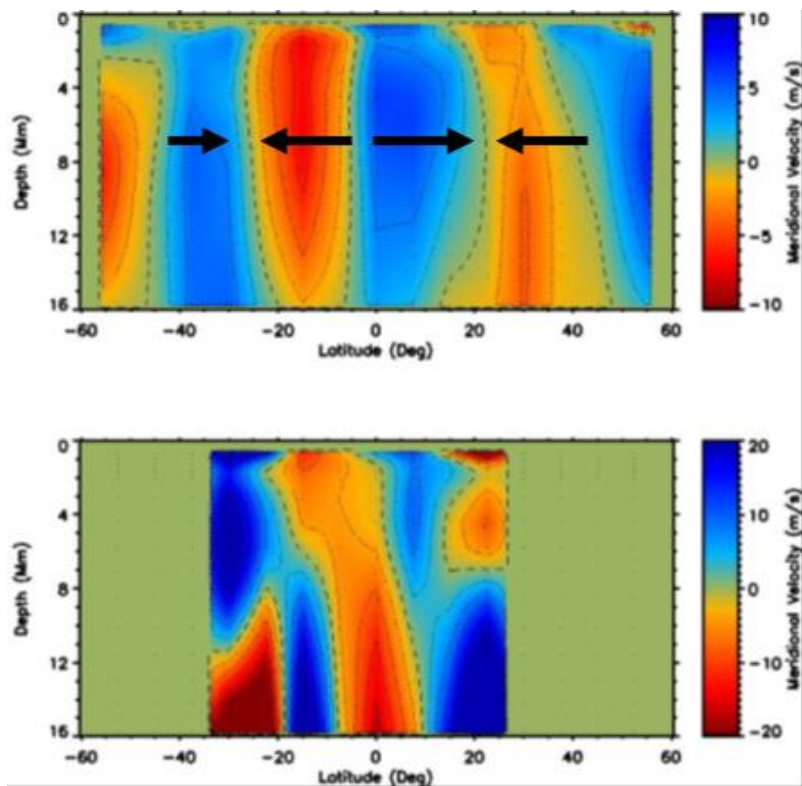


Figure 22. Même chose que sur la Figure 21 mais pour la circulation méridienne résiduelle.

I.4 Conclusion

Les outils que j'ai développés tant pour l'analyse des modes f que pour l'analyse ring diagram ont été extensivement utilisés et le sont toujours par la communauté. Ils ont servi à l'exploitation des données GONG+, SoHO/MDI et maintenant SDO/HMI.

Récemment notre principal résultat d'une dérivée logarithmique du gradient de rotation proche de -1 de l'équateur jusqu'à au moins 40° de latitude obtenu par l'analyse des modes f des données MDI a été confirmé avec les données HMI et une version révisée des données MDI (Barekat, Schou et Gizon 2014). Les nouvelles données semblent néanmoins repousser à une plus haute latitude ($>75^\circ$) l'inversion éventuelle du gradient radial sub-photosphérique de rotation.

L'héliosismologie locale apporte des contraintes pour les modèles de la dynamo et notamment ceux qui invoquent une circulation méridienne et un transport du flux magnétique. Même si de grandes incertitudes demeurent sur la validité des résultats aux hautes latitudes ou au-delà de 15 Mm sous la photosphère, ces travaux ont stimulé les modélisateurs qui ont par exemple trouvé que l'apparition d'une cellule de circulation méridienne dans un seul hémisphère pouvait expliquer le décalage d'un an observé entre les inversions de polarité aux pôles nord et sud lors du maximum d'activité du cycle 23 (Dikpati, et al. 2004). Les circulations méridiennes complexes avec plusieurs cellules en latitude et en profondeur sont maintenant étudiées d'un point de vue théorique pour leurs implications potentielles sur l'horloge du cycle, la distribution et l'amplitude du champ magnétique polaire (Belucz, Dikpati et Forgács-Dajka 2015).

La chaîne de traitements ring-diagram est utilisée en routine par les équipes de GONG et de HMI qui l'ont intégrée aux traitements systématiques de leurs données. Les cartes synoptiques des vitesses horizontales mais aussi des gradients, de la divergence, de la vorticité ou d'hélicité cinétique sont maintenant produites de manière systématique ouvrant de nouvelles perspectives pour l'exploitation statistique de ces traceurs. Une hélicité cinétique importante peut notamment être associée aux tubes de flux magnétiques qui ont le plus de probabilité de produire des éruptions. Si il existe une telle corrélation entre la probabilité d'éruptions et l'apparition d'hélicité cinétique (Komm et al. (2005) ; Reinard et al. (2010)) alors nous pourrions imaginer détecter cette augmentation de l'hélicité cinétique en profondeur avant que ses effets de surface ne soient visibles comme le suggèrent Komm et al. (2008). De nombreux travaux de ce type sont actuellement poursuivis qui utilisent les cartes produites par l'analyse ring-diagram ouvrant ainsi des perspectives d'applications de cette technique également en météorologie de l'espace.

PARTIE II. L'astrométrie solaire à haute résolution

II.1 Introduction : objectifs et contexte historique

Les observations spatiales couvrant un cycle solaire entier suggèrent que le diamètre solaire et sa forme (asphéricité) sont remarquablement constants. Dans ce contexte je veux tout d'abord discuter pourquoi je pense que des observations sur le plus long terme sont utiles. Ensuite je montrerai comment les efforts entrepris depuis plus de 10 ans pour comprendre les effets de la turbulence optique sur les mesures d'astrométrie solaire nous ont conduits à utiliser l'imagerie du disque solaire entier simultanément depuis le sol et depuis l'espace et à développer un moniteur de turbulence dans le cadre du projet PICARD-SOL (Meftah, Corbard, et al. 2013).

II.1.1 Les variations du rayon solaire à différentes échelles

II.1.1.1 L'échelle du cycle d'activité magnétique

Les observations récentes depuis SoHO/MDI (Bush, Emilio et Kuhn 2010) ont posé des contraintes fortes sur les limites de possibles variations du rayon solaire au cours du cycle 23 (1996-2010). Ils ont trouvé une limite supérieure de 23 mas (mili-arcsecondes) pic à pic pour toutes variations qui seraient synchrone ou anti-synchrone avec le cycle. Les mesures que nous avons effectuées au sol à Calern avec l'astrolabe DORAYSOL (Morand, Delmas, Corbard et al. (2010)) n'ont également pas montré de corrélations ou anti-corrélations claires sur cette période mais avec une variabilité environ cinq fois plus importante c'est-à-dire 100 mas pic à pic. Les résultats de MDI sont en apparence contradiction non seulement avec les données simultanées obtenues au sol mais aussi avec les mesures ballon (Egidi, et al. 2006) obtenues au-dessus de l'essentiel de l'atmosphère entre 1992 et 1996. D'après ces mesures le rayon solaire est vu comme augmentant d'environ 200 mas alors que le cycle d'activité était dans sa phase descendante. Après une ré-analyse indépendante de ces mêmes données en 2008 les auteurs concluent que cette tendance est « réelle et ne peut être attribuée à un problème d'analyse » (Djafer, et al. 2008). Cette différence entre les mesures spatiales et des mesures ballon dédiées semble difficile à comprendre si les deux analyses sont correctes sauf si la phase descendante du cycle 22 se comportait différemment du cycle 23. Pour ce qui concerne les mesures au sol, il est possible d'invoquer des effets inconnus de changements à long terme affectant l'atmosphère terrestre ou un mauvais traitement des effets connus de la turbulence optique, de la diffusion atmosphérique ou encore de la réfraction astronomique qui peuvent potentiellement biaiser les résultats ou conduire à

une sous-estimation des incertitudes. Dans tous les cas, avoir des mesures simultanées depuis l'espace et depuis le sol doit nous donner une opportunité unique de quantifier expérimentalement les effets de l'atmosphère sur les mesures d'astrométrie solaire menées depuis le sol.

Les résultats de SoHO donnent une limite de 0.03 pour le rapport entre les variations relatives du rayon et de l'éclairement total (TSI, Total Solar Irradiance) au cours du cycle 23. Cela implique que les processus physiques conduisant à ces variations doivent être confinés proche de la surface (Gough, Sizing up the Sun 2001). Ceci est cohérent à la fois avec le fait que la modélisation des contributions des taches, facules et plages est capable d'expliquer 90% des variations observées de la TSI (e.g. Ball et al. (2012)), et avec le fait qu'aucune variation observable du rayon n'est anticipée pour de tels effets de surface (Spruit 1991). Il faut cependant garder à l'esprit que l'instrument MDI n'a pas été conçu comme un instrument dédié à l'astrométrie. Ses mesures astrométriques font l'objet de corrections instrumentales importantes qui sont obtenues par l'application à posteriori de modèles optico-mécaniques corigeant des variations brutes du rayon mesuré qui sont plusieurs ordres de grandeurs supérieurs au résultat final. Ces variations brutes sont le résultat de l'existence de gradients radiaux sur la fenêtre d'entrée et d'une défocalisation variable sur la lentille primaire de l'instrument MDI (J. R. Kuhn, R. I. Bush, et al. 2004). Ces résultats, même s'ils sont souvent considérés comme les plus fiables à ce jour, gagneraient certainement à être confirmés sur des échelles de temps plus grandes ou par d'autres missions spatiales dédiées. C'étaient les objectifs de la mission PICARD et du projet sol associé PICARD-SOL dont les premiers résultats sont donnés paragraphe II.4 .

II.1.1.2 Les échelles plus longues, évolution à long terme.

Il est important de suivre les paramètres globaux du Soleil tels que son rayon ou son éclairement continûment non seulement sur un cycle d'activité mais aussi sur des échelles de temps plus longues. Nous pouvons tout d'abord remarquer qu'une anti-corrélation trouvée significative sur 30 ans de mesures depuis le sol peut être trouvée beaucoup moins significative ou avec une phase différente quand des échelles de temps plus courtes sont analysées (cf. Figures 6 et 7 de Morand et al. (2010) ci-dessous). Les échelles de temps supérieures au cycle sont également nécessaires notamment pour contraindre les modèles du forçage solaire qui sont pertinents pour les études du climat ((Lean, Beer et Bradley 1995) ; (Lean, Wang et Sheeley 2002)). La question clé pour ces études est la variation d'irradiance non pas sur un cycle mais sur plusieurs dizaines, centaines ou milliers d'années. Pour cela nous devons comprendre non seulement la dynamo solaire sur un cycle mais aussi comment les processus en jeu à l'intérieur du Soleil peuvent conduire à la modulation observée du cycle sur des échelles plus longues (e.g. le cycle de Gleissberg d'environ 90 ans) et produire des périodes prolongées de faible activité comme celle du minimum de Maunder au 17^{ème} siècle (Lean (2000), voir aussi la revue de Foukal et al. (2006)) mais aussi les grands minima antérieurs au début du

comptage des taches (Spörer, Wolf) qui ont pu être mis en évidence par d'autre proxy de l'activité à long terme (Figure 23).

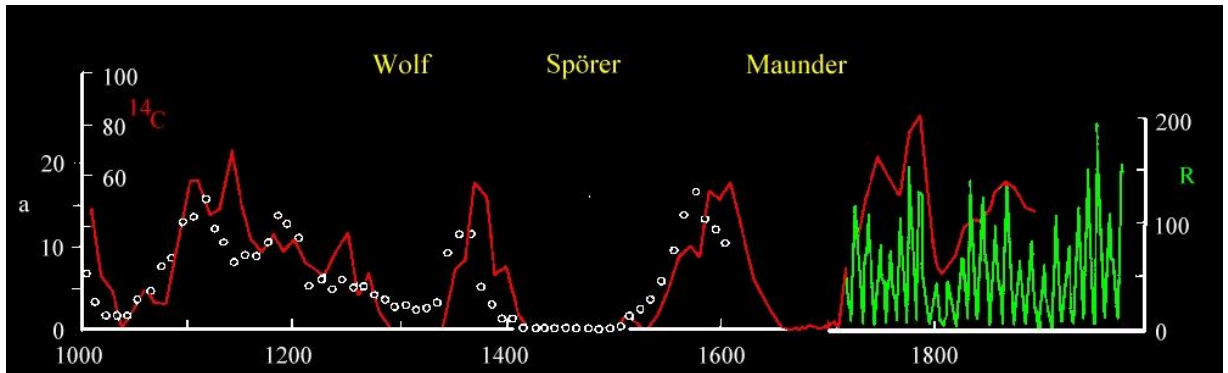


Figure 23. Trois indices indépendants démontrent l'existence de périodes prolongées de baisse du niveau de l'activité solaire comme les grand minima de Maunder et Spörer. La moyenne annuelle du nombre de taches observées depuis 1700 (échelle de droite en vert) suit également le cycle de 11 ans. La courbe en rouge qui va de 1000 à 1900 est un proxy du nombre de taches construit à partir de la mesure du taux de Carbone 14 dans les anneaux des arbres. L'augmentation du Carbone 14 est tracée inversée (échelle à gauche), donc une augmentation de l'activité et un proxy du nombre de taches plus élevé correspondent à une quantité réduite de radiocarbone dans l'atmosphère terrestre Les cercles sont un indice du nombre d'aurores dans l'hémisphère Nord (d'après John A. Eddy.)

Les reconstructions de la TSI basées sur des modèles et divers proxy de l'activité solaire sur le long terme conduisent à des estimations de variations de TSI depuis le minimum de Maunder qui vont de 1 à 10 fois son amplitude de variation actuelle sur un cycle (voir par exemple la revue de Solanki et Unruh (2013)). Ce n'est que récemment que, avec des données radiométriques spatiales couvrant 30 ans, Lockwood et Fröhlich (2007) ont pu mettre en évidence une première indication d'une diminution séculaire de la TSI d'environ 0.02% sur 20 ans ce qui représente 20% de la variation pic à pic observée au cours du cycle 23. Ces résultats restent très controversés car les mesures absolues de la TSI sont très difficiles à obtenir sur le long terme et ces tendances résultent de la fabrication de composites entre différents instruments et missions spatiales qui donnent des valeurs brutes de la TSI sensiblement différentes (Figure 24). Sur la Figure 25 nous voyons que différentes tendances à long terme peuvent être trouvées si l'on ne s'accorde pas sur la manière d'inter-calibrer les données pour fabriquer ces composites. Même si la balance entre les contributions à la TSI des structures magnétiques sombres et brillantes expliquent presque complètement les 0.1% de variations de TSI observées sur un cycle, Fröhlich (2009 (a) (b)) argumente que la tendance à long terme ne peut pas être expliquée par les mêmes processus.

TOTAL SOLAR IRRADIANCE MONITORING RESULTS: 1978 to Present

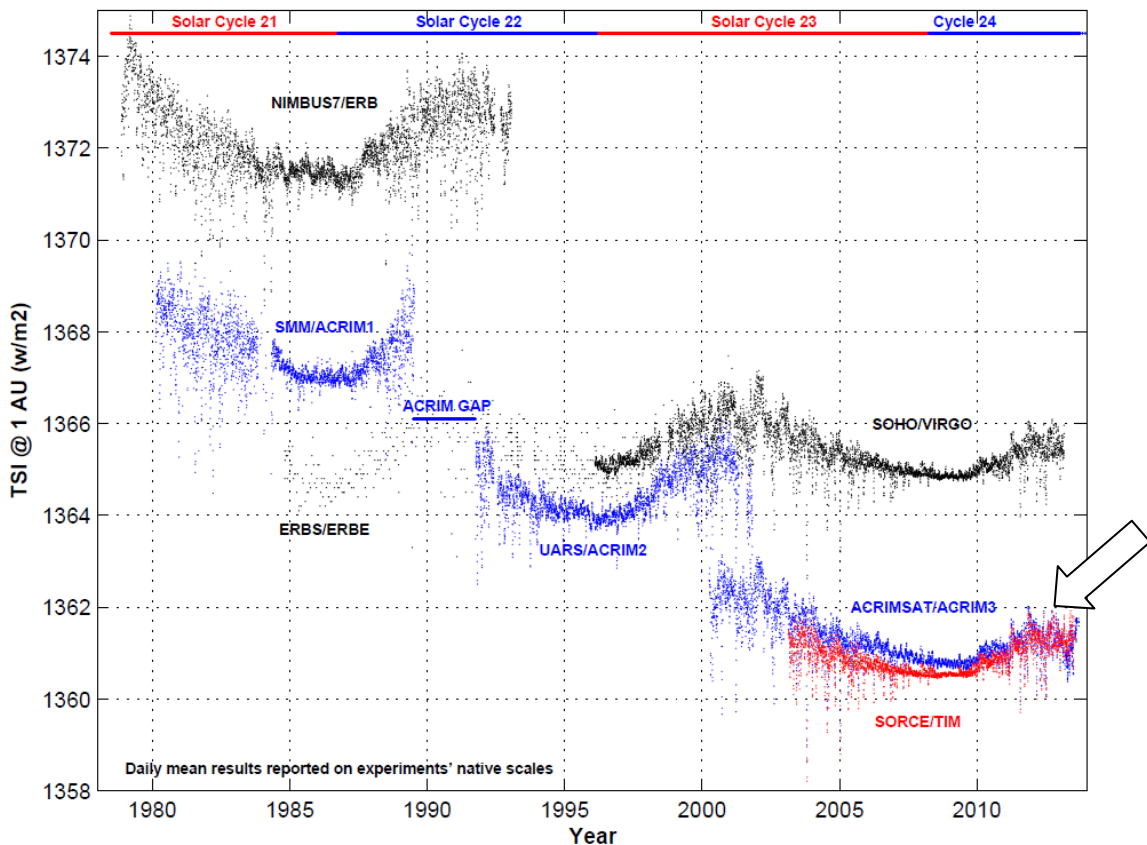


Figure 24. Les mesures brutes de l'éclairement (TSI) par les différentes missions spatiales depuis 1979 (Scafetta et Willson 2014). La flèche sur la droite indique valeur moyenne $1362 \pm 2.4 \text{ Wm}^{-2}$ obtenue par l'instrument SOVAP sur le satellite PICARD pour la période 2011-2013 (Meftah, Dewitte, et al. 2014).

Une des façons d'identifier les processus en jeu et à quelle profondeur ils prennent place est d'essayer de détecter les variations de rayon associées (Gough (1981) ; Spruit (1991)). Il existe, comme pour la TSI, des difficultés d'inter-calibration des mesures du rayon pour obtenir des séries sur le long terme mais contrairement à l'éclairement, les mesures astrométriques sont apriori possibles depuis le sol. Les mesures astrolabe au sol menées pendant 30 ans montrent une anti-corrélation entre l'activité (nombre de taches) et le rayon avec une pente positive d'environ 8 mas/an (Voir la Figure 6 de Morand et al. (2010) ci-après). Ceci était compatible avec les premières analyses des données MDI (Emilio et al. (2000) ; Kuhn et al. (2004)) qui fixaient la limite supérieure à 9 et 7 mas/an respectivement. Néanmoins une ré-analyse finale des données MDI sur tout le cycle 23 a conduit à une limite à 2σ de 1.2 mas/an avec une pente positive qui n'est pas trouvée significative sur les 12 ans analysés (Bush, Emilio et Kuhn 2010). Toutefois, comme pour l'éclairement les processus en jeu aux différentes échelles de temps peuvent être différents et nous ne pouvons pas conclure sur les tendances possibles à long terme en se basant juste sur l'analyse d'un cycle.

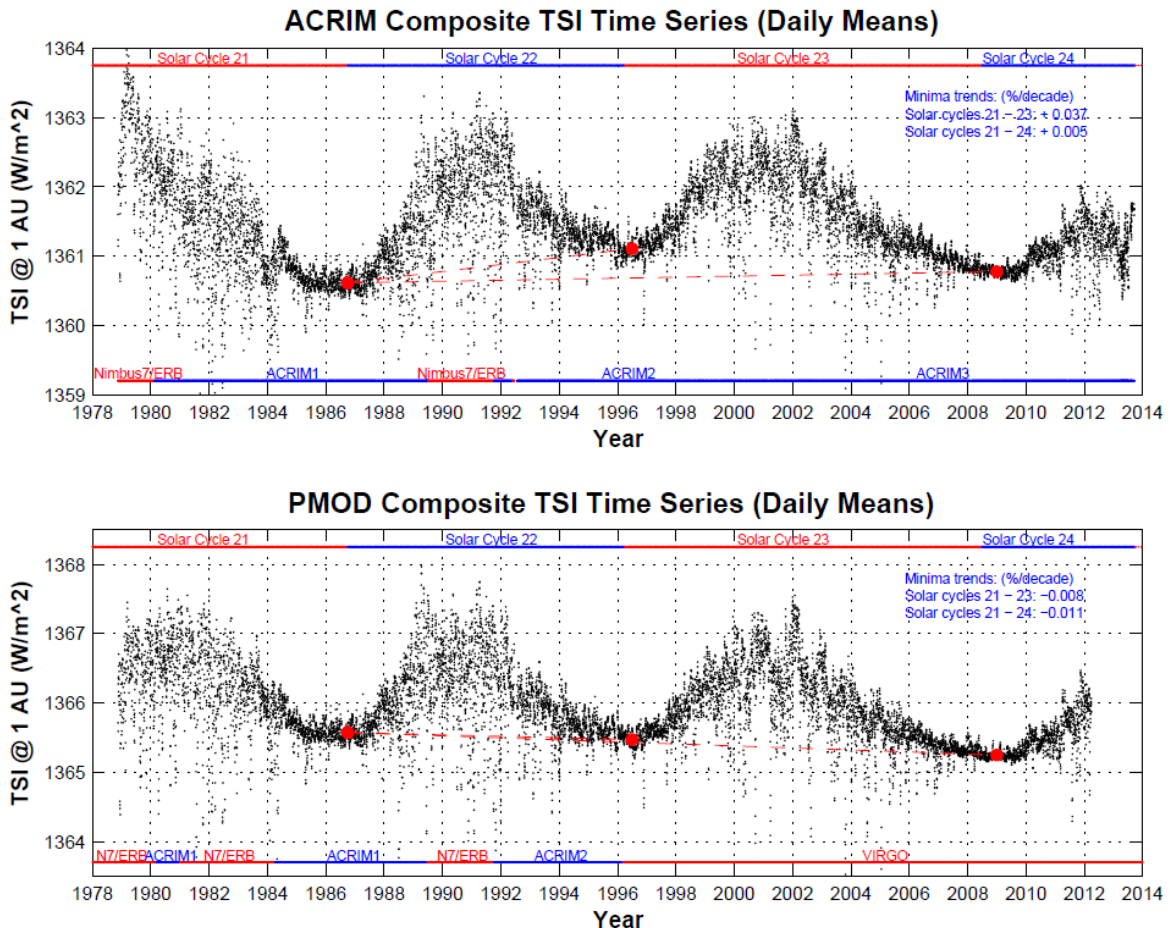


Figure 25 Composite des mesures de l'éclairement depuis l'espace. Déférantes approches pour combler les périodes sans données ACRIM conduisent à différentes tendances (Scafetta et Willson 2014)

Les limites supérieures obtenues depuis l'espace sur un cycle représentent de fortes contraintes pour tout programme d'astrométrie au sol. Mais, parce qu'il est important d'être capable de suivre plus d'un cycle, elles représentent aussi une chance de calibrer les mesures au sol et sont une motivation forte pour aller dans le détail de toutes les sources d'incertitudes liées à ces mesures.

II.1.2 Les observations de type astrolabe (article)

ARTICLE : Mesures du rayon solaire avec l'instrument DORAYSOL (1999–2006) sur le site de Calern (observatoire de la Côte d'Azur), Morand, Delmas, Corbard et al. (2010)

L'instrument DORAYSOL (Définition et Observation du RAYon SOLaire) est un astrolabe dédié à l'astrométrie solaire conçu par C. Delmas, F. Morand et F. Laclare pour intégrer un prisme variable permettant les mesures à différentes distance zénithales. Il a pris la suite des astrolabes visuels et CCD utilisés par Francis Laclare depuis 1974 et a fonctionné jusqu'en 2011. J'ai contribué aux observations et à l'exploitation de cet instrument entre 2004 et 2010. Nous avons publié en 2010 le bilan des résultats obtenus dans les comptes rendus de l'académie des sciences reproduit ci-dessous. Cet article présente également sur sa Figure 6 le bilan de l'ensemble des mesures astrolabes.



ELSEVIER

Comptes Rendus Physique

www.sciencedirect.com



Astrophysique/Soleil

Mesures du rayon solaire avec l'instrument DORAYSOL (1999–2006) sur le site de Calern (observatoire de la Côte d'Azur)

*Solar radius measurements with the DORAYSOL instrument (1999–2006) at the Calern site of the observatoire de la Côte d'Azur*Frédéric Morand^a, Ch. Delmas^a, Thierry Corbard^b, Bertrand Chauvineau^c, Abdanour Irbah^d, M. Fodil^e, Francis Laclare^{a,*}^a Univ. Nice Sophia Antipolis, CNRS UMR 6525, observatoire de la Côte d'Azur, station de Calern, 06460 Caussols, France^b Univ. Nice Sophia Antipolis, CNRS UMR 6202, observatoire de la Côte d'Azur, boulevard de l'observatoire, BP 4229, 06304 Nice, France^c Univ. Nice Sophia Antipolis, CNRS UMR 6162, observatoire de la Côte d'Azur, avenue Copernic, 06130 Grasse, France^d CNRS/LATMOS, quartier des Garennes, 11, boulevard d'Alembert, 78280 Guyancourt, France^e Observatoire d'Alger, CRAAG, BP 63, Bouzareah, 16340 Alger, Algérie

INFO ARTICLE

Historique de l'article :

Reçu le 30 mai 2010

Accepté après révision le 19 octobre 2010

Disponible sur Internet le 17 novembre 2010

Présenté par Jean Kovalevsky

Mots-clés :

Soleil

Rayon

Variations apparentes du diamètre

Mots-clés :

Sun

Radius

Diameter apparent variations

RÉSUMÉ

La série d'observations du rayon solaire sur le site de CALERN à l'Observatoire de la Côte d'Azur s'étend sur près de 30 ans. Les mesures d'abord visuelles, faites par le même observateur, sont devenues progressivement impersonnelles par l'usage de capteurs CCD. Pour améliorer encore le rendement et la qualité des observations du demi-diamètre nous avons réalisé un nouvel instrument : DORAYSOL. Le principe de l'instrument est toujours basé sur le passage du Soleil à hauteur constante mais il permet un plus grand nombre d'observations le même jour par l'emploi d'un prisme d'angle variable. Un système d'acquisition numérique CCD des images du Soleil rend les mesures plus crédibles et l'instrument est semi-automatique par la motorisation de ses principales fonctions. Les résultats présentés ici couvrent huit années d'observations et comptent près de 20 000 mesures obtenues entre 1999 et 2006. Une analyse des principaux biais de mesures instrumentaux montre en particulier que l'écart entre les mesures des passages à l'est et à l'ouest est systématique, ce qui justifie notamment l'utilisation de moyennes pour le calcul du rayon. Ainsi, les mesures obtenues par DORAYSOL sont en bon accord avec celles acquises sur la série antérieure avec l'Astrolabe solaire, qu'il s'agisse de la valeur moyenne du rayon ($959,48'' \pm 0,01''$), de son caractère variable dans le temps ou encore de l'éventuelle dissymétrie apparente de la photosphère observée. Nous souhaitons que ce programme, interrompu depuis 2007 par manque de personnel, soit à nouveau repris pour que les observations du rayon solaire faites au sol soient simultanées à celles obtenues depuis l'espace par la mission PICARD. Nous développons également sur le site de CALERN l'instrument MISOLFA, destiné à évaluer les paramètres qui caractérisent la turbulence au sol et le télescope SODISM 2, réplique du télescope embarqué sur le satellite. Notons que les travaux d'étude, de réalisation et de mise au point de ces deux instruments ont retardé l'analyse des résultats obtenus par DORAYSOL et donc leur exposé dans la présente note. Il convient enfin de souligner que seule, la poursuite de ces mesures pendant une longue durée, permettra la recherche de variations à long terme de la géométrie globale du Soleil.

© 2010 Académie des sciences. Publié par Elsevier Masson SAS. Tous droits réservés.

* Auteur correspondant.

Adresse e-mail : francis.laclare@obs-azur.fr (F. Laclare).

The series of measurements of the Solar radius at CALERN site of the observatoire de la Côte d'Azur (OCA) spans about 30 years. Measurements of the Sun were first achieved visually by the same single observer, then gradually grew more man-independent with the use of CCD acquisitions. The DORAYSOL instrument was designed and built up to keep improving the number and the quality of these semi-diameter measurements. The principle of this instrument remains the same as that of the Solar Astrolabe (timing the crossing of a parallel of altitude by the Sun) but a varying prism enables larger numbers of daily measurements. Digital CCD acquisition of images improves the credibility of the data and five computer-driven motors are giving a better control of the attitude of the instrument. The results for eight years and nearly 20,000 measurements are presented. Analysis of instrumental biases shows that differences between East and West measurements are systematic and then allow one to choose the mean values to calculate the Solar radius. This results display a good agreement with the Solar Astrolabe series, namely the mean value of the Sun radius ($959.48'' \pm 0.01''$), its time-dependence and the apparent dissymmetry of the photosphere.

In the framework of the PICARD CNES Space mission, Solar radius ground measurements at CALERN simultaneously with the onboard SODISM telescope were projected. It appeared in 2007 that the maintenance of the DORAYSOL program was not possible alongside the development of the atmospheric turbulence monitor MISOLFA and the preparation for setting up the model of the SODISM 2 telescope, the staff at hand becoming insufficient. We do hope that it will be resumed, in a fully automated way. A continuation of the ground-based series would permit one to detect possible long time variations of the global geometry of the Sun.

© 2010 Académie des sciences. Publié par Elsevier Masson SAS. Tous droits réservés.

Abridged English version

The DORAYSOL instrument (Definition et Observation du RAYon SOLaire) was designed and developed at CALERN observatory in view of strengthening the survey of the Solar radius in the framework of the PICARD Space mission. Fig. 1 displays a sketch of DORAYSOL [1]:

- A *Cassegrain reflector* (110 mm diameter; 3450 mm focal length) is horizontally disposed on a rotating plate, in order to ensure azimuth pointing;
- A *varying prism*, whose edge has to remain horizontal and perpendicular to the optical axis, ensures the altitude pointing. Associated with the *mercury surface* materializing the horizon, it allows to image in the focal plane of the telescope the two symmetric components of the Solar edge;
- A *CCD camera* and its acquisition system reconstruct the Solar edge; they also time its transit through the parallel of altitude. A spectral filter limits the wavelength range at a bandwidth of 60 nm around a central wavelength of 548 nm. A *rotating shutter*, in front of the telescope, alternately triggers the acquisition of the direct and reflected images of the Solar edge;
- A *4.5 density filter* and a shield (not sketched here) protect the whole instrument;
- *Five computer-driven motors* pilot the instrument: rotating plate (azimuth), angle of the prism (altitude) and inclination of the density filter. Accurate controls of the horizontality of the edge of the prism and of the optical axis are achieved.

Measurements and the questions the data raise, including their quality, are presented in the first part. The mean radius obtained between 2000 and 2006 is $959.48'' \pm 0.01''$. The second part confirms two results known from the CALERN Astrolabe series: the time-dependence (globally out of phase) with the magnetic activity, and the dissymmetry of the photosphere.

Observations

Observations with this new instrument started in 1999 while the Solar radius survey, initiated in 1978 with the Solar Astrolabe, was extended for the sake of controlling the new results. The strong point of both instruments lies [2] in timing the upper and lower edges of the Sun when they cross the same parallel of altitude, a few minutes apart, the atmospheric refraction being the same (at the first order); these corrective terms eventually cancel each other in the process of calculating the semi-diameter. Favorable DORAYSOL features are: many quasi-automatic CCD measurements (up to 80 a day) and the possibility of evaluating parameters linked to the image quality (scattering effect around regression lines). Two difficulties remain unsolved: possible focal length variations if a few minute thermal changes occur, which are unverifiable (opposite to the Astrolabe) and the variable prism displaying a constant discrepancy between East and West measurements (Fig. 2). Nevertheless, the similar conditions of observation (mean zenith distances and Sun position angles) at both sides of

the m possible to choose the arithmetic mean as the relevant value. Let us notice that a new varying prism was built up to cope with these problems but it has not yet been operated.

As it was the case with the Astrolabe [3], a zenith distance effect arises (Fig. 3) between 60° and 30° , that might be linked with outside thermal variations: Eastward, the radius is greater by $0.13''$ at low zenith distances, correlated with a serious increase in temperature (up to 5°C in the morning). Westward, the radius is smaller by $0.09''$ at 30° than at 60° , with a smaller change of 0.5°C in the afternoon temperature.

As regards the image quality, let us recall their acquisition procedure, tested since 1989 on the Astrolabe [4]: the 752×582 pixels camera covers a field of $379''$ by $287''$ on the sky, with a 60 nm bandwidth centered at 548 nm. The inflection point on a CCD line is detected by numerical derivatives [5] and the modeling of the Sun edge allows several choices and is still being debated [6,7]. The time accuracy of recording events is about 15 μs , well above the needed precision. A crossing of an edge is determined from the acquisition of 50 direct and 50 reflected images, each one lasting 250 ms.

The Fried parameter can be evaluated [8,9] to an average of $r_0 = 4$ cm. Nevertheless we think that the exposure time (20 ms) and the 25 s acquisition time are not perfectly relevant for such a characterization. A better marker of the image quality seems to be the rms scattering around the data regression lines, with an average of $1.35''$ ($1.30''$ in the morning, better than $1.45''$ in the afternoon) as shown on Figs. 4(a) and 4(b). One can also notice that the spreading of images, proportional to the scattering, reduces the value of the radius because of the shift of the inflection point towards the center [10]. We could use this index to qualify and weight the measurements, but we preferred to keep the plain data. We did use it to eliminate the data related to a dysfunction of the rotating shutter.

Figs. 5(a) and 5(b) compare the statistical characteristics of both instruments, after discarding 191 DORAYSOL measurements farther than 3σ from the annual averages as well as the 1999 "experimental" data. The 19 169 retained DORAYSOL measurements give on Fig. 5(b) a Gaussian histogram, justifying the definition of the radius as the average between East and West observations. The root mean square is the same for the two series, $\sigma = 0.32''$.

Results

DORAYSOL mean radius of $959.48'' \pm 0.01''$ with $\sigma = 0.32''$ is deduced from 11 663 Eastern ($959.79'', \sigma = 0.30''$) and 7506 Western measurements ($959.17'', \sigma = 0.34''$). To compare with the 371 Solar Astrolabe observations between years 2000 and 2006, it would be relevant to correct DORAYSOL data by the zenith distance effect giving $959.51'' \pm 0.01''$ with $\sigma = 0.32''$ to compare with $959.55'' \pm 0.01''$ with $\sigma = 0.26''$ for the Astrolabe. Fig. 6 displays a good consistency between the two series, especially if the zenith distance effect ($0.07''$ increase over the raw measurements) is taken out from the Astrolabe data. The remaining discrepancy is probably due to a combination of the differences in spectral sensitivities, filters, observational procedures, and/or the low density of the Astrolabe data.

Fig. 6 also shows the regression line of monthly means of the Solar activity, whose slope is the exact opposite of the Astrolabe and DORAYSOL's ones. This opposition is a feature of the CALERN series and it is well known that different results are obtained by different instruments [11,12]. So, we expect that the data from space will solve the problem. We would like recalling the good agreement with the selective data of the Solar Disk Sextant [11,13]. The conclusion is that, for the Sun parameters variations, long time-series are needed [14,15]: The first 10 years (Fig. 6) show a phase opposition between the Solar radius and the Solar magnetic activity, followed by 15 years of evolution, leading at the beginning of cycle 23 (April 1996 to June 1998) to in-phase variations as shown by SOHO/MDI [16]. Finally, at the end of cycle 23, as shown on Fig. 7, DORAYSOL data confirm a seemingly opposing phase.

As regards the shape of the photosphere, the Astrolabe already gave a few indications [15], supported by measurements in the southern hemisphere [17,18]. On Fig. 8(a), points of equal heliographic latitudes have been plotted for the Astrolabe (1 point stands for 1100 measurements) and DORAYSOL (1 point = 2700 measurements) in the range $(20^\circ\text{--}90^\circ)$, the equatorial zones being out of reach from CALERN). The adjusted parabolas look alike.

The higher density of DORAYSOL data is given in Fig. 8(b), which covers $20^\circ\text{--}160^\circ$ heliographic inclinations. The deviations from the mean radius are computed every year and are unaffected by the previously mentioned systematic East-West effect. The smoothing with an 8-degree polynomial gives a correlation of 0.83. Nevertheless, the limit of accuracy of such instruments is reached, these deviations being not recorded at the same times and high zenith distances measurements being of a lesser quality.

Let us stress that the 2007 interruption of this program was decided by the OCA in view of the priority put on the PICARD ground segment project and the lack of dedicated staff. The 3-year delay for publishing this article can be accounted as well. We hope that it will be possible to resume the DORAYSOL series to foster the data of MISOLFA and SODISM 2 (the same as the onboard imager).

Conclusion

The new CALERN instrument made it possible to measure some 20 000 Solar radii during 8 years, twice more than the Solar Astrolabe in 30 years. These personal-free data display the same quality and give the same values and time variations as the visual ones, over their common observing periods. Nevertheless, this period is too short compared with the Sun cycles to draw conclusions from DORAYSOL as we did with the Astrolabe [14,15]. The varying prism should be substituted by a

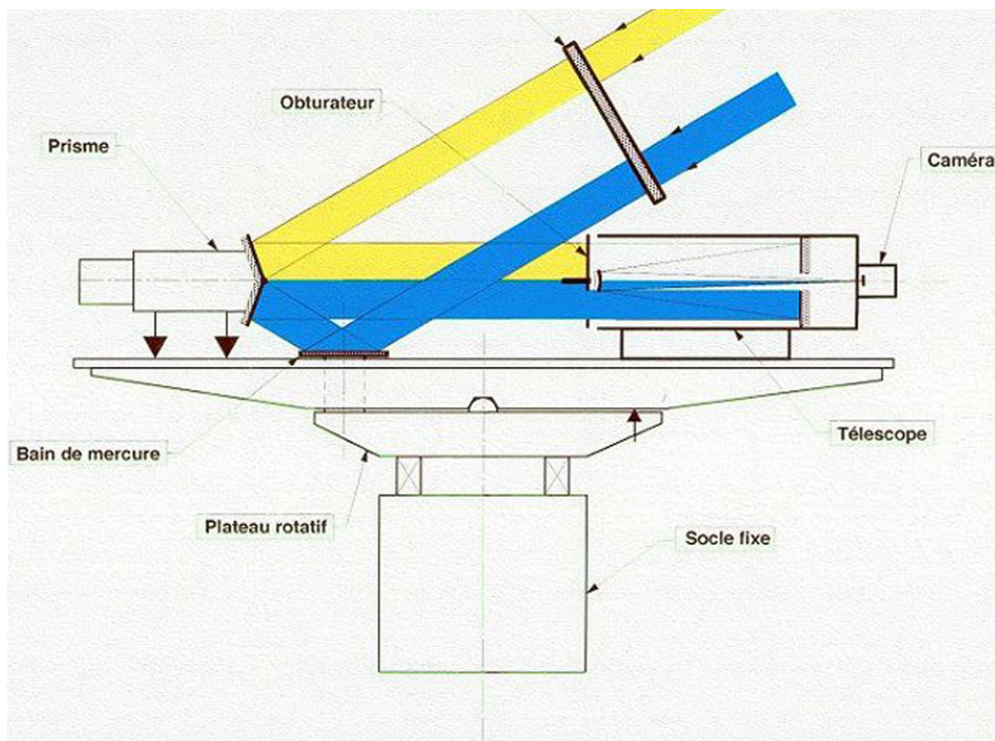


Fig. 1. L'instrument DORAYSOL.

Fig. 1. The DORAYSOL instrument.

more metrological one [19] and a thorough automation would optimize the ground measurements of DORAYSOL. Only space observations will provide answers to the questions raised by the last decades of ground data, but a long time survey of the Sun would be easier from the ground than from short-lived satellites. Calibrating the atmosphere distortion by simultaneous space and ground measurements at well chosen sites seems to be an urgent task. Along with PICARD satellite, the telescopes MISOLFA and SODISM 2 will fill the gap at CALERN site. DORAYSOL could play its part in this exciting course.

1. Introduction

Dans le but de continuer à l'Observatoire de CALERN le programme de surveillance du rayon solaire couvrant près de 30 ans, et dans la perspective de la mission spatiale PICARD nous avons étudié et développé un nouvel instrument : DORAYSOL (Définition et Observation du RAYon SOLaire) (Fig. 1).

Cet instrument présente de nombreux avantages par rapport à l'Astrolabe solaire dont il a gardé le principe de l'observation du passage du Soleil par un cercle de hauteur [2]. Il permet d'une part, de manière quasi-automatique un grand nombre de mesures par l'emploi d'un prisme d'angle variable, d'autre part ces mesures sont impersonnelles par l'usage d'une caméra CCD située dans le plan focal et enfin, elles rendent possible une évaluation objective de certains paramètres affectant la qualité des images.

Les éléments constituant l'instrument [1] sont :

- Un télescope de type Cassegrain, de 110 mm de diamètre de miroir primaire et de 3450 mm de focale. Ce télescope est disposé à l'horizontale sur un plateau rotatif qui permet d'assurer le pointage en azimut de l'instrument ;
- Un prisme réflecteur d'angle variable dont l'arête doit être horizontale et perpendiculaire à l'axe optique, associé à un bain de mercure qui matérialise le plan de l'horizon permettent de former dans le plan focal du télescope les deux composantes symétriques de l'image du bord solaire. La variation de l'angle du prisme permet d'assurer le pointage en hauteur de l'instrument ;
- Une caméra CCD et son système d'acquisition permettent de reconstituer et de dater le passage du bord solaire par le cercle de hauteur. Un filtre, centré sur 548 nm de longueur d'onde et d'une largeur de 60 nm, est placé devant la caméra et limite la bande spectrale observée. Enfin, un obturateur en rotation, situé à l'entrée du télescope, déclenche alternativement l'acquisition des images directe et réfléchie du bord solaire ;
- Un filtre, constitué d'une lame plan-parallèle en borosilicate crown (BK7), de densité voisine de 4,5, ajuste le flux incident aux caractéristiques de la caméra et protège l'instrument dans son ensemble ;
- L'instrument est piloté par 5 moteurs contrôlés par ordinateur. Les trois moteurs de pointage concernent l'azimut (i.e. l'orientation du plateau rotatif), la hauteur (i.e. l'angle du prisme) et le déplacement et l'orientation de la lame filtre.

D^l la fois longitudinalement (réglage de l'horizontalité de l'axe optique du télescope) et transversalement (réglage de l'horizontalité de l'arête du prisme); la référence étant le plan horizontal matérialisé par la surface du bain de mercure.

2. Mesures

Les observations avec ce nouvel instrument ont commencé en 1999. Le programme de mesures conduit avec l'Astrolabe solaire de manière régulière depuis 1978, a été poursuivi jusqu'en 2006 de manière concomitante à DORAYSOL, à seule fin de contrôler les résultats. L'ensemble des mesures révèle une bonne cohérence apparente des données acquises par les deux instruments sur la période commune entre 1999 et 2006, comprenant près de 20 000 observations faites avec DORAYSOL. Le choix de l'Astrolabe solaire de CALERN pour qualifier les mesures acquises par l'instrument DORAYSOL se justifie d'abord par la présence des deux instruments sur le même site et leur exploitation simultanée mais aussi par la qualité des résultats obtenus avec l'Astrolabe solaire sur la longue série de mesures du diamètre à CALERN.

L'interruption du programme en 2007 a été décidée par notre établissement pour donner la priorité au développement de la composante sol de la mission PICARD comprenant les deux instruments MISOLFA et SODISM 2, [19] qui permettront d'évaluer les paramètres définissant la turbulence. Les travaux qui en ont résulté et le manque de personnel disponible pour ce service, sont la cause du retard de plus de trois ans apporté à l'analyse des mesures DORAYSOL et donc à leur présentation. Nous espérons disposer prochainement des moyens nécessaires à une remise en fonctionnement de DORAYSOL, au moins partielle, qui permettra de valider l'ensemble des observations au sol par comparaison directe avec les mesures que fournira le satellite PICARD. Seul, le rapprochement des mesures faites au sol à celles obtenues depuis l'espace conduira à qualifier et donc à clarifier de manière objective l'ensemble des observations et des résultats obtenus depuis plus de trente ans sur le site de CALERN.

2.1. Effets instrumentaux «et ou» observationnels

Les mesures sont faites au passage Est et au passage Ouest du Soleil, entre 30° et 60° de distance zénithale. En été par ciel dégagé, on peut compter jusqu'à quatre-vingts mesures le même jour. Rappelons aussi l'intérêt de la méthode d'observation du disque solaire à hauteur constante, méthode qui réduit considérablement les incertitudes relatives à la réfraction astronomique, inhérentes à d'autres techniques de mesure du diamètre solaire. Seules interviennent ici les variations des conditions locales de température, de pression et d'hygrométrie pendant les quelques minutes qui séparent les passages des deux bords successifs du Soleil à l'Est ou à l'Ouest par le cercle de hauteur; la réfraction est calculée pour chacun des deux instants de passage. Cependant, malgré les avantages que nous avons cités, DORAYSOL ne possède pas toute la qualité métrologique qui caractérise l'Astrolabe de CALERN :

1. D'une part on ne maîtrise pas, comme on peut le faire avec l'Astrolabe solaire par autocollimation sur un miroir situé en avant de l'objectif, les éventuelles variations de la focale qui affectent la distance zénithale d'observation et qui sont essentiellement liées aux variations thermiques.

2. D'autre part, le prisme d'angle variable, bien que construit avec précision au laboratoire des prototypes du C.N.R.S. est de nature composite puisqu'il est constitué d'un ensemble mécanique sur lequel sont serties les lames réflectrices. Cet ensemble présente quelques imperfections, eu égard à la précision recherchée. Dès la mise en service de l'instrument, on a constaté un effet persistant affectant les résultats, les rayons mesurés à l'Est étant systématiquement supérieurs à ceux observés à l'Ouest d'environ 0,60''. Sur la totalité des mesures traitées année par année entre 1999 et 2006, l'écart moyen est : (EST-OUEST) = 0,60'' ± 0,04''.

Nous n'avons pas été en mesure d'éliminer ce défaut qui a très certainement son origine dans le système opto-mécanique du prisme dont l'arête n'est pas ou mal définie. L'origine la plus plausible de cette différence entre les résultats Est et Ouest résulte du fait que l'observation du Soleil ne correspond pas au passage par le cercle de hauteur mais plutôt par un petit cercle dont le pôle n'est pas le zénith. Ce petit cercle sur la sphère locale est alors incliné sur le cercle de hauteur d'un angle identique à l'Est comme à l'Ouest. Il en résulte que les temps de passage sont systématiquement plus longs à l'Est et plus courts à l'Ouest d'une quantité équivalente, qui est fonction des valeurs de l'angle à l'astre et de la distance zénithale.

Sur l'ensemble de la série 1999–2006 nous avons des conditions d'observations analogues à l'Est comme à l'Ouest, notamment pour la distance zénithale et l'angle à l'astre moyens observés, la distance zénithale moyenne étant de 47° et la valeur absolue de l'angle à l'astre de 50°. Cette symétrie des conditions d'observations du matin et du soir contribue à rendre stable l'écart (Est–Ouest) et justifie la définition du rayon moyen par la moyenne des rayons Est et Ouest. La Fig. 2 illustre la stabilité de l'écart déduit des droites de régression ajustées sur les séries mensuelles établies à l'EST et à l'OUEST, dont la variation n'excède pas 0,03'' entre mars 2000 et octobre 2006.

3. De la même manière qu'il existait sur l'Astrolabe solaire un effet lié à la hauteur d'observation [3], cet effet apparaît sur les mesures DORAYSOL et en particulier sur celles obtenues à l'EST, la valeur du rayon devenant plus grande aux faibles distances zénithales. L'accroissement du rayon mesuré est ainsi de 0,13'' entre 60° et 30° de distance zénithale le matin.

La pente est de signe contraire et plus faible pour les observations à l'Ouest, le rayon augmentant de 0,09'' entre 30° et 60° de distance zénithale. Ce désaccord entre Est et Ouest pourrait résulter des variations de température importantes pendant la matinée, pouvant atteindre 5 °C et nettement plus faibles durant l'après midi, en deçà de 0,5°C (Fig. 3).

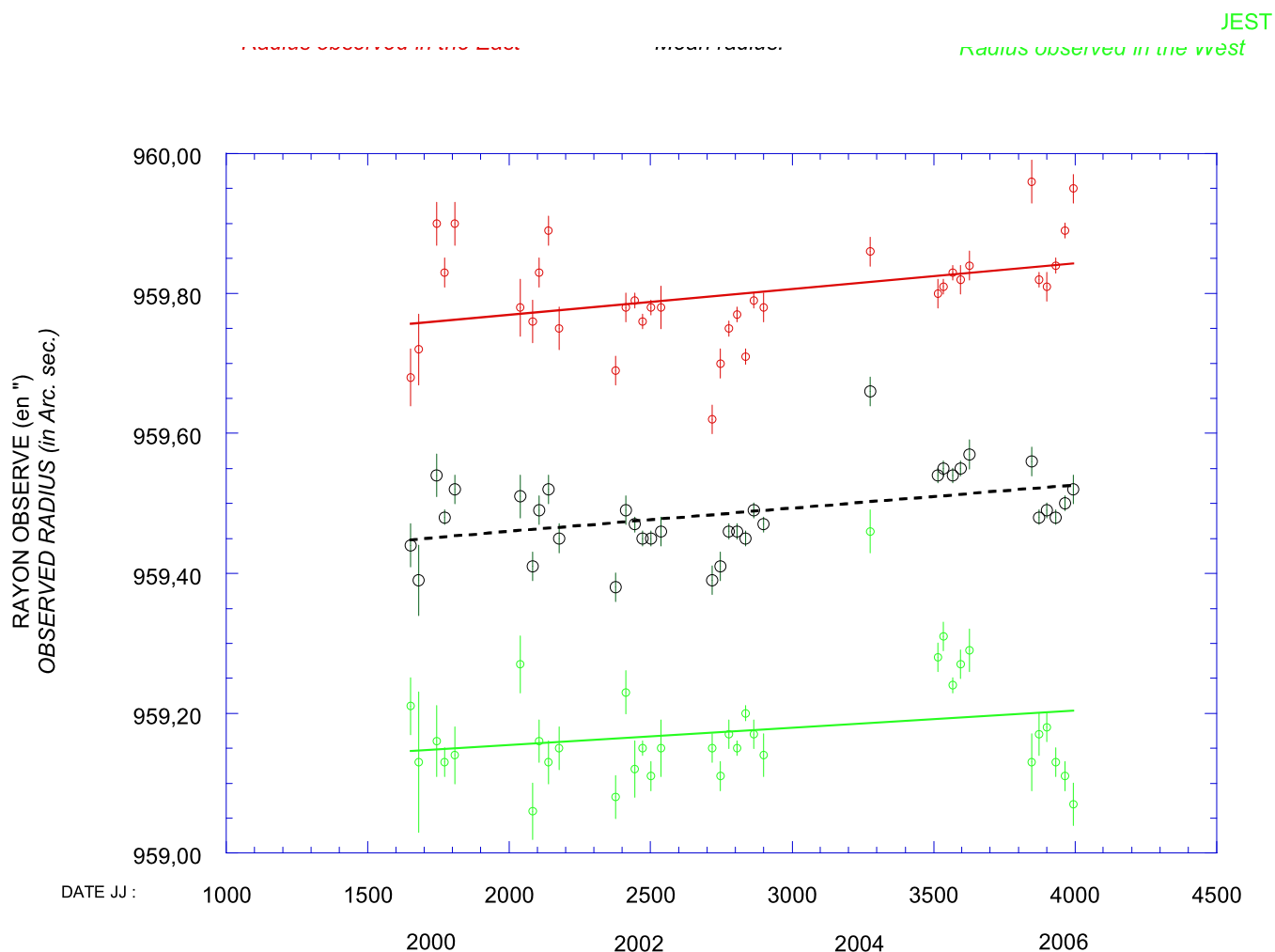


Fig. 2. DORAYSOL 2000–2006, stabilité de l'écart [Est–Ouest].

Fig. 2. DORAYSOL 2000–2006, stability of the East–West discrepancy.

2.2. Qualité des mesures

– Le mode d'acquisition des images à partir de la caméra CCD était en usage sur l'Astrolabe solaire depuis 1989 [4]. D'abord en mode analogique ce type d'enregistrement est devenu numérique à partir de 1996. La caméra installée sur DORAYSOL comporte 752×582 pixels, le champ ainsi couvert par la matrice étant de $379''$ sur $287''$. Pour la détection du point d'inflexion, nous avons encore utilisé la méthode par dérivation numérique déduite du mode analogique [6,5], la modélisation du bord solaire observé par DORAYSOL et d'autres instruments similaires faisant toujours l'objet d'investigations [7].

Les acquisitions de chaque image sont datées à partir de la carte chronomètre pilotée par les fréquences de 1 MHz et 1 Hz fournies par une horloge à césum de l'observatoire. La précision des instants observés est de l'ordre de 15 μ s, donc largement suffisante pour la seule détermination du demi-diamètre.

Chaque pixel est caractérisé par 256 niveaux d'éclairement. La dimension utile du pixel, étalonnée en distance zénithale est de $0,50''$ tandis qu'elle est de $0,49''$ sur l'axe des azimuts. Rappelons que l'enregistrement d'un passage comprend l'acquisition de 100 images (50 directes et 50 réfléchies) toutes les 250 ms et que chaque image est acquise en 20 ms.

Le système de traitement des données permet d'évaluer le paramètre de Fried [8] rendant compte de l'aire de cohérence au niveau de la pupille [9]; ce paramètre est voisin de 4 cm en moyenne pour l'ensemble des mesures dont nous disposons. Cependant, nous pensons que le temps de pose et la durée du passage de 25 s sont trop grands pour que ce paramètre conserve ses caractéristiques significatives. En revanche, la dispersion des mesures sur les droites ajustées aux trajectoires (écart quadratique moyen des mesures) demeure quant à elle un indice objectif de la qualité des observations. Sur l'ensemble de la série, cette dispersion moyenne est de $1,35''$ et comme on pouvait s'y attendre, elle est sensiblement plus grande l'après-midi, de $1,45''$ contre $1,30''$ le matin. Cette détérioration sur les passages Ouest était perceptible avec l'Astrolabe solaire bien que non quantifiable. Elle résulte très probablement de la turbulence due au bilan thermique environnant l'instrument et dans les basses couches de l'atmosphère sur le site; la température l'après midi est en moyenne supérieure de 2°C à celle du matin.

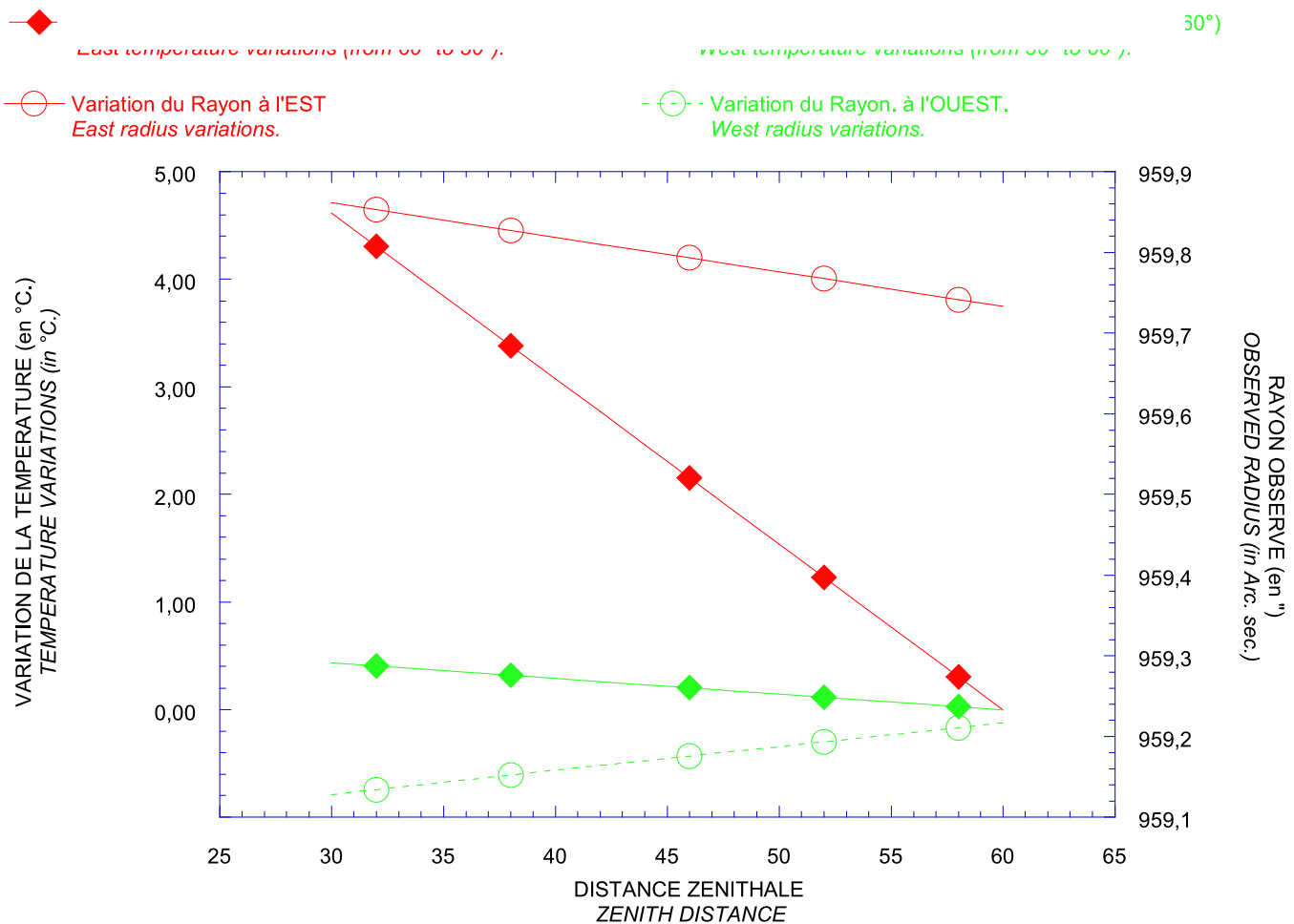


Fig. 3. DORAYSOL 2000–2006, variation de la température et du rayon observé.

Fig. 3. DORAYSOL 2000–2006, variations of temperature and observed radius.

Les observations à l'Est ou à l'Ouest, Figs. 4(a) et 4(b), confirment également la relation connue entre l'étalement de l'image, fonction de la dispersion, et le retrait du point d'inflexion vers le centre réduisant alors la valeur du rayon observé [10].

Cet indice de dispersion permettrait de manière indubitable la qualification des mesures. Néanmoins, dans le but de maintenir le caractère brut des observations, nous n'avons pas fait usage de pondération pour les résultats présentés dans cette Note.

Sur l'ensemble des observations réparties entre 2000 et 2006, soit 19 360 mesures, nous avons été conduits à éliminer 191 mesures s'écartant à plus de 3σ de la valeur moyenne, soit près de 1% sur l'ensemble des observations. L'acquisition de ces mesures était douteuse, assez fréquemment par suite d'une mauvaise synchronisation de l'obturateur en rotation et de l'enregistrement des images. Par ailleurs nous considérons l'année 1999 comme une période de mise au point de l'instrument, qui ne doit pas être prise en compte pour apprécier la qualité des résultats de DORAYSOL. La Fig. 5(b) représente l'histogramme de l'ensemble des observations ainsi retenues. Nous nous sommes assurés que la distribution des mesures DORAYSOL est gaussienne, ce qui confirme le bien fondé de la définition du rayon moyen obtenu par la moyenne des observations Est et Ouest.

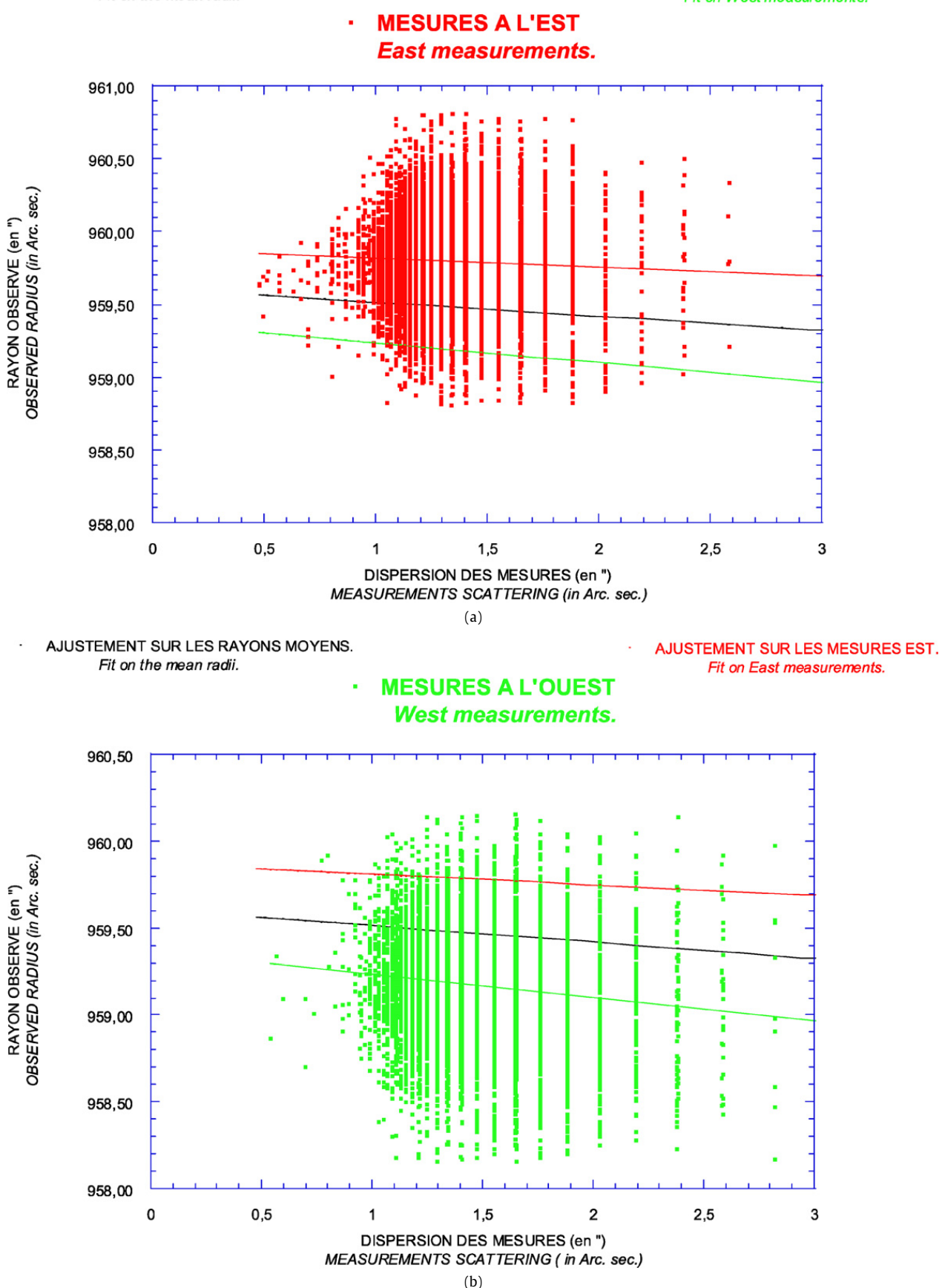
Pour comparaison, les Figs. 5(a) et 5(b) donnent la distribution des mesures obtenues avec l'Astrolabe solaire et DORAYSOL. Rappelons que les observations faites avec l'Astrolabe solaire sont ramenées au zénith ; les caractéristiques statistiques des deux séries sont voisines, notamment pour les écarts type qui sont identiques, égaux à $0.32''$.

3. Résultats

3.1. Valeur moyenne et variations apparentes du rayon

Un premier exposé des mesures acquises par DORAYSOL entre 1999 et 2003 montrait le bon accord des mesures Astrolabe solaire et DORAYSOL sur le site de CALERN et aussi l'opposition de phase apparente entre rayon observé et activité magnétique [19]. La période couverte par nos observations correspondait alors au sommet du cycle 23 et au début de la phase descendante de l'activité. La poursuite du programme que nous présentons ici concerne en outre la fin du déclin du

AJ

**Fig. 4.** (a) DORAYSOL 2000–2006, dispersion des mesures à l'Est ; (b) Dispersion des mesures à l'Ouest.**Fig. 4.** (a) DORAYSOL 2000–2006, eastward scattering of measurements (in arc.sec); (b) Westward scattering of measurements (in arc.sec).

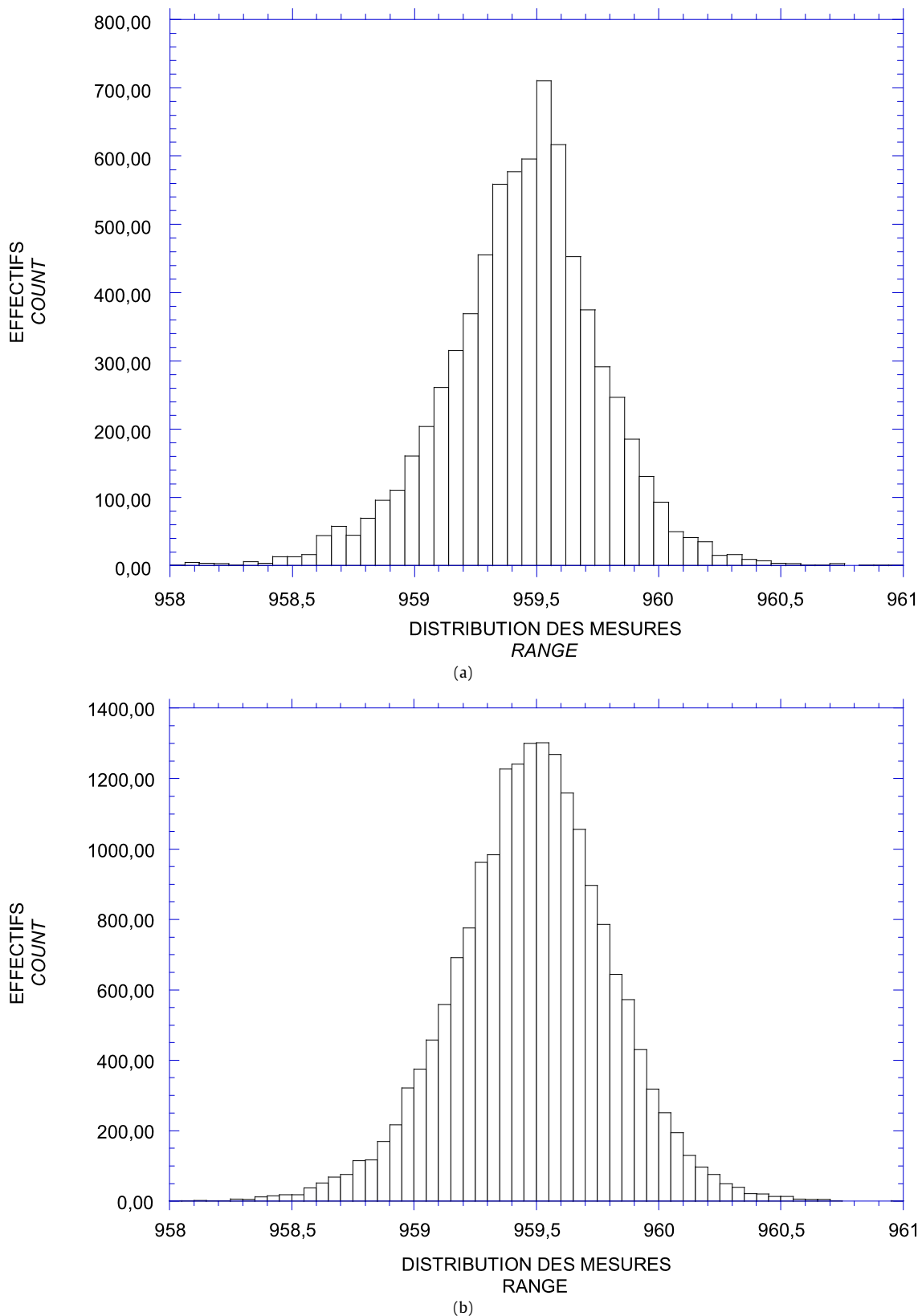


Fig. 5. (a) Histogramme ASTROLABE SOLAIRE (1975–2006, 7279 mesures visuelles à sec $z = 1$, $R = 959.52'' \pm 0.01''$) (observateur : F. Laclare); (b) Histogramme DORAYSOL (2000–2006, 19 169 mesures CCD, $R = 959.48'' \pm 0.01''$).

Fig. 5. (a) Solar Astrolabe (1975–2006, 7279 visual measurements at sec $z = 1$, $R = 959.52'' \pm 0.01''$) (observer: F. Laclare); (b) DORAYSOL (2000–2006, 19 169 CCD measurements, $R = 959.48'' \pm 0.01''$).

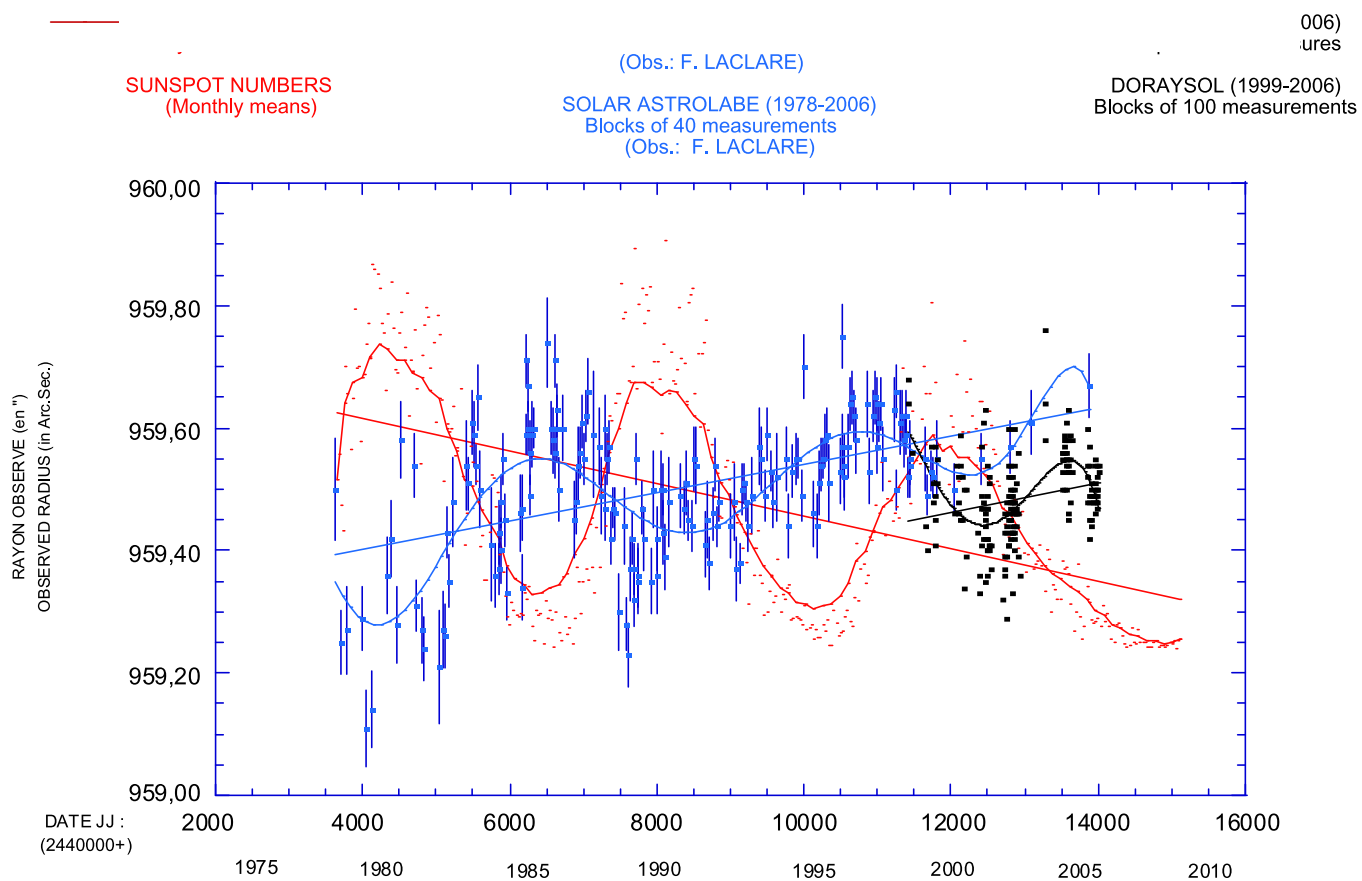


Fig. 6. Mesure du rayon à CALERN et activité magnétique (1978–2006).

Fig. 6. Solar radius at CALERN and magnetic activity (1978–2006).

cycle 23 avant le long minimum d'activité qui caractérise ce cycle. Notons aussi que l'analyse de l'ensemble des mesures DORAYSOL, qui a été réalisée pour la présentation de cette note, conduit à une meilleure définition des valeurs observées qui permettra leur future exploitation.

Le rayon moyen DORAYSOL défini comme nous l'avons écrit à partir des mesures Est et Ouest entre 2000 et 2006, soit 19 169 observations, est de $959,48'' \pm 0,01''$ avec un écart quadratique moyen $\sigma = 0,32''$. Cette valeur moyenne étant déduite de l'ensemble des mesures à l'Est, soit 11 663 observations, pour une valeur moyenne de $959,79''$ avec un écart type $\sigma = 0,30''$ et de 7506 mesures à l'Ouest dont la valeur moyenne est de $959,17''$ et l'écart type $\sigma = 0,34''$. La grande différence entre les effectifs de mesures à l'Est et à l'Ouest résulte de la fréquente nébulosité qui affecte le site de CALERN, notamment en été, après le passage du Soleil au méridien.

Pour mieux comparer les séries, si nous tenons compte de l'effet de distance zénithale comme nous l'avions fait pour l'Astrolabe solaire, les mesures de DORAYSOL ramenées au zénith ($\sec z = 1$) conduisent à la valeur moyenne du rayon de $959,51'' \pm 0,01''$ avec la même dispersion $\sigma = 0,32''$. Cette valeur est à rapprocher de celle obtenue avec l'Astrolabe solaire de CALERN durant la même période, de 2000 à 2006 comprenant 371 observations, qui est de $959,55'' \pm 0,01''$ avec un écart type $\sigma = 0,26''$.

Une bonne cohérence des variations des mesures visuelles de l'Astrolabe solaire et CCD faites avec DORAYSOL apparaît sur la Fig. 6. Les mesures Astrolabe solaire et DORAYSOL sont approximées par un polynôme de degré 8, l'activité magnétique est interpolée sur les moyennes mensuelles.

L'écart sur les deux séries de mesures du rayon est d'environ $0,1''$ entre 1999 et 2006. Il pourrait sembler peu significatif étant donné la faible densité d'observations assurées avec l'Astrolabe solaire à partir de 2001 mais il rend certainement compte des différences de sensibilités spectrales entre les modes d'observations visuel et CCD et aussi de la transmission par des filtres différents utilisés sur chaque instrument. Rappelons en outre que l'ensemble des mesures faites avec l'Astrolabe solaire sont corrigées de l'effet de distance zénithale, très stable sur toute la série, et que ces mesures ainsi ramenées au zénith sont d'environ $0,07''$ supérieures aux mesures brutes.

– Notons que les droites ajustées sur les séries Astrolabe solaire et DORAYSOL sont parallèles et de signes contraires à celle ajustée sur les moyennes mensuelles de l'activité magnétique.

La Fig. 6 montre sur les 10 premières années une assez nette opposition de phase entre rayon et activité magnétique qui évolue ensuite pendant les 15 années qui suivent. C'est ainsi qu'apparaît au début du cycle N°23 pendant 26 mois, entre avril 1996 et juin 1998, une apparente variation du rayon en phase avec l'activité qui a été observée également depuis

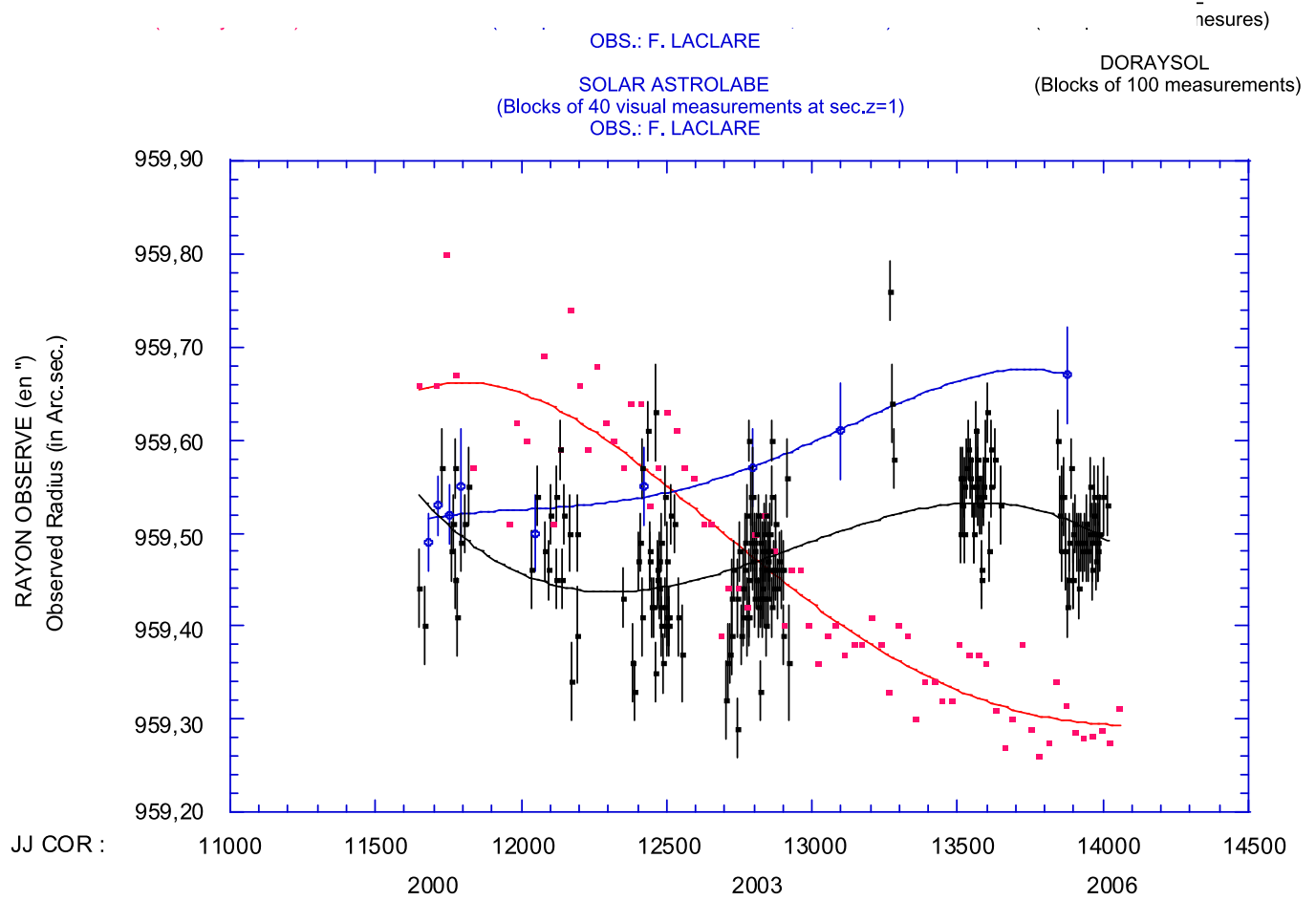


Fig. 7. Rayon et activité magnétique, fin du cycle 23 (2000–2006).

Fig. 7. Solar radius and Magnetic activity, end of cycle 23 (2000–2006).

l'espace à partir de l'expérience SOHO/MDI [16]. Cet aspect montre bien la nécessité de très longues séries de mesures pour conclure à l'existence ou non de la corrélation entre rayon et activité [20].

Les observations de DORAYSOL montrent sur la Fig. 7, en prolongement de la série de l'Astrolabe solaire, la relative persistance de la relation «rayon–activité» pendant l'intervalle 2000–2006 correspondant à la fin du cycle d'activité N°23. Mentionnons que l'année 2004 ne compte qu'un assez faible nombre d'observations (306), réparties en fin de campagne pendant les mois de septembre et octobre et donc à grandes distances zénithales.

3.2. Variations du rayon détectées par d'autres instruments

– Les observations faites à partir de techniques variées sur des sites de qualité inégale et traitées de manières diverses peuvent effectivement conduire à des résultats différents voire divergents. Il en va de même à partir d'instruments issus de l'Astrolabe de Danjon. Dans ce cas, précisons encore, que sous ce même vocable d'Astrolabe, les instruments servant à l'astrométrie solaire peuvent être de conception radicalement distincte et donc aboutir à des résultats disparates [11,12]. Rappelons que l'Astrolabe solaire de CALERN, unique dans son genre, a été conçu pour assurer exclusivement la surveillance du diamètre solaire contrairement à d'autres Astrolabes destinés aussi à l'astrométrie stellaire et dès lors moins adaptés à la seule observation du rayon solaire. Cependant, bien qu'un seul et même observateur ait conduit l'ensemble du programme de mesures sur l'Astrolabe solaire de CALERN, il subsiste une incertitude liée à l'appréciation personnelle de la mesure (équation personnelle); cet inconvénient affecte tous les instruments utilisant la méthode visuelle. L'usage de capteurs CCD contribue amplement à pallier cette incertitude et l'emploi de tels systèmes sur des Astrolabes solaires s'est généralisé ces dernières années; il a conduit à la mise en place d'une organisation appropriée : le Réseau de suivi au Sol du Rayon Solaire, (R2S3) [19]. Une première analyse faite à partir d'Astrolabes équipés de CCD montre une cohérence remarquable sur trois séries de mesures du rayon acquises en 2001 sur les astrolabes solaires situés au Brésil, en Turquie et sur DORAYSOL à CALERN [21].

– La corrélation ou l'anticorrélation entre rayon et activité solaire observées au sol par différentes méthodes ont fait et font encore l'objet de multiples points de vue le plus souvent contradictoires. Ces divergences résultent pour une grande part des moyens utilisés mais aussi des périodes de surveillance du rayon solaire et de leurs durées. Le but de cette note

n'est pas c e plus de nos mesures en signe et en valeur absolue citons les mesures faites en ballon dans la stratosphère entre 1992 et 1996 par l'instrument S.D.S. (SOLAR DISK SEXTANT). Bien que les mesures de S.D.S. n'aient pas le caractère continu de notre programme, la cohérence des valeurs du rayon observé par les deux méthodes entre 1992 et 1996 contribue à qualifier nos observations faites depuis le sol [7,13].

3.3. Figure apparente de la photosphère

Un autre aspect de ces résultats concerne la forme de la photosphère observée avec l'instrument DORAYSOL.

A partir des mesures visuelles de l'Astrolabe solaire, nous avions détecté une légère variation du rayon en fonction de sa latitude héliographique, le rayon étant plus grand d'environ $0,03''$ aux latitudes moyennes, dans la zone royale, tandis qu'il diminuait sensiblement d'environ $0,05''$ autour de 75° de latitude [3]. Notons que les observations faites à CALERN ne donnent pas accès aux régions équatoriales contrairement aux mesures faites à l'observatoire de VALINHOS au Brésil, qui semblent en accord avec celles de CALERN [17].

D'autres observations visuelles faites avec l'astrolabe à SANTIAGO du CHILI pourraient également aller dans le même sens [18]. Ces mesures appellent cependant quelque réserve, puisque l'instrument en usage à Santiago n'est pas identique, par construction, à celui de CALERN. Il en résulte une différence sensible quant à la qualité, caractérisée par un écart type de $0,50''$ au Chili tandis qu'il est de $0,28''$ à CALERN. Mentionnons également la grande amplitude de la variation du demi-diamètre observée entre 1991 et 2003, de l'ordre de $1''$ à Santiago qui est 5 à 6 fois supérieure à celle observée sur la même période à CALERN et enfin l'apparente opposition de phase des deux séries.

Sur la Fig. 8(a) nous avons reporté l'ensemble des écarts au rayon moyen annuel observés visuellement avec l'Astrolabe solaire ou avec le système CCD DORAYSOL dans le quadrant de 20° à 90° . Chaque point compte en moyenne 1100 mesures pour l'Astrolabe solaire et 2700 pour DORAYSOL. Les arcs de paraboles ajustées dans les deux séries présentent une assez grande similitude.

Les observations de cette «asphéricité» qui révèlent des valeurs du rayon photosphérique plus basses à haute latitude semblent confirmées par les mesures obtenues au télescope du Mont Wilson et aussi par l'héliomètre de J. Rösch au Pic du Midi [22].

La densité de mesures avec DORAYSOL permet de mieux répartir cet effet sur l'intervalle de 20° à 160° d'inclinaisons héliographiques, Fig. 8(b). Les écarts à la valeur moyenne du rayon, corrigée de l'effet de distance zénithale, sont calculés chaque année. Ils ne sont pas affectés par l'écart systématique Est-Ouest que nous avons discuté et qui ne concerne que les seules valeurs des rayons observés. Les observations des années 1999 et 2004 ne couvrant que trop partiellement l'année ne permettent pas une bonne répartition des inclinaisons, elles n'ont pas été retenues ; on dispose ainsi d'un ensemble de 18 862 écarts au rayon moyen.

C'est au pôle que l'on voit la baisse la plus nette du rayon tandis qu'il devient plus grand aux moyennes et faibles latitudes. Mentionnons qu'entre 20° et 90° de latitude, il s'agit essentiellement de passages observés le matin quand la qualité des mesures est meilleure comme nous l'avons vu et de plus, les effectifs sont les plus nombreux. Chaque point représente en moyenne 1700 écarts. La région de 100° à 160° , comprend essentiellement des observations faites à l'Ouest où le nombre moyen d'écarts mesurés pour chaque point est moindre, de l'ordre de 1100.

L'approximation des écarts observés par DORAYSOL par un polynôme de degré 8 conduit à un coefficient de corrélation élevé, de l'ordre de 0.83 qui pourrait affirmer l'idée d'une liaison réelle entre le rayon et son inclinaison sur l'équateur solaire. Il convient toutefois d'émettre quelques réserves concernant ce résultat, des effets systématiques ne sont pas à exclure, les écarts au rayon moyen mesurés sur la photosphère n'étant pas observés simultanément.

Ainsi, la région voisine du pôle, entre 80° et 100° d'inclinaison héliographique correspond aux effectifs de mesures les moins nombreux. Cette région n'est jamais accessible pendant les mois d'été mais seulement à l'Est, en début de campagne jusqu'au début du mois de mai, et à l'Ouest en fin de campagne à partir de la fin du mois d'août. Ces périodes d'observations à CALERN ne comprennent alors que de grandes distances zénithales et par conséquent des mesures de moindre qualité.

4. Conclusion

Le nouvel instrument installé sur le site de CALERN a procuré en 8 ans près de 20 000 mesures du rayon solaire, soit plus de deux fois l'effectif des mesures faites avec l'Astrolabe solaire sur une trentaine d'années. Les mesures acquises par DORAYSOL au moyen de CCD sont exemptes des effets personnels qui affectent les observations visuelles. Leur qualité et leur accord avec les mesures de l'Astrolabe solaire sur la période commune d'observations contribuent à qualifier la série visuelle pour la valeur moyenne et les variations apparentes du rayon. Le rayon moyen obtenu avec l'instrument DORAYSOL est de $959,48'' \pm 0,01''$, sa variation ressemble à celle que révélait la série de l'Astrolabe solaire, à savoir une apparente opposition de phase avec l'activité magnétique.

L'instrument réalisé pour sa plus grande part sur le site de CALERN requiert encore des améliorations concernant en particulier le prisme d'angle variable. Le prisme utilisé jusqu'ici n'a pas toute la qualité métrologique qui est nécessaire pour ce type de mesure. Un nouveau prisme existant [19] et des modifications à venir conduiront à l'automatisation de l'instrument pour assurer le programme d'observations au sol dans les meilleures conditions.

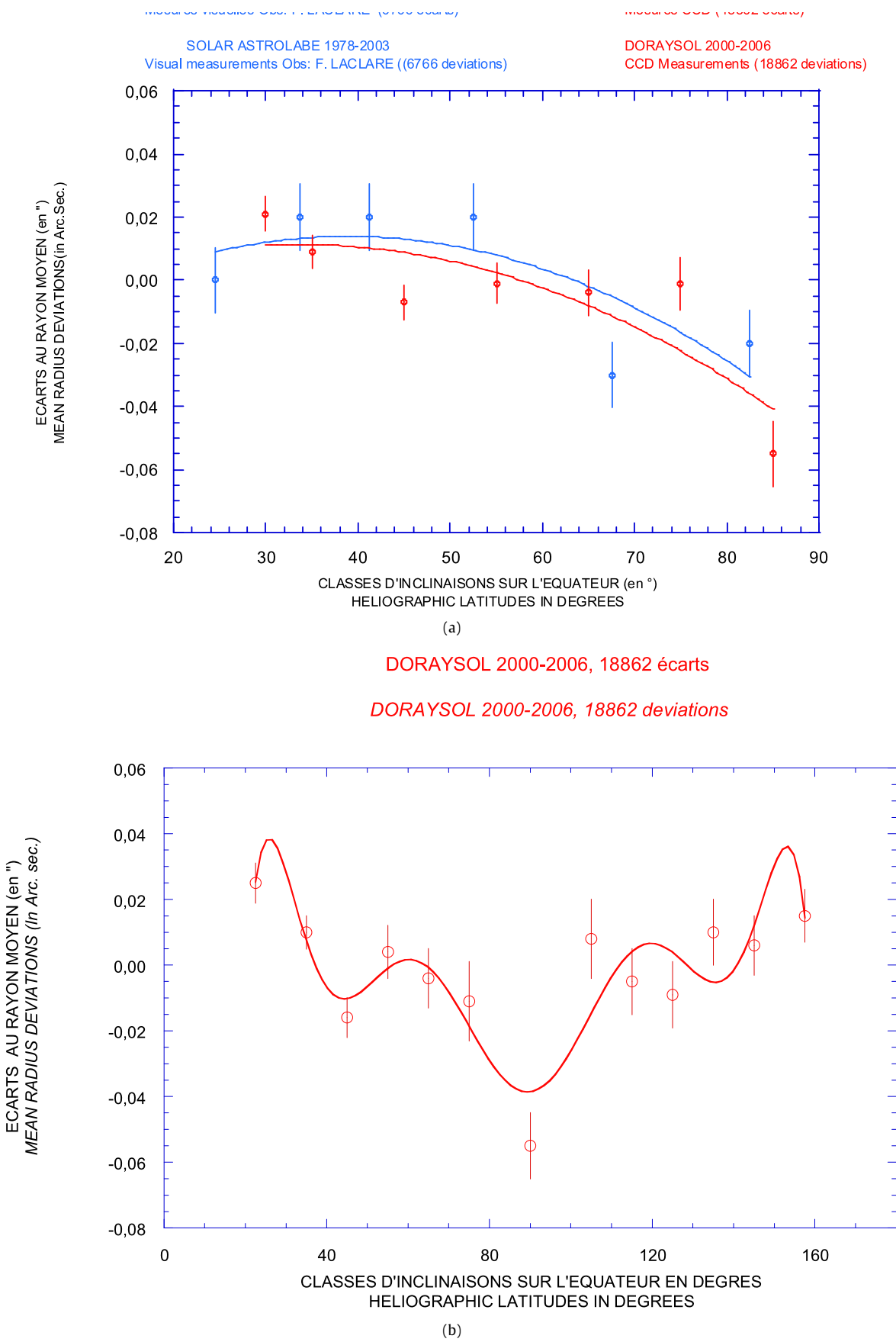


Fig. 8. (a) DORAYSOL et ASTROLABE SOLAIRE : Inclinaisons héliographiques de 20° à 90° ; (b) DORAYSOL. Inclinaisons héliographiques de 20° à 160° .

Fig. 8. (a) DORAYSOL and Solar Astrolabe, from 20° to 90° heliographic latitudes; (b) DORAYSOL, from 20° to 160° heliographic latitudes.

La duré

voir détecter avec un degré de confiance satisfaisant d'éventuelles variations du demi-diamètre, comme nous avons pu le faire sur la série de l'Astrolabe solaire [14,15]. Néanmoins, la tendance observée par DORAYSOL entre 2000 et 2006 prolonge de manière satisfaisante la série de mesures visuelles du rayon et pourrait confirmer l'anti-corrélation avec l'activité magnétique.

Enfin, ces mesures montrent également certaines dissymétries apparentes de l'image photosphérique du Soleil que nous avions observées avec l'Astrolabe solaire et que par ailleurs d'autres techniques révèlent [22].

Malgré les améliorations apportées à nos instruments au sol, seules les mesures depuis l'espace répondront de manière claire aux questions concernant la géométrie du Soleil, son rayon et ses éventuelles variations, à condition que le suivi des observations couvre de longues durées, voire plusieurs cycles. Ce type de « surveillance » n'est généralement pas dévolu aux expériences spatiales dont la durée de vie est brève, de l'ordre de quelques années ; c'est donc au sol, par des mesures continues et calibrées sur les mesures spatiales que l'on doit conduire un tel programme. C'est bien dans cet esprit que nous avons commencé le programme DORAYSOL qui vient continuer la longue série de mesures faites avec l'Astrolabe solaire et qui devrait être simultané à l'expérience du satellite PICARD. C'est également dans ce but que l'instrument MISOLFA,¹ installé sur le site au voisinage immédiat de DORAYSOL, permettra, par la mesure des paramètres de la turbulence, de qualifier les mesures faites depuis le sol. Enfin, nos mesures seront à rapprocher de celles qu'obtiendra la réplique SODISM² du satellite PICARD dont nous préparons depuis plusieurs années l'installation sur le site de CALERN avec l'aide du C.N.E.S. et du LATMOS.³

Remerciements

Jean Pierre COIN, Ingénieur à l'Observatoire de la Côte d'Azur a dirigé l'ensemble de la réalisation optique et mécanique de l'instrument DORAYSOL.

Victor SINCEAC, étudiant de l'Observatoire de Paris a développé et mis au point sur l'Astrolabe solaire l'ensemble du système d'acquisitions numériques utilisé par DORAYSOL.

G. COLAS, étudiant stagiaire en informatique à l'I.U.T. de Limoges a largement contribué au programme d'observations.

Pierre BOURGET a conçu et réalisé le nouveau prisme d'angle variable.

Références

- [1] F. Morand, E. Hunaut, Ch. Delmas, J.P. Coin, P. Bourget, Automatisation de l'instrument DORAYSOL, Compte-rendus de la deuxième réunion annuelle R2S3, 2003.
- [2] F. Laclare, Mesures du diamètre solaire à l'Astrolabe, *Astron. Astrophys.* 125 (1983) 200–203.
- [3] F. Laclare, Ch. Delmas, J.P. Coin, A. Irbah, Measurements and variations of the solar diameter, *Solar Phys.* 166 (1996) 211–229.
- [4] F. Laclare, G. Merlin, L'Astrolabe solaire impersonnalisé par l'emploi d'une camera CCD. Application à la mesure du diamètre solaire, *C. R. Acad. Sci. Paris, Sér. II* 313 (1991) 323–330.
- [5] V. Sinceac, Thèse de doctorat, 1998, Observatoire de PARIS.
- [6] F. Chollet, V. Sinceac, Analysis of solar radius determinations obtained by the modern CCD Astrolabe of the CALERN observatory, a new approach of the solar limb definition, *Astron. Astrophys. Suppl. Ser.* 139 (2) (1999) 219–229.
- [7] D. Djajaer, G. Thuillier, S. Sofia, A. Egidi, Processing methods effects on solar diameter measurements: Use of data gathered by the solar disk sextant, *Solar Phys.* 247 (2008) 225–248.
- [8] D.L. Fried, Optical resolution through a randomly inhomogeneous medium for very long and very short exposures, *J. Opt. Soc. Am.* 56 (1966) 1372–1379.
- [9] A. Irbah, F. Laclare, J. Borgnino, G. Merlin, Solar diameter measurements with CALERN Observatory Astrolabe and atmospheric turbulence, *Solar Phys.* 149 (1994) 213–230.
- [10] L. Lakhal, A. Irbah, M. Bouzaria, J. Borgnino, F. Laclare, Ch. Delmas, Error due to atmospheric turbulence effects on solar diameter measurements performed with an Astrolabe, *Astron. Astrophys. Suppl. Ser.* 138 (1999) 155–162.
- [11] D. Djajaer, G. Thuillier, S. Sofia, A comparison among solar diameter measurements carried out from the ground and outside Earth's atmosphere, *Astrophys. J.* 676 (2008) 651–657.
- [12] G. Thuillier, S. Sofia, M. Herberreiter, Past, Present and future measurements of the solar diameter, *Adv. Space Res.* 35 (2005) 329–340.
- [13] A. Egidi, B. Caccin, S. Sofia, W. Heaps, W. Hoegy, L. Twigg, High-precision measurements of the solar diameter and oblateness by the solar disk sextant (SDS) experiment, *Solar Phys.* 235 (2006) 407–408.
- [14] Ph. Delache, F. Laclare, H. Sadsaoud, Long period oscillations in solar diameter measurements, *Nature* 317 (1985) 416–418.
- [15] F. Laclare, Ch. Delmas, A. Irbah, Variations apparentes du rayon solaire observées à l'Observatoire de la Côte d'Azur (Astrolabe solaire du site de CALERN : 1975–1978), *C. R. Acad. Sci. Paris, Sér. II b* 327 (1999) 1107–1114.
- [16] M. Emilio, J.R. Kuhn, R.I. Bush, P. Sherrer, On the constancy of the solar diameter, *Astrophys. J.* 543 (2000) 1007.
- [17] M. Emilio, Estudo das variações do semi diâmetro solar, Master of sciences thesis, IAG/Universidade de São Paulo, 1997.
- [18] F. Noël, On solar radius variations observed with Astrolabe, *Solar Phys.* 232 (2005) 127–141.
- [19] Ch. Delmas, F. Morand, F. Laclare, A. Irbah, G. Thuillier, P. Bourget, Ground solar radius survey in view of micro satellite missions, *Adv. Space Res.* 3 (2006) 1564–1568.
- [20] Ch. Delmas, F. Laclare, Short VS Long time series: Example of the solar diameter, *Solar Phys.* 209 (2002) 391–396.
- [21] A.H. Andrei, S.C. Boscardin, F. Chollet, C. Delmas, O. Golbasi, E.G. Jilinski, H. Kilic, F. Laclare, F. Morand, J.L. Penna, E. Reis Neto, Comparison of CCD astrolabe multi-site solar diameter observations, *A&A* 427 (2004) 717–723.
- [22] S. Lefebvre, L. Bertello, R.K. Ulrich, J.E. Boyden, J.P. Rozelot, Solar radius measurements at Mount Wilson Observatory, *Astrophys. J.* 649 (2006) 444–451.

¹ MISOLFA : Moniteur d'Image solaire Franco-Algérien.

² SODISM 2 : Réplique du télescope embarqué SODISM : Solar Diameter Imager and Surface Mapper.

³ LATMOS : Laboratoire Atmosphères, Milieux, Observations Spatiales.

II.2 Développements instrumentaux : PICARD-SOL

PICARD-SOL désigne un ensemble de 5 instruments qui ont été installés sur le site de Calern en juin 2011 soit un an après le lancement du satellite PICARD. Il s'agit de SODISM-2, le modèle de qualification du télescope embarqué sur le satellite, un moniteur de turbulence MISOLFA qui a été conçu spécifiquement pour répondre aux besoins de l'astrométrie solaire, un photomètre multi-bandes faisant partie du réseau AERONET (AErosol RObotic NEtwork) pour la mesure des Aérosols, un pyranomètre et une caméra grand champ pour la qualification de la qualité du ciel.

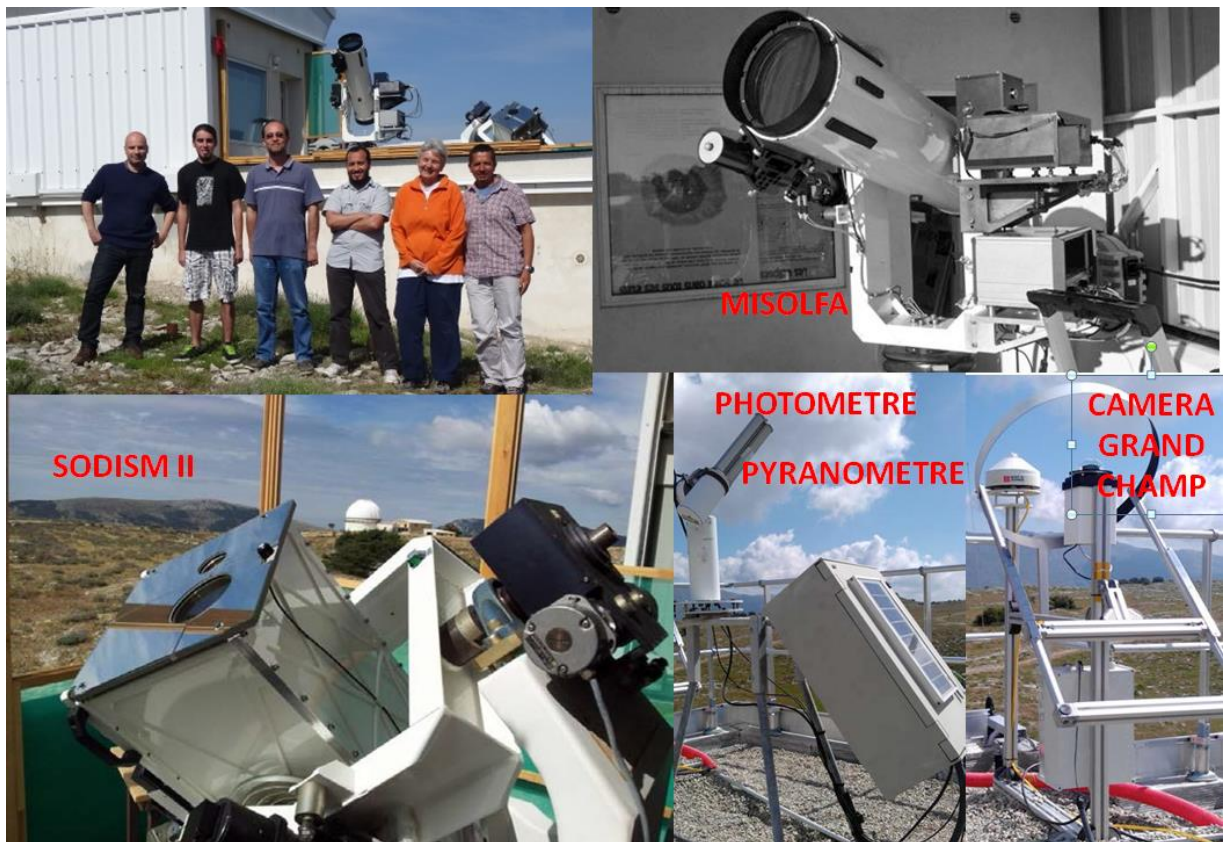


Figure 26 Les 5 instruments du programme PICARD-SOL ainsi qu'une partie de l'équipe locale (de gauche à droite : T. Corbard, A. Metge, F. Morand, R. Ikhlef, C. Renaud, M. Fodil) sur le plateau de Calern

II.2.1 L'instrument SODISM-2

Nous avons publié une description détaillée de l'instrument SODISM de la mission PICARD (Meftah, Hochedez, et al. 2014).

L'étude de l'adaptation au sol de SODISM (Morand, Corbard, et al. 2009) s'est faite en ayant pour guide les deux objectifs généraux suivant :

- SODISM-2 devait rester la copie la plus conforme possible de SODISM 1 et dans la mesure du possible, ses différents éléments ne devaient pas être modifiés. SODISM-2 devait en effet rester un modèle susceptible de voler.
- SODISM-2 doit travailler dans des conditions de fonctionnement les plus similaires possibles à celles de SODISM 1.

Le respect de ces deux objectifs a induit de nombreuses contraintes et adaptations dont notamment :

- SODISM est conçu pour fonctionner dans le vide ; il a donc été nécessaire d'enfermer l'instrument dans une enceinte à vide,
- Les conditions thermiques au sol sont très différentes de celles de l'Espace : le radiateur ne voit plus une température très basse et constante, mais des températures fluctuantes au cours de la journée et de l'année, proches de la température de fonctionnement de l'instrument. Une régulation thermique spécifique au sol a donc été mise en œuvre.
- La transmission de l'atmosphère, qui est nulle dans l'ultraviolet, interdit l'utilisation de certaines longueurs d'onde sur SODISM-2. Seules les longueurs d'onde 393 nm, 536.7 nm, 607 nm et 782 nm sont utilisées au sol. Le filtre à UV 205 nm utilisé sur SODISM a donc été remplacé par un filtre IR à 1025 nm sur SODISM-2.
- Le simulateur de l'OBC (OnBoard Computeur) est relativement lent, il ne permet pas d'augmenter la vitesse d'acquisition à plus d'une image par minute et surtout il ne permet pas de visualiser les images en temps réel. Celles-ci ne sont accessibles que quelques minutes (3 à 6 minutes) après leur acquisition. Le système de rétro-control du guidage, basé sur l'analyse des images acquises (détermination de la position du centre du disque solaire par transformée de Hough circulaire) a dû être adapté pour prendre en compte ce délai.

II.2.2 Effets atmosphériques sur la mesure du diamètre avec SODISM-2

La mesure du diamètre du soleil est obtenue avec SODISM-2, en formant directement son image sur une caméra CCD. Le diamètre est défini par la position des points d'infexion du limbe qui est la fonction radiale d'assombrissement centre-bord de l'intensité du soleil. L'atmosphère terrestre crée des effets qui peuvent perturber les mesures du diamètre.

II.2.2.1 Les principaux effets et leur importance relative

- **La turbulence atmosphérique** affecte la formation des images avec un instrument d'observation au sol. Le formalisme est basé sur la loi de Kolmogorov. Lorsqu'on ajoute à un fluide turbulent un constituant passif (ne modifiant pas les propriétés dynamiques du milieu) et conservatif (ne disparaissant pas par réaction chimique ou autre), la concentration du constituant suit aussi la loi de Kolmogorov. Ce résultat s'applique au mélange air/vapeur d'eau (Roddier 1981). Cette loi permet de déduire la densité spectrale des fluctuations de température et de concentration en vapeur d'eau et en conséquence celles de l'indice de réfraction qui conditionnent la propagation du front d'onde et ses perturbations.

Le front d'onde qui arrive sur la pupille de l'instrument d'observation, présente des perturbations qui évoluent au rythme de la turbulence caractérisée par sa constante de temps (temps caractéristique). La pente moyenne du front d'onde sur la pupille, donne la direction suivant laquelle se forme l'image qui généralement, est différente de l'axe optique. L'évolution temporelle de la turbulence fait varier la pente moyenne du front d'onde et en conséquence la position où se forme l'image dans le plan focal : c'est le phénomène d'agitation des images au foyer des télescopes. L'intégration temporelle des images avec une caméra CCD dont le temps de pose est supérieur au temps caractéristique de la turbulence, donne une image moyenne où les hautes fréquences spatiales sont filtrées. C'est le cas des images du soleil où ce filtre aura pour conséquence d'étaler le limbe et d'affecter ainsi la mesure du diamètre. Les dégradations du front d'onde n'étant similaires que sur des zones angulaires de quelques dizaines de secondes d'arc dans le cas des observations de jour, le limbe sera affecté différemment dans l'image du soleil dont la taille est environ égale à 30 minutes d'arc. La turbulence atmosphérique induit aussi des fluctuations de l'amplitude du front d'onde : c'est le phénomène de scintillation.

- **La présence d'aérosol dans l'atmosphère** peut induire de la lumière diffusée qui dans le plan focal de l'instrument d'observation, viendra se superposer à l'image de l'objet (le soleil). Cet effet est fortement réduit lorsque l'image du soleil est corrigée avec celle du fond de ciel. La mesure du diamètre n'est donc pas affectée par cette lumière diffusée. Les aérosols ont également pour effet d'absorber en

partie le rayonnement. Cela se traduit donc par des fluctuations d'intensité dans l'image qui se superposeront à ceux induits par la scintillation. Ces effets sont négligeables par rapport aux fluctuations de phase responsables de l'agitation. De plus, les aérosols en absorbant de façon plus ou moins importante le rayonnement solaire, modifient le profil vertical de température et sont par conséquent, pris en compte dans le formalisme de formation des images avec un instrument au sol au travers du modèle de Kolmogorov.

- **La qualité des images** est conditionnée par le moment du second ordre de l'amplitude complexe (fonction de cohérence mutuelle ou fonction de transfert long temps de pose correspondant à l'atmosphère terrestre) qui permet de définir le paramètre de Fried (critère de Strehl). Généralement, ce seul moment, fonction de la turbulence optique, est utilisé pour quantifier la qualité des images. Il est cependant possible (Lutomirski 1978) de définir également des fonctions de cohérence mutuelle pour quantifier l'effet des aérosols (prises en compte des coefficients de diffusion et d'extinction) et des molécules (prise en compte de la diffusion de Rayleigh). Les différents processus étant décorrélés la fonction de cohérence mutuelle (fonction de transfert) totale sera obtenue en multipliant les différentes fonctions de cohérence mutuelle. On peut ensuite prendre en compte l'effet de filtrage introduit par l'instrument d'observation. Il est donc possible, théoriquement, de prendre en compte non seulement la turbulence mais aussi les aérosols et les molécules. Là encore, ces études montrent que, pour les fréquences spatiales apparaissant dans le traitement des images astronomiques, la présence d'aérosols (comme de molécules) se traduit au premier ordre par une extinction de l'objet observé et que la turbulence est la seule cause de l'étalement (voir aussi Bruscagnoli et al., (1993), Kopeika et al. (1981))
- **La réfraction astronomique** affecte la forme de l'image et modifie son rayon moyen lorsque nous observons proche de l'horizon ou à des distances zénithales supérieures à 70°. Nous avons étudié cette question en détail pour définir les corrections de réfractions et connaître, quantitativement, l'incertitude qu'elles introduisent dans la détermination du rayon en fonction de la distance zénithale d'observation (voir paragraphe 0).

II.2.2.2 Comment traiter les effets de la turbulence optique ?

La principale source d'incertitudes et de biais pour tout programme d'astrométrie au sol est donc certainement l'effet de la turbulence optique. Des tentatives pour réduire cet effet ont historiquement été menées en utilisant une définition du bord solaire basée sur la transformée de Fourier finie (FFTD, Hill et al. (1975) ; Brown (1982)). Cette définition du

bord solaire est basée sur une intégrale filtrée du signal au niveau du limbe solaire. Cela minimise l'influence de la pente variable de la fonction d'assombrissement contre-bord observée qui est induite notamment par les conditions atmosphériques variables c'est-à-dire le seeing et la diffusion. Cela a été utilisé par exemple pour les mesures photoélectriques de transit au méridien avec le Solar Diameter Monitor (SDM, Brown et al. (1982)). Néanmoins le bruit résiduel mesuré par la dispersion journalière sur plusieurs mois était de l'ordre de 200 mas et très probablement lié aux fluctuations d'images induites par l'atmosphère. En mesurant également la pente de la fonction d'assombrissement centre-bord SDM essayait de mesurer un proxy de la turbulence optique. Il a cependant été reconnu plus tard que ce proxy n'était probablement pas complètement indépendant du signal solaire lui-même (Ribes, et al. 1991). Pour les mesures astrolabes, des analyses détaillées à posteriori des effets de la turbulence ont également été menées (Irbah et al. (1994) ; Lakhel et al. (1999)) montrant que le biais introduit par la turbulence dépend non seulement du seeing tel que mesuré par le paramètre de Fried mais aussi de l'échelle externe de la turbulence et du temps d'exposition. Comme pour SDM, les mesures de l'astrolabe produisent seulement un proxy approximatif des paramètres de la turbulence et il a été réalisé à partir de toutes ces expériences qu'un moniteur de turbulence dédié était nécessaire pour accompagner les mesures d'astrométrie solaire. Les techniques de transit, astrolabe ou SDM, reposent sur un minutage précis et par conséquent de courtes poses sont nécessaires. D'un autre côté en utilisant des images longues poses du disque solaire (c'est-à-dire avec un temps d'exposition supérieur au temps de cohérence de la turbulence), l'effet de la turbulence est réduit essentiellement à un biais sur l'estimation de la position du point d'inflexion de la fonction d'assombrissement centre-bord. De plus, Berdja (2007) a montré que ce biais peut être modélisé et corrigé si tous les paramètres spatio-temporels et spectraux de la turbulence optique peuvent être mesurés. Cela nous a conduit au développement d'un moniteur appelé MISOLFA (Moniteur d'Images SOLaires Franco-Algérien) capable d'estimer simultanément le paramètre de Fried, l'angle d'isoplanétisme, la taille de l'échelle externe et le temps caractéristique à plusieurs longueurs d'onde (Assus et al. (2000) ; Irbah et al. (2001) (2010) ; Corbard et al. (2010); Ikhlef et al. (2012 (a) (b)) (2016)). Avec ce moniteur le biais sur toute mesure individuelle peut en principe être estimé de manière fiable pour n'importe quelle condition raisonnable de seeing, améliorant ainsi l'exactitude des moyennes journalières et mensuelles. Ensuite, en augmentant la taille de l'échantillon, c'est à dire le nombre de mesures journalières nous pouvons augmenter la précision. Ces incertitudes peuvent encore être réduites si nous pouvons moyenner les mesures du rayon obtenues pour n'importe quel angle héliographique autour du disque solaire. Ceci n'a pas été fait dans le passé car les mesures astrolabe ne donnent accès qu'au diamètre vertical et les mesures photoélectriques étaient limitées à, au plus, trois angles différents. Mais cela suppose que le Soleil soit effectivement sphérique ou que l'on sache corriger de toute asphéricité qui serait d'origine instrumentale et non solaire. Or le résultat le plus robuste de l'astrométrie solaire depuis l'espace est certainement

celui concernant la forme du Soleil (Fivian et al. (2008); Kuhn et al. (2012); Irbah et al. (2014) ; Meftah et al. (2015)). Ceci est dû au fait que, contrairement aux mesures du rayon moyen, les effets instrumentaux peuvent être découplés sans ambiguïté du signal solaire en faisant pivoter le satellite autour de son axe de visée. Ces études montrent que la différence entre les rayons polaires et équatoriaux du Soleil reste significativement inférieure à 10 mas. Cette différence est même parfois trouvée inférieure aux 8 mas attendues de par le seul effet de la rotation différentielle, ce qui n'est pas sans soulever de nouvelles difficultés (Gough 2012). Mais, dans tous les cas, ces nouveaux résultats peuvent être utilisés pour calibrer tout effet instrumental ou atmosphérique quand nous utilisons l'imagerie à haute résolution du disque entier. Pour une image ayant une résolution d'une arcseconde par pixel, nous pouvons maintenant de manière certaine considérer que toute distorsion observée de la forme du Soleil qui serait au-delà du centième de pixel n'est pas d'origine Solaire une fois que les effets des éléments magnétiques de surface ont été filtrés, ce que permet également l'imagerie à haute résolution.

II.2.2.3 L'instrument MISOLFA (article)

ARTICLE : MISOLFA: a generalized monitor for daytime spatio-temporal turbulence characterization, Ikhlef, Corbard et al. (2016)

Le développement de ce moniteur de turbulence a été initié au début des années 2000 (Assus et al. (2000) ; Irbah et al. (2001)), il a fait l'objet d'une thèse théorique en 2007 (Berdja 2007) mais il n'a réellement commencé à être pleinement opérationnel, sur ces deux voies d'analyse, que très récemment. Son développement et l'analyse des résultats est l'objet principal du travail de R. Ikhlef que j'encadre en tant que directeur de thèse dans le cadre d'une co-tutelle avec l'Université d'Alger. Ces travaux et les résultats obtenus ont fait l'objet d'une publication en 2016.



MISOLFA: a generalized monitor for daytime spatio-temporal turbulence characterization

R. Ikhlef,^{1,2*} T. Corbard,¹ F. Morand,¹ C. Renaud,¹ M. Fodil,² A. Ziad,¹ J. Borgnino,¹ M. Meftah,³ P. Assus,¹ B. Chauvineau,¹ A. Hauchecorne,³ P. Lesueur,³ G. Poiet,³ F. Ubaldi,¹ M. Hamadouche⁴ and T. Abdelatif²

¹Laboratoire Lagrange, UMR7293, Université Côte d’Azur, Observatoire de la Côte d’Azur (OCA), CNRS, Bd. de l’Observatoire CS 34229, F-06304 Nice Cedex 4, France

²Centre de Recherche en Astronomie Astrophysique et Géophysique (CRAAG), Observatoire d’Alger, 16340, Algiers, Algeria

³Université Versailles St-Quentin; Sorbonne Universités, UPMC Univ. Paris 06; CNRS/INSU, LATMOS-IPSL, 11 Boulevard D’Alembert, F-78280 Guyancourt, France

⁴Université M’Hamed Bougara Boumerdes (UMBB), 35000 Boumerdes, Algeria

Accepted 2016 January 27. Received 2016 January 18; in original form 2015 October 21

ABSTRACT

Ground-based solar observations are strongly affected by optical turbulence. The concept of a new instrument which allows one to measure both spatial and temporal parameters of atmospheric turbulence has been proposed in the late 1990s. The instrument MISOLFA (Moniteur d’Images Solaire Franco-Algérien) is based on this concept and has been developed over the past 10 years in the framework of a ground-based solar astrometry programme and in parallel to the development of several night time turbulence monitors at Calern Observatory, south of France. In this paper, we first describe its instrumental concept, the technical choices that were made to meet the specifications and discuss the difficulties encountered. Using numerical simulations, we present and test the methods that can be used in order to estimate the turbulence parameters from both MISOLFA image and pupil planes. The effect of finite outer scale on Fried parameter estimation from a simple estimate of the angle-of-arrival variance is clearly shown. Finally, we present the first results obtained with the instrument fully operating in its two observing planes. We obtained a mean value of angle-of-arrival coherence time of 5.3 ms, and good agreement is found between spatial parameters obtained with image and pupil planes. First estimates of the atmospheric structure constant $C_n^2(h)$ and outer scale $L_0(h)$ profiles are also presented which illustrates the profiling capacities of the new instrument.

Key words: atmospheric effects – site testing – telescopes – Sun: general.

1 INTRODUCTION

The wavefront of light propagating through earth atmosphere is randomly perturbed due to atmospheric turbulence. Angle-of-arrival (AA) fluctuations, which are fluctuations of the normal to the perturbed wavefronts, are commonly studied to characterize the degree to which turbulence affects ground-based astronomical observations. Several parameters describing the mean spatio-temporal properties of turbulence can be derived from the records of these AA-fluctuations. It is useful to first recall the definitions of these parameters.

(1) The atmospheric structure constant of the air refractive index fluctuations $C_n^2(h)$ showing the turbulence energy distribution with altitude.

(2) The outer scale vertical profile $L_0(h)$ which represents the distribution for the characteristic scale of the largest velocity inhomogeneities in turbulent layers. This parameter is strictly related to the turbulent energy in each layer (Borgnino 1990).

(3) Fried parameter r_0 (Fried 1965) which is the diameter of the coherence zone of the degraded wavefront. It corresponds also to the image resolution obtained with the telescope of diameter r_0 placed outside the atmosphere.

(4) The spatial coherence outer scale \mathcal{L}_0 which defines the maximal size of wavefront perturbations remaining coherent. It traduces the low-frequency evolution of the wavefront and affects long baseline or large telescope observations. \mathcal{L}_0 is an estimator related to

*E-mail: rabah.ikhlef@oca.eu

the optical quality of the perturbed wavefront. For a single turbulent layer, \mathcal{L}_0 is equal to L_0 of that layer (Borgnino 1990).

(5) The isoplanatic patch θ_0 which is the angle where phase or speckles remain correlated.

(6) The correlation time τ_0 which is the time during which the atmosphere may be considered as frozen for the considered structures (phase, speckles), i.e. the time during which they keep their coherence.

For night time observations, several instruments were developed. The most used method consist in analysing fluctuations of a star position with a differential method for estimating Fried parameter r_0 , case of the Differential Image Motion Monitor (DIMM; Sarazin & Roddier 1990) or the four parameters r_0 , \mathcal{L}_0 , θ_0 and τ_0 with the Generalized Seeing Monitor (GSM; Martin et al. 1994; Ziad et al. 2000). Other instruments such as the Monitor of Outer Scale Profile (MOSP; Maire et al. 2007) or, more recently, the Profiler of the Moon Limb (PML; Ziad et al. 2013) analyse the AA-fluctuations by the observation of the lunar limb. However, for daytime atmospheric turbulence, few instruments were developed such as the Solar Differential Image Motion Monitor (S-DIMM; Beckers 2001) for seeing measurements and the Shadow Band Ranger SHABAR for estimating the atmospheric structure constant $C_n^2(h)$ (Beckers 1999, 2001). They provide useful information on the spatial scales of turbulence and are commonly associated for site testing campaigns (Beckers & Mason 1998; Beckers 2001; Liu & Beckers 2001; Berkefeld et al. 2010). The need for high-resolution solar observations from ground has led to the development of multi-conjugate adaptive optics systems for solar observatories. In order to build such system, information about the statistical properties of turbulence as a function of height is needed (Kellerer et al. 2012; Schmidt et al. 2014). Using Shack–Hartmann (SH) sub-apertures as S-DIMM can provide r_0 estimates (Kawate et al. 2011). Furthermore, the measurement of the covariance of differential image displacements at different field angles for pairs of sub-apertures can provide C_n^2 profiles (Scharmer & van Werkhoven 2010).

By recording AA-fluctuations over a given angular extent of the solar limb, MISOLFA (Moniteur d'Images Solaire Franco-Algérien) also provides such profiling capability from its image way. In many situations however, estimates of atmospheric turbulence characteristic temporal scales τ_0 are also needed in order to properly model the effects of the instantaneous equivalent point spread function (PSF) of the instrument through the atmosphere. In the case of solar astrometric measurements using equal-altitude method (solar astrolabe, Laclare 1983; DORAYSOL, Morand et al. 2010), the solar diameter estimates revealed a dependence with the seeing conditions represented by Fried parameter r_0 (Irbah et al. 1994). It has been established that optical turbulence introduces a bias in the estimated position of the inflexion point of the limb-darkening function, the apparent diameter being smaller for bad seeing conditions (Lakhal et al. 1999). This bias also shows weak dependence on the outer scale \mathcal{L}_0 for a small-aperture telescope [case of the solar astrolabes $D = 10$ cm in Lakhal et al. (1999)]. Besides this systematic effect, random errors are also introduced by optical turbulence. They decrease with the seeing but are also strongly conditioned by turbulence AA-coherence times (see Lakhal et al. 1999, fig. 2). The coherence time plays also an important role for the optimization of adaptive optics systems; corrections must be faster than the wavefront evolution. In the case of SH sensors used in the adaptive optics systems, AA-fluctuations are directly observed in the image plane. It has been shown however that these fluctuations

can also be recorded in the pupil plane through the analysis of the so-called *flying shadows* (Borgnino & Martin 1977).

The concept of the generalized daytime turbulence monitor MISOLFA is based on the idea that a single instrument could provide both the spatial and temporal turbulence scales by analysing AA-fluctuations simultaneously in its image and pupil ways (Assus et al. 2002; Irbah et al. 2010; Ikhlef et al. 2012b). The instrument has been developed at Calern Observatory and is now operating continuously to monitor daytime turbulence parameters. The estimated spatial parameters are Fried parameter r_0 , spatial coherence outer scale \mathcal{L}_0 , size of the isoplanatic patch θ_0 and optical turbulence profiles from the observation of solar limb. The monitor estimates in the same time AA-characteristic time with its pupil-plane observation way.

Section 2 gives a detailed description of MISOLFA instrument. Section 3 is devoted to the theoretical background and the techniques used for parameter estimation. In Section 4, we describe numerical simulations made to validate the parameter extraction methods, and the first results using the full capacities of the instrument are presented in Section 5.

2 INSTRUMENTAL CONCEPT

In the case of daytime turbulence characterization, except for some particular sites (like Dome C), the only target that is always available is the Sun, which is a spatially extended object. Sunspots may be used as targets for a DIMM but they change their shape and position from a day to another, so the solar limb in generally chosen (Kawate et al. 2011). MISOLFA (Fig. 1) uses both image- and pupil-plane observations to measure turbulence parameters. Its optical layout is presented in Fig. 2. It is based on a Cassegrain coudé telescope of 25.4 cm diameter and an equivalent focal length of 10 m mounted on an alt-azimuthal mount. This mount configuration (alt-az) has been chosen to

- (1) provide a Nasmyth focus, which allows heavier and larger focal instrumentation,
- (2) simplify mechanical conception and realization,
- (3) always keep Sun horizontal edges on the field of the CCD.

After passing through a prismatic entrance window (P1, see section 2.1), the light falls on a concave primary mirror (M1), then is reflected towards a convex secondary mirror (M2). A small tertiary flat mirror (M3) reflects the light to the telescope Nasmyth focus. The derotating prism (P2) allows one to have along the day the two horizontal limbs in a vertical orientation on the camera field. The derotating prism consists of two prisms aluminized and bonded by molecular adhesion, which avoids the alignment problems inherent in conventional derotators made of mirrors. At the telescope output, the focal box contains several optical parts. A filter wheel allows one to select the observation wavelength, and then a beam splitter (P3) divides the optical rays into two ways.

The first one, named in the following *image-plane observation way*, allows one to measure the AA-fluctuations from images of the solar limb recorded on a CCD camera placed on the focal plane (see Fig. 5). Observations taken from this way are similar to those made by MOSP (Maire et al. 2007). The main difference is that the two opposite horizontal solar limbs are observed. They are obtained by the mean of the entrance window (P1), whose principle is shown in Fig. 3(a) and described in Section 2.1.

The second way, named in the following *pupil-plane observation way*, in which the telescope pupil is observed through a lens and



Figure 1. MISOLFA instrument with its entrance window, the alt-azimuthal mount and its focal box on a Nasmyth focus (on the top). In the bottom, we can see the pupil-plane amplification device. The two boxes are connected with optical fibres.

a narrow slit (L1) placed on the solar limb image. This slit is kept perpendicular to the limb thanks to the derotating prism (P2). The slit size is 5 arcsec in the direction parallel to the solar limb (x -direction) and about 25 arcsec in the direction perpendicular to the solar limb (y -direction). The prism (P4) is made of two components, a beam splitter and a reflecting prism of 90° . The two output are the pupil image and the global way which integrates the global flux of the pupil focalized by the lens (L2). The pupil image intensity presents fluctuations which are proportional to the AA-fluctuations (see Section 3.1.2). As shown in Fig. 3, optical fibres with different diameters are positioned in the pupil plane to bring light fluctuations to an electronic device. Light fluctuations are then converted to electrical signals by photodiodes. The output signals are very weak; two amplification stages are needed, the first of them is a low-noise amplifier. A National Instruments data acquisition system is then used to record these signals at a rate of 1 kHz. The amplification circuits are shielded and grounded to avoid the effect of parasites such as 50 Hz and the acquisition is connected to the computer via a fibred USB cable.

Due to the important focal length of the telescope (10 m), the guiding system of the alt-az mount was very complex. We developed a fine guiding system based on a solar limb detector algorithm which provides, in near real time, the location of that particular limb point that corresponds to the solar radius which is parallel to the CCD x -axis. This point can be found inside or outside the CCD frame and the goal is to act on the guiding system in order to keep it always at the same nominal location on the CCD. This fine

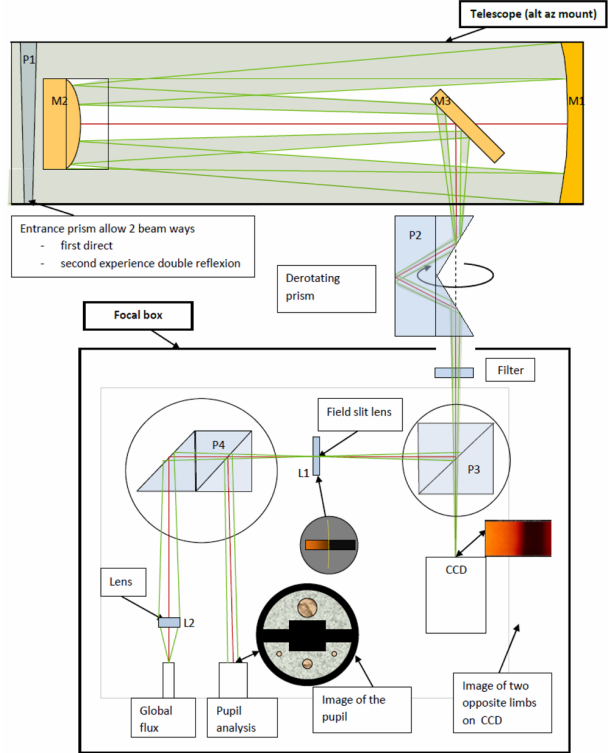


Figure 2. MISOLFA: experimental device. The compact optical configuration allows one to obtain a focal length of about 10 m. The beam splitter (P3) separates the beam into two ways with proportions 30 per cent/70 per cent. In the pupil plane, the use of different diameters allows the detection of different AA-coherence times and also to estimate spatial parameters.

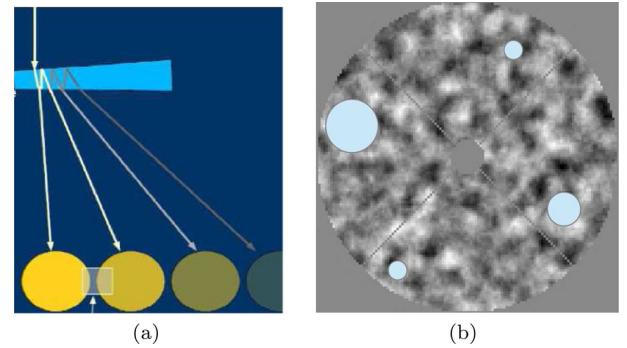


Figure 3. Panel (a) represents the prismatic entrance window allowing one to obtain the two opposite limbs of the solar disc. Separation between the two limbs is most important in summer. Panel (b) shows the optical fibre position on the pupil plane; three diameters are used: 2, 1 and 0.5 mm (two fibres). These values are chosen according to the mean value of Fried parameter recorded at Calern Observatory.

guiding system is only activated between acquisition sequences which last around 1 min and during which we do not want to introduce spurious movements. The components and instrumental parameters of MISOLFA are summarized in Table 1 and, in the following two sections, we discuss in more details the particular choices made for the entrance window and slit dimensions.

Table 1. The Components and instrumental parameters of MISOLFA.

<i>Telescope:</i>	
Model	Cassegrain coudé, Nasmyth focus
Mount	Alt-azimuthal
Aperture	254 mm, $f/40$
Focal length (f_T)	10 m
<i>Prismatic window:</i>	
Prism angle	10 arcmin 54 arcsec
External diameter	270 mm
Internal diameter	256 mm
Thickness	35 mm
<i>Filter:</i>	
Diameter	25.4 mm
Wavelengths	535.7 nm, 607 nm, $\Delta\lambda = 0.5$ nm
<i>CCD Camera:</i>	
Model	PCO PixelFly VGA
Sensor	Sony ICX074AL
Exposure time	1 ms
Frame rate	32 frame/s
Pixel size	9.9 μm (0.2 arcsec)
Number of pixels	640 \times 480
<i>Diaphragm (slit):</i>	
Length	25 arcsec
width	5 arcsec
Lens L1 focal length (f_L)	200 mm
<i>Photodiodes:</i>	
Reference	Hamamatsu S2592-03

2.1 The prismatic entrance window

The goal of MISOLFA is to obtain as maximum as possible information about how turbulence affects solar images and then solar diameter measurements. To separate effects of turbulence from other phenomena such as atmospheric refraction, we chose to estimate turbulence parameters from horizontal solar limbs, i.e. limb points on the solar radii that are parallel to the local horizon. The use of the entrance prism allows one to obtain the two opposite horizontal limbs. However, as shown in Figs 3(a) and 5, the two opposite limbs are not of the same intensity, due to reflections. The three constraints for this optical device were to keep both solar limbs on the CCD at different seasons, to have enough intensity on the reflected image and to keep the intensity ratio between the direct and reflected images stable in time. Because the apparent diameter of the Sun evolves with the season due to the elliptic Earth orbit, the separation between the two images which depends on the prism angle and the angular diameter of the Sun will also be time dependent. The prism angle (see Table 1) was therefore chosen to match this first constraint.

Given the overall transmission of the desired entrance prism (1 per cent), the best theoretical flux ratio of the reflected image to the direct image is 0.8. Several coating methods from different suppliers were tested. Unfortunately, the coatings meeting the specifications were rapidly degraded with time and robust coatings gave a very weak reflected image. The best compromise found between these two criteria has led to a flux ratio of about 0.5 between the two images. With this ratio, it is not possible to have the same quality of turbulence parameter estimates on both sides and, in the following, only the direct images were used. The opposite limb image could however still be used to separate movements due to telescope vibrations or drift, which affect both images in the same way, from the movements of interest induced by turbulence and AA-fluctuations.

2.2 The slit dimensions choice

For an extended source as the Sun, anisoplanatism prevents the use of a simple edge to obtain *solar flying shadows* like for a basic Foucault test. Instead, a thin rectangular slit is used where the two lateral sides limit the angular position observed on the limb and the small side on which the limb is observed performs a Foucault test. However, the use of a diaphragm of finite size in the focal plane introduces additional effects which limit AA-fluctuation analysis from intensity measurements of the pupil-plane images. Two effects were highlighted and have been studied by Borgnino & Martin (1977, 1978). They are related to the diffraction and angular filtering by the diaphragm. First, the presence of a diaphragm with an angular width w_x in the focal plane is equivalent to a high spatial frequency filter with a cut-off frequency f_d given by

$$f_d \approx \frac{w_x}{\lambda}. \quad (1)$$

On the other hand, geometrical considerations allow us to say that details in a turbulent layer located at an altitude h have spatial dimensions on the pupil plane of about hw_x . We can then define a spatial cut-off frequency f_a for the angular filter as

$$f_a \approx \frac{1}{hw_x}. \quad (2)$$

Borgnino & Martin (1977, 1978) have shown that the best compromise is to put $f_a = f_d$. The effect of the two filterings is presented in a synthetic way in Borgnino & Martin (1977, fig. 7). A wheel containing slits of different sizes is installed behind the beam splitter which allows selecting different filtering as a function of altitude. This capacity of our instrument has however not been used so far. For a slit having an angular width equal to 5 arcsec (Table 1) and for observations in the visible (535 nm), the filtering by diffraction is dominating until a height $h = 911$ m. This filtering of the elements lower than 2.2 cm in size is the same whatever is the height from 0 to 911 m. For higher altitudes, the angular filtering becomes dominant.

Finally, the diameters of the four sub-pupils have been chosen equal to 0.5, 1 and 2 mm so that they correspond, respectively, in the entrance pupil, to half, one time and twice a mean value of r_0 of about 3 cm. The position of these sub-pupils is shown in Fig. 3(b).

3 MEASUREMENT PRINCIPLE, THEORETICAL MODELS AND TURBULENCE PARAMETER ESTIMATION

3.1 Theoretical background

3.1.1 The image-plane observation way

In this section, we recall the theoretical basic equations. They are obtained in the same way as those used to interpret the night time observation data given by GSM (Martin et al. 1994; Ziadi et al. 2000) and MOSP (Maire et al. 2007). In the case of MISOLFA, observations of the solar limb are performed with a single telescope (pupil of diameter D) in directions on the sky separated by angles θ up to 96 arcsec. The atmospheric turbulence can be described by the Von Kàrmà̄n model with a coherence inner scale taken equal to zero. The phase power spectrum is related to the turbulence energy and the outer scale distributions with altitude. For each layer at an altitude h_0 (with a thickness δh), the Von Kàrmà̄n phase power

spectrum is expressed as (Borgnino, Martin & Ziad 1992)

$$W_\phi(f, h_0) = 0.38\lambda^{-2} \int_{h_0}^{h_0+\delta h} C_n^2(h) \left[f^2 + \frac{1}{L_0(h)^2} \right]^{-\frac{11}{6}} dh, \quad (3)$$

where f is an angular frequency and λ is the wavelength. We can then introduce the transverse (in the y -direction) AA angular structure function $D_\alpha(\theta)$ which gives an estimation of the AA angular decorrelations. It is expressed in the case of Von Kármán model with a multilayer turbulence as (Borgnino et al. 1992; Avila et al. 1997; Maire et al. 2007)

$$\begin{aligned} D_\alpha(\theta) = 2.4 \sec(z) \int_0^{+\infty} dh C_n^2(h) \int_0^{+\infty} df f^3 \left(f^2 + \frac{1}{L_0(h)^2} \right)^{-\frac{11}{6}} \\ \times [1 - J_0(2\pi f\theta h) - J_2(2\pi f\theta h)] \left[\frac{2J_1(\pi Df)}{\pi Df} \right]^2, \end{aligned} \quad (4)$$

where z is the zenith distance and J_0, J_1, J_2 are Bessel functions of the first kind. This structure function can also be expressed as

$$D_\alpha(\theta) = 2[\sigma_\alpha^2 - C_\alpha(\theta)], \quad (5)$$

where $C_\alpha(\theta)$ is the covariance and $\sigma_\alpha^2 = C_\alpha(0)$ is the variance of AA-fluctuations. If we further assume that it exists an equivalent impulse layer, located at altitude h , giving the same optical effects at ground level as the whole turbulent terrestrial atmosphere (one-layer model), then the transverse angular structure function is given by (Bouzid et al. 2002; Seghouani, Irbah & Borgnino 2002)

$$\begin{aligned} D_\alpha(\theta) = 0.1437 \lambda^2 r_0^{-\frac{5}{3}} \int_0^{+\infty} df f^3 \left(f^2 + \frac{1}{L_0^2} \right)^{-\frac{11}{6}} \\ \times [1 - J_0(2\pi f\theta h) - J_2(2\pi f\theta h)] \left[\frac{2J_1(\pi Df)}{\pi Df} \right]^2. \end{aligned} \quad (6)$$

3.1.2 The pupil-plane observation way

Geometrical optics is helpful to understand how AA-fluctuations are put in evidence in the pupil plane. Light rays of the atmospheric perturbed wavefront undergo random angles and pass or not through the diaphragm (slit). The pupil illumination observed through the diaphragm will then be related to the local slopes of the wavefront. Intensity variations in the pupil-plane image are therefore directly related to AA-fluctuations at the telescope entrance pupil when an extended source is observed.

Previous works have effectively shown the good linear relationship between intensity fluctuations of flying shadows observed in the pupil plane and AA-fluctuations from theoretical background, numerical simulations and observations (Borgnino & Martin 1977, 1978; Borgnino 1978; Berdja et al. 2004; Borgnino et al. 2007). The formalism explaining this proportional relationship was explained in detail by these authors; we recall hereafter the main ideas. We first consider a monochromatic plane wave (with wavelength λ) passing through atmospheric turbulence. Arriving at the ground, it is characterized by its complex amplitude

$$\psi(\mathbf{r}) = A(\mathbf{r}) \exp(\varphi(\mathbf{r})), \quad (7)$$

where $A(\mathbf{r})$ is the amplitude and $\varphi(\mathbf{r})$ is the phase. \mathbf{r} is a vector in planes perpendicular to the optical axis. The AA-fluctuations are defined as the slope of the wavefront phase. For a given point whose coordinates are $\mathbf{r}(x, y)$, the two components of the AA-fluctuations are

$$\alpha(\mathbf{r}) = -\frac{\lambda}{2\pi} \frac{\partial \varphi(\mathbf{r})}{\partial x}$$

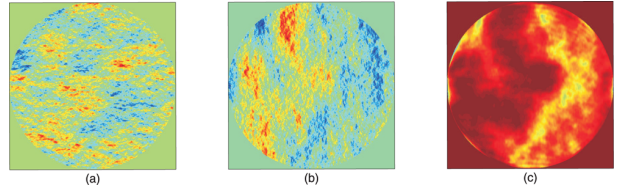


Figure 4. Simulated AA-fluctuations (from the work of Berdja in 2004) computed directly from the perturbed wavefront phase and observed as intensity fluctuations in pupil-plane image. Panels (a) and (b) show, respectively, x and y AA components at the entrance pupil, while panel (c) shows the y component observed in the pupil-plane image as intensity fluctuations. The perturbed wavefront was simulated in the near-field approximation case considering $r_0 = 4$ cm, $L_0 = 10$ m, $h = 1000$ m. The diaphragm width was taken equal to few arcseconds.

$$\beta(\mathbf{r}) = -\frac{\lambda}{2\pi} \frac{\partial \varphi(\mathbf{r})}{\partial y}. \quad (8)$$

We can divide the optical system into two parts. First, a telescope characterized by its pupil function $P(\mathbf{r})$ and a focal length f_T . The second part is a diaphragm through which we observe the image of the telescope entrance pupil and characterized by its transmission function $t(\mathbf{r})$ and the focal length f_L of a lens (L1) placed behind it. Intensity distribution in the obtained pupil image formed by the lens L1 may be obtained according to Fourier optics calculations. If we assume that the limb profile is linear with the angular direction, intensity fluctuations in the pupil image are expressed as a function of $\beta(-\mathbf{r})$, the y component of the AA-fluctuations (Borgnino 1978; Berdja et al. 2004; Borgnino et al. 2007):

$$I_0(\mathbf{r}) = a \frac{f_T}{f_L} \left[\frac{\lambda f_T}{f_L} \right]^2 |\hat{t}\left(\frac{\mathbf{r}}{\lambda f_L}\right)|^2 * \left[P\left(-\mathbf{r} \frac{f_T}{f_L}\right) \beta\left(-\mathbf{r} \frac{f_T}{f_L}\right) \right], \quad (9)$$

where $\hat{\cdot}$ denotes the Fourier transform and $*$ symbolizes a convolution product; a is a proportionality factor in linear solar limb model.

So, using a linear model of solar limb, the intensity fluctuations in the pupil image vary linearly with the slope of the wavefront observed in the direction perpendicular to this limb (y -direction). The pupil-plane observation way introduces a spatial filtering in the image due to the diaphragm. We therefore measure AA-fluctuations in the y -direction (Fig. 4). Berdja et al. (2004) have shown the good linear relationship between AA-fluctuations and intensity fluctuations as modelled with equation (9) when the solar limb is observed. In fact, we can consider that the limb-darkening profile is almost linear in the small angular field of view allowed by the diaphragm so the hypothesis of linearity remains valid.

3.2 Data analysis and parameter extraction

3.2.1 Image-plane measurements

As described above, the method is based on statistical analysis of AA-fluctuations. For that, to have sufficient samples, data sets consist in series of about 2000 images recorded at a rate of 32 frames per second. According to H. M. Martin, exposure time of the detector is a crucial parameter for seeing studies. It should be shorter than 10 ms to freeze the atmospheric image motion (Martin 1987). Thus, the exposure time of the video CCD camera is adjusted to a constant value of 1 ms. Fig. 5 shows an image of the Sun recorded on 2014 September 09 with this observation way at 607 nm. The pixel size

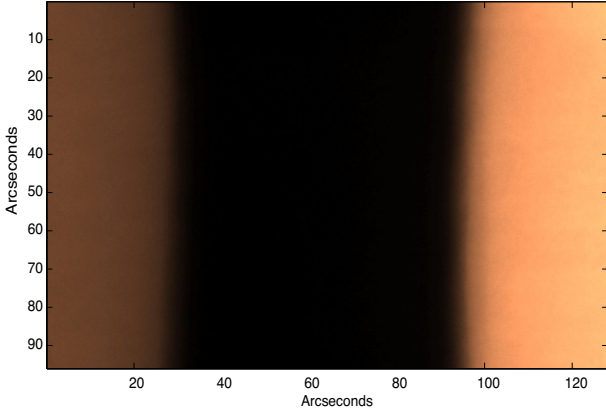


Figure 5. A solar image obtained with the image-plane observation way of MISOLFA. On the left the reflected limb and the direct limb is on the right.

is about 0.2 arcsec which leads to an image size of approximately 96 by 128 arcsec. Each CCD pixel line in the direct and reflected limb images is such as it is located on a direction parallel to the local horizon. For each image, the following processing steps are performed.

(1) Noise estimation using *standard deviation histogram algorithm* (Gao 1993). The estimation of noise is useful for the next step (wavelet denoising).

(2) Image cleaning by wavelet denoising process to eliminate sunspots which can make difficult the limb detection step (Mousaoui & Irbah 2000; Djafer & Irbah 2012).

(3) Limb detection using the second derivative over each line of the CCD. We first apply wavelet denoising on an image, then we compute its horizontal gradient, and finally we apply wavelet denoising on the gradient and a second derivation is performed. By choosing suitable thresholds, limbs are well detected in good observational conditions.

(4) Each limb is then corrected from medium edge (correction from the curvature of the solar limb) to extract at the end only fluctuations due to turbulence.

(5) The above steps are performed to extract AA-fluctuations from temporal series of solar images allowing one to compute the two main output which are the experimental AA transverse covariance function $C_{\alpha \perp \text{Exp}}(\theta)$ (and so the variance) and the structure function $D_{\alpha \perp \text{Exp}}(\theta)$ which equation is given by (Maire et al. 2007)

$$D_{\alpha \perp \text{Exp}}(\theta) = \frac{1}{N} \sum_{i=1}^N \frac{1}{\theta_m - \theta} \sum_{k=1}^{\theta_m - \theta} [\alpha_{\perp}(k) - \alpha_{\perp}(k + \theta)]^2, \quad (10)$$

where θ is the angular separation in pixels, θ_m is the maximal extent accessible in the image (i.e. 480 pixels in our case), N is the number of processed images (about 2000) and $\alpha_{\perp}(k)$ is the AA-fluctuations retrieved at the position k . To get a statistical convergence, the number N of short exposure images to be considered has to be as large as possible within the time the atmosphere keeps the same statistical properties. This time is expected to be greater than the 1 min duration of our sequences (Sarazin & Roddier 1990). In the case of the DIMM experiment, the total number of samples considered for image motion variance estimation is about 200 (Sarazin & Roddier 1990) or 300 for the ATST site testing campaign (Beckers, Liu & Jin 2003). The relative statistical error on the variance is equal to $\sqrt{\frac{2}{n-1}} \cdot n = 2000$ images will give a 2 per cent relative error on r_0

(proportional to $\sigma^{-3/5}$) and less than that for different points of the structure function ($n = 2000(\theta_m - \theta)$; Maire et al. 2007). Increasing N within the coherence time of seeing will reduce the relative statistical error but we are limited by the CCD transfer delay and the hard disks storage (1.2 Gb for each series).

Using numerical simulations, Berdja (2007) has shown that AA-fluctuations are also proportional to photometric integral variation with suitable thresholding near the limb over a series of successive images. According to the author, this method should be less sensitive to noise than estimating the position of the zero crossing of the second derivative of the limb profile. In practice, this method can effectively be used to provide a quick proxy of fluctuations σ_{α}^2 but is not able to reliably provide the full structure function.

Considering equation (4) and using a subsequent non-linear fit, one can retrieve the $C_n^2(h)$ and $L_0(h)$ profiles together by minimizing the cost function (Maire et al. 2007): $E = \sum_{\theta} [D_{\alpha \perp \text{Exp}}(\theta) - D_{\alpha \perp \text{Th}}(\theta)]^2$, where $D_{\alpha \perp \text{Th}}(\theta)$ is the theoretical structure function in equation (4). The Levenberg–Marquardt method is used in our case; limits are assumed for the parameters in order to obtain realistic values and to reduce convergence time to the optimal solution.

The integrated parameters Fried parameter r_0 , the spatial coherence outer scale \mathcal{L}_0 , the altitude of the equivalent impulse layer H and the isoplanatic angle θ_0 are then estimated using the following equations (Roddier 1981; Maire et al. 2007):

$$r_0 = \left[0.423 \left(\frac{2\pi}{\lambda} \right)^2 \sec(z) \int dh C_n^2(h) \right]^{-\frac{3}{5}} \quad (11)$$

$$\mathcal{L}_0 = \left[\frac{\int dh C_n^2(h) L_0(h)^n}{\int dh C_n^2(h)} \right]^{\frac{1}{n}} \quad (12)$$

$$H = \sec(z) \left[\frac{\int dh C_n^2(h) h^{\frac{5}{3}}}{\int dh C_n^2(h)} \right]^{\frac{3}{5}} \quad (13)$$

and

$$\theta_0 = 0.31 \frac{r_0}{H}, \quad (14)$$

where the factor n in equation (12) varies according to the instrument which measures the integrated parameter \mathcal{L}_0 . Borgnino (1990) found that for AA-fluctuations $n = -1/3$ is appropriate, whereas Maire et al. (2007) suggested another value $n = 11/3$ to match between MOSP and GSM measurements. We took $n = 11/3$ because MISOLFA is similar to MOSP.

In a particular case of a dominant layer at a given altitude, one can consider the one-layer model of equation (6) to retrieve the three parameters r_0 , \mathcal{L}_0 and the altitude of dominant layer h using a non-linear fitting.

The Fried parameter r_0 can also be estimated from the variance of AA-fluctuations σ_{α}^2 which is the first value of the covariance ($C_{\alpha}(0)$) according to a given model. If one consider Von Kármán model, r_0 is related to AA variance by the following expression (Ziad et al. 1994):

$$r_{0v} = 8.25 \cdot 10^5 \lambda^{\frac{6}{5}} \sigma_{\alpha}^{-\frac{6}{5}} \left[D^{-\frac{1}{3}} - 1.525 \mathcal{L}_0^{-\frac{1}{3}} \right]^{\frac{3}{5}}, \quad (15)$$

where σ_{α} is expressed in arcseconds.

This equation takes into account the effect of a finite outer scale. The estimation method (from limb motion) is very sensitive to telescope vibration and wind. The use of the full structure function equation (6) should be more robust with this respect. Another possibility would be to use a differential estimation (Fried 1975; Acton

1995) like in the S-DIMM or PML instruments. As we will see in the next section, MISOLFA pupil way can also be used to retrieve r_0 by using two sub-pupils of the same diameter which is also a form a differential estimation. We note that for large values of the outer scale \mathcal{L}_0 , equation (15) reduces to the Kolmogorov model for r_0 estimation (Borgnino et al. 1982; Irbah et al. 1994):

$$r_0 = 8.25 \cdot 10^5 \lambda^{\frac{6}{5}} D^{-\frac{1}{5}} \sigma_{\alpha}^{-\frac{6}{5}}. \quad (16)$$

3.2.2 Pupil-plane measurements

The main purpose of observing intensity fluctuations at high cadence (1 KHz) in the pupil plane is to estimate the turbulence AA-coherence time. However, it is also possible to reach again the spatial parameters (r_0 and \mathcal{L}_0). Four photodiodes allow one to record the intensity fluctuations with optical fibres positioned on the image behind diaphragms of different sizes (2, 1 and 0.5 mm diameter); a fifth photodiode behind a fibre of 2 mm diameter integrates the global flux of the whole pupil plane. This later signal is used to separate the AA-fluctuations from intensity fluctuations due to scintillation and other effects. This kind of correction is similar to a flat-field in the image plane. The corrected signals given by the four photodiodes are recorded simultaneously and a spatio-temporal analysis is performed.

Temporal covariance functions (and temporal structure functions) are obtained by autocorrelation of the signals. To obtain the characteristic time, each signal is divided into portions of 100 ms each, then the temporal structure function is obtained by the same way as equation (10) replacing the angular separation θ by the sampling time. The temporal characteristic time τ_0 is obtained from temporal covariance (or from temporal structure functions). It is defined as the time for which the covariance decreases from the origin by a factor k or using the structure function as the time of the drop of a constant k' from the saturation of the AA-temporal structure function (Ziad et al. 2012).

In practice, once the temporal structure function is obtained from intensity fluctuations of a given sub-pupil, we fit it by a function of the form

$$F(t) = A_{\max} (1 - e^{-t/\tau}). \quad (17)$$

Using this function, the characteristic time τ_0 is thus the corresponding time to the A_{\max}/k' (generally k' is taken equal to e).

The spatial coherence parameters r_0 and \mathcal{L}_0 may be obtained from the pupil-plane observation way together with AA-fluctuation characteristic times. The structure function of AA-fluctuations recorded by mean of a pair of photodiodes of the same size positioned in the pupil image may be expressed as (Sarazin & Roddier 1990; Borgnino et al. 2007)

$$D_{\alpha}(S) = 0.364 \left[1 - 0.541 \left(\frac{S}{D_p} \right)^{-\frac{1}{3}} \right] \lambda^2 r_0^{-\frac{5}{3}} D_p^{-\frac{1}{3}}, \quad (18)$$

where S is the baseline formed by the two photodiodes of the same integration size D_p . The structure function $D_{\alpha}(S)$ is expressed in arcseconds. equation (18) will be used to calculate r_0 . This involves the computation of the difference between the variance and the covariance between the two sub-pupils (cf. equation 5). This expression does not depend on \mathcal{L}_0 .

On the other hand, the ratio between the covariance and variance, called also the normalized covariance, does not depend on r_0 (Avila

et al. 1997),

$$\Gamma_{\alpha} = \frac{C_{\alpha}(S, D_p, \mathcal{L}_0)}{\sigma_{\alpha}^2(D_p, \mathcal{L}_0)}. \quad (19)$$

This ratio remains a function of the baseline S and the diameter but is no longer dependent on r_0 because both the variance and covariance are proportional to $r_0^{-5/3}$. \mathcal{L}_0 is determined numerically from this equation by using the asymptotic expressions of covariance and variance (Conan 2000; Conan et al. 2000):

$$C_{\alpha}(S, D_p, \mathcal{L}_0) = 0.0589 \lambda^2 r_0^{-\frac{5}{3}} D_p^{-\frac{1}{3}} \left[-3.001 \left(\frac{\pi D_p}{\mathcal{L}_0} \right)^{\frac{1}{3}} - 1.286 \left(\frac{\pi D_p}{\mathcal{L}_0} \right)^{\frac{7}{3}} + \left(\frac{S}{D_p} \right)^{-\frac{1}{3}} (5 - \cos(2\gamma)) \times \left[0.411 + 0.188 \left(\frac{\pi D_p}{\mathcal{L}_0} \right)^2 \right] \right], \quad (20)$$

where putting $\gamma = \frac{\pi}{2}$ gives the transverse component of the covariance whereas $\gamma = 0$ corresponds to the longitudinal one (Avila et al. 1997). And

$$\sigma_{\alpha}^2(D_p, \mathcal{L}_0) = 0.1697 \lambda^2 r_0^{-\frac{5}{3}} D_p^{-\frac{1}{3}} \left[1 - 1.041 \left(\frac{\pi D_p}{\mathcal{L}_0} \right)^{\frac{1}{3}} + 0.565 \left(\frac{\pi D_p}{\mathcal{L}_0} \right)^2 - 0.446 \left(\frac{\pi D_p}{\mathcal{L}_0} \right)^{\frac{7}{3}} \right]. \quad (21)$$

If we consider the case for which \mathcal{L}_0 is large in regard to D_p , this expression becomes (Ziad et al. 1994)

$$\sigma_{\alpha}^2(D_p, \mathcal{L}_0) = 0.1697 \lambda^2 r_0^{-\frac{5}{3}} \left[D_p^{-\frac{1}{3}} - 1.525 \mathcal{L}_0^{-\frac{1}{3}} \right]. \quad (22)$$

One can see from variance equation (22) that it is, in principle, possible to estimate the \mathcal{L}_0 parameter when Fried parameter is known. But this method is sensitive to errors in r_0 estimation.

Finally, we note that \mathcal{L}_0 may also be obtained from equation (22) applied to two photodiodes of different area integration sizes D_{p1} and D_{p2} . In this case, it is also possible to compute a ratio $R_{\mathcal{L}_0}$ involving only the two variances and which is independent from r_0 (Ziad et al. 1994):

$$R_{\mathcal{L}_0} = \frac{\sigma_{\alpha}^2(D_{p1}, \mathcal{L}_0) - \sigma_{\alpha}^2(D_{p2}, \mathcal{L}_0)}{\sigma_{\alpha}^2(D_{p1}, \mathcal{L}_0)} = \frac{D_{p1}^{-\frac{1}{3}} - D_{p2}^{-\frac{1}{3}}}{D_{p1}^{-\frac{1}{3}} - 1.525 \mathcal{L}_0^{-\frac{1}{3}}}. \quad (23)$$

Borgnino et al. (2007) advocate that the ratio between the diameters of the two sub-pupils should be at least equal to 3. In practice, we were unable to use this approach with our current setting, the sizes of our sub-pupils are probably too close and the signal-to-noise ratios of the different sub-pupils are too different.

4 NUMERICAL SIMULATIONS

The step of numerical simulation is very important while doing physical measurements. It allows one to see the response of a system while varying input parameters and eventually to select an appropriate model describing a physical phenomenon. We performed numerical simulations to verify the feasibility of parameter extraction method. Another important goal of these simulations is to obtain error bars on the measured parameters.

These simulations can be divided into three steps: image simulation without turbulence, turbulent wavefront generation and obtention of perturbed images. Then the same processing steps as for real

data can be applied. Berdja et al. (2004) have done numerical simulations related to the pupil-plane observation way and have shown excellent agreement between input AA-fluctuations and intensity fluctuations in the pupil. Here we are interested in the image plane.

First, simulation of solar image (without turbulence) with the appropriate sampling ($0.2 \text{ arcsec pixel}^{-1}$ as MISOLFA images) is made using a limb-darkening model. We used the model proposed by Hestroffer & Magnan (1998, HM98) at a wavelength equal to 535 nm.

A disturbed turbulent wavefront is then generated which is due to a single layer at a given altitude and characterized by spatial parameters r_0 and \mathcal{L}_0 . The most common method for phase screen generation is based on Fourier transform (Nakajima 1988; Schmidt 2010). The phase from this method is obtained by the inverse Fourier transform of the spectral phase density calculated according to the Von Kàrmàn model. We assume that the optical effect induced by the whole atmosphere is equivalent to the effect of a single layer at an altitude h . The sub-harmonics method is implemented to compensate the poorness of the spectral density in lower spatial frequencies.

Special attention must be given to the sampling of the generated phase screen. If L_x and L_y are the dimensions of the screen, choosing a spatial sampling dx will impose a maximum frequency sampling $f_{\max} = 1/2dx$ in the x -direction and the number of points N_x will define the frequency sampling $df = 2f_{\max}/N_x$. Constraints are applied while choosing these quantities; we will see them next.

If the turbulence is characterized by spatial parameters: r_0 and \mathcal{L}_0 , the size of the perturbed phase screen L_x (and L_y) is chosen very much larger than \mathcal{L}_0 and the spatial sampling must stay much lower than r_0 . The disturbed solar image is obtained by a convolution between the simulated Sun image and the pupil-atmosphere equivalent PSF. The angular limitation by a $N_p \times N_p$ pupil introduces an angular sampling on the resulting PSF defined by

$$\Delta\theta = \frac{\lambda}{N_p \delta_x}, \quad (24)$$

where δ_x is the spatial sampling step on the pupil. We have now two cases: isoplanatic and anisoplanatic imaging.

First we have the case of isoplanatism, in which we suppose that all the rays coming from an object pass through the same turbulence. This is equivalent to a turbulence localized at ground level ($h = 0$). In this case, one can obtain the resulting perturbed image by a direct convolution with a unique PSF.

In the case of anisoplanatism, simulation is made by generating a PSF for every incident angle of the angular domain allowed by the entrance pupil sampled by $\Delta\theta$. This is made by displacing the pupil on the phase screen (localized at an altitude h) by a step $dr = h\Delta\theta$. A convolution product is performed for each point of the object to obtain the corresponding point on the resulting image. Fig. 6 shows an example image obtained in this way. A series of 1000 images are simulated by randomly generating phase screens with the same input parameters (r_0 , \mathcal{L}_0 and h). The resulting images are processed following the same steps: edge detection, covariance and structure functions computing, non-linear curve fitting according to the Von Kàrmàn model and using Levenberg–Marquardt method. The whole process is repeated to achieve a Monte Carlo simulation allowing us to obtain mean values and standard deviations.

For a turbulence characterized by spatial parameters $r_0 = 6.5 \text{ cm}$, $\mathcal{L}_0 = 3 \text{ m}$ and $h = 3500 \text{ m}$, we obtained the structure function given by Fig. 7. The value of \mathcal{L}_0 has been chosen relatively small compared to night time values and we took it very small to see the result of neglecting its effect. Because turbulence is generated

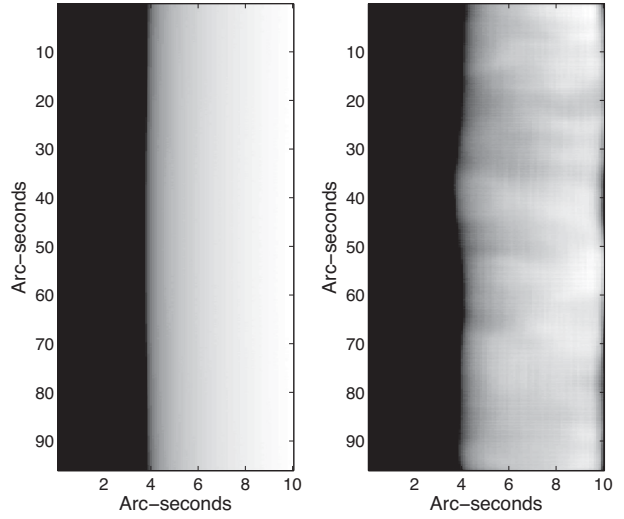


Figure 6. Simulated MISOLFA images. Left image is obtained using limb-darkening function described by the HM98 model. The right image is the result of anisoplanatic imaging through the one-layer turbulent wavefront characterized by $r_0 = 6.5 \text{ cm}$, $\mathcal{L}_0 = 3 \text{ m}$, $h = 3500 \text{ m}$.

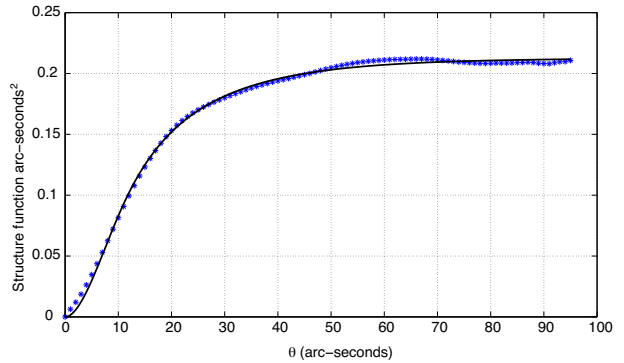


Figure 7. Simulated (stars) AA-structure function obtained by simulations in image plane and its non-linear fit by theoretical one (solid line, obtained using equation 6). The perturbed wavefront was simulated considering $r_0 = 6.5 \text{ cm}$, $\mathcal{L}_0 = 3 \text{ m}$, $h = 3500 \text{ m}$.

with a single layer, equation (6) can be directly used to extract parameters by a non-linear fit. From structure function in Fig. 7, the extracted parameters are (mean values and standard deviations through 20 realizations) $r_0 = 6.8 \pm 0.8 \text{ cm}$, $\mathcal{L}_0 = 3.4 \pm 1.3 \text{ m}$ and $h = 4617 \pm 470 \text{ m}$.

For the structure function of Fig. 7, inverting equation (4) by a non-linear iterative fit gives the $C_n^2(h)$ profile (mean profile through 20 realizations) of Fig. 8 and the outer scale profile. The grid resolution in altitude is 100 m. Equations (11) through (14) allow one to estimate the values: $r_0 = 6.5 \pm 0.4 \text{ cm}$, $\mathcal{L}_0 = 3.7 \pm 1.7 \text{ m}$, the equivalent altitude $H = 3503 \pm 60 \text{ m}$ and $\theta_0 = 1 \pm 0.1 \text{ arcsec}$ which are in excellent agreement with the input values. Fig. 8 shows a dominant layer localized at an altitude of 3500 m as expected. Another effect has been studied by the simulations. Observations made with telescopes suffer from vibrations, drift in mount tracking and wind effect. All these parameters will make image motion contaminated by noise, i.e. motions that are not due to turbulence. To simulated solar edges, we have intentionally added a drift which was

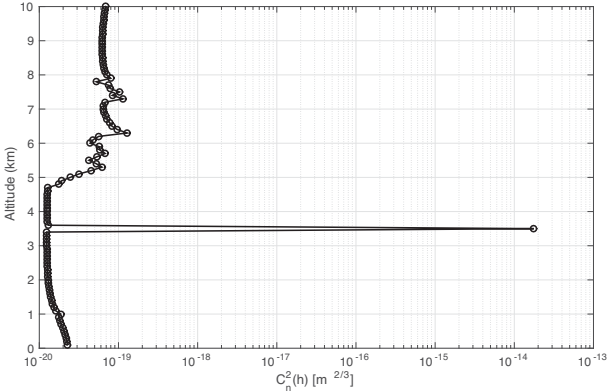


Figure 8. C_n^2 profile retrieved (using equation 4) from the structure function obtained by simulation in image plane. The perturbed wavefront was simulated considering one layer characterized by $r_0 = 6.5$ cm, $L_0 = 3$ m and localized at an altitude $h = 3500$ m.

chosen to be representative of the observed drifts with MISOLFA. Before doing AA-fluctuation structure function computation, summits of parabolas fitting each image edge have been estimated. A polynomial fit was then applied to the temporal evolution of the resulting summits and subtracted from each limb edge. While computing the structure function, correction from mean limb is made every 100 images. The resulting structure function non-linear fitting using steps described above gave spatial parameters: $r_0 = 6.8 \pm 1.2$ cm, $L_0 = 3.1 \pm 1.3$ m and $h = 4617 \pm 980$ m using the one-layer model. These values are in good agreement with input parameters except for h . Considering the multilayer model, the retrieved profiles give the following integrated parameters: $r_0 = 6.3 \pm 0.5$ cm, $L_0 = 3.7 \pm 2.2$ m and $H = 3630 \pm 125$ m. As a conclusion, usual drift effect can be considered as compensated by this technique which is employed to process data from image-plane observation way of MISOLFA. Of course, unusual jumps or strong drifts due to wind or anomalous instrumental effects still need to be detected and processed separately.

In order to check the case of multiple layers, we simulated the anisoplanatic imaging through two turbulent layers localized respectively at 3500 and 7000. The fractional turbulence energies were chosen to be 0.7 and 0.3, respectively, with an integrated Fried parameter of 6.5 cm and $L_0(h) = 3$ m for the two layers. The resulting $C_n^2(h)$ profile is given by Fig. 9. The two layers are put in evidence in the retrieved profile and the resulting integrated parameters for that realization are $r_0 = 6.6$ cm, $L_0 = 4.3$ m and $H = 4900$ m. The fractional energies of the two layers in the retrieved $C_n^2(h)$ profile are 0.62 and 0.38. We note that, like in the more general multiple-layer case, the solution of the two-layer case is not unique. If both the heights of the two layers and the amplitudes of the outer scale and structure constant are left without constraint, i.e. a priori knowledge, it is possible to find layers at different altitudes that will reproduce equally well the structure function. In the example discussed here, the heights of the layers and the amplitudes of the structure constant were left free of constraints but an a priori on the outer scale was introduced by bounding its possible values.

Borgnino et al. (1992) have shown the effect of finite outer scale on the covariances of AA-fluctuations. They concluded that the structure functions are less sensitive to the effect of outer scale than

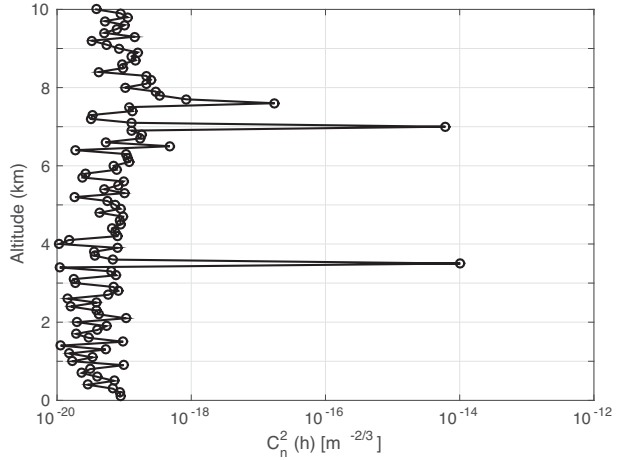


Figure 9. C_n^2 profile retrieved from a structure function obtained by simulation in image plane. The perturbed wavefront was simulated considering two layers localized at altitudes of 3500 and 7000 m, an integrated Fried parameter $r_0 = 6.5$ cm and $L_0(h) = 3$ m for the two layers.

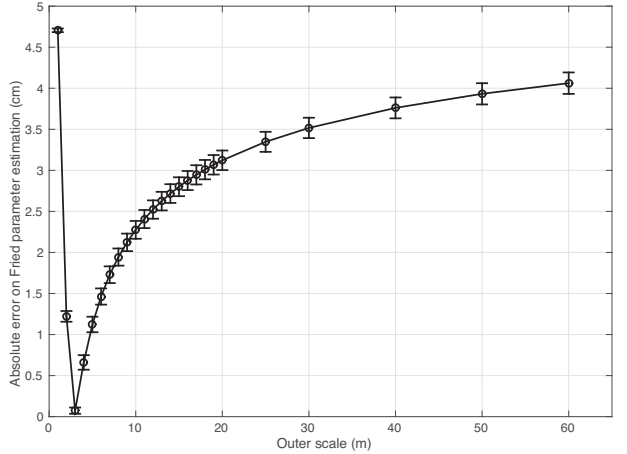


Figure 10. Errors on Fried parameter estimation as a function of outer scale obtained by simulation in image plane. The perturbed wavefront was simulated considering $r_0 = 6.5$ cm, $L_0 = 3$ m and $h = 3500$ m.

covariance and that for values of L_0 lower than 4 m, the effect of the finite outer scale on structure functions becomes increasingly important. In our simulation, if one assumes Kolmogorov model and use equation (16) to estimate Fried parameter from AA-fluctuation variance, the resulting value from simulation is $r_{0k} = 12.45 \pm 0.16$ cm which is significantly different from input. To see the effect of neglecting the outer scale until having Kolmogorov regime, one can compute the value of Fried parameter considering equation (15) by varying outer scale values from 1 to 60 m. Errors on Fried parameter estimation are then computed by subtracting the input value. The result is shown in Fig. 10. It is clearly seen that if we want to retrieve Fried parameter from only AA-fluctuation variance, preliminary knowledge of outer scale range is required. Otherwise, the estimated values of r_0 would be wrong especially in the case of finite outer scale values.

5 RESULTS AND DISCUSSIONS

The first light from the instrument was obtained on early 2009. Only the image plane was operating. We presented statistics on Fried parameter measurements between 2010 June and 2012 May in conference proceedings (Ikhlef et al. 2012a,b) using the Kolmogorov model to compute Fried parameter from solar limb motion. First measurements were obtained from the pupil plane on 2011 June. A first attempt to obtain the linear relationship as expected between the AA-fluctuations from image plane (position of the limb) and pupil-plane intensity fluctuations was presented in Irbah et al. (2011). In 2011 however, the instrument was still subject to important mount drift, clearly seen in Fig. 6 of that proceeding, and this may have contaminated our first calibration attempts. Furthermore, to improve again the pupil signal level, we replaced in 2014 the beam splitter and changed the electronic gain of all channels. We are now able to obtain many sequences where no drift signal is seen and for which we are more confident that fluctuations that we observe on both image and pupil planes are due mainly to AA-fluctuations. This allows us to properly cross-calibrate the two observing ways and to compare for the first time the estimates of the turbulence spatial parameters obtained from them.

Here we present some recent results obtained after many improvements of our instrument for minimizing drift and vibrations, improving the signal-to-noise ratio and taking into account the results of our simulations for validating the turbulence parameter extraction procedures. We first give the results for the coherence times obtained directly from the pupil way. Then we present the cross-calibration of the pupil and image planes and compare for the first time the results obtained in both ways for the spatial parameters of turbulence. The following results were obtained at 535.7 nm.

5.1 Coherence time

We present in Fig. 11 an example of intensity fluctuation signal obtained with the 1 mm diameter sub-pupil and the corresponding temporal structure function from which we extract AA-coherence time. The signals from each sub-pupil are divided by the signal which integrates the global flux of the pupil plane; this is similar to a flat-field correction in the image plane. In Fig. 12, we present the daily evolution of measurements performed with the sub-pupil of 1 mm diameter on 2014 October 31. We can see that good observational conditions with higher AA-coherence times are in the early morning, and it degrades with time. This degradation is due to the temperature gradient which generates strong turbulence near the ground. Fig. 13 shows the histogram of measured AA-coherence time values using signals of a sub-pupil of 0.5 mm diameter from 2014 September to 2015 August (about 14 000 measurements). The obtained mean value is 5.34 ms, while the standard deviation is 2.6 ms. This verify a posteriori that our 2000 samples recorded at a rate of one image every 30 ms can be considered as uncorrelated. From the other sub-pupils, the obtained mean values are 5.3 ± 3.2 , 7.5 ± 3.2 and 9.2 ± 3.9 ms for the 0.5, 1 and 2 mm sub-pupils, respectively. The measured AA-coherence time is effectively expected to be a function of diameter of the pupil for given wind speed and outer scale (Ziad et al. 2012).

From equation 10 of Ziad et al. (2012), our measured mean values of the AA-coherence time for the different sub-pupils are compatible within one standard deviation with an average wind speed of about 2.8 ms^{-1} (for a wind direction $\gamma = \frac{\pi}{4}$) and a mean value of 5 m for the outer scale.

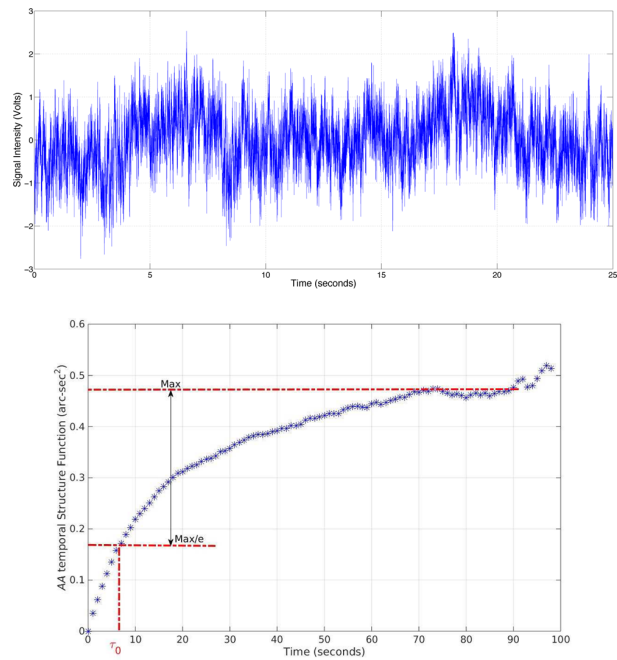


Figure 11. Example of AA-temporal structure function obtained with pupil-plane observation way. The signal was acquired by the 1 mm diameter fibre and its electronics on 2013 June 12.

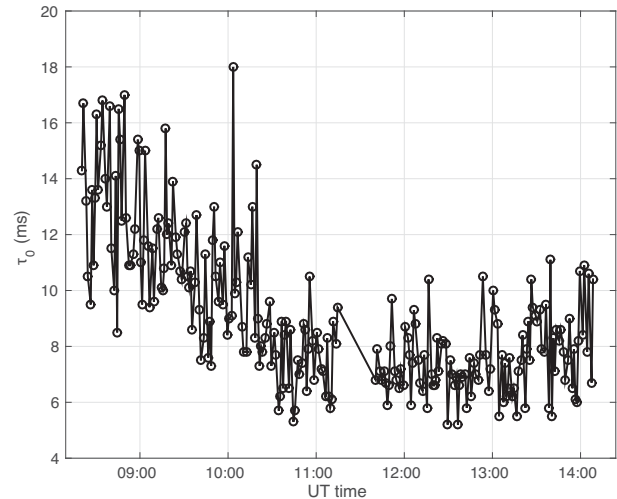


Figure 12. Evolution of measured AA-coherence time on 2014 October 31.

We note that the measured AA-coherence time is different from the coherence time introduced by Roddier, Gilli & Lund (1982) which is the phase coherence time. We could evaluate the Roddier's coherence time either knowing the wind speed profile which is usually given by balloon flights or using the method given by Ziad et al. (2012) which consists in retrieving wind speed from their equation 10 and then use the ratio between the Fried parameter and the wind speed, times a factor 0.31, to estimate the phase coherence time. This supposes that the Fried parameter, the spatial coherence outer scale and the wind speed following the x -direction are known. The mean values of the AA-coherence times given above and the mean values obtained for the spatial parameters (next section) are

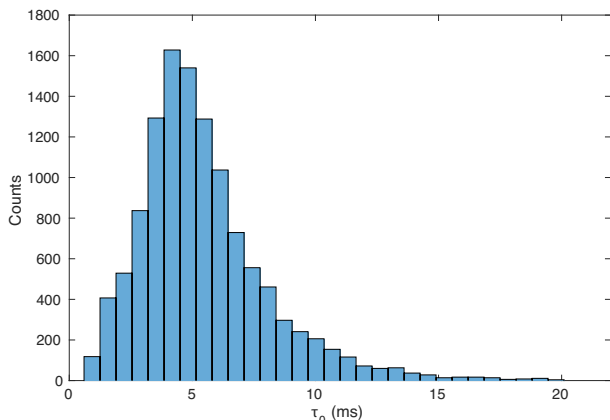


Figure 13. AA-coherence time measurements made by the pupil-plane observation way (0.5 mm sub-pupil) from 2014 September to 2015 August (about 14 000 measurements).

compatible with a phase coherence time ranging between 2.7 and 4.7 ms (for a wind direction $0 \leq \gamma \leq \frac{\pi}{2}$).

5.2 Spatial parameters of turbulence

First we show in Fig. 14 an example of non-linear fitting of structure functions obtained on 2014 October 24 from the image-plane observation way. The error bars represent the statistical error which depends on the considered angular separation and the total number of images; the maximal relative statistical error is about 1.5 per cent corresponding to the maximal angular separation. Other errors may contribute to the total error on the structure function estimation such as the error due the curvature of the limb and the CCD readout noise but they are found negligible as for the MOSP instrument at night (Maire et al. 2007). Assuming the Von Kàrmàn multilayer turbulence model (equation 4), we retrieved the $C_n^2(h)$ and $L_0(h)$ profiles together. For the inversion purpose, the choice of the initial parameters (profiles) and resolution are important to ensure convergence. Like in our two-layer simulation (Section 4), the inverse problem with multiple layers is ill-posed in the sense that several solutions, i.e. $C_n^2(h)$ and $L_0(h)$ profiles, are able to reproduce equally well the observed structure function within its error bars. We have tested the

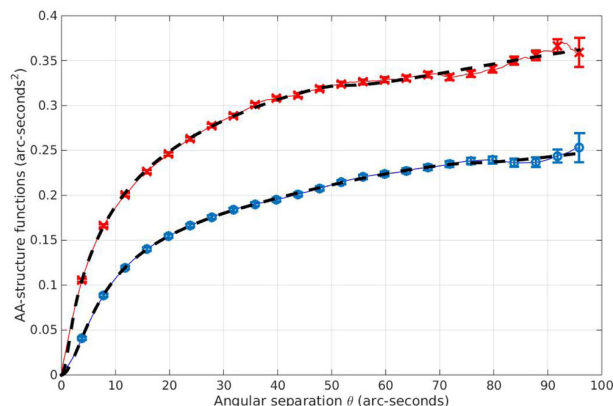


Figure 14. Experimental structure functions obtained on 2014 October 24 at 08:27 UT (red crosses) and 08:11 UT (blue circles). The non-linear curve fitting (dashed lines) allowed us to extract spatial parameters.

inversion starting with a constant value for the C_n^2 profile but keeping the L_0 one close to the solution. In this case, we are still able to converge to the solution for $C_n^2(h)$. On the other hand, doing the opposite ($L_0(h)$ constant and $C_n^2(h)$ close to its solution) or starting with two constant profiles does not allow us to converge to the solution. Here an a priori is introduced by starting the procedure with parametric models for realistic daytime turbulence profiles $C_n^2(h)$ and $L_0(h)$. For $C_n^2(h)$, we started the inversion process using the Hufnagel–Valey model (Hufnagel 1974; Valey 1980):

$$C_n^2(h) = 0.00594 \left(\frac{V}{27} \right)^2 (10^{-5}h)^{10} \exp \left(-\frac{h}{1000} \right) + 2.710^{-16} \exp \left(-\frac{h}{1500} \right) + A \exp \left(-\frac{h}{100} \right), \quad (25)$$

where h is the altitude (in m), V is the rms wind speed at high altitude taken equal to 21 m s^{-1} and A is a constant defining the turbulence strength at ground level; it is taken equal to $1.7 \times 10^{-14} \text{ m}^{-2/3}$ for daytime turbulence.

For the outer scale profile $L_0(h)$, we started the inversion process using the model proposed by Coulman et al. (1988):

$$L_0(h) = \frac{4}{1 + \left(\frac{h-8500}{2500} \right)^2}. \quad (26)$$

Fig. 15 presents the profiles obtained from the structure functions of Fig. 14, and integrated parameters using equations (11) and (12) are $r_0 = 7.9 \text{ cm}$, $\mathcal{L}_0 = 6.2 \text{ m}$ for the first one (blue curve) and $r_0 = 5.5 \text{ cm}$, $\mathcal{L}_0 = 6.1 \text{ m}$ for the second one (red curve). We notice that most of the turbulence is localized in the surface layer; this is due to air heating by the solar rays near the ground. For ground layers and a telescope diameter of 25 cm, simulations show that there is a limit around $L_0 = 4 \text{ m}$ above which the instrument is not sensitive. In other words, for greater values of L_0 in the ground layers, the observed structure function will not change significantly in the range 0–96 arcsec sensed by MISOLFA. This implies that the integrated values obtained should be considered as lower limits only. If we fix the L_0 profile, then the inverse problem of retrieving the C_n^2 profile (equation 4) becomes linear and we can compute the optimal resolution kernels (Backus & Gilbert 1968) for realistic uncertainties on the observed structure function. This provides intrinsic resolution of the inverse problem for a given L_0 profile and clearly shows that MISOLFA can provide information up to at least 20 km with a resolution ranging from about 2 km at an altitude of 2 km up to 6 km at an altitude of 20 km. For lower layers, the resolution reachable on the C_n^2 profile will be more sensitive to the real L_0 profile. This led us to choose an altitude sampling step of 100 m in this region of the atmosphere and a relatively higher sampling (1 km) in the free atmosphere. In a future work, we plan to test the use of an iterative process that would adapt the number of layers at each step as the L_0 profile evolves.

As described in Section 3.2.2, spatial parameters from pupil plane can also be estimated. For that a calibration of pupil intensity fluctuations (in volts) according to AA-fluctuations (in arcseconds) is needed. In Fig. 16, we present the correlation between the two entities. A linear fit leads to a calibration of intensity fluctuations in arcseconds. Each signal from the sub-pupils is calibrated separately because each acquisition channel has its own amplification device with different gains and offsets. This calibration is made every time the gains are changed. The resulting signals are used to estimate spatial parameters.

To compare estimated parameters between image and pupil planes, we show first in Fig. 17 daily evolution of simultaneous

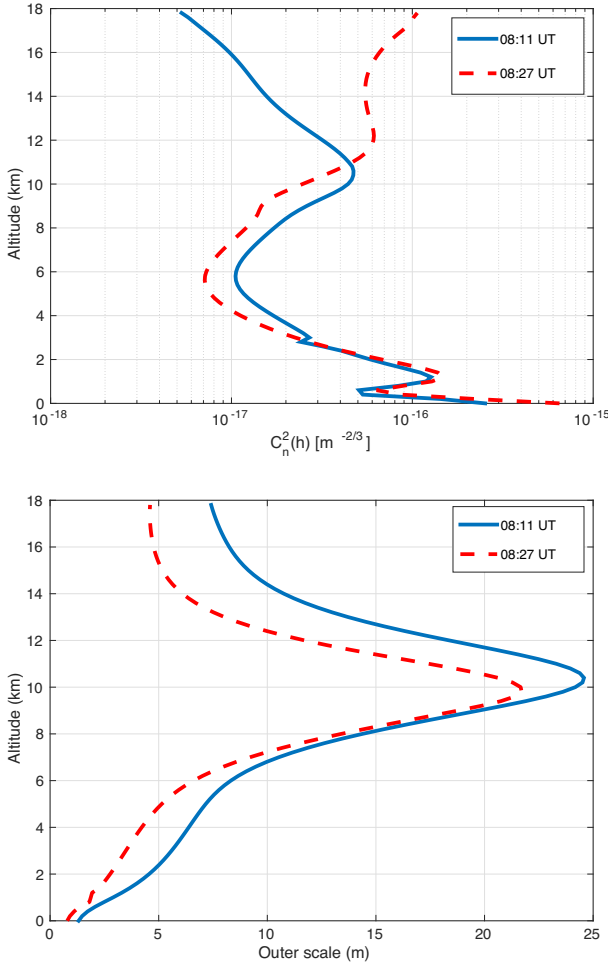


Figure 15. $C_n^2(h)$ and $L_0(h)$ profiles retrieved from structure functions obtained on 2014 October 24.

r_0 measurements from the pupil and image planes. The estimations from image motion (black circles) are obtained considering the Von Kàrmàn model (equation 15). The values of L_0 are retrieved from the integration of the $L_0(h)$ profiles weighted by the $C_n^2(h)$ profiles (equation 12). Fig. 18 represents the latter outer scale estimations and simultaneously estimations from pupil plane by a numerical resolution of equation (19). The mean values from the two curves are 11.2 ± 5.1 and 8.3 ± 7.0 m for the outer scale values from the image and pupil planes, respectively. These estimates are in good agreement and give the same order of outer scale values.

One can notice that pupil-plane observations are in good agreement with estimations from integrated $C_n^2(h)$. We can also see that good seeing conditions are observed early in the morning. We believe that most reliable from these estimations is made from pupil plane because it is based on a differential estimation method. But its disadvantage is that it is sensitive to noise in the sub-pupils (0.5 mm) used during the estimation and because of filtering due to the slit (see Section 2.2), there is a limitation in observed atmospheric perturbation and so Fried parameter estimation. In Fig. 17, we can see that the estimations from image motion give lower values compared to the two other estimations. This is because it is based on the variance which is overestimated in the presence of drift (or drift residuals after some corrections). On the other hand, this estimation

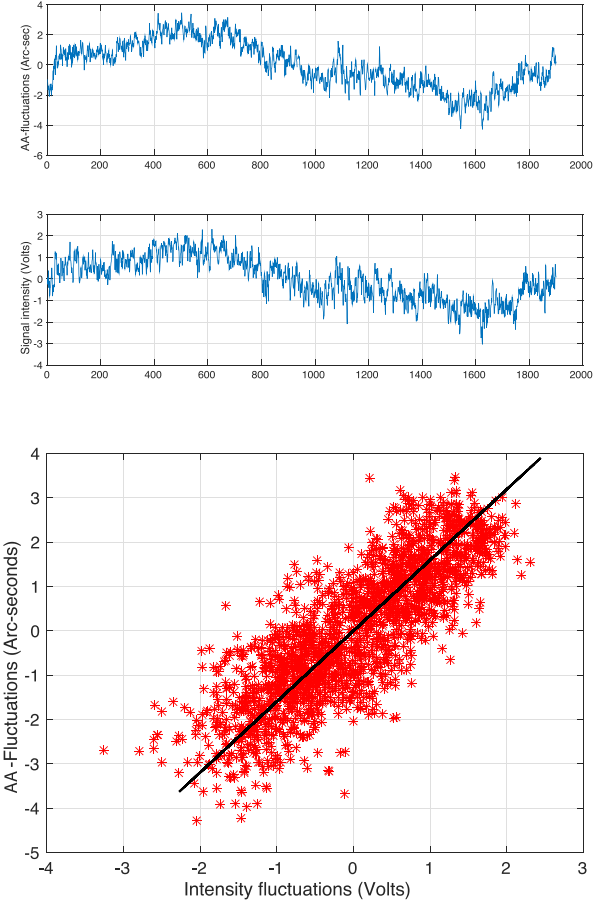


Figure 16. Correlation between temporal evolution of AA-fluctuations from solar limb in image plane (top), as a function of pupil-plane temporal signal (bottom). The data were recorded on 2014 October 24; the pupil signal was obtained with the sub-pupil of 1 mm diameter.

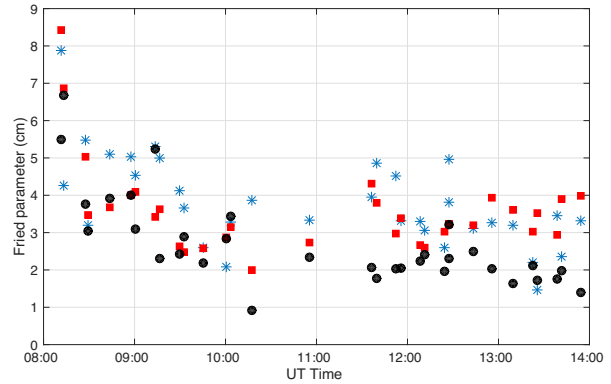


Figure 17. Fried parameter measurements from the pupil plane (red squares), image agitation (black circles) and from integrated $C_n^2(h)$ profiles (blue stars) of the image-plane observation way on 2014 October 24.

method uses an outer scale value retrieved from profiles. For the inversion technique, because we have to retrieve the two profiles ($C_n^2(h)$ and $L_0(h)$) together, the solution is not unique and can give different values of integrated parameters. Indeed, we simulated a structure function with the profiles of equations (25) and (26) in

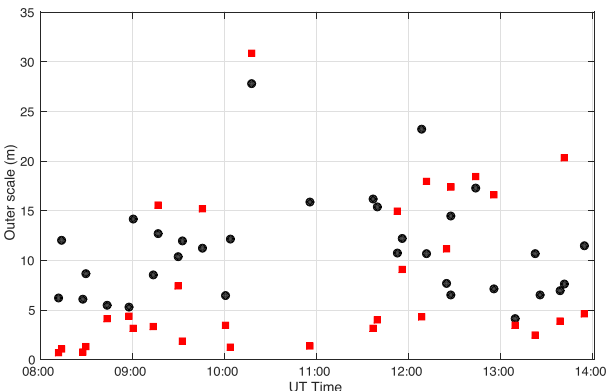


Figure 18. Outer scale measurements from the pupil plane (red squares) and from the integration of the $L_0(h)$ profiles (black circles) of the image plane; observations were performed on 2014 October 24.

order to test the inversion procedure. It gives good results (close to input parameters), but a small variation in retrieved profiles gives slightly different values of integrated parameters. Also the use of different resolutions in altitude gives similar profiles but different values of integrated parameters. Maire et al. (2007) did the same thing in order to test the simulated annealing inversion technique and concluded that the results are more reliable when unknowns are only $L_0(h)$.

Considering the pupil-plane observation way, we evaluated the mean values of the spatial parameters over one year of observations. We obtained a median value of Fried parameter of 3.3 cm, while the outer scale median value is about 6.3 m. The mean Fried parameter estimated using MISOLFA image way over 2 years has already been used for the solar ground-based astrometric measurements carried at Calern Observatory (Meftah et al. 2014, 2015). At this time, only the image way was operating. In the present work, we obtain similar values for the Fried parameter and our results are further validated by analysing also the pupil way of the instrument.

We have demonstrated that we have the capacity with MISOLFA not only to estimate the integrated values but also the $C_n^2(h)$ and $L_0(h)$ profiles. Simulations have shown that this approach could give even better results than fitting the structure function for the integrated parameters. When confronted to the observations, this approach is however less robust and it is hard to assure good convergence in all conditions. A calibration with another instrument would help to fully exploit this additional capacity of retrieving these profiles.

6 CONCLUSION

A generalized daytime turbulence monitor is presented in this paper allowing estimation of both spatial and temporal parameters of optical turbulence. It is based on the statistics of AA-fluctuations observed in both image and pupil planes. On top of what would give the use of SHABAR and S-DIMM instruments (r_0 , $C_n^2(h)$), we are able, with a single instrument, to estimate the outer scale and characteristic time of turbulence. This is an important new tool for site testing and for real-time atmospheric monitoring during high-resolution ground-based solar observations. It has been shown by both numerical simulations and from real data that Fried parameter for daytime observations can be deduced from AA-fluctuation variance considering the Von Kàrmà̄n model and introducing a finite

value of outer scale. This confirms the theoretical results obtained by Borgnino et al. (1992).

Using a grid ranging from 100 m in the planetary layer up to 1 km in the free atmosphere, we have also shown from both simulations and real data that MISOLFA allows us to retrieve the atmospheric structure constant $C_n^2(h)$ and outer scale $L_0(h)$ profiles. First simultaneous estimated profiles obtained from observations made in 2014 October are presented, and we have shown that the integrated parameters deduced from these profiles are compatible with the ones deduced for the variance of the limb motion if one takes into account a finite value of outer scale.

We presented the first fully calibrated measurements from the pupil-plane observation way after many improvement in the data quality, data acquisition systems and telescope guiding. Using its pupil-plane observation way, we obtained an estimation of turbulence AA-coherence time $\tau_{0\text{AA}}$ and its statistic over one year. We obtained a mean value of about 5 ms with larger values up to 18 ms typically obtained in early morning.

The spatial parameters r_0 and L_0 at 535 nm have also been deduced from the use of two sub-pupils and have been found in good agreement with the measurements made directly in the image plane. This good agreement found between the image- and pupil-plane observation ways constitutes a first internal calibration of the instrument not available on other systems. It also validates our parameter extraction procedures. We have shown from simulations that retrieving first the profiles $C_n^2(h)$ and $L_0(h)$ from the structure function and then integrating them to retrieve the integrated parameters is the most reliable procedure. We were able to apply it to real data acquired in good conditions and to successfully compare the results with the ones extracted from the pupil way. The inversion procedure to solve the integral equation remains however an ill-posed problem sensitive to the choices made for the initial parameters. Our conclusion, at this stage of our work, is that the most robust procedure is to use both observing ways to cross-validate our results concerning the spatial parameters of turbulence.

MISOLFA is a complex instrument, and some of its initial specifications have been made to allow testing various theoretical approaches of turbulence parameter extraction. The reflected images were not fully exploited because a coating stable in time could be obtained only with a ratio between the direct and reflected intensities less than initially specified. Since the two limbs coming from the two sides of the solar disc are separated by more than 1900 arcsec, we could use them to compute a structure function with large separation allowing in principle to reach the saturation even for the low-altitude layers. The use of the different size sub-pupils to estimate the outer scale via equation (23) was not successful probably because their differences in size were probably not large enough. The ratio between covariance and variance for two sub-pupils of the same size however gives results in good agreement with results from the image way. Finally, we note that we have not used the slit wheel, the purpose of which was to allow us to test different filterings in the pupil way. We needed to accumulate data without changing the configuration and the initial slit choice revealed itself appropriate. If not filtered, instrument vibrations could be interpreted as a signal coming from the turbulence and therefore bias the results. An efficient method to correct from vibrations is the use of differential observations (case of the DIMM and PML). In MISOLFA, the same is made in the pupil plane where we look at the correlations between intensity fluctuations coming from two sub-pupils both normalized by the global flux. In this way, the vibrations should not affect the measurements. In the image way however, the vibrations are not taken into account. This, in principle, could have been achieved by

looking at the two opposite limbs which are affected in the same way. But again, the poor signal-to-noise ratio of the reflected limb image prevented us to apply this method at this stage. An alternative could be to measure the vibrations with accelerometers and filter their frequencies which are expected to lie in the lower part of the absolute motion spectrum (below 1 Hz; Martin 1987). Part of the differences sometimes obtained between the image and pupil ways may come from these different sensitivities to vibrations.

The two observing ways of MISOLFA are now fully operational in their actual configuration. Our results could however still be consolidated and probably improved by calibrating it with other instruments such as S-DIMM or with similar instruments such as MOSP or PML with adaptation for solar observations. A simultaneous measurement of vertical distribution of temperature and wind speed with altitude using balloon flight would also be useful. Measurement of structure constant of temperature fluctuations ($C_T^2(h)$) coupled with mean values of temperature and pressure distribution with altitude would lead to an independent estimate of the energy distribution $C_n^2(h)$ and the size of the isoplanatic patch θ_0 (Roddier 1981). Furthermore, the wind speed distribution would give access to phase coherence time.

In a future work, we intend to cross-calibrate MISOLFA with other turbulence monitors in order to further consolidate our results not only for the temporal variation of the turbulence parameters but also for their fully calibrated absolute values.

ACKNOWLEDGEMENTS

We thank the anonymous referee for careful and helpful advice and comments. This work is dedicated to the memory of Francis LA-CLARE who was at the origin of the ground based solar astrometry program at Calern Observatory. This project is supported by the Centre National des Etudes Spatiales (CNES) and the Programme National Soleil-Terre (PNST).

REFERENCES

- Acton D. S., 1995, *Appl. Opt.*, 34, 4526
 Assus P., Borgnino J., Martin F., Bouzid A., Chibani M., Irbah A., Seghouani N., 2002, in Vernin J., Benkhaldoun Z., Muñoz-Tuñón C., eds, ASP Conf. Ser. Vol. 266, Astronomical Site Evaluation in the Visible and Radio Range. Astron. Soc. Pac., San Francisco, p. 134
 Avila R., Ziad A., Borgnino J., Martin F., Agabi A., Tokovinin A., 1997, *J. Opt. Soc. Am.*, 14, 11
 Beckus G. E., Gilbert F., 1968, *Geophys. J. R. Astron. Soc.*, 16, 169
 Beckers J. M., 1999, in Schmieder B., Hofmann A., Staude J., eds, ASP Conf. Ser. Vol. 184, Third Advances in Solar Physics Euroconference: Magnetic Fields and Oscillations. Astron. Soc. Pac., San Francisco, p. 309
 Beckers J. M., 2001, *Exp. Astron.*, 12, 1
 Beckers J. M., Mason J., 1998, *Proc. SPIE*, 3352, 858
 Beckers J. M., Liu Z., Jin Z., 2003, *Proc. SPIE*, 4853, 273
 Berdja A., 2007, PhD thesis, Univ. Nice Sophia-Antipolis
 Berdja A., Irbah A., Borgnino J., Martin F., 2004, *Proc. SPIE*, 5237, 238
 Berkefeld T. et al., 2010, *Proc. SPIE*, 7733, 773341
 Borgnino J., 1978, PhD thesis, Univ. Nice Sophia-Antipolis
 Borgnino J., 1990, *Appl. Opt.*, 29, 1863
 Borgnino J., Martin F., 1977, *J. Opt. (Paris)*, 8, 319
 Borgnino J., Martin F., 1978, *J. Opt. (Paris)*, 9, 15
 Borgnino J., Ceppatelli G., Ricort G., Righini A., 1982, *A&A*, 107, 333
 Borgnino J., Martin F., Ziad A., 1992, *Opt. Commun.*, 91, 267
 Borgnino J., Berdja A., Ziad A., Maire J., 2007, in Cherubini T., Businger S., eds, Proc. Symp. on Seeing
 Bouzid A., Irbah A., Borgnino J., Lantéri H., 2002, in Vernin J., Benkhaldoun Z., Muñoz-Tuñón C., eds, ASP Conf. Ser. Vol. 266, Astronomical Site Evaluation in the Visible and Radio Range. Astron. Soc. Pac., San Francisco, p. 64
 Conan R., 2000, PhD thesis, Univ. Nice Sophia-Antipolis
 Conan R., Borgnino J., Ziad A., Martin F., 2000, *J. Opt. Soc. Am. A*, 17, 1807
 Coulman C. E., Vernin J., Coquegniot Y., Caccia J. L., 1988, *Appl. Opt.*, 27, 155
 Djafer D., Irbah A., 2012, *Sol. Phys.*, 281, 863
 Fried D. L., 1965, *J. Opt. Soc. Am. A*, 56, 1372
 Fried D. L., 1975, *Radio Sci.*, 10, 71
 Gao B. C., 1993, *Remote Sens. Environ.*, 43, 23
 Hestroffer D., Magnan C., 1998, *A&A*, 333, 338
 Hufnagel R. E., 1974, ‘Variations of atmospheric turbulence,’ in Optical Propagation through Turbulence, OSA Technical Digest Series, Optical Society of America, Washington, D.C., Paper WA1
 Ikhlef R. et al., 2012a, in Faurobert M., Fang C., Corbard T., eds, EAS Publ. Ser. Vol. 55, Understanding Solar Activity: Advances and Challenges, p. 369
 Ikhlef R. et al., 2012b, *Proc. SPIE*, 8444, 84446C
 Irbah A., Borgnino J., Laclare F., Merlin G., 1994, *Sol. Phys.*, 149, 213
 Irbah A. et al., 2010, *Proc. SPIE*, 7735, 77356F
 Irbah A. et al., 2011, *Proc. SPIE*, 8178, 81780A
 Kawate T., Hanaoka Y., Ichimoto K., Miura N., 2011, *MNRAS*, 416, 2154
 Kellerer A., Gorceix N., Marino J., Cao W., Goode P. R., 2012, *A&A*, 542, A2, 10
 Laclare F., 1983, *A&A*, 125, 200
 Lakhal L., Irbah A., Bouzaria M., Borgnino J., Laclare F., Delmas C., 1999, *A&AS*, 138, 155
 Liu Z., Beckers J. M., 2001, *Sol. Phys.*, 198, 197
 Maire J., Ziad A., Borgnino J., Martin F., 2007, *MNRAS*, 377, 1236
 Martin H. M., 1987, *PASP*, 99, 1360
 Martin F., Tokovinin A., Agabi A., Borgnino J., Ziad A., 1994, *A&AS*, 108, 173
 Meftah M. et al., 2014, *A&A*, 569, A60
 Meftah M. et al., 2015, *ApJ*, 108, 173
 Morand F., Delmas C., Corbard T., Chauvineau B., Irbah A., Fodil M., Laclare F., 2010, *C. R. Phys.*, 11, 660
 Moussaoui R., Irbah A., 2000, *Ap&SS*, 273, 25
 Nakajima T., 1988, *J. Opt. Soc. Am. A*, 5, 1477
 Roddier F., 1981, Progress in Optics, Vol. 19. North-Holland, Amsterdam, p. 281
 Roddier F., Gilli J. M., Lund G., 1982, *J. Opt. (Paris)*, 13, 263
 Sarazin M., Roddier F., 1990, *A&A*, 227, 294
 Scharmer G. B., van Werkhoven T. I. M., 2010, *A&A*, 513, A25
 Schmidt J. D., 2010, Numerical Simulation of Optical Wave Propagation. SPIE, Bellingham
 Schmidt D., Berkefeld T., Heidecke F., Fischer A., von der Lühe O., Soltau D., 2014, *Proc. SPIE*, 9148, 1
 Seghouani N., Irbah A., Borgnino J., 2002, in Vernin J., Benkhaldoun Z., Muñoz-Tuñón C., eds, ASP Conf. Ser. Vol. 266, Astronomical Site Evaluation in the Visible and Radio Range. Astron. Soc. Pac., San Francisco, p. 36
 Valev C. G., 1980, *Appl. Opt.*, 19, 574
 Ziad A., Borgnino J., Martin F., Agabi A., 1994, *A&A*, 282, 1021
 Ziad A., Conan R., Tokovinin A., Martin F., Borgnino J., 2000, *Appl. Opt.*, 39, 30
 Ziad A., Borgnino J., Dali-Ali W., Berdja A., Maire J., Martin F., 2012, *J. Opt.*, 14, 8
 Ziad A. et al., 2013, in Esposito S., Fini L., eds, Proc. Third AO4ELT Conf.

This paper has been typeset from a TeX/LaTeX file prepared by the author.

II.3 L'analyse des images

Avant les calibrations géométriques et traitements nécessaires pour extraire l'information sur le rayon solaire et son éventuelle évolution, il y a des étapes indispensables de calibration radiométrique à accomplir pour les images CCD : soustraction du courant d'obscurité et division par une carte de champ plat (Flat-Field). Ces étapes sont apriori standards mais elles ont cependant nécessité de longs mois pour être opérationnelles dans notre cas. Ces étapes ne sont pas détaillées dans les publications et je les présente ici. De même je présente ensuite le détail de la procédure de correction de réfraction. Les détails de l'analyse plus spécifique pour l'extraction de l'information sur le rayon et son évolution (correction de distorsion, calibrations stellaires pour l'évolution du facteur d'échelle, correction des biais introduit par la turbulence, prise en compte de la qualité des images, etc..) sont détaillés dans la publication (Meftah, Corbard, et al. 2014) reproduite au paragraphe II.4.

II.3.1 Calibrations radiométriques

- **Courant d'obscurité.**

Le CCD utilisé pour SODIM-2 est du même type que ceux utilisés par COROT (CCD à transfert séparé en deux matrices distinctes) mais présente des défauts importants.

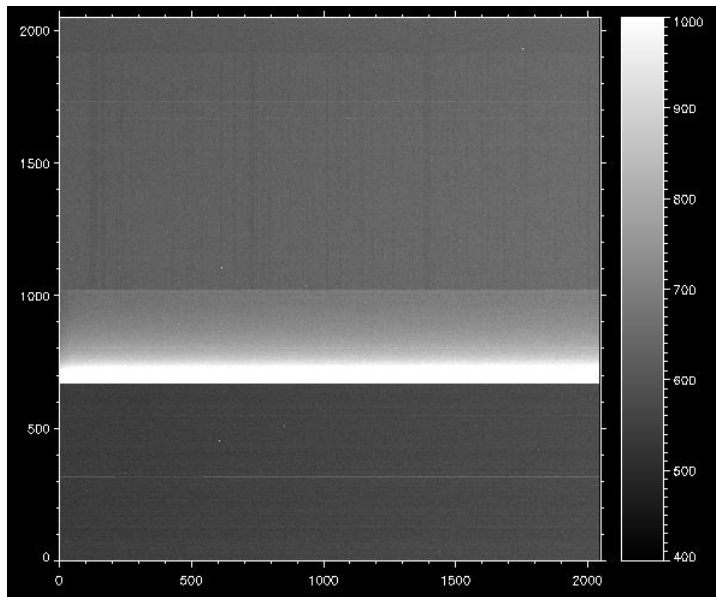


Figure 27. Exemple d'image de courant d'obscurité du CCD de SODISM2. Les lignes 0-1023 correspondent au premier CCD et lignes 1024-2047 au second. Les lignes 675-679 sont défectueuses et toute la zone supérieure du premier CCD est très affectée avec un fort courant d'obscurité et une sensibilité réduite. Un gradient horizontal est visible qui correspond au fait qu'il s'agit d'un CCD à transfert, les photoélectrons de la zone exposée sont transférés vers la zone mémoire de droite à gauche.

Une zone de quelques lignes complètement défectueuses est suivie d'une zone dite 'chaude' très étendue dans laquelle la sensibilité du courant d'obscurité aux variations de température est très importante (Figure 27). De plus les offsets entre les deux parties du CCD estimés par la médiane des zones d'overscan n'est pas directement utilisable. Ainsi la simple correction par les offsets fournis par le système et la soustraction d'une image moyenne de courant d'obscurité s'est avérée complètement insuffisante pour nos objectifs. Suivant les travaux de Hochedez et al. (2014) sur le courant d'obscurité de SODISM à bord PICARD nous avons donc développé un modèle de courant d'obscurité de notre CCD en y ajoutant une dépendance en température car la régulation au sol n'est pas aussi bonne que dans l'espace. Une base de carte du courant d'obscurité pour différentes températures du CCD est maintenue et un processus d'optimisation cherche la meilleure combinaison linéaire de cartes pour corriger chaque image. La meilleure façon d'estimer l'offset s'est avérée être d'assurer la continuité de la fonction d'assombrissement centre-bord solaire sur tous les pixels de la colonne interface entre les deux sous CCD.

- **Les cartes de champ plat (Flat-Field)**

L'idée initiale pour la construction de ces cartes était de suivre la procédure consistant à prendre une série d'images solaires pleines décalées pour pouvoir comparer la réponse de différents pixels à la même source (Kuhn, Lin et Loranz 1991). Au sol cela suppose cependant que les conditions atmosphériques soient stables durant toute la séquence. Avec un système d'acquisition ne pouvant pas acquérir plus d'une image par minute, obtenir une séquence exploitable d'image décentrées pour chacun des 6 filtres de SODISM-2 nécessite alors d'utiliser complètement les meilleures journées d'observation pour ces séquences de calibration. De plus, en principe, il est important de renouveler régulièrement ces calibrations pour prendre en compte toute évolution dans le temps des filtres ou de tout autre élément du système optique. Nous avons donc profité du fait qu'il existe une oscillation en alpha et des sauts en delta, résultants probablement de défauts moteurs ou d'équilibrage du télescope dans sa cuve, pour exploiter le décentrage naturel de nos séquences d'images. Des « cartes de contraste » sont construites en ajustant à chaque image une fonction théorique d'assombrissement centre bord puis en divisant les images par la fonction ajustée. La médiane des différentes cartes de contrastes donne ensuite une estimation du Flat-Field en assurant que les zones d'activité, qui donnent un signal loin de la médiane, ne perturbent pas le résultat. Cette procédure nous permet de ne pas jouer de séquences spéciales pour la calibration, nous exploitons les séquences d'images elles-mêmes avec leur défaut de centrage. Cela nous permet aussi de mettre à jour régulièrement les cartes de champ plat en

exploitant les meilleures images chaque jour pour actualiser la carte médiane (Figure 28).

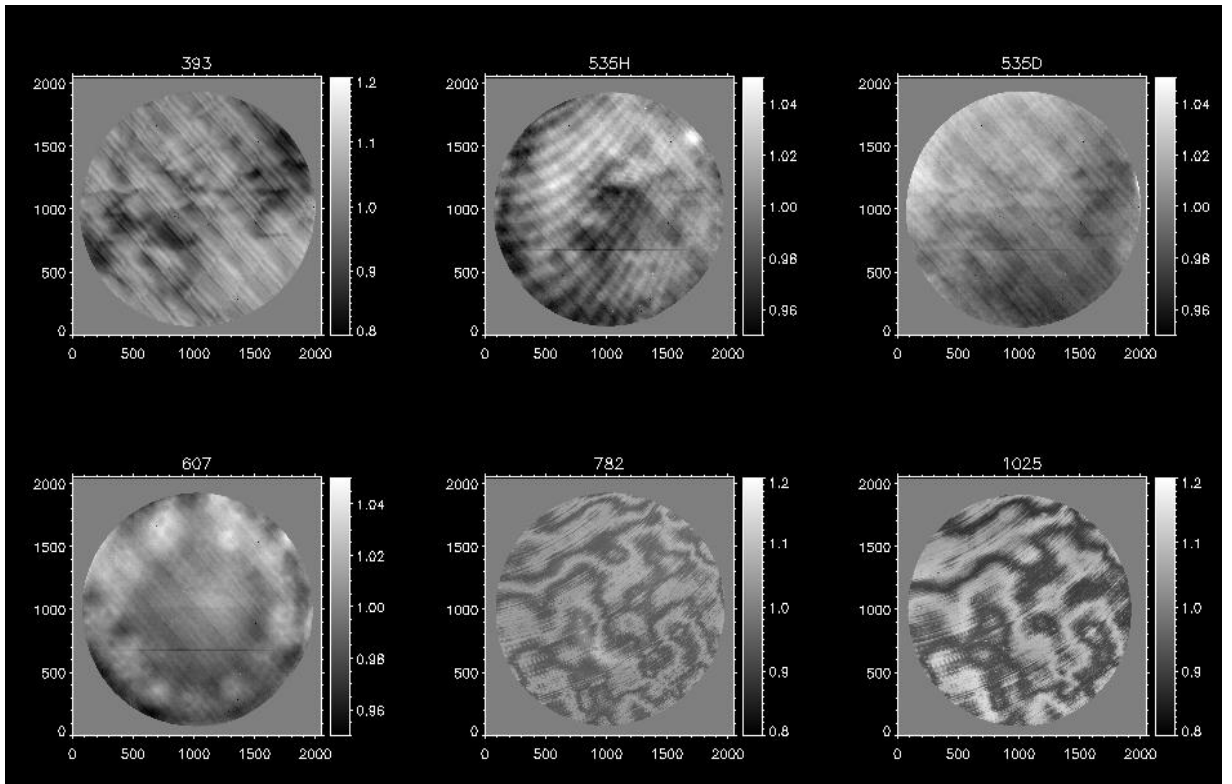


Figure 28. Les cartes de champ plat (Flat Field) obtenues pour chaque filtre de SODISM-2 par une méthode développée spécifiquement pour SODISM2 (voir texte).

- **Le traitement des lignes défectueuses (Image Inpainting)**

Nous ne pouvons pas inventer l'information qui n'a pas été enregistrée. Cependant nous pouvons voir plusieurs intérêts à ne pas laisser une bande noire dans nos images. Un intérêt esthétique, non scientifique, tout d'abord. Notamment lorsque nous voulons créer des séquences animées d'images. Les images étant recentrées et tournée (de l'angle P) pour que le nord solaire soit toujours en haut, l'existence d'une bande sombre constante dans le référentiel du CCD se traduit par une bande variable et pivotante sur l'animation. Cela capte toute l'attention au détriment de ce que voulait montrer l'animation sur le reste de l'image. Mais il y aussi un intérêt scientifique. Les lignes manquantes vont impacter l'analyse scientifique. Nous pouvons prendre deux exemples :

- Les lignes défectueuses traversent parfois des zones d'activité telles que les taches ou les plages visibles notamment sur les images Ca II. Si nous essayons d'utiliser un algorithme de segmentation pour identifier ces structures, les discontinuités géométriques introduites par la zone défectueuse vont impacter le résultat. Il en serait de même pour la détection de filaments sur une image H-alpha par exemple.

- Si nous voulons faire une analyse statistique ou spectrale de tout ou partie de l'image, les lignes défectueuses vont introduire des artefacts et ces analyses vont devoir traiter l'échantillonnage irrégulier qu'elles produisent.

Dans un premier temps nous avons simplement rempli les lignes défectueuses en faisant une interpolation colonne par colonne. Le résultat est visuellement satisfaisant mais probablement pas exploitable scientifiquement. Récemment nous avons testé une méthode de restauration (image inpainting) par continuité des isophotes et qui préservent les propriétés statistiques de la zone restaurée par rapport aux zones adjacentes. Ces deux propriétés sont a priori adaptées aux deux cas d'exploitation scientifique évoqués plus haut. Les premiers tests montrent de plus que cette approche est visuellement supérieure à la simple interpolation notamment lorsque le contraste de l'image est faible.

Une illustration du résultat de l'application de ces trois corrections est donnée sur la Figure 29. Depuis mai 2011 environ 140 000 images pleines du Soleil dans 5 longueurs d'onde (393.37, 535.7 607.1, 782.2, 1025.0 nm) ont été acquises, traitées en suivant cette procédure, et distribuées (via le serveur local à l'OCA et MEDOC).

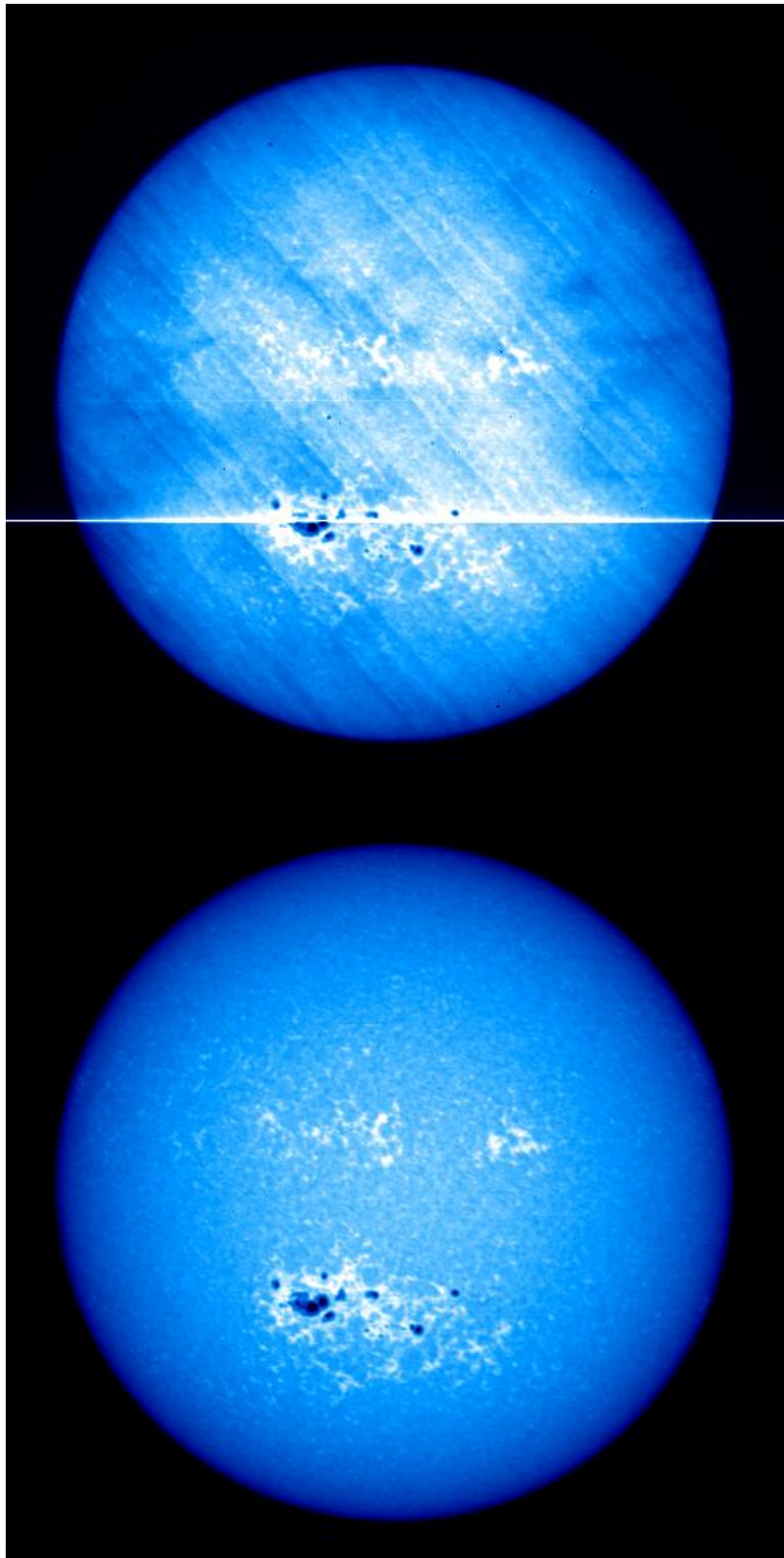


Figure 29. Image SODISM-2 à 393.7 nm (Ca IIK) acquise le 29/01/2016 à 10 :54 UTC.
En haut : image brute. En bas : Image corrigée.

II.3.2 Correction de la réfraction astronomique (article)

ARTICLE : On the importance of astronomical refraction for modern Solar astrometric measurements (Corbard, Morand, et al. 2013)

La réfraction astronomique a pour effet de changer la hauteur apparente des astres. Cela se traduit de manière très visible par le fait que nous observions encore le soleil alors qu'il est physiquement entièrement sous l'horizon et par l'apparence aplatie du disque solaire à l'horizon. Aux distances zénithales plus faibles l'effet diminue mais doit être pris en compte pour des mesures astrométriques à la précision que nous cherchons (la dizaine de mas). Pour les mesures astrolabe, le temps de passage de chaque bord du Soleil est mesuré à hauteur constante. Seule la réfraction différentielle due aux changements de conditions atmosphériques (température, pression) entre les deux instants de mesure sont donc à prendre en compte. Pour l'astrométrie par imagerie directe du disque entier, il n'en est pas de même et la forme du disque observé est potentiellement affectée par la réfraction si nous observons trop bas. Les conditions de turbulence étant parfois les meilleures quand le soleil est relativement bas nous avons voulu quantifier précisément cet effet. Nous avons rédigé une note détaillée, reproduite ci-dessous, pour la prise en compte de la réfraction astronomique lors de l'analyse des images pour l'astrométrie solaire.

On the importance of astronomical refraction for modern Solar astrometric measurements

T. Corbard¹, F. Morand¹, F. Laclare¹, R. Ikhlef^{1,2}, and M. Meftah³

¹ Laboratoire Lagrange, UMR7293, Université de Nice Sophia-Antipolis, CNRS, Observatoire de la Côte d'Azur, Bd. de l'Observatoire, 06304 Nice, France
 e-mail: Thierry.Corbard@oca.eu

² CRAAG, Observatoire d'Alger BP 63 Bouzarah Alger, Algérie

³ Laboratoire Atmosphères, Milieux, Observations Spatiales, CNRS, Université Paris VI & Université de Versailles Saint-Quentin-en-Yvelines, IPSL, F-78280 Guyancourt, France

March 31, 2013

ABSTRACT

Context. Several efforts are currently made from space missions in order to get accurate solar astrometric measurements i.e. to probe the long term variations of solar radius or shape, their link with solar irradiance variations and their influence on earth climate. These space missions use full disk solar imagery. In order to test our ability to perform such measurements from ground on the long term, we need to use similar techniques and instruments simultaneously from ground and space. This should help us to model and understand how the atmosphere affect ground based metrologic measurements. However, using full imagery from ground instead of the traditional astrolabe technique immediately raise the question of the effect of refraction and how well we can correct from it.

Aims. The goal is to study in details the influence of pure astronomical refraction on solar metrologic measurements made from ground-based full disk imagery and to provide the tools for correcting the measurements and estimating the associated uncertainties.

Methods. We use both analytical and numerical methods in order to confront commonly or historically used approximations and exact solutions.

Results. We provide the exact formulae for correcting solar radius measurements at any heliographic angle and for any zenith distance. We show that these corrections can be applied up to 80° of zenith distance provided that full numerical integration of the refraction integral is used. We also provide estimates of the absolute uncertainties associated with the differential refraction corrections and shows that approximate formulae can be used up to 80° of zenith distance for computing these uncertainties. For a given instrumental setup and the knowledge of the uncertainties associated with local weather records, this can be used to fix the maximum zenith distance one can observe depending on the required astrometric accuracy.

Key words. Atmospheric effects – Sun: fundamental parameters – Astrometry

1. Introduction

Ground based solar astrometric measurements have up to now been based on the so-called equal altitudes method (Débarbat & Guinot 1970). They have historically been made from transit instruments or astrolabes. Several instruments, derived from Danjon astrolabe, have been dedicated to solar diameter measurements, as DORaySol experiment (Morand et al. 2011). Observations consist in determining the transit times, through the same equal zenith distance circle, of the two solar limbs which are the extremities of a vertical solar diameter. Accuracy of these measurements is then mainly determined by datation accuracy and not by the optical resolution of the instrument. As the two limbs are observed at equal zenith distances, influence of astronomical refraction is inherently reduced (e.g. Laclare et al. 1996). Only the small climatic conditions variations (temperature, pressure, relative humidity) between the two crossings, distant from a few minutes of time, can still play a role. The main drawback of this method is that only vertical diameters can be determined.

Recent work in the field of solar metrology involve measurements from space using full disk solar images (Dame et al. 1999; Kuhn et al. 2012). PICARD-SOL (Meftah et al. 2013) is a ground based project that was set up at Calern observatory in

order to use the same technique simultaneously from ground and space and in order to inter-calibrate the different measurements. Using full disk imagery from ground raise however the question of the influence of astronomical refraction and how well we can correct for it.

The effect of atmospheric refraction is to change the true topocentric zenith angle z' of a celestial object to a lower observed one z . The refraction function $R(z)$ is defined by:

$$z = z' - R(z) \quad (1)$$

Alternatively, we may take the true angles as argument and define the associated refraction function $\bar{R}(z')$ by:

$$z = z' - \bar{R}(z') \quad (2)$$

If the refraction function $R(z)$ is known, the associated function $\bar{R}(z')$ can easily be evaluated for any true zenith distance z' by solving the non linear equation $x - R(z' - x) = 0$.

2. fundamental equations for astronomical refraction

From Snell's law of refraction applied to a spherical atmosphere, the curvature of a light path is linked to the local refractive index n through the so-called refractive invariant :

$$n r \sin(\xi) = \text{constant} \quad (3)$$

where ξ is the local zenith distance i.e. the angle between the light ray and the radius vector r from Earth center. From this, the differential refraction along the light ray is obtained by:

$$dR = -\tan \xi \frac{dn}{n} \quad (4)$$

In order to find the total amount of refraction at observer position, we can integrate along the full ray path from $n = n_{\text{obs}}$ and $\xi = z$ at observer position up to $n = 1$ outside the atmosphere.

$$R = \int_1^{n_{\text{obs}}} \tan \xi \frac{dn}{n} \quad (5)$$

This can be done either by direct numerical integration of Eq. (5) after an appropriate change of variable (Auer & Standish 2000) or by using a full ray-tracing procedure solving the system of coupled differential equations provided by Eq. (4) and the differentiation of Eq. (3) (van der Werf 2003, 2008). This, in principle, requires a model of the full atmosphere i.e. temperature, pressure, density etc..at any point through the light path. In the next section we recall why this is in fact not needed if we avoid areas close to the horizon and give some usual approximations of the refraction integral.

3. Approximation to the refraction integral

For zenith distance up to 70° , the refraction integral can be evaluated with good accuracy without any hypothesis about the structure of the atmosphere: it depends only on temperature and pressure at the observer (Oriani's theorem, see also: Ball 1908; Young 2004). This justifies that, over time, a large number of nearly equivalent approximate formulae have been derived that do not require the full knowledge of the structure of the real atmosphere. A development of the refraction integral into semi-convergent series of odd power of $\tan(z)$ is what is commonly found in textbooks (e.g. Ball 1908; Smart 1965; Woolard & Clemence 1966; Danjon 1980). An example of this will be given in Sect. 3.1. In fact the first two terms of such expansion (up to \tan^3) corresponds to what is known as Laplace formulae of which Fletcher (1931) said that *no reasonable theory differs by more than a few thousandths, hundredths, tenths of a second at $z = 60^\circ, 70^\circ, 75^\circ$ respectively*.

For large zenith distance, $\tan(z)$ power series will diverge at the horizon and are not appropriate. Closed formula valid at low zenith distance and that are finite at the horizon can however still be found (see e.g. Wittmann 1997). Assuming an exponential law for the variation of air density with height, it's possible for instance to derive a formula involving the error function (Fletcher 1931; Danjon 1980). Another example is Cassini's exact formula for an homogeneous atmosphere model. While physically un-realistic, the model of Cassini, thanks to Oriani's theorem, gives also excellent results up to at least 70° of zenith distance while remaining finite down to the horizon (Young 2004). For large zenith distances however, Young (2004) have shown that the lowest layers of the atmosphere and especially the lapse rate at observer becomes progressively dominant as one observe

closer to the horizon. This therefore should be included in atmospheric models and we can not avoid anymore the full numerical evaluation of the refraction integral.

In the following sub-sections we present first in details the refraction model as it was used for reducing solar astrolabe data at Calern observatory, then we give the full error function model from which the Calern model was actually derived and finally we recall Cassini's formula. In Sect. 5, these three approximations will then be compared to full numerical integration of the refraction integral using a standard atmosphere model.

3.1. Refraction model used at Calern observatory for Solar metrology

The refraction model that was used for the reduction of astrolabe measurements at Calern observatory is a truncation of the expansion in odd power of $\tan(z)$ (Danjon 1980). For an observer at geodetic latitude φ and altitude h above the reference ellipsoid, the refraction R is obtained as a function of the observed zenith angle, the wavelength (λ) and local atmospheric conditions i.e. pressure (P), absolute temperature (T), and relative humidity ($f_h \in [0, 1]$) by:

$$R(z, \lambda, P, T, f_h, h, \varphi) = \alpha(1 - \beta) \tan(z) - \alpha(\beta - \frac{\alpha}{2}) \tan^3(z) + 3\alpha(\beta - \frac{\alpha}{2})^2 \tan^5(z) \quad (6)$$

where

$$\alpha(T, P, f_h, \lambda) = n_{\text{obs}} - 1 \quad (7)$$

is the air refractivity for local atmospheric conditions and the given wavelength, and

$$\beta(T, h, \varphi) = \ell(T)/r_c(\varphi, h) \quad (8)$$

is the ratio between the height ℓ of the homogeneous atmosphere and the earth radius of curvature r_c at observer position. The homogeneous atmosphere has by definition a constant air density ρ equal to the one at observer position and its height is such that it would give the same pressure as the one recorded at observer position. Note that we do not assume here that the atmosphere is homogeneous, we just use the reduced height that can be obtained for any real atmosphere just from the pressure and density at observer. Assuming furthermore ideal gas law for dry air we have:

$$\ell(T) = \frac{P}{\rho g} = \frac{P_0}{\rho_0 g_0} \frac{T}{T_0}, \quad (9)$$

where $\rho_0 = 1.293 \text{ kg m}^{-3}$ for $T_0 = 273.15 \text{ K}$, $P_0 = 101325 \text{ Pa}$ and normal gravity $g_0 = 9.80665 \text{ ms}^{-2}$. The radius of curvature for Calern observatory ($\varphi = 43^\circ 45' 7''$, $h = 1323 \text{ m}$) was approximated by the minimum reference ellipsoid curvature at latitude 45° and sea level (Chollet 1981, see Appendix A):

$$r_c(45^\circ, 0) = 6367.512 \text{ km} \quad (10)$$

Ambient air refractivity was deduced from the refractive index $n_0(\lambda)$ under standard conditions and the partial pressure of water vapor p by applying the formula recommended by the first resolution of the 13th General Assembly of the International Union of Geodesy and Geophysics (IUGG 1963; Baldini 1963). After conversion to Pa (Pascal) as the pressure unit, the equation becomes:

$$\alpha(T, P, f_h, \lambda) = \frac{T_0}{T} \left\{ (n_0(\lambda) - 1) \frac{P}{P_0} - 4.13 \cdot 10^{-10} p(f_h, T) \right\} \quad (11)$$

Refractivity under standard condition (sea level, $T = T_0$, $P = P_0$, 0% humidity, 0.03% of carbon dioxide) was taken from the work of Barrel and Sears (1939):

$$n_0(\lambda) - 1 = \left\{ 2876.04 + \frac{16.288}{(10^6 \lambda)^2} + \frac{0.136}{(10^6 \lambda)^4} \right\} 10^{-7}. \quad (12)$$

Partial pressure of water vapor for the current temperature and relative humidity was deduced from a fit of water vapor pressure data published by the Bureau Des Longitudes (1975) for temperatures between -15°C and $+25^\circ\text{C}$. The resulting equation, converted to Pa, is (Chollet 1981):

$$p(f_h, T) = f_h 6.1075 10^2 e^{7.292 10^{-2}(T-T_0)-2.84 10^{-4}(T-T_0)^2} \quad (13)$$

Finally, we note that local atmospheric pressure P was measured from the height H (in mm) of a mercurial barometer and its temperature θ (in $^\circ\text{C}$). Taking into account corrections for local gravity (latitude and altitude) and for temperature (through the volume thermal expansion of mercury and the coefficient of linear thermal expansion of the tube), P was obtained by¹ (see Appendix B):

$$P = H \{ 1 - 2.64 10^{-3} \cos(2\varphi) - 1.96 10^{-7} h - 1.63 10^{-4} \theta \} \quad (14)$$

3.2. Error function formula

In fact, in Eq. (6), only the first two terms which correspond to Laplace formula can be found without any hypothesis on the real atmosphere (only the reduced height ℓ and the refractivity at observer are needed). The term in \tan^5 comes from an additional assumption, namely the fact that air density follows an exponential decrease with height (actually with a well chosen variable which vary almost linearly with height, see Danjon (1980), Fletcher (1931)). This leads to the following equation:

$$R = \alpha \left(\frac{2 - \alpha}{\sqrt{2\beta - \alpha}} \right) \sin(z) \Psi \left(\frac{\cos(z)}{\sqrt{2\beta - \alpha}} \right) \quad (15)$$

with :

$$\Psi(x) = e^{x^2} \int_x^\infty e^{-t^2} dt = \frac{\sqrt{\pi}}{2} e^{x^2} (1 - \text{erf}(x)) \quad (16)$$

from which Eq. (6) was derived by keeping only the three first terms of its asymptotic expansion.

3.3. Cassini

By comparing the results with a full integration method, Young (2004) shows the superiority of Cassini's formula over the series-expansion approach and advocates its use by astronomers. Cassini assumed an homogeneous atmosphere for which he obtained the exact formula:

$$R = \text{asin} \left(\frac{n_{obs} r_c \sin(z)}{r_c + \ell} \right) - \text{asin} \left(\frac{r_c \sin(z)}{r_c + \ell} \right) \quad (17)$$

Again, it can be shown (Ball 1908) that expanding this formula also leads to the to first two terms of Eq. (6) i.e. to Laplace formula.

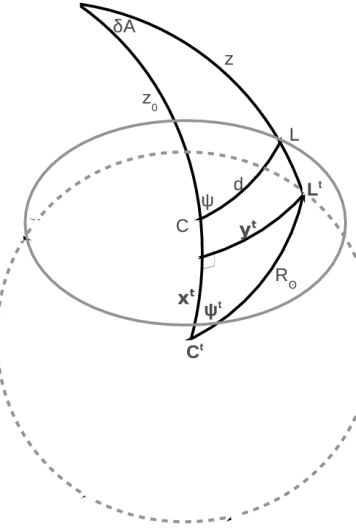


Fig. 1. Geometry for the solar shape due to astronomical refraction. The dashed circle represents the true solar disk of centre C' and radius R_\odot while the elliptical shape (full line) represents the observed Sun of centre C . The point at the top represents observer's zenith.

4. On the observed shape of the Sun due to pure astronomical refraction

In this section, we assume that the Sun is a perfect sphere of angular radius R_\odot at 1 AU and that there is no other effect affecting its observed shape than astronomical refraction defined by Eq. (2).

In the horizontal coordinate system (zenith distance-azimuth), we note (z'_\odot, A_\odot) the true position of the Sun centre (C') observed at zenith angle z_\odot ; (z^t, A) the true position of a point (L^t) of the solar limb observed at zenith angle z ; $\delta z = z - z_\odot$ and $\delta A = A - A_\odot$. Figure 1 shows all the angles involved. Each true limb point position can be defined by the angle $\psi^t \in [-\pi, \pi[$ between the direction $\overline{C'L^t}$ and the vertical circle. Similarly, each observed limb point can be located by the angle $\psi \in [-\pi, \pi[$ between the observed direction \overline{CL} and the vertical circle. However, because the figure is symmetric with respect to the vertical circle, we consider only the interval $[0, \pi]$ for ψ and ψ^t in the following. For observation with an Alt-Az mount this would correspond directly to the angle with one of the CCD axis. For an equatorial mount, one CCD axis is aligned with the hour circle passing through the celestial poles and the Sun and therefore the vertical circle can be materialized on the solar image by computing first the parallactic angle between these two circles.

If $d(\psi) = \bar{d}(\psi^t)$ is the angular distance between the observed position of the Sun centre and the observed limb points, we define by:

$$\langle d \rangle = \left[\frac{1}{\pi} \int_0^\pi d(\psi)^2 d\psi \right]^{1/2} = \left[\frac{1}{\pi} \int_0^\pi \bar{d}(\psi^t)^2 d\psi^t \right]^{1/2} \quad (18)$$

the geometric mean radius of the observed Sun. The horizontal and vertical angular extent of the observed Sun are noted D_h and D_v respectively and, the flattening is given by:

$$f = \frac{D_h - D_v}{D_h} \quad (19)$$

¹ Chollet (1981) used erroneously $2.64 10^{-4}$ in this equation.

Following Mignard (2002), we define the magnification Γ as the ratio between the vertical size of the image (δz) of a small object to its true size ($\delta z'$). From Eqs. (1) and (2), we have:

$$\Gamma = \frac{dz}{dz'} = 1 - \frac{d\bar{R}}{dz'} = \left(\frac{dz'}{dz} \right)^{-1} = \left(1 + \frac{dR}{dz} \right)^{-1} \quad (20)$$

The distortion Δ is then defined as the rate of change of the magnification:

$$\Delta = \frac{d\Gamma}{dz} = -\Gamma^2 \frac{d^2 R}{dz^2} = -\frac{1}{\Gamma} \frac{d^2 \bar{R}}{dz'^2} \quad (21)$$

4.1. Approximate formulae for all zenith angles

Any limb point true position can be located by its projections on the vertical circle passing through the true Sun centre, and on the great circle perpendicular to this vertical circle passing through the limb point (see Fig. 1). Because all the angles involved are small, we can write:

$$x' = R_\odot \cos(\psi') \quad (22)$$

$$y' = R_\odot \sin(\psi') \quad (23)$$

and:

$$x'^2 + y'^2 = R_\odot^2 \quad (24)$$

By looking at the expression of the observed values x and y of these projections, one can obtain an approximate formula for the observed shape of the Sun.

The projection x' on the vertical circle can be approximated by keeping the two first terms of a Taylor expansion of the refraction:

$$x' \approx z' - z'_\odot = \delta z + R(z) - R(z_\odot) \approx \delta z \left(1 + \frac{dR}{dz} \right) + \frac{(\delta z)^2}{2} \frac{d^2 R}{dz^2} \quad (25)$$

The observed projection y is linked to z and δA both by the cosine and sine rules:

$$\cos(y') \approx \cos^2(z') + \sin^2(z') \cos(\delta A) \quad (26)$$

$$\sin(y') = \sin(\delta A) \sin(z') \quad (27)$$

Differentiating Eq. (26) and using Eq. (27) with $\sin(y') \approx y'$, $\sin(\delta A) \approx \delta A$ and $dz' = -\bar{R}(z')$ leads to:

$$dy' = \frac{-y' \bar{R}(z')}{\tan(z')} \quad (28)$$

The observed distance y is then obtained by:

$$y \approx \delta A \sin(z) = y' + dy' = y' \left(1 - \frac{\bar{R}(z')}{\tan(z')} \right) \quad (29)$$

Finally, by reporting Eqs. (25) and (29) in Eq. (24) and using Eqs. (20) and (21), we obtain:

$$\left[\frac{\delta z}{\Gamma} - \frac{\Delta}{2} \left(\frac{\delta z}{\Gamma} \right)^2 \right]^2 + \left[\frac{\delta A \sin z}{1 - \frac{\bar{R}(z')}{\tan(z')}} \right]^2 = R_\odot^2 \quad (30)$$

where the magnification and distortion are taken at z_\odot . From this we can deduce the position of the two vertical limb points

and the observed vertical extent of the image. For $\Delta \ll R_\odot$ and $\delta A = 0$, we find:

$$d(\pi) \approx \Gamma R_\odot \left(1 + \frac{\Delta R_\odot}{2} \right) \quad (31)$$

$$d(0) \approx \Gamma R_\odot \left(1 - \frac{\Delta R_\odot}{2} \right) \quad (32)$$

and thus:

$$D_v = d(0) + d(\pi) \approx 2 \Gamma R_\odot \quad (33)$$

In the horizontal direction we obtain from Eq. (30) with $\delta z = 0$:

$$D_h = 2d(\pi/2) \approx 2R_\odot \left(1 - \frac{\bar{R}(z'_\odot)}{\tan(z'_\odot)} \right) \quad (34)$$

4.2. Approximate formulae for small zenith angles - elliptic shape

Keeping only the first term in Eq. (6) is equivalent to neglecting Earth curvature. We obtain the following approximation valid close to the zenith only ($z < 45^\circ$):

$$R(z) = k \tan(z) \text{ with : } k = \alpha(1-\beta) \quad (35)$$

For this flat-Earth approximation we can also write:

$$\bar{R}(z') \approx k' \tan(z') \text{ with : } k' = k(1 - k \sec^2(z')) \quad (36)$$

In that case and if we neglect the distortion, Eq. (30) is reduced to the equation of a simple ellipse (see also e.g. Ball 1908):

$$\frac{x^2}{(1 - k' \sec^2(z'_\odot))^2} + \frac{y^2}{(1 - k')^2} = R_\odot^2 \quad (37)$$

where $x = \delta z$ and $y = \sin(z) \delta A$ can be assimilated to Cartesian coordinates on two perpendicular axes on the image. The major axis of the observed ellipse is thus given by:

$$\frac{D_h}{2} = R_\odot(1 - k') \quad (38)$$

while the observed minor axis is:

$$\frac{D_v}{2} = R_\odot \left(1 - k' \sec^2(z'_\odot) \right) \quad (39)$$

We note from these equations that the Sun is shrunken in all directions. The observed horizontal diameter is smaller than the true diameter but remains the same for all zenith angles (c.f. Fig. 7) while the observed vertical diameter decreases with increasing zenith distance. The combination of these two effects leads to the apparent flattening of the setting Sun (but keeping in mind that this approximate formula is not valid close to the horizon). From Eqs. (19), (38) and (39), the flattening for small zenith angles is:

$$f \approx k \tan^2(z'_\odot) \quad (40)$$

while, near the horizon, Eq. (30) implies that the flattening is simply given by the vertical magnification taken at the the Sun's centre. For small zenith angles, the observed elliptic shape can be written as:

$$d(\psi) = \frac{D_v}{2 \sqrt{1 - (2f - f^2) \sin^2(\psi)}} \quad (41)$$

which can be approximated by:

$$d(\psi) \simeq R_{\odot} \left(1 - k' \left(1 + \cos^2(\psi) \tan^2(z'_{\odot}) \right) \right), \quad (42)$$

and the mean radius is obtained by:

$$\langle d \rangle = \frac{\sqrt{D_v D_h}}{2} \simeq R_{\odot} \left(1 - k' - \frac{k'}{2} \tan^2(z'_{\odot}) \right) \quad (43)$$

4.3. Exact formulae for all zenith angles

The classical approximate formulae above are useful for understanding the shape of the observed Sun in terms of magnification and distortion induced by refraction. Equation (30) shows that the general shape is a distorted ellipse with more flattening in the lower part than in the upper's. However, the shape of the observed Sun can also easily be obtained, in the general case, without any approximation. In the following, we obtain first the solution of the forward problem: for given true Sun radius R_{\odot} and true zenith distance z'_{\odot} , we obtain the shape of the observed Sun for any given refraction model. Then, we give the solution of the inverse problem: from the observed solar shape, the knowledge of z'_{\odot} (from ephemeris) and assuming a refraction model, we deduce the true angular solar radius.

4.4. Forward problem

Here we assume that the true zenith distance of the Sun centre z'_{\odot} and its true angular radius R_{\odot} are known. For any refraction model $\bar{R}(z')$, and true angle ψ' , we deduce the observed angle ψ and angular distance $d(\psi)$. Applying the cosine and sine formulae respectively, we have :

$$\begin{cases} z' = \arccos[\cos(z'_{\odot}) \cos(R_{\odot}) + \sin(z'_{\odot}) \sin(R_{\odot}) \cos(\psi')] \\ \delta A = \arcsin\left(\frac{\sin(R_{\odot}) \sin(\psi')}{\sin(z')}\right) \end{cases} \quad (44)$$

From Eq. (2), we can get the observed zenith distances:

$$z = z' - \bar{R}(z') \quad \text{and} \quad z_{\odot} = z'_{\odot} - \bar{R}(z'_{\odot}) \quad (45)$$

and finally angular distances $\bar{d}(\psi')$ between the observed Sun centre and the observed positions of each limb point are obtained by application of the cosine rule:

$$\bar{d}(\psi') = d(\psi) = \arccos(\cos(z) \cos(z_{\odot}) + \sin(z) \sin(z_{\odot}) \cos(\delta A)) \quad (46)$$

where the observed angle ψ can be deduced from the true one by applying the sine rule:

$$\psi = \arcsin\left(\frac{\sin(\delta A) \sin(z)}{\sin(\bar{d}(\psi'))}\right) = \arcsin\left(\frac{\sin(z) \sin(R_{\odot})}{\sin(z') \sin(\bar{d}(\psi'))} \sin(\psi')\right) \quad (47)$$

The smallest observed diameter of the Sun is obtained on the vertical direction:

$$D_v = d(0) + d(\pi) = 2R_{\odot} - (\bar{R}(z'_{\odot} + R_{\odot}) - \bar{R}(z'_{\odot} - R_{\odot})) \quad (48)$$

and the largest angular extent, observed in the direction parallel to the astronomical horizon is obtained by:

$$D_h = 2d(\pi/2) \quad (49)$$

We note that Eqs. (44) and (45) lead back to the approximation Eq. (34) for the largest observed angular extent. This is however

more easily obtained using the sine rule rather than Eq. (46). With $\sin(d(\pi/2)) \simeq d(\pi/2)$, $\sin(R_{\odot}) \simeq R_{\odot}$ and $\cos(R_{\odot}) \simeq 1$, we obtain:

$$d(\pi/2) \simeq \sin(z) \sin(\delta A) = \sin(z'_{\odot} - \bar{R}(z'_{\odot})) \frac{R_{\odot}}{\sin(z'_{\odot})}. \quad (50)$$

which, with a first order expansion of the sine function around z'_{\odot} , leads to Eq. (34).

4.5. Inverse problem

Here we give the solution of the inverse problem: given a refraction model $(R(z), \bar{R}(z'))$, knowing z'_{\odot} from ephemeris and the observed angular distance $d(\psi)$ between the observed Sun centre and a limb point at an observed angle ψ with the vertical circle, we deduce the true angular radius R_{\odot} . One can compute successively:

$$\left\{ \begin{array}{l} z_{\odot} = z'_{\odot} - \bar{R}(z'_{\odot}) \\ \delta A = \arctan\left[\frac{\sin(\psi)}{\sin(z_{\odot}) \cot(d(\psi)) + \cos(z_{\odot}) \cos(\psi)}\right] \\ z = \arcsin\left[\frac{\sin(\psi) \sin(d(\psi))}{\sin(\delta A)}\right] \\ z' = z + R(z) \\ \psi' = \arctan\left[\frac{\sin(\delta A)}{\cos(z') \cos(\delta A) - \sin(z') \cot(z')}\right] \\ R_{\odot} = \arcsin\left[\frac{\sin(\delta A) \sin(z')}{\sin(\psi')}\right] \end{array} \right. \quad (51)$$

5. Results

5.1. On the absolute value of refraction

We first look at the absolute value of refraction and compare the various approximate formulae of Sect. 3 to the full numerical integration of the refraction integral using a standard atmosphere (Sinclair 1982). This atmosphere is assumed to be spherically symmetric, in hydrostatic equilibrium and made of a mixture of dry air and water vapor that follows the perfect gas law. It is made of two layers: the troposphere with a constant temperature gradient which extends from the ground up to the tropopause at 11 km, and an upper isothermal stratosphere. Like in the US Standard Atmosphere (1976), the temperature and pressure at the surface are 288.15 K and 101325 Pa and the constant tropospheric lapse rate is 6.5 K km⁻¹. In the troposphere, the relative humidity f_h is assumed constant and equal to its value at the observer. The partial pressure of water vapor in a tropospheric layer at temperature T is then obtained by:

$$p(f_h, T) = f_h \left(\frac{T}{247.1} \right)^{\delta} 10^2 \quad (52)$$

which, with $\delta = 18.36$, never depart by more than 0.5 hPa from Eq. (13) for temperature lower than 30°. Dry air is assumed in the stratosphere. Finally, Eq. (11) and its derivatives with respect to T and P are used to find air refractivity along the integral path.

The numerical integration was performed by using the method of Auer & Sandish (2000) also recommended by the Astronomical Almanac (Seidelmann 1992). The program used

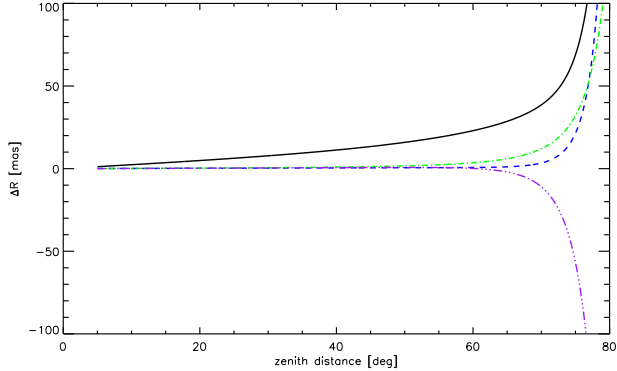


Fig. 2. Absolute differences (in mas) between a reference model and the different approximate refraction formulae as a function of the true zenith distance. The reference model is obtained by full numerical integration of the US Standard Atmosphere (1976) and Ciddor (1996) equation for air refractivity. From top to bottom: \tan^5 expansion Eqs. (6)-(13), full error function Eq. (15), \tan^5 expansion Eq. (6), Cassini's formula Eq. (17). All approximate formulae but the top one use Ciddor (1996) air refractivity

is based on the one published by Hohenkerk & Sinclair (1985) but adapted in order to use a dispersion equation based on the work of Peck & Reeder (1972) in replacement of the less accurate equation of Barrel & Sears (1939) (Eq. (12)). For $T = 15^\circ\text{C}$, $P = P_0$, 0% humidity and 0.045% of carbon dioxide, we take:

$$n_0(\lambda) - 1 = \left\{ \frac{0.05792105}{238.0185 - (10^6\lambda)^{-2}} + \frac{0.00167917}{57.362 - (10^6\lambda)^{-2}} \right\} \quad (53)$$

This dispersion equation was also used by Ciddor (1996) who derived a new set of equations for calculating the refractive index of air which was subsequently adopted by the International Association of Geodesy (IAG 1999) as a new standard. In the following, all computations have been made using $\lambda = 535.7\text{ nm}$ which is one of the wavelengths used by the PICARD-SOL project.

Figure 2 shows the absolute differences in milliarcseconds (mas) between the approximate formulae and the exact integral evaluation for zenith distances up to 80° . We immediately see that for zenith distance lower than 75° , all the approximate formulae lead to less than 50 mas of absolute error. The full line corresponds to the \tan^5 formula Eq. (6) described in Sect. 3.1 while the dashed line corresponds to the same formula but using the new Ciddor (1996) equations instead of Eqs. (11)-(13) for computing air refractivity. For zenith distances lower than 80° , the impact of using the old formula for refractivity never exceed 80 mas. The superiority of Ciddor equations to better fit observations and this for a wider range in wavelengths is however clearly established. The two other lines correspond to the error function (dot-dash) and Cassini (triple dots-dash) formulae both using the Ciddor (1996) equation for refractivity. These two last formulae were selected mainly because, unlike the series expansions in $\tan(z)$, they are finite at the horizon. The full integration with standard atmosphere conditions leads to a refraction of about $1980''$ at the horizon. The error function and Casini formulae lead respectively to $2088''$ and $1180''$ corresponding to relative errors of 5% and 40% respectively. This tends to favour the use of the error function formula over Cassini's one very close to the

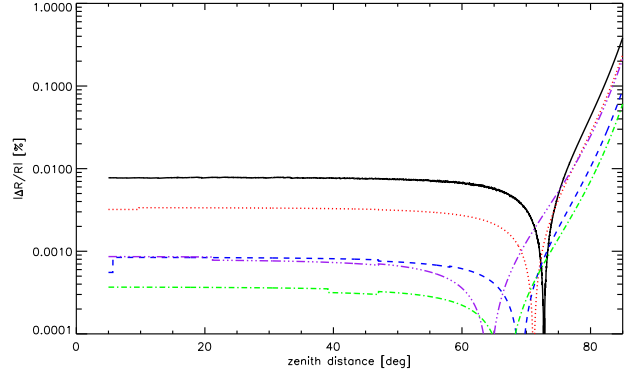


Fig. 3. Relative error on refraction as a function of zenith distance for different tropospheric lapse rate. The reference model use US Standard Atmosphere (1976) with a lapse rate of 6.8 K km^{-1} . The top curve correspond to an isothermal model and other atmosphere models have lapse rate of 2.5, 5, 10 and 7.5 K km^{-1} (from top to bottom at low zenith distance). All models are computed using full numerical integration.

horizon. The hypothesis made to derive the error function formula are indeed more realistic than Cassini's hypothesis of an homogeneous atmosphere. It has however been shown that refraction below 5° of the horizon is variable and strongly depend on the local lapse rate and properties of the boundary layer above or below the observer's eye (e.g. Young 2004). Within few degrees from the horizon, refraction may be influenced by thermal inversion boundary layers, ducting or other phenomena leading to extreme refraction. In this range, the local lapse rate must be known and it is not expected that any formula using just the temperature and pressure at observer could give an accurate absolute refraction.

It is however probably more interesting to look in the range between 60° and 85° of zenith distance, which is more important to astronomers willing to push in that range the limits of their astrometric measurements using only temperature and pressure recorded at observer position. We first note from Fig. 2 that, between 60° and 77° , the \tan^5 expansion formula is actually giving slightly better absolute refraction values than the error function formula. If we now assume that temperature and pressure at observer position are perfectly known, the only remaining important unknown in the atmospheric model is the tropospheric lapse rate. We can however fix limits for a realistic lapse rate: it must lie between an isothermal model and a lapse rate of 10 K km^{-1} which would correspond to an adiabatic atmosphere (Young 2004). Figure 3 shows the absolute value of the relative error for such models with lapse rate ranging from 0 to 10 K km^{-1} when they are compared to the standard model with a lapse rate of 6.8 K km^{-1} . From this we can deduce that, no matter what is the real atmosphere, if the conditions at observer are known, the relative error on refraction is lower than 0.01% for zenith angles below 77° and lower than 0.4% for zenith angles between 77° and 85° .

5.2. On the mean solar radius correction

Figure 4 shows the difference between the true radius of the Sun and the mean radius of the observed Sun as defined by Eq. (18) as a function of the true zenith distance of the centre of the Sun. The exact formula Eq. (46) was used and we took standard con-

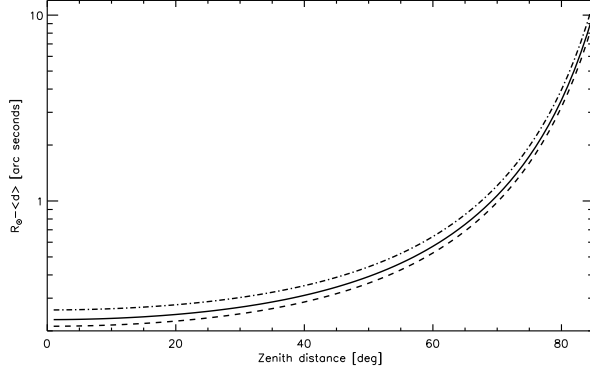


Fig. 4. Difference between the true solar radius and the observed one as a function of the true zenith distance. The full line corresponds to average weather conditions at Calern ($T = 15^\circ\text{C}$, $P = 875 \text{ hPa}$). The dashed and dot-dashed lines correspond respectively to $T = -10^\circ\text{C}$, $P = 900 \text{ hPa}$ and $T = 30^\circ\text{C}$, $P = 850 \text{ hPa}$. All calculations are made using the exact formulae Eqs. (18) and (46) for Calern station assuming 50% humidity.

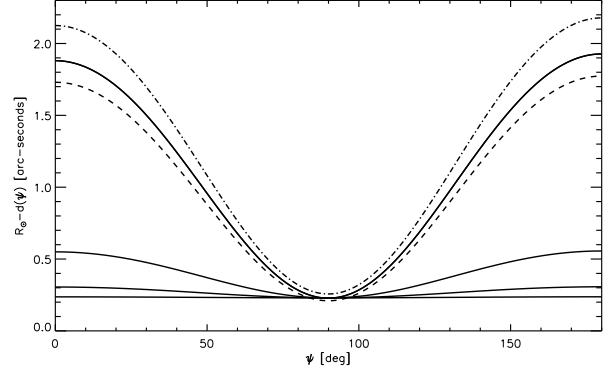


Fig. 6. Difference between the true solar radius and the angular distances between the observed Sun centre and the observed positions of each limb points between the vertical (north for $\psi = 0^\circ$ and south for $\psi = 180^\circ$) and the horizon ($\psi = 90^\circ$). The full lines are for $z'_\odot = 70^\circ$, 50° , 30° and 10° respectively from top to bottom and are for average weather conditions at Calern. The dashed and dot-dashed lines are for $z'_\odot = 70^\circ$ and the same extreme weather conditions as in Fig. 4.

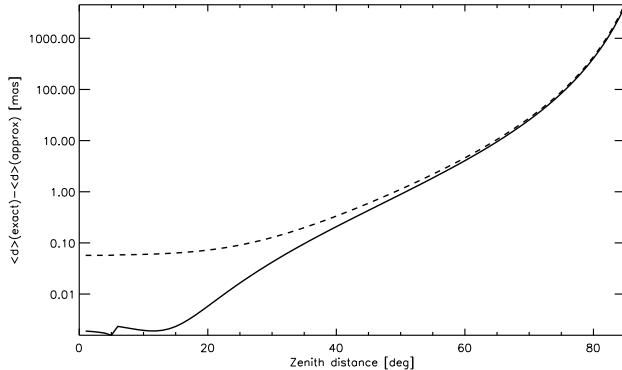


Fig. 5. Difference between the correction due to refraction on the mean solar radius as calculated from integrating the exact formula Eq. (46) or using the approximate formula Eq. (43). The dashed line is obtained by replacing k' by k in Eq. (43)

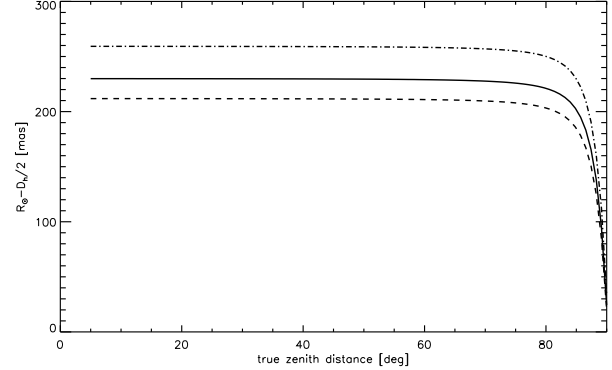


Fig. 7. Contraction of the horizontal radius ($R_\odot - d(\pi/2)$) as a function of the true zenith distance z'_\odot . The full line is for average weather conditions at Calern. The dashed and dot-dashed lines are for the same extreme weather conditions as in Fig. 4.

ditions for Calern observatory ($T = 15^\circ\text{C}$, $P = 875 \text{ hPa}$). The dashed and dot-dashed lines are for $T = -10^\circ\text{C}$, $P = 900 \text{ hPa}$ and $T = 30^\circ\text{C}$, $P = 850 \text{ hPa}$ respectively in order to illustrate the maximum amplitude of the effect at Calern station. The difference in the mean radius correction between the two extreme weather conditions range from 50 mas at the zenith up to 1850 mas at $z' = 85^\circ$. It reaches 100 mas around $z' = 55^\circ$ and 200 mas around $z' = 70^\circ$. This represents always less than 0.2% of the correction.

Figure 5 shows the difference between the exact formula obtained by integrating Eq. (46) and the approximate formula Eq. (43) corresponding to an elliptical shape. The dashed line illustrates the result if k' is approximated by k (see Eq. (36)). In both cases the difference remains less than 20 mas for zenith distances lower than 70° . For larger zenith distances however, errors increase rapidly and the refraction function should be evaluated using full numerical integration.

5.3. On the angular dependence of solar radius correction

For precise metrologic measurements of the Sun and in order to correct for other effects (optical aberrations, turbulence, etc..) that are dependent on the position on the image, one may want to correct not the mean radius but each individual radius measured at all angles ψ . This can be done by following the procedure given in Sect. 4.5. Figure 6 is obtained from Eq. (46) and illustrates the amplitude of the correction as a function of ψ for different values of z'_\odot , the true zenith distance of the Sun centre. We see that the horizontal diameter ($\psi = 90^\circ$) is affected by refraction (by about $2 \times 0.23'' = 0.46''$ for the chosen weather conditions) in agreement with Eq. (34). The north and south vertical corrections ($\psi = 0^\circ$ and 180° respectively) are also slightly different in agreement with Eqs. (31)-(32). Figure 7 shows that the contraction of the horizontal radius lies between 210 and 260 mas depending on the actual weather conditions and remains constant for all zenith distances below 80° . It then decreases rapidly towards zero at the horizon.

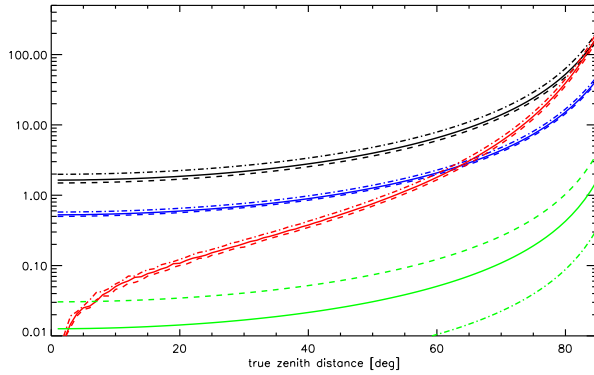


Fig. 8. Partial derivatives of the vertical diameter correction (δ_v) as a function of the true zenith distance. Partial derivatives in temperature, pressure, zenith distance and relative humidity are given in mas K $^{-1}$, mas hPa $^{-1}$, mas arcmin $^{-1}$ and mas/% from top to bottom (at 40°) respectively. The full, dashed and dot-dashed lines are for the same weather conditions as on Fig. 4.

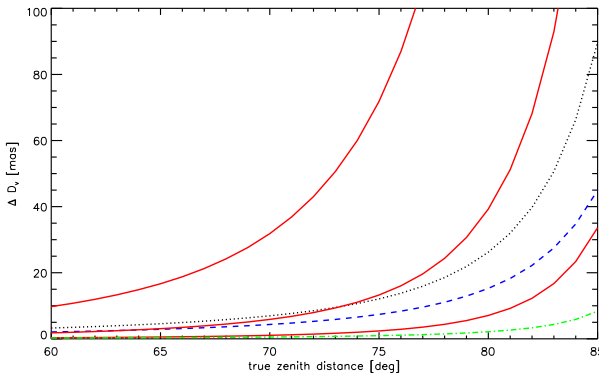


Fig. 9. Uncertainties on the vertical diameter correction assuming $\Delta T = 0.5$ K (dotted line), $\Delta P = 1$ hPa (dashed line), $\Delta f_h = 5\%$ and $\Delta z_\odot^t = 5.4'$, $1.0'$ or $0.2'$ (full lines from top to bottom). The total error is obtained by summing the four contributions.

5.4. On uncertainties associated to radius corrections

We have shown that, apart from weather conditions at observer's position, differences in atmospheric models and especially different tropospheric lapse rates will not play any significant role at least up to 85° of zenith distance. The four main contributions are therefore uncertainties in temperature, pressure, humidity and, for large zenith distance, uncertainties on the true zenith distance itself.

$$\Delta d(\psi) = \sum_{i=1}^4 \left| \frac{\partial d(\psi)}{\partial X_i} \right| \Delta X_i \quad X = \{T, P, f_h, z_\odot^t\} \quad (54)$$

It should be noted that we assume here observations made using filters with a narrow bandwidth around λ . For broadband filters, an additional term $\partial d(\psi)/\partial \lambda$ should be added by differentiating Eq. (53). The largest uncertainty will be obtained for the vertical diameter ($D_v = d(0) + d(\pi)$) which is the most affected by refraction. Figure 8 shows the four partial derivatives contributing to ΔD_v between the two extreme weather conditions chosen above for Calern (see Sect. 5.2). The partial derivatives shown

have been obtained by numerically differentiating Eq. (46) but we have also checked that the analytical expressions that can be derived from the approximate elliptical shape Eq. (42) are actually valid up to 80° of zenith distance. Closer to the horizon the partial derivative over the zenith distance becomes significantly overestimated (c.f. Fig. 10). From Eq. (42) and taking $k' \approx k$, we obtain:

$$\begin{cases} \left| \frac{\partial d(\psi)}{\partial X_i} \right| = \left| \frac{\partial k}{\partial X_i} \right| (1 + \cos^2(\psi) \tan^2(z_\odot^t)) R_\odot & i = 1..3 \\ \left| \frac{\partial d(\psi)}{\partial z_\odot^t} \right| = 2k \cos^2(\psi) \sec^2(z_\odot^t) \tan(z_\odot^t) R_\odot \end{cases} \quad (55)$$

and from Eqs. (8), (9), (11), (36), (52), we obtain:

$$\begin{cases} \frac{\partial k}{\partial T} = -C_1 \frac{P}{T} (n_0(\lambda) - 1) + C_3 T^{\delta-1} f_h (C_2 - \frac{\delta-1}{T}) \\ \frac{\partial k}{\partial P} = C_1 (T^{-1} - C_2) (n_0(\lambda) - 1) \\ \frac{\partial k}{\partial f_h} = -C_3 (T^{-1} - C_2) T^\delta \end{cases} \quad (56)$$

where:

$$C_1 = T_0/P_0, \quad C_2^{-1} = C_1 r_c \rho_0 g_0, \quad C_3 = 4.13 \cdot 10^{-8} T_0 (247.1)^{-\delta} \quad (57)$$

For temperature, pressure and humidity, we assume uncertainties of $\Delta T = 0.5$ K, $\Delta P = 1$ hPa and $\Delta f_h = 5\%$ which are typical for a standard weather station. The precision on the true zenith distance relies on ephemeris calculations and a correct timing. At any given time ephemeris can give not only z_\odot^t but also the instantaneous rate dz_\odot^t/dt and, from the knowledge of the image exposure time Δt , one can deduce an uncertainty on z_\odot^t by:

$$\Delta z_\odot^t = \left| \frac{dz_\odot^t}{dt} \right| \Delta t \quad (58)$$

The maximum rate is about $650'' \text{ min}^{-1}$ at summer solstice. Image exposures of 1 s, 5.5 s or 30 s would then correspond to a maximum uncertainty Δz_\odot^t of $0.18'$, $1'$ or $5.4'$ respectively. Figure 9 shows the contribution of these uncertainties to the total uncertainty on vertical diameter correction for large zenith distances. We can see for instance that for $1'$ precision on the zenith distance (or 5.5 s exposure), the uncertainty coming from zenith distance can become, above 70°, of the same importance as the combined uncertainties coming from temperature and pressure records. The total relative error on the vertical diameter correction ($\Delta D_v / (2R_\odot - D_v)$) remains however below 1% up to $z_\odot^t = 85^\circ$.

6. Conclusions

We have obtained in Sec. 4.5, the exact formulae that can be used to correct solar radius measurements at any heliographic angle and any zenith distance from the effect of astronomical refraction. Using full integration of the refraction integral, we have shown that this correction can be applied for any true zenith distance up to 85° with a relative uncertainty on the correction that remains less than 1%. Absolute uncertainties on these corrections are also derived that allows us to fix the maximum zenith distance one should observe depending on the needed metrologic accuracy. Figure 10 shows the maximum total absolute

uncertainty obtained on the solar radius assuming that the vertical radii have been observed at different zenith distances. We use $\lambda = 535.7$ nm and two exposure times used by the PICARD-SOL project at this wavelength. Because we took the maximum value for dz'_\odot/dt , this curves represent only upper limits, the actual value of dz'_\odot/dt should be used for each measurement. From this, one can deduce that observing below 70° , 75° or 80° of zenith distances will keep the absolute uncertainties on refraction corrections below 10, 20 and 50 mas respectively. The comparison between numerical derivatives (full lines) and the use of approximate formulae Eqs. (54)-(58) (dashed lines) shows that, even if the approximate formulae should not be used above 70° for correcting the measurements (c.f. Fig. 5), they can be used at least up to $z'_\odot = 80^\circ$ for estimating the uncertainties.

In summary, the process that we suggest to correct ground based radii measurements from refraction for true zenith distances up to 80° is as follow. Inputs are: the measurements $d(\phi)$ and eventually their associated errors $\delta d(\phi)$ where ϕ is an arbitrary angle defined on the solar image; the time of image record and the exposure time Δt ; weather records (P , T , f_h) and their associated uncertainties (ΔT , ΔP and Δf_h); the wavelength (λ) and observer's geodetic coordinates (φ, h). One can then successively:

- find the direction of the zenith on the image and associate each angle ϕ to its corresponding angle ψ (c.f. Fig. 1). Depending on the instrumental setup, this may require the computation of the parallactic angle from ephemeris,
- determine z'_\odot and dz'_\odot/dt from ephemeris at the time of image record,
- calculate R_\odot using Eqs. (51) and full numerical integration for the refraction function $R(z, \lambda, P, T, f_h, h, \varphi)$,
- estimate $\Delta d(\psi)$ from Eqs. (54)-(58) and the knowledge of ΔT , ΔP , Δf_h , Δt and dz'_\odot/dt ,
- estimate ΔR_\odot from:

$$\Delta R_\odot = R_\odot \frac{\Delta d(\psi) + \delta d(\psi)}{d(\psi)}. \quad (59)$$

For zenith distances lower than 70° full numerical integration can be replaced by Eq. (6) in order to evaluate the refraction function (c.f. Fig. 2). In both cases Ciddor (1996) equations should be used for computing air refractivity at observer position. The corresponding codes are available from the authors upon request.

It is important to keep in mind that, at all zenith distances, other phenomena such as extinction or optical turbulence must be taken into account for ground based solar metrology. We know that they will dominate refraction effects at low zenith distances. Close to the horizon extinction is proportional to refraction (Laplace's extinction theorem) and effects of optical turbulence (e.g. Ikhlef et al. 2012 and reference therein) will become increasingly important knowing that the Fried parameter varies as $\sec(z)^{-0.6}$. It is interesting however to know that for any zenith distance up to 80° refraction can be reliably corrected and uncertainties on this correction estimated. After these correction are applied, all other phenomena impacting metrologic measurements can therefore be investigated without fearing contamination by astronomical refraction even at high zenith distances. The mean radius correction presented here (c.f. Fig. 4) as well as mean turbulence corrections have been applied to correct the first PICARD-SOL measurements (Meftah et al. 2013). The corrections that can be applied individually for each heliographic

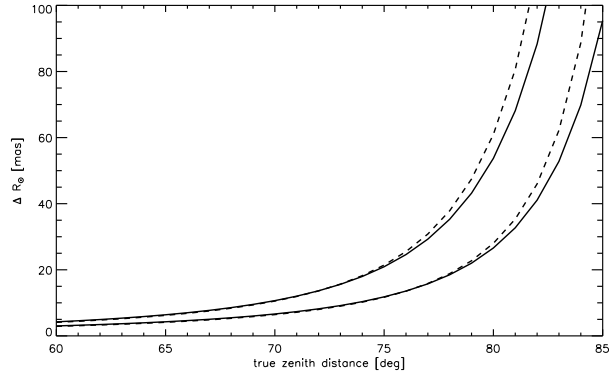


Fig. 10. Maximum absolute uncertainties on radius estimates using measurements in the vertical direction corrected from refraction. This curves are obtained for $\lambda = 535.7$ nm, $T = (15 \pm 0.5)^\circ\text{C}$, $P = (875 \pm 1)$ hPa, $f_h = 50\% \pm 5\%$ and $dz'_\odot/dt = 650'' \text{ min}^{-1}$. The top and bottom lines are for 8.9 s and 1.3 s of exposure time respectively. Full lines give the results from full numerical derivatives calculations while dashed lines are obtained using approximate formulae Eqs. (54)-(58).

angles should be used in future work in order to disentangle the different effects.

Finally we note that we have considered only the radial symmetric-component of refraction also called pure or normal refraction. There also exists an asymmetric component known as anomalous refraction (e.g. Teleki 1979) resulting from the tilted atmospheric layers. Anomalous refraction may depend not only on zenith distance but also on azimuth and it can lead to seasonal or high frequency effects (see e.g. Hirt (2006) and references therein). The amplitude of such effect has however been found to be lower than $0.2''$ for local effects and one order of magnitude less for regional effects that may originate higher in the atmosphere (e.g. Hu 1991). Moreover it has been shown that anomalous refraction is spatially coherent at scales of at least 2° (Pier et al. 2003) and it has been established from dedicated observations that its main source is confined in the layer immediately above ground level (less than 60 m, see Taylor et al. (2013)). It is therefore difficult to believe that differential effects of anomalous refraction and especially the one that may be triggered in the Upper Troposphere - Lower Stratosphere (UTLS) interface (c.f. Badache-Damiani et al. 2007) could lead to significant bias on solar astrometric measurements relying on direct solar disk imaging.

Acknowledgements. The authors acknowledge financial support from CNES in the framework of PICARD-SOL project. We thank P. Exertier and J. Paris for useful discussions on the precise geodetic coordinates of Calern station, S. Y. van der Werf (Univ. of Groningen) for providing is ray tracing code also used to check our results and K. Reardon (INAF) for making available his IDL codes for computing refractivity from Ciddor (1996) equations.

References

- Auer L., & Sandish, E. M. 2000, ApJ, 119, 2472
 Badache-Damiani, C., Rozelot, J. P., Coughlin, K., & Kilifarska, N. 2007, MNRAS, 380, 609
 Baldini, A. A. 1963, GIMRADA Research Note, 8
 Ball, R. S. 1908, A treatise on spherical astronomy, Cambridge University Press
 Barrel, H. & Sears, J. E. 1939, Phil. Trans. R. Soc., A238
 Annuaire du Bureau Des Longitudes, 1975
 Cassini, G. D. 1662, in Ephemerides Novissimae Motuum Coelestium Marchionis C. Malvasiae (Modena: A. Cassini)

- Chollet F. 1981, PhD thesis, Université Pierre et Marie Curie (Paris VI)
- Ciddor, P. E. 1996, Appl. Opt., 35, 1566
- Damé, L., Hersé, M., Thuillier, G., et al. 1999, Adv. in Space Res., 23, 205
- Débarbat, S. & Guinot, B., 1970, La Méthode des Hauteurs Égales en Astronomie, Gordon & Breach Science Publishers
- Danjon, A. 1980, Astronomie Générale (Seconde édition), ed. Albert Blanchard, Librairie Scientifique et Technique, Paris.
- Fletcher, A. 1931, MNRAS, 91, 559
- Hirt, C. 2006, A&A, 459, 283
- Hohenkerk, C. Y., & Sinclair, A. T. 1985, HM Naut. Alm. Off. Tech. Note No. 63
- Hu, N. 1991, Ap&SS, 177, 235
- IAG (International Association of Geodesy), 1999, Resolutions, 22nd General Assembly (see <http://www.gfu.ku.dk/~iag/resolutions>), 19-30 July 1999, Birmingham, U.K.
- Ikhdlef, R., Corbard, T., Irbah, A., et al. 2012, EAS Publications Series, 55, 369
- IUGG (International Union of Geodesy and Geophysics), 1963, Resolutions, 13th General Assembly, 19-31 August 1963, Berkeley, California, USA. Bulletin Géodésique, 70, 390
- Kuhn, J. R., Bush, R., Emilio, M., & Scholl, I. F. 2012, Science, 1638
- Laclare, F., Delmas, C., Coin, J. P., & Irbah, A. 1996, Sol. Phys., 166, 211
- Meffah, M., Corbard, T., Irbah, A., et al. 2013, JPCS, accepted
- Mignard, F. 2010, Technical Note, OCA-TN-FM-Corsica, Univ. Nice Sophia Antipolis, CNRS, OCA
- Morand, F., Delmas, Ch., Corbard, T., Chauvineau, B., Irbah, A., Fodil, M. & Laclare, F., 2011, Comptes Rendus Physique, vol. 11, 660-673
- Nicolas, J., Nocquet, J.-M., Van Camp, M., et al. 2006, Geophys. J. Int., 167, 1127
- Peck, E. R., & Reeder, K. 1972, J. Opt. Soc. Am., 62, 958
- Pier, J. R., Munn, J.A., Hindsley, R. B., et al. 2003, AJ, 125, 1559
- Princo Instruments inc., Instruction booklet for use with PRINCO Fortin type mercurial Barometers, <http://www.princoinstruments.com/booklet2007.pdf>
- Seidelmann, P. K., ed. 1992, Explanatory Supplement to the Astronomical Almanac (Mill Valley, CA; Univ. Sci. Books)
- Sinclair, A. T., 1982, NAO Technical Note no. 59, Royal Greenwich Observatory
- Smart, W. M., 1965, Text-Book on Spherical Astronomy (Fifth Edition), Cambridge University Press
- Taylor, M. S., McGraw, J. T., Zimmer, P. C., & Pier, J. R. 2013, AJ, 145, 82
- Teleki, G. 1979, In IAU Symposium Refractive Influences in Astrometry and Geodesy, ed. E. Tengström & G. Teleki, 103
- U.S. Standard Atmosphere, 1976, U.S. Government Printing Office, Washington, D.C., 1976
- van der Werf, S. Y. 2003, Applied Optics, 42, 354
- van der Werf, S. Y. 2008, Applied Optics, 47, 153
- Wittmann, A. D. 1997, AN, 318, 305
- Woolard, E. W., & Clemence, G. M. 1966, Spherical Astronomy, New York and London Academic Press
- Young, A. T. 2004, AJ, 127, 3622

Appendix A: Note on the radius of curvature at Calern observatory

According to the WGS84 reference ellipsoid, the Earth's equatorial and polar radii are given respectively by $a = 6378.137$ km and $b = 6356.752$ km. The curvature in the (north-south) meridian and at the geodetic latitude of Calern solar astrometric instruments $\varphi = 43^\circ 45' 7''$ is then given by:

$$r_c^0 = \frac{(ab)^2}{(a^2 \cos^2(\varphi) + b^2 \sin^2(\varphi))^{3/2}} = 6365.985 \text{ km} \quad (\text{A.1})$$

One could also consider the mean radius of curvature calculated for Calern. From the curvature in the prime vertical (normal to the meridian):

$$r_c^{90} = \frac{a^2}{\sqrt{a^2 \cos^2(\varphi) + b^2 \sin^2(\varphi)}} = 6388.371 \text{ km} \quad (\text{A.2})$$

we can deduce the radius of curvature for any azimuth angle A by:

$$r_c^A = \frac{1}{\frac{\cos^2(A)}{r_c^0} + \frac{\sin^2(A)}{r_c^{90}}} \quad (\text{A.3})$$

from which we can deduce the mean radius of curvature averaging over all directions, by:

$$\langle r_c \rangle = \sqrt{r_c^0 r_c^{90}} = \frac{a^2 b}{a^2 \cos^2(\varphi) + b^2 \sin^2(\varphi)} = 6377.168 \text{ km} \quad (\text{A.4})$$

If, instead of the radius of curvature, one considers the distance from geocenter, we have:

$$R = \sqrt{\frac{a^4 \cos^2(\varphi) + b^4 \sin^2(\varphi)}{a^2 \cos^2(\varphi) + b^2 \sin^2(\varphi)}} = 6367.955 \text{ km} \quad (\text{A.5})$$

One should add to these values the elevation of the observer above the reference ellipsoid ($h = 1.323$ km for Calern observatory). If we consider that, on average, we observe the sun closer to the north-south direction than east-west direction we can take:

$$r_c = r_c^0 + h = 6367.308 \text{ km} \quad (\text{A.6})$$

which is very close to the value used by Chollet (1981).

Finally we note that, for ephemeris calculations, the geodetic latitude should be corrected for the local gravimetric deflection. For Calern solar astrometric instruments this lead to an astronomic latitude $\varphi_{\text{ast}} = 43^\circ 44' 53''$ which is also compatible within $1''$ with the direct measurements made using a full entry pupil astrolabe on the same site. Similarly, we note that taking into account the local undulation with respect to the reference ellipsoid leads to a height above sea level of $h_{\text{sl}} = 1.271$ km for Calern solar astrometric station.

Appendix B: Note on the corrections applied to mercurial barometer reading

The two corrections (for gravity and barometer temperature) can be written as multiplicative factors (e.g. Princo 2007):

$$P = H \left(\frac{1 + L \theta}{1 + M \theta} \right) \frac{g}{g_0} \quad (\text{B.1})$$

where P is the corrected atmospheric pressure, H is the barometer reading, $M = 1.818 \cdot 10^{-4} \text{ K}^{-1}$ is the coefficient of volume thermal expansion of mercury, and $L = 1.84 \cdot 10^{-5} \text{ K}^{-1}$ is the coefficient of linear thermal expansion of brass. According to the 1967 reference system formula (Helmert's equation), we have:

$$g = g_{45} \left(1 - a \cos(2\varphi) - b \cos^2(2\varphi) \right) \quad (\text{B.2})$$

where $g_{45} = 9.8061999 \text{ ms}^{-2}$ is the gravity acceleration at mid latitude, $a = 2.64 \cdot 10^{-3}$ and $b = 1.96 \cdot 10^{-6}$. This can be corrected from the so-called Free Air Correction (FAC) which accounts for the fact that gravity decreases with height above sea level ($C_{\text{FAC}} = -3.086 \cdot 10^{-6} \text{ s}^{-2}$), itself corrected in order to take into account the increasing gravity due to the extra mass assumed for a flat terrain (Bouger correction, $C_B = 4.2 \cdot 10^{-10} \text{ m}^3 \text{ s}^{-2} \text{ kg}^{-1}$). For a mean rock density of $\rho_r = 2.67 \cdot 10^3 \text{ kg m}^{-3}$ this leads to:

$$C_g = (C_{\text{FAC}} + \rho_r C_B) = -1.96 \cdot 10^{-6} \text{ s}^{-2} \quad (\text{B.3})$$

Close to 45° of latitude, the second term of Eq. (B.2) can be neglected and, if we note $\epsilon = 1 - g_{45}/g_0 = 4.6 \cdot 10^{-5}$, Eq. (B.1) can be approximated by:

$$P = H (1 - \epsilon) \left(1 - (M-L) \theta \right) \left\{ 1 - a \cos(2\varphi) + \frac{C_g}{g_{45}} h \right\} \quad (\text{B.4})$$

Neglecting second order terms leads to Eq. (14).

We note that absolute gravity measurements have now been made at Calern geodetic observatory leading to $g = (980215549.2 \pm 12.6) 10^{-8} \text{ m s}^{-2}$ (Nicolas et al. 2006). This shows that the relative error on the correction g/g_0 discussed above and previously used for refraction calculations was less than $5 10^{-5}$. One could however now directly use Eq. (B.1) with the measured value of local gravity.

II.4 Résultats (article)

ARTICLE : Ground-based measurements of the solar diameter during the rising phase of solar cycle 24 (Meftah, Corbard, et al. 2014)

Dans cette première publication nous présentons l'ensemble du dispositif expérimental PICARD-SOL ainsi que les détails de la méthode d'analyse. Nous avons analysé plus de 20000 images acquises entre 2011 et 2013 dans quatre longueurs d'onde du continuum photosphérique (535.7, 607, 782 et 1025 nm). Le rayon moyen à 535.7nm est de 959.78 ± 0.19 arc-secondes et nous avons pu mettre une limite à 50 mas sur les variations possibles sur cette période. L'ensemble des résultats aux différentes longueurs d'onde observées est résumé dans la Table 7 de Meftah et al. (2014). A 607.1 nm le résultat couvrant la période 2011-2013, 959.86 ± 0.18 arc-secondes, est très similaire à celui obtenu par SDO/HMI lors du transit de Venus (959.90 ± 0.06 arc-secondes). Bien que nos incertitudes soient plus grandes, notamment par l'incertitude liée aux corrections de turbulence, l'accord en valeur absolue conforte nos calibrations et la stabilité instrumentale de SODISM-2 sur cette première phase nous permet de continuer la série pour couvrir le cycle 24 et au-delà.

Ground-based measurements of the solar diameter during the rising phase of solar cycle 24

M. Meftah¹, T. Corbard², A. Irbah¹, R. Ikhlef^{2,3}, F. Morand², C. Renaud², A. Hauchecorne¹, P. Assus², J. Borgnino², B. Chauvineau², M. Crepel¹, F. Dalaudier¹, L. Damé¹, D. Djafer⁴, M. Fodil³, P. Lesueur¹, G. Poiet¹, M. Rouzé⁵, A. Sarkissian¹, A. Ziad², and F. Laclare²

¹ Université Versailles St-Quentin; Sorbonne Universités, UPMC Univ. Paris 06; CNRS/INSU, LATMOS-IPSL,
11 boulevard d'Alembert, 78280 Guyancourt, France
e-mail: Mustapha.Meftah@latmos.ipsl.fr

² Laboratoire Lagrange, UMR 7293, Université de Nice Sophia-Antipolis, CNRS, Observatoire de la Côte d'Azur,
Bd. de l'Observatoire, 06304 Nice, France
e-mail: Thierry.Corbard@oca.eu

³ CRAAG, Observatoire d'Alger, BP 63 Bouzareah, Alger, Algérie

⁴ Unité de Recherche Appliquée en Énergies Renouvelables (URAER), Centre de Développement des Energies Renouvelables (CDER), BP 88, Ghardaïa, Algérie

⁵ CNES – Centre National d'Études Spatiales, Rue Édouard Belin, 31000 Toulouse, France

Received 7 February 2014 / Accepted 5 August 2014

ABSTRACT

Context. For the past thirty years, modern ground-based time-series of the solar radius have shown different apparent variations according to different instruments. The origins of these variations may result from the observer, the instrument, the atmosphere, or the Sun. Solar radius measurements have been made for a very long time and in different ways. Yet we see inconsistencies in the measurements. Numerous studies of solar radius variation appear in the literature, but with conflicting results. These measurement differences are certainly related to instrumental effects or atmospheric effects. Use of different methods (determination of the solar radius), instruments, and effects of Earth's atmosphere could explain the lack of consistency on the past measurements. A survey of the solar radius has been initiated in 1975 by Francis Laclare, at the Calern site of the Observatoire de la Côte d'Azur (OCA). Several efforts are currently made from space missions to obtain accurate solar astrometric measurements, for example, to probe the long-term variations of solar radius, their link with solar irradiance variations, and their influence on the Earth climate.

Aims. The *Picard* program includes a ground-based observatory consisting of different instruments based at the Calern site (OCA, France). This set of instruments has been named “*Picard Sol*” and consists of a Ritchey-Chrétien telescope providing full-disk images of the Sun in five narrow-wavelength bandpasses (centered on 393.37, 535.7, 607.1, 782.2, and 1025.0 nm), a Sun-photometer that measures the properties of atmospheric aerosol, a pyranometer for estimating a global sky-quality index, a wide-field camera that detects the location of clouds, and a generalized daytime seeing monitor allowing us to measure the spatio-temporal parameters of the local turbulence. *Picard Sol* is meant to perpetuate valuable historical series of the solar radius and to initiate new time-series, in particular during solar cycle 24.

Methods. We defined the solar radius by the inflection-point position of the solar-limb profiles taken at different angular positions of the image. Our results were corrected for the effects of refraction and turbulence by numerical methods.

Results. From a dataset of more than 20 000 observations carried out between 2011 and 2013, we find a solar radius of 959.78 ± 0.19 arcsec ($696\,113 \pm 138$ km) at 535.7 nm after making all necessary corrections. For the other wavelengths in the solar continuum, we derive very similar results. The solar radius observed with the Solar Diameter Imager and Surface Mapper II during the period 2011–2013 shows variations shorter than 50 milli-arcsec that are out of phase with solar activity.

Key words. astrometry – Sun: fundamental parameters – Sun: activity

1. Introduction

Measurements of the solar radius are of great interest within the scope of the debate on the role of the Sun in climate change (Rozelot 2001a,b; Schröder 2001). The solar radius is mainly related to the knowledge of the solar atmosphere. However, it is very difficult to measure this fundamental parameter of astrophysical interest. Solar radius determination is one of the oldest problems in astrophysics. Systematic measurements of the solar radius have been made since Antiquity (Rozelot & Damiani 2012). At the end of the nineteenth century, an investigation of the value of the solar radius obtained by meridian observations was carried out by Arthur Auwers (Auwers 1891). He published

a value for the solar radius of 959.63 arcsec that he derived from heliometer measurements made by 29 observers (Wittmann 1977) during the period 1873–1886. In solar modeling, this canonical value has been commonly used and was adopted by the International Astronomical Union (IAU). Solar radius measurements (mostly from ground) are plotted in Fig. 1, showing inconsistent results that are probably caused by different instruments, different spectral domains of measurements, different calculation methods, different definitions (Haberreiter et al. 2008b), and different sites where the conditions of observations are not comparable. Thus, the accurate absolute value of the solar radius is not the subject of a consensus. Indeed, the Earth

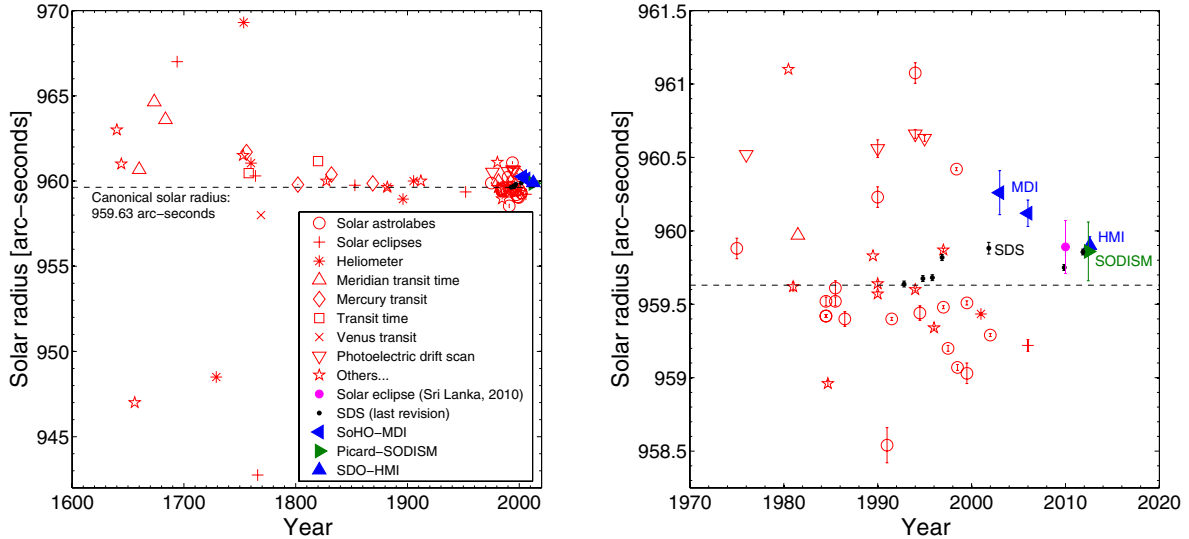


Fig. 1. *Left:* solar radius measurements (red symbols) made since the seventeenth century (Rozelot & Damiani 2012). The mean value of all these measurements is close to 960 arcsec. *Right:* focus on solar radius measurements made since 1970. Solar Disk Sextant (SDS) measurements (Sofia et al. 2013) are represented with black circles. Solar and Heliospheric Observatory – Michelson Doppler Imager (SoHO-MDI) and Solar Dynamics Observatory – Helioseismic and Magnetic Imager (SDO-HMI) records are represented with blue symbols. The Solar Diameter Imager and Surface Mapper (SODISM) measurement obtained during the transit of Venus is represented with a green symbol. Adassuriya et al. (2011) found a solar radius of 959.89 ± 0.18 arcsec (see magenta circle symbol) during solar eclipse in Sri Lanka.

atmosphere generates various hindrances that make morphometric and photometric studies subject to discussion concerning the distinction between solar activity and atmospheric effects merged in ground-based measurements. They include refraction, turbulence, scattering, extinction, and diurnal alternation. It is suspected that the past inconsistencies of the temporal dependence of the solar radius measured from the ground stem primarily from such contingencies (Ribes et al. 1991; Delache & Kroll 1994; Badache-Damiani et al. 2007). Efforts have been made in the past to understand and quantify the effects of atmospheric disturbances on ground-based observations (Brown 1982; Lakhal et al. 1999). The interpretation of ground-based observations, however, remains controversial to date, and recent measurements obtained outside the atmosphere (balloon flights and space instruments) indicate that the canonical value of the solar radius is under-estimated. Ideally, space instrumentation is required for solar radius measurements, but this instrumentation is a high-level technical challenge given the desired accuracy (a few milli-arcsec), and mission duration in a harsh environment (BenMoussa et al. 2013). From the ground, the instruments are not affected by degradation due to space environment, and maintenance can be easily provided. If, in addition, the atmospheric effects are properly monitored and taken into account, they represent our best chance to build the needed long time-series records. That is why an important program of measurements from the ground is associated with the space operations during and after the *Picard* mission. The *Picard* program (Thuillier et al. 2006) owes its name to Jean Picard, considered as a pioneer of precise modern astrometry. *Picard Sol* comprises the Solar Diameter Imager and Surface Mapper II or SODISM II (a copy of the SODISM space instrument), the turbulence monitor (Moniteur d'Images Solaires Franco-Algérien or MISOLFA), and the additional instrumentation. The main objectives of the *Picard Sol* mission are:

- to understand the influence of the atmosphere on the solar radius;

- to determine the relation between the turbulence parameters and the measured solar radius;
- to determine whether small-angle scattering by aerosols could also impact significantly the metrologic accuracy;
- to compare the solar radius measurements obtained with SODISM II and ground-based instruments (to identify possible biases);
- to continue solar radius measurements with ground-based instruments.

2. Historical solar radius measurements at Calern Observatory

The solar radius survey was initiated in 1975 with the Solar Astrolabe at Calern Observatory (France). Simultaneously with visual observations on the same instrument, a program of charge-coupled device (CCD) records was conducted, which started in 1989. The coherence of visual and CCD measurements thus obtained over ten years permitted qualifying the whole visual series, which appeared to be free of systematic personal effects (Laclare et al. 1999). The DORAYSOL (Définition et Observation du Rayon Solaire) instrument was then designed and also developed at Calern Observatory. The principle of this instrument remains the same as that of the Solar Astrolabe (timing the crossing of a parallel of altitude by the Sun), but a prism at a varying angle enables more daily measurements. The DORAYSOL mean solar radius of 959.48 arcsec (with $\sigma = 0.32$ arcsec) was deduced from 19 169 measurements between years 2000 and 2006 (Morand et al. 2010). Data were corrected for atmospheric refraction, but not for turbulence. For the same period, a mean solar radius of 959.55 arcsec (with $\sigma = 0.26$ arcsec) was deduced from 371 Astrolabe measurements (with the same corrections). Measurements of the solar radius made at Calern with the Solar Astrolabe over two solar cycles (between 1978 and 1994) show apparent variations anti-correlated with solar activity defined by the number of sunspots (Laclare et al. 1996). These results have raised many questions

and led to the development of the dedicated *Picard* mission. Simulation of atmospheric effects on the solar radius measurements made at the Solar Astrolabe also showed the influence of seeing conditions and the importance of having a monitor that records the image quality (Lakhal et al. 1999). The idea of developing MISOLFA (Irbah et al. 2001; Assus et al. 2002) established itself, to run in conjunction with the *Picard* space mission and SODISM II. Thus, the *Picard* program contributes to the historical solar radius series initiated at Calern Observatory.

3. Solar radius variability

Possible temporal variations of the solar radius are important as an indicator of internal energy storage and as a mechanism for changes in the total solar irradiance (TSI). Long-term or cyclic variations in the solar luminosity can be related to the corresponding changes in the solar radius R_{\odot} and effective temperature T_{eff} of the Sun by deriving the Stefan-Boltzmann equation:

$$\frac{\Delta \text{TSI}}{\text{TSI}} = 2 \times \frac{\Delta R_{\odot}}{R_{\odot}} + 4 \times \frac{\Delta T_{\text{eff}}}{T_{\text{eff}}} \quad (1)$$

Thus, it is interesting to estimate the solar radius variations with the solar cycle. If we assume that the observed TSI variations over a solar cycle ($\sim 0.1\%$) represents an upper limit for the luminosity variation and assuming no variation in T_{eff} , the strongest possible variation ΔR_{\odot} of the solar radius cannot exceed 0.5 arcsec during a solar cycle. Periodicities of solar activity with periods longer than the sunspot cycle (e.g., the 87 year Gleissberg cycle or the 210 year Suess cycle) have been found and fueled a discussion on the influence of solar variability on the Earth's climate (Braun et al. 2005). The potential link between solar activity and solar radius variations remains a matter of debate, however, requiring both modeling and measurements with enough accuracy over long periods. The relationship between the solar radius and the solar activity is the field of measurements and solar modeling. One of the first researchers to raise questions about the solar radius variations was Hermann Helmholtz (1821–1894), who proposed a theory for the solar luminosity that states that the Sun had been larger in the past and was slowly collapsing into itself because of its own gravity, releasing gravitational energy in the form of light and heat. But that was before nuclear fusion was discovered. Eddy & Boornazian (1979) were pioneers in the field of measuring solar radius variations. From the analysis of Greenwich meridian transit measurements over more than a century (1836–1853), they found a statistically significant secular decrease of the solar diameter of about 0.1% per century, which is even more than the rate proposed by Helmholtz in 1854 to explain solar luminosity. Later, however, while analyzing larger datasets spanning 265 years, Gilliland (1981) reported a marginally significant secular decrease of only around 0.1 arcsec per century. Other analyses concluded that there has been no detectable variation of the Sun over the past 250 years (Parkinson et al. 1980). Michel Toulmonde compiled all the solar radius measurements made between 1660 to 1995 and concluded that the mean solar radius at one astronomical unit is 960.0 ± 0.1 arcsec. His investigations did not reveal any substantial secular variation in the solar radius (Toulmonde 1997). However, it is very difficult to extract a trend in the solar radius from historical data. Thus, a possible long-term trend in solar radius records is still a matter of debate. On the one hand, the variability of the solar radius can be analyzed during a solar cycle. Historical solar radius measurements performed at the Calern

site have revealed an anticorrelation with solar activity (Laclare et al. 1996) for a period covering solar cycles 21 and 22 (1978–1994). However, during solar cycle 23, ground-based records (Solar Astrolabe and DORAYSOL) showed no clear correlation or anticorrelation between the solar radius and the activity of the Sun (Morand et al. 2010). The Solar Disk Sextant (SDS) experiment shows the solar radius variability through its seven balloon flights during the years 1992 to 2011. The solar radius is found to vary over that period by up to 0.2 arcsec (Sofia et al. 2013), but the variation is not in phase with solar activity. Data from the Michelson Doppler Imager (MDI) instrument onboard the Solar and Heliospheric Observatory (SoHo) cover the whole solar cycle 23 and show no evidence of secular trends in the solar radius, or variations attributable to the 11 year cycle. Systematic changes in the solar radius with the sunspot cycle must be smaller than 23 milliarcsec (mas) peak-to-peak (Kuhn et al. 2004; Bush et al. 2010). Solar radius variations for different instruments are plotted in Fig. 2, showing some inconsistent results. The MDI result, even if often considered as the most reliable to date, would therefore certainly gain in being confirmed by other dedicated solar missions, such as *Picard*. Foukal et al. (2006) concluded that it is unlikely that solar radius measurements can reveal deeper-lying sources of solar irradiance variations, as was originally hoped. This is coherent with both the fact that modeling the net contribution of sunspots, faculae and plages is able to explain at least 90% of the observed cycle TSI variations (Ball et al. 2012), and the fact that no observable solar radius variation is expected from these surface effects (Spruit 1991). Therefore, changes in the size of the solar disk contribute probably negligibly to the TSI variations during a solar cycle. Coherent long-term measurements are therefore still needed to determine any significant variations of the solar radius during a solar cycle or any secular trend. This is the aim of the *Picard SOL* project in continuation of the series started at Calern observatory in 1978.

4. Picard Sol, a ground-based facility for long-term measurements

The *Picard* program includes a ground-based observatory consisting of different instruments based at the Calern site (Observatoire de la Côte d'Azur, France). *Picard Sol* and its instruments were described in detail by Meftah et al. (2012). SODISM II is a multiwavelength full disk solar imager specially designed for metrological solar radius measurements. MISOLFA (Corbard et al. 2010; Irbah et al. 2010; Ikhlef et al. 2012) is a high-cadence solar limb imager allowing us to measure the spatio-temporal parameters of the local turbulence. The photometer provides a quality index of pictures taken by SODISM II (aerosol optical depth or thickness and water vapor). The pyranometer measures the luminous flux received and provides another quality index for SODISM II measurements. The visible wide-field camera is used to detect the location of clouds.

4.1. The SODISM II ground-based instrument and solar radius measurements

For the space mission, two identical units were developed. One unit named SODISM (Meftah et al. 2014b) was launched on 15 June 2010, and the second was installed some months later at Calern Observatory (N $43^{\circ}44'53''$ latitude, E $6^{\circ}55'36''$ longitude and altitude of 1271 m). This ground-based unit, named SODISM II, is placed in a vacuum tank (Fig. 3) and pointed toward the Sun.

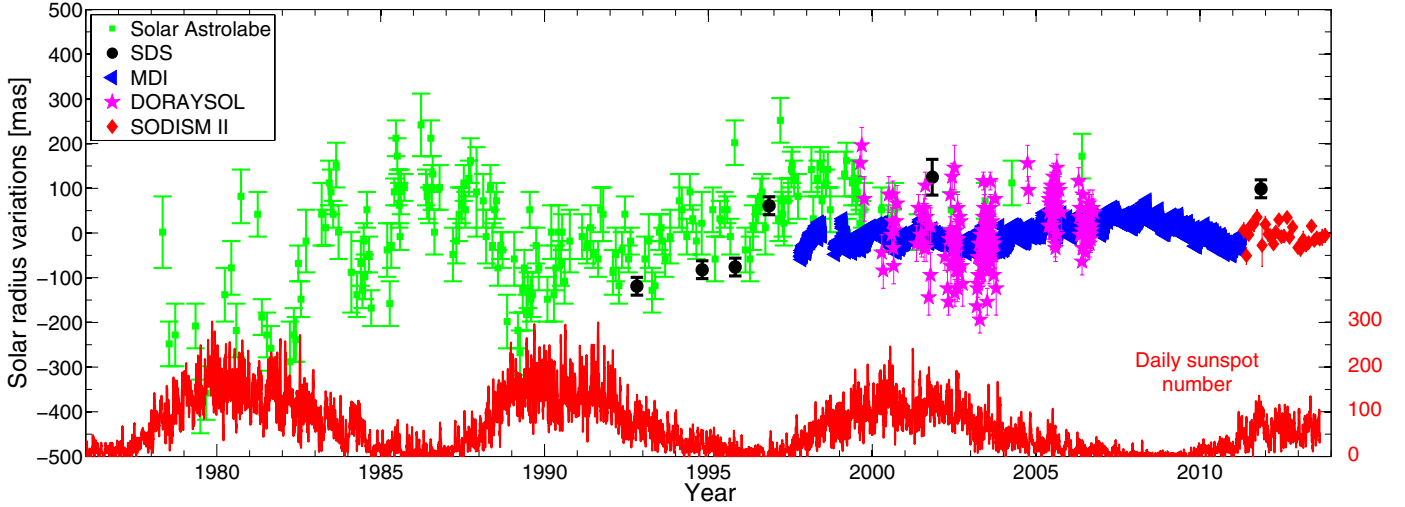


Fig. 2. Evolution of the solar radius variations over time for ground instruments (Solar Astrolabe, DORAYSOL and SODISM II monthly mean at 782.2 nm), balloon experiment (SDS), and space instrument (MDI) vs. daily sunspot number time-series. For each series, the mean has been taken as reference value.



Fig. 3. View of the SODISM II equatorial mount. The ground-based telescope is placed in a vacuum tank closed by a glass window.

SODISM II is an 11 cm diameter telescope with a CCD at its focal plane. One image is recorded every minute with the instrument. It is a Ritchey-Chrétien telescope (to minimize both spherical and coma aberrations) with a focal length of 2626 mm, and an aperture of F/23 with a central obscuration of 40% in diameter (F/30 and 50% for the main channel). This aperture was chosen for geometric resolution. The field of view is $\sim 36 \times 36$ arcmin. The detector is a 2048 by 2048 pixel CCD array with square $13.5 \mu\text{m}$ pixels (~ 1.06 arcsec per pixel). During nominal operations (solar pointing), the Sun is the only significant light source and it almost fills the field of view. This is why no external baffles were foreseen. This design has some field curvature, but image quality is only required at the Sun edge, so the focus is adjusted to this. The SODISM II main optical path consists essentially of a front window, a primary mirror (M1), a secondary mirror (M2), interchangeable interference filters, and a CCD. These choices about the optical configuration and spectral channels determine the core design of SODISM II, but the instrument has been supplemented with a number of important design features that augment its capacities:

1. the whole SODISM II instrument is in primary vacuum at ~ 10 mbar;

2. the whole SODISM II assembly is thermally regulated at ~ 20 °C;
3. the Sun image is stabilized on the detector by the equatorial mount (better than ± 0.5 arcsec during the exposure time);
4. a front window bears a reflective and absorbing coating on its inner side, which divides the penetration of solar flux inside the instrument by ~ 20 ;
5. two successive filter wheels permit inserting one of the spectral filters (between 393.37 and 1025.0 nm) and other refractive elements (lens for stellar operations), or to leave the optical path open;
6. a $2k \times 2k$ frame-transfer CCD is placed at the focal plane. A shutter mechanism provides it with dark conditions except within the duration of its electronic exposures. The CCD is anti-reflective coated;
7. a Peltier and a cold finger remove the heat at the back of the CCD to cool it (-10 °C ± 0.2 °C) and decrease its dark-signal during nominal operations. The low CCD temperature and the dark conditions granted by the shutter provide the relatively slow readout of the camera (~ 22 s).

Two filters wheels carry a set of interference filters with specific roles, as shown in Table 1. The central wavelengths of the five spectral bands (viz. 393.37, 535.7, 607.1, 782.2 nm, and 1025.0 nm) ensue from the following rationale. The photospheric bandpasses (535.7 to 1025.0 nm) were selected for being quasi-free of Fraunhofer lines to account for the solar continuum and to therefore neglect any overlying structure. They also had to perpetuate valuable historical series, or to initiate new time-series if a compelling case could be made. A narrow bandpass centered around 535.7 nm was chosen for its heritage with the Calern measurements (Solar Astrolabe and DORAYSOL), although they were carried out in a wider bandpass of around 548 nm (Lacleare et al. 1996). SODISM II is a replica of the space instrument and used two different filters at 535.7 nm for solar astrometry (a) and helioseismic observations (b). Furthermore, SODISM probes the solar interior via an helioseismic analysis of the solar disk and limb images at 535.7 nm (b), and via astrometric investigations at the limb. For our ground-based measurements, we kept these two filters at 535.7 nm to monitor the aging process. In both cases, we are beyond the characteristic time of the turbulence, which is

Table 1. SODISM II channels, characteristics, and relationship with other instruments.

Wavelength	Solar atmosphere	Bandwidth [nm]	Exposure time [s]	Role/relationship
393.37 nm	Ca II K line	~0.7	1.70	Chromosphere influence
535.7 nm (a)	Continuum	~0.5	1.30	Solar Astrolabe and DORAYSOL
535.7 nm (b)	Continuum	~0.5	8.90	Solar Astrolabe and DORAYSOL
607.1 nm	Continuum	~0.7	1.28	PSPT, SDS, SDO-HMI
782.2 nm	Continuum	~1.6	1.43	SDM
1025.0 nm	Continuum	~6.4	1.70	New time-series

Table 2. Solar radius observations in arcsec (") at one astronomical unit (AU).

Instrument, site, authors	Years	Solar radius ["']	λ [nm]
Solar Astrolabe, Calern (Fr), Laclare et al. (1999)	1975–1998	$959.51 \pm 0.01^*$	540.0
SDM, Boulder (US), Brown & Christensen-Dalsgaard (1998)	1981–1987	$959.65 \pm 0.01^{**}$	800.0
SDS, Balloon experiment (mean value), Sofia et al. (2013)	1992–2011	959.76 ± 0.01	615.0
DORAYSOL, Calern (Fr), Morand et al. (2010)	1999–2006	$959.48 \pm 0.01^*$	548.0
SoHO-MDI, in space (Transit of Mercury), Emilio et al. (2012)	2003, 2006	960.12 ± 0.09	676.78
Picard-SODISM, in space (Transit of Venus), Meftah et al. (2014a)	2012	959.86 ± 0.20	607.1
SDO-HMI, in space (Transit of Venus), Hauchecorne et al. (2014)	2012	959.90 ± 0.06	617.3

Notes. (*) Solar Astrolabe and DORAYSOL data were corrected for atmospheric refraction and for zenith distance, but not for turbulence.

(**) Corrected data to one astronomical unit.

measured in milliseconds. A second narrow channel was adopted at 607.1 nm. It can be compared with the 590–670 nm spectral range of the SDS balloon experiment (Sofia et al. 1984, 2013). This band has been used by the Precision Solar Photometric Telescope (PSPT) and produces images at 607.1 nm (Coulter et al. 1996) in the red continuum¹. It can also be compared with the 617.3 nm continuum spectral range of the SDO-HMI space experiment (Scherrer et al. 2012; Schou et al. 2012). A third Fraunhofer-line-free bandpass is centered on 782.2 nm. It can relate to the Solar Diameter Monitor (SDM) measurements at 800 nm (Brown & Christensen-Dalsgaard 1998). A last Fraunhofer-line-free bandpass is centered on 1025.0 nm. With this wavelength, we initiate a new time-series, and while remaining in the photospheric continuum, we hope to minimize the impact of turbulence for ground-based observations. The chromospheric channel is centered on 393.37 nm (Ca II K line, singly ionized calcium, which is magnetically active). This permits us to image the low chromosphere and particularly, to observe the regions with an enhanced contrast. It can be compared with the PSPT experiment. References to solar radius observations corresponding to our channels are listed in the Table 2. It is important to note, however, that the uncertainties quoted by the authors for each set of measurements are not directly comparable because they cover periods of different lengths and do not all include estimates of the contribution from systematic effects.

SODISM II has recorded more than 75 000 solar images since the beginning of the mission in May 2011. Figure 4 shows a sample of Level-1 solar images at the six wavelengths recorded in 2013. All images were corrected for dark-current and flat-field. Thus, we can track the solar radius.

4.2. The MISOLFA instrument and turbulence monitoring

Simulation of atmospheric effects on the solar radius measurements shows the influence of seeing conditions (Lakhal et al. 1999). There are three common descriptions of the astronomical seeing conditions at an observatory of (i) the Fried parameter r_0 (size of a typical lump of uniform air within the turbulent

atmosphere) and τ_0 (the time-scale over which the changes in the turbulence become significant); (ii) the turbulence vertical profile $C_n^2(h)$; and (iii) the full width at half maximum (FWHM) of the seeing disk. Using the Von Kàrmà̄n's model, it is shown that turbulence simulated through the Fried parameter (r_0) modifies the measured solar radius (Ikhlef et al. 2012). Figure 5 presents the effect of turbulence as a function of r_0 on SODISM II solar radius for each wavelength and shows that the systematic bias decreases as r_0 increases. At 535.7 nm, we note that for r_0 equal to 7 cm, the asymptotic value is reached, but with a bias of ~0.18 arcsec. Figure 6 shows the limb-shape evolution for different values of r_0 (FWHM of the solar limb first derivative decreases as r_0 increases). This indicator may also be used to correct the solar radius measurements obtained by SODISM II (see also Fig. 13). Thus, atmospheric turbulence modifies the ground-based observed shape of the solar limb, and this effect is always considered to be the source of the discrepancies among the radius determinations. These numerical results confirmed turbulence as a perturbing phenomenon that needs correcting for about few tens of arcsec, and led to build a dedicated instrument (MISOLFA) to measure the turbulence parameters. MISOLFA is a solar seeing monitor associated with a CCD detector at its focal plane. This instrument is placed on an Alt-Azimuth mount support, which rotates MISOLFA about two perpendicular axes. The instrument has been described in detail by Irbah et al. (2010). Thirty-two solar limbs are recorded every second with the instrument. It is a Cassegrain-coudé telescope with a focal length of 10 000 mm, a main entrance pupil of 252 mm, and an aperture of F/40. The field of view is $\sim 2.1 \times 1.6$ arcmin. The detector is a 640 by 480 pixel CCD array with square $9.9 \mu\text{m}$ pixels (~ 0.20 arcsec per pixel). The MISOLFA design is based on the statistical analysis of the entry angle fluctuations defined as the slope in each point of the wavefront through the pupil. In the case of diurnal conditions, these fluctuations are shown by the observation of the solar limb. Two measurement channels are provided:

1. a direct channel in which the Sun image is formed on a CCD camera with suitable magnification. This channel enables the evaluation of the spatial coherence parameters of

¹ http://lasp.colorado.edu/pspt_access/

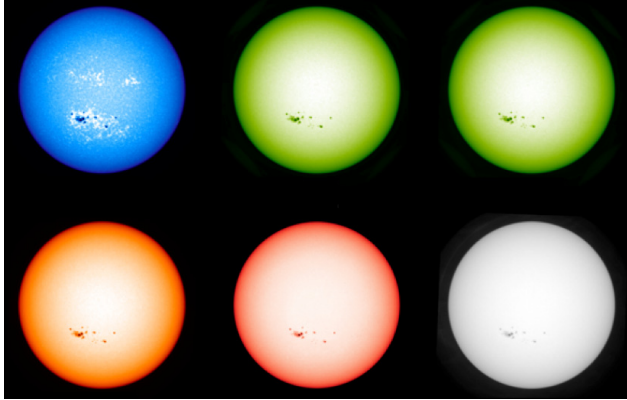


Fig. 4. Top: solar images in the different SODISM II channels (Level-1 data products): 393.37, 535.7 (a) and 535.7 nm; (b) starting from left to right. Bottom: solar images for other wavelengths: 607.1, 782.2 and 1025.0 nm starting from left to right.

the wavefront (Fried parameter, outer scale and isoplanatism domain) as well as the turbulence profiles;

2. a second channel (pupil channel) that forms the image of the pupil through a diaphragm placed on the solar limb is used to evaluate the wavefront temporal parameters using photo-electric detectors (photodiodes).

The first MISOLFA objective is to quantify the atmosphere effects on the ground-based solar radius measurements made by SODISM II, and the second is to validate the correction methods for this effect. To achieve these goals, the MISOLFA instrument measures all the optical parameters, which allows the observation conditions in which the measurements are made to be quantified. These parameters are the Fried parameter r_0 , the spatial coherence outer scale L_0 , the isoplanatism domain θ_0 , the temporal characteristic(s) of the wave front evolution τ_0 , and the turbulence vertical profile $C_n^2(h)$. To perform solar radius measurements, the chosen wavelengths are the same as that of the SODISM II instrument (393, 535, 607, 782, and 1025 nm). Currently, only one wavelength is operational (535 nm with $\Delta\lambda = 2.5$ nm). The exposure time of SODISM II images at 535.7 nm (a) is 1.3 s. The mean recorded turbulence characteristic time (τ_0) is about 20 ms, therefore SODISM II images can be considered as long-exposure times (see Fig. 5).

4.3. The PAPS photometer and aerosols detection

Details about liquid and solid aerosols, especially cirrus, sub-visible cirrus, and generally transparency of the atmosphere above the observation site are required to properly correct the SODISM II observations. Aerosol influence on solar radius measurements has motivated our interest. Indeed, all the atmospheric effects may have an impact on our measurements. Thus, an automatic photometer (Photomètre Automatique *Picard Sol* or PAPS) provides a quality index for the pictures taken by SODISM II. The main purpose of PAPS is measuring Sun and sky radiance to derive the total column water vapor (cm), ozone, and aerosol properties using a combination of spectral filters. This instrument is included in the aerosol robotic network (AERONET) program (Holben et al. 2001). Aerosol optical thickness (AOT) is a quantitative measurement of the extinction of solar radiation by aerosol scattering and absorption between the point of observation and the top of the atmosphere. AOT can be determined from the ground through measurements of the spectral transmission of solar

radiation through the atmosphere using the *Picard Sol* photometer. To perform solar radius measurements, the wavelengths (340 nm, 380 nm, 440 nm, 500 nm, 675 nm, 870 nm, and 1020 nm) are chosen very close to those used by the SODISM II instrument. Diffusion by aerosols affects image contrasts, and Fig. 7 shows the effect of different atmospheric conditions on two adjacent days on the limb-shape and its first derivative. The interpretation of Fig. 7 in terms of the influence of aerosols alone is not possible because the optical turbulence in the two cases is not necessarily the same. Simulations show that the decrease of contrast does not lead to significant bias on the location of the inflection point. It affects the precision of the measurement, however.

4.4. The PPS pyranometer and solar radiation monitoring

The *Picard Sol* pyranometer (Pyranomètre *Picard Sol* or PPS) is a radiometer that measures on a flat surface the sum of the luminous flux received from the Sun and the scattered solar light by the atmosphere after many reflections between the ground and atmosphere particles (molecules and aerosols). In clear atmospheric conditions, the received energy has a distribution as a function of time (shape with maximum at local solar noon). If there are clouds or more generally aerosols, this distribution departs from the previous shape by a decrease of the energy received by the instrument. This is seen by comparing the received energy distribution measured on an adjacent clear day. However, there are cases of enhanced solar irradiance at ground level that occur when there are high altitude cloud such as altocumulus and cirrus. This instrument detects this effect by an increase of the received energy. Figure 8 shows such an occurrence. The pyranometer detects these circumstances, but integrates the whole sky and therefore does not provide the relevant information in the direction of the Sun alone. An automatic determination of cloud type is possible with these data (Duchon & O’Malley 1999), however, which would be interesting to combine in a future work with the information on aerosols provided by PAPS.

4.5. The CPS visible wide-field camera and nature of the detected clouds

A *Picard Sol* visible wide-field camera (Caméra *Picard Sol* or CPS), operating in color (SBIG AlISky-340, Santa Barbara Instrument Group) is used to detect the location of clouds, which the pyranometer and photometer do not allow. This instrument permits detecting thin cirrus because of its great sensitivity and provides complementary information to the pyranometer and the photometer (aerosols). CPS brings us information about the quality of the sky (Fig. 9) and high-altitude clouds.

5. Picard Sol instrumental calibrations and operations

5.1. Picard Sol instrumental calibrations

5.1.1. Angular calibration for the SODISM II plate-scale determination

The knowledge of the SODISM II plate-scale is a fundamental parameter to derive an absolute value of the solar radius. Moreover, to discuss its wavelength dependence, we also need to obtain the plate-scale at different wavelengths. This can first be estimated theoretically using the appropriate optical

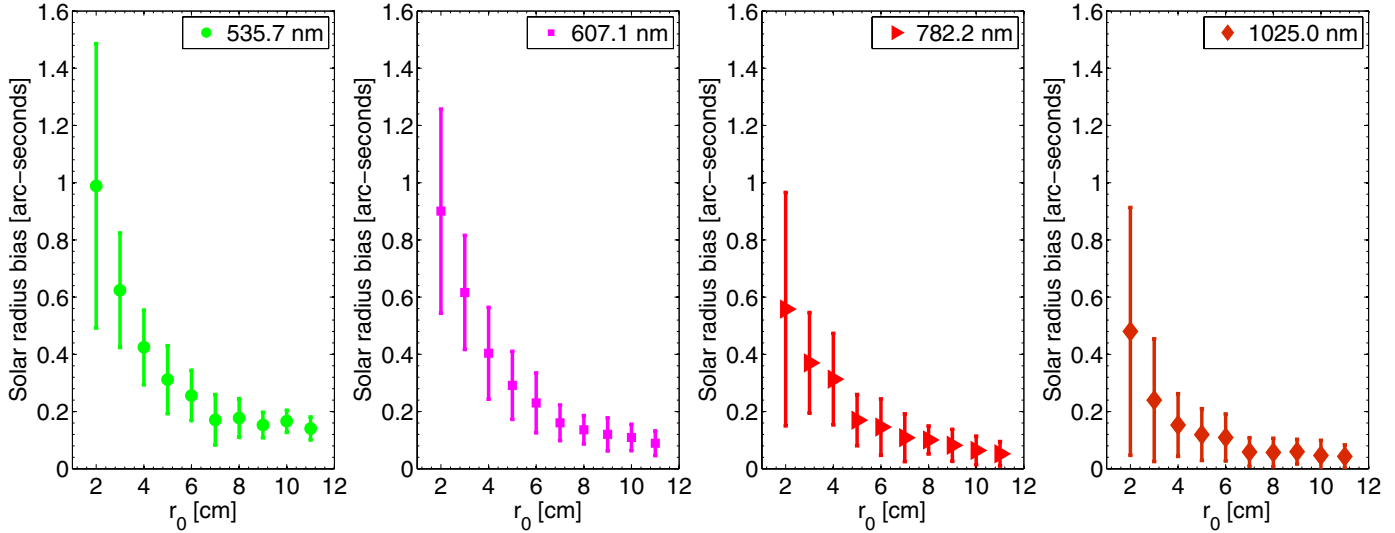


Fig. 5. Simulation of the bias due to Fried parameter (r_0) on SODISM II measurements (Von Kàrmàn model) with long-exposure times ($50 \times \tau_0$).

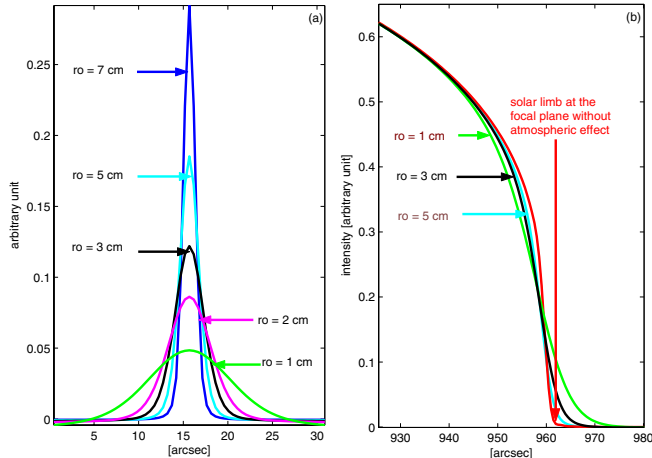


Fig. 6. Effect of turbulence on the limb-shape **b)** and its derivative **a)** as a function of r_0 .

configuration (optical thickness of the different filters, point spread function (PSF), etc.). However, given the level of accuracy required for our measurements, a specific experimental calibration is also required. This is achieved by observing pairs of stars selected according to their brightness and angular distances, which must be close to 30 arcmin. The highest acceptable magnitude is 5 and the elevation must be greater than 20 arc-degrees given the limitation of the equatorial mount and to avoid strong atmospheric refraction. Five pairs of stars have been selected for measurements at different periods of the year (Meftah et al. 2012). Data processing includes three types of corrections:

1. proper motion of the star, parallax depending on the position of Earth around the Sun, and aberration;
2. chromatic effects, because the measurements are made without interference filter using stars of different types to infer the plate-scale conversion at the wavelength of the SODISM II measurements through an interference filter of known optical thickness;
3. thermal effects, because the measurements are made in the night-time. Thermal corrections to the focus applied for night-time star observing are weak. Indeed, our front window is inside the vacuum tank, which is controlled in temperature.

Another way for estimating SODISM II plate-scale is to use the solar radius obtained by the SODISM space instrument during the Venus transit as reference (Meftah et al. 2014a). The synthesis associated with these three approaches is given in Table 3. Two experimental calibrations (ACPS and SRPS) lead to results that agree at a level better than 5×10^{-5} . These results and the wavelength dependence are strongly linked to the knowledge and proper modeling of the instrumental optical configuration, however. In the following, we adopt the SRPS values, with which we associate conservative uncertainties of 10^{-4} . This introduces an uncertainty of ± 0.090 arcsec on the determination of the absolute value of the solar radius.

5.1.2. SODISM II radiometric calibrations

The image data of the SODISM II solar telescope require dark-signal corrections (Hochedez et al. 2014). SODISM II dark-current images have been performed every day and with an exposure time of 1.4 s. All images have been corrected for dark-current.

Our images also require flat-field corrections, which consist of measurements allowing to set the pixels responsivity on the same photometric scale. This is potentially important for the precise determination of the limb-shape from which the solar radius is obtained. The whole SODISM II system must be used, including the interference filters. For flat-field measurements, the absence of clouds is mandatory, which is ensured by taking into account the observations gathered by the PAPS photometer, the PPS pyranometer, and the CPS camera. We used the method developed by Kuhn et al. (1991), which is based on the displacement of multiple images from the same source, here, the Sun. The set of images covers the CCD by scanning the Sun using the solar mounting. During the displacement, the Sun irradiance constancy is checked by using the pyranometer data and the integrated intensity within the image. As expected, operation made around solar noon is preferable. For each wavelength, the duration of the operation is around 80 minutes for acquiring 64 images. It is difficult to ensure that we keep excellent and stable conditions over such a long period and therefore it is very difficult to obtain a good flat-field on a regular basis for all wavelengths this way. A new method based on contrast maps has been developed and is being tested. This method basically assumes that the limb darkening function (LDF) is theoretically

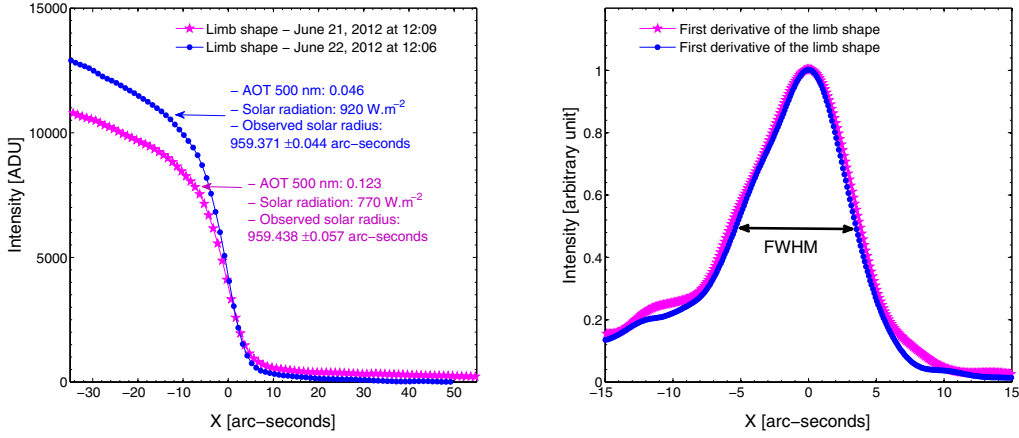


Fig. 7. *Left:* atmospheric effect on limb-shape at 535.7 nm (b). *Right:* evolution of the limb-shape first derivative. FWHM of the solar limb first derivative decreases as AOT decreases.

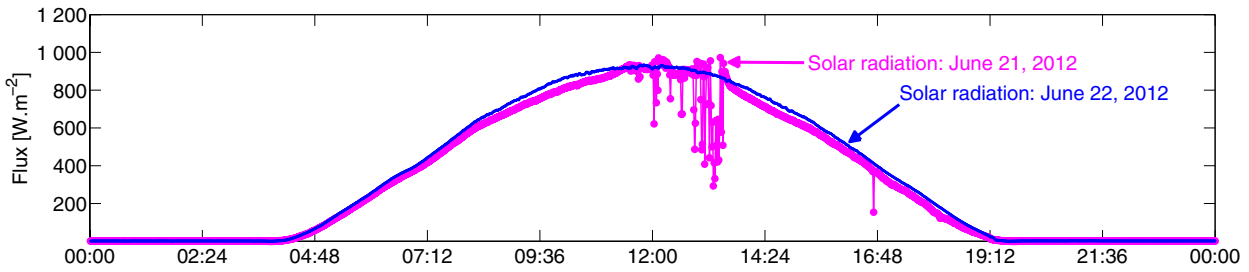


Fig. 8. Superposed solar radiation received on an horizontal plane in clear and slightly perturbed atmospheric conditions. The blue curve shows the measurement on the next day to allow a comparison with clear air conditions.

Table 3. SODISM II plate-scale for different wavelengths.

Wavelength [nm]	Optical thickness [mm]	TPS	ACPS	SRPS	SRPS-ACPS
393.37	12.328	1.060818	1.061076	1.061102	2.63×10^{-5}
535.7 (a)	12.297	1.060792	1.061057	1.061060	2.75×10^{-6}
535.7 (b)	12.303	1.060796	1.061061	1.061064	2.92×10^{-6}
607.1	12.225	1.060757	1.061016	1.061025	9.42×10^{-6}
782.2	12.341	1.060781	1.061083	1.061049	-3.40×10^{-5}
1025.0	12.080	1.060679	1.060931	1.060947	1.54×10^{-5}

Notes. The optical thickness column corresponds to a characterization of the different filters. SODISM II interference filters do not have the same optical thickness (index, thickness of optical elements used, etc.). Thus, each wavelength has its own plate-scale correction factor. Theoretical plate-scales (TPS in arcsec pixel^{-1}) are obtained from an optical model using the appropriate optical configuration. Angular calibration plate-scales (ACPS in arcsec pixel^{-1}) are obtained during specific campaigns on star doublets. SODISM reference plate-scales (SRPS in arcsec pixel^{-1}) are obtained from the knowledge of the solar radius measured by SODISM at 607.1 nm during the Venus transit. Six digits of the TPS, ACPS, and SRPS entries are significant.



Fig. 9. Three typical situations encountered during operations that show different atmosphere transparency. They provide additional information for the instrumental calibration.

well known at least up to 0.8 solar radius and can be removed from each image after a proper normalization. The resulting contrast map is then assimilated to a uniformly illuminated plane, and the imperfect tracking of the Sun center during an observation sequence is used to build the flat-field. The effects of active

regions are eliminated by taking for each pixel a median value over the whole sequence of contrast maps (Fig. 4). Our first tests have shown that the effect of flat-field corrections on the determination of the mean inflection point location is lower than 1 mas.

5.2. Picard Sol operations

The seeing monitor MISOLFA and the solar imager SODISM II have observed the Sun together since March 2011. SODISM II records full solar images at several wavelengths, with an optimal cadence of one image per minute (nominal operations since May 6, 2011). At the same time, MISOLFA records a continuous sequence of high-resolution (0.2 arcsec) and high-cadence (32 images per second) limb images at 535 nm from the two opposite sides of the solar disk as well as the temporal irradiance fluctuations on the pupil channel.

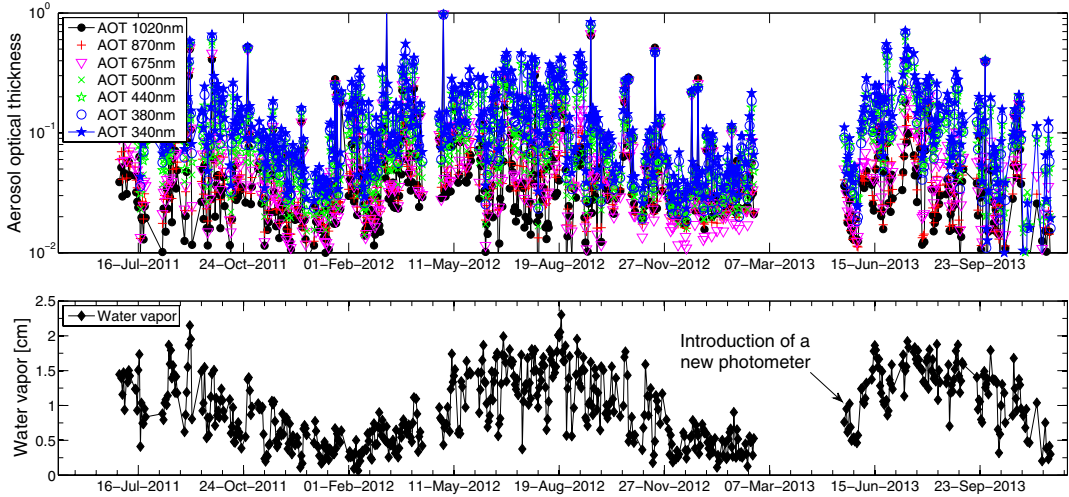


Fig. 10. Aerosols optical thickness (AOT) and water vapor content as a function of time at the observation site of Calern. The measurements obtained are part of data selection process.

6. Data selection, SODISM II corrections, and uncertainty budget

6.1. SODISM II data selection

The main causes of perturbation acting on the solar images are the transparency of the atmosphere and turbulence. The transparency of the atmosphere is of prime importance for the quality of the measurements. Scattered light has an effect on the image contrast and the limb-shape. Correcting for it would be difficult even if the detailed structures of the aerosols cloud (solid or liquid) were known. The best way consists of performing a drastic data selection. To achieve it, we dispose of key information about the aerosols load and presence of cirrus, which is more frequent in summer (constituting June, July, and August) than in winter (December, January, and February). The additional instrumentation (photometer, pyranometer and camera) provides a quality index for solar images taken by SODISM II and allows us to reject all data that are contaminated by atmospheric effects. Figure 10 shows that in terms of atmospheric aerosol, local winter is preferable. However, the lower mean Sun elevation in winter corresponds to a higher air mass, which also affects the mean image contrast. This is why both summer and winter images can pass the data selection process. The only way to minimize the presence of aerosol or to reduce its seasonal variations would be to observe from an observatory at a higher altitude.

6.2. SODISM II corrections

6.2.1. SODISM II correction for Sun-Earth distance (Calern-Sun distance)

The average Sun-Earth distance is called the astronomical unit (1 AU is equal to 149 597 870.700 km). It is a simple matter to correct the solar radius measurements within any time to their corresponding values at 1 AU based on the well-known ephemeris (Calern observatory). An error of one minute on dating images (impact on ephemeris value) would correspond to a maximum of 1 mas uncertainty on the determination of the solar radius.

6.2.2. Refraction and SODISM II computational method

Effect of refraction on the mean solar radius is corrected. The key inputs for this correction are temperature (T), pressure (P), and relative humidity (f_h) locally measured with the additional instrumentation. The standard conditions for Calern site are: (i) $T = 15^\circ\text{C}$; (ii) $P = 875 \text{ hPa}$; and (iii) $f_h = 50\%$. For temperature, pressure, and relative humidity, we assumed uncertainties of $\Delta T = 0.5^\circ\text{C}$, $\Delta P = 1 \text{ hPa}$, and $\Delta f_h = 5\%$, which are typical for a standard weather station. Thus, the uncertainty on the correction is smaller than 20 mas for zenith distances lower than 70° . In this work, the correction for refraction is directly applied on the mean solar radius. For more accurate measurements, the corrections can be applied individually for each heliographic angle. This method should be used in future work to distinguish and understand the different effects on solar radius measurements (optical aberrations, turbulence, etc.).

6.2.3. Turbulence and MISOLFA measurements

The main source of uncertainty and bias for any ground-based measurement is certainly the effect of optical turbulence. Attempts to reduce this effect were historically made by using the finite Fourier transform definition of an edge on the solar disk (Brown 1982). This definition of the solar edge is based on a filtered integral of the solar signal at the solar limb. This minimizes the influence of the varying slope of the observed LDF that is induced mostly (but not only) by the varying atmospheric conditions such as seeing and scattering. Thus, the effect of turbulence is a spreading of the limb-shape that leads to a decrease of the solar radius. In other terms, turbulence generates a biased solar radius measurement. This bias can be estimated by using a model of turbulence and a given limb-shape. The results are shown in Fig. 5 using the model of Von Kármán (Ikhlef et al. 2012). The bias on solar radius is decreasing with increasing r_0 and reaches an asymptotic value that depends on the wavelength (for solar continuum). As we show below, r_0 found in our observations is around 3 cm (at 535 nm), which implies a bias correction of about 0.6 arcsec, with a root mean square (RMS) of about 0.2 arcsec (at 535.7 nm). MISOLFA and SODISM II are simultaneously operated, which allows us, in principle, to correct each solar radius. The detailed treatment of MISOLFA records is still underway, however, and in this preliminary work, we use

Table 4. Fried parameter measurement performed between June 2010 and May 2012 (monthly median values r_0 and standard deviation σ).

Month	Jan.	Feb.	Mar.	Apr.	May	Jun.	Jul.	Aug.	Sep.	Oct.	Nov.	Dec.
r_0 [cm]	2.82	3.42	2.92	3.71	4.10	4.20	3.88	2.50	3.70	3.45	3.50	2.75
σ [cm]	0.94	1.26	1.11	1.28	1.32	1.32	1.76	1.16	1.24	1.19	0.91	0.50

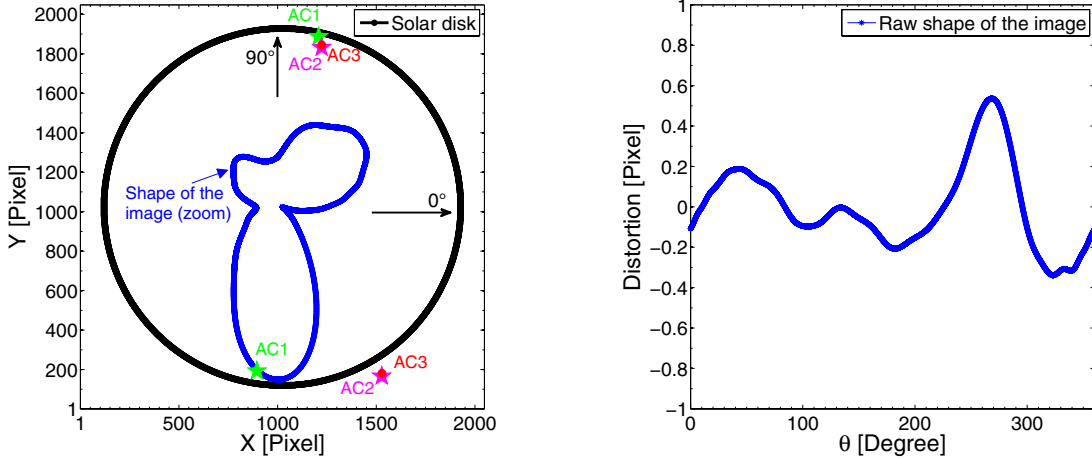


Fig. 11. *Left:* the solar disk as seen on the CCD shown with the black curve. The raw shape of the SODISM II image (solar radius at a given angle minus its lowest value) is represented with the blue curve. The scale is amplified by a factor of 1000. The three stellar angular calibrations (AC) that have been performed are represented by star symbols. The SODISM II plate-scale also depends on the shape of the image. *Right:* average limb position vs. central angle plotted in pixel units. The shape of the image corresponds to a SODISM II optical default (astigmatism). This shape does not change significantly over time (few mas).

only an average value of r_0 . In a future work, the use of monthly averages of the Fried parameter should remove most of the seasonal effects induced by turbulence, but the ultimate goal with MISOLFA is to obtain reliable estimates of r_0 every minute. The Fried monthly averaged parameter measured from 2010 to 2012 is shown in Table 4.

6.2.4. SODISM II distortion and shape of the raw image

We defined the solar radius by the inflection-point position (IPP) of the solar-limb profiles taken at different angular positions (θ) of the image. The IPP is obtained by the passage through zero of the solar limb second derivative. The shape of SODISM II raw image (contour) is obtained from the calculation of all inflection points. Figure 11 shows the raw shape of SODISM II images obtained at low zenith distance to avoid astronomical refraction effects. The shape of the image is at most one pixel (around one arcsec). Knowledge of the image shape is critical for different calibrations (plate-scale) and corrections. Measurements of solar oblateness are not achievable with SODISM II instrument. It has been established from space missions that the difference in equator-to-pole radius is smaller than 10^{-2} arcsec (Kuhn et al. 2012). Thus, we can consider that the shape of the Sun is a perfect solar disk. Therefore, the shape of the image depends on the refraction, turbulence, and optical aberrations. In Fig. 11, the positions of three pairs of stars used for the plate-scale calibration are shown. The values of the plate-scale deduced from the measurements of their angular distance on the CCD were corrected using the information on image distortion provided by the observed shape of the solar disk.

6.2.5. SODISM II PSF

The SODISM II PSF and its effect on the solar limb were studied for the nominal optical configuration (Fig. 12), wherein the

instrument is diffraction limited. Indeed, the SODISM II design and dimensions are such that the size of the Airy diffraction disk is about one arcsecond in the bluest case, which is still larger than any of the expected aberrations. The LDF of HM98 (Hestroffer & Magnan 1998), the COSI code for solar irradiance (Haberreiter et al. 2008a; Shapiro et al. 2010) and 3D hydrodynamic and magneto-hydrodynamic simulations or 3D model (Piau et al. 2011) were convolved by the theoretical PSF of the telescope, and the results for each wavelength are represented in Fig. 12 (LDF, PSF, and first derivative of the LDF convolved with the instrument PSF). The first derivative of the limb is spread over about two arcsec, and the location of the inflection point (maximum of the first derivative) appears to be clearly defined for all LDF models. We then studied the quality of the SODISM II images to see whether a solar radius measurement can be achieved with those data. We show in Fig. 7 (left panel) the solar limb intensity darkening extracted from solar images recorded at 535.7 nm (b) in two typical cases. We next compute the first derivative of these two LDFs to better evaluate their spread (right panel in Fig. 7). The observational curve gives an indication of image quality. The first derivative of the solar limb recorded with SODISM II is significantly wider than the spread expected from the model (Fig. 12, bottom panel at 535.7 nm). The slope of the observed intensity profile – defined as the full width at half maximum of its first derivative – is wider than expected by ~ 6 arcsec. This might be caused by a misalignment of the optical elements (astigmatism), combined with turbulence effects, and thermo-optical effects, which can also blur the image. In itself, this does not disqualify the scientific objective since it is equivalent to having a telescope with a smaller aperture, giving the observed PSF. But it would have to be time invariant that is constant during the entire mission. Thus, we do not seek to obtain the best focus. We simply wish to have a stable instrument. The daily means of observed LDF first derivative FWHM (Fig. 13) show a slight seasonal modulation,

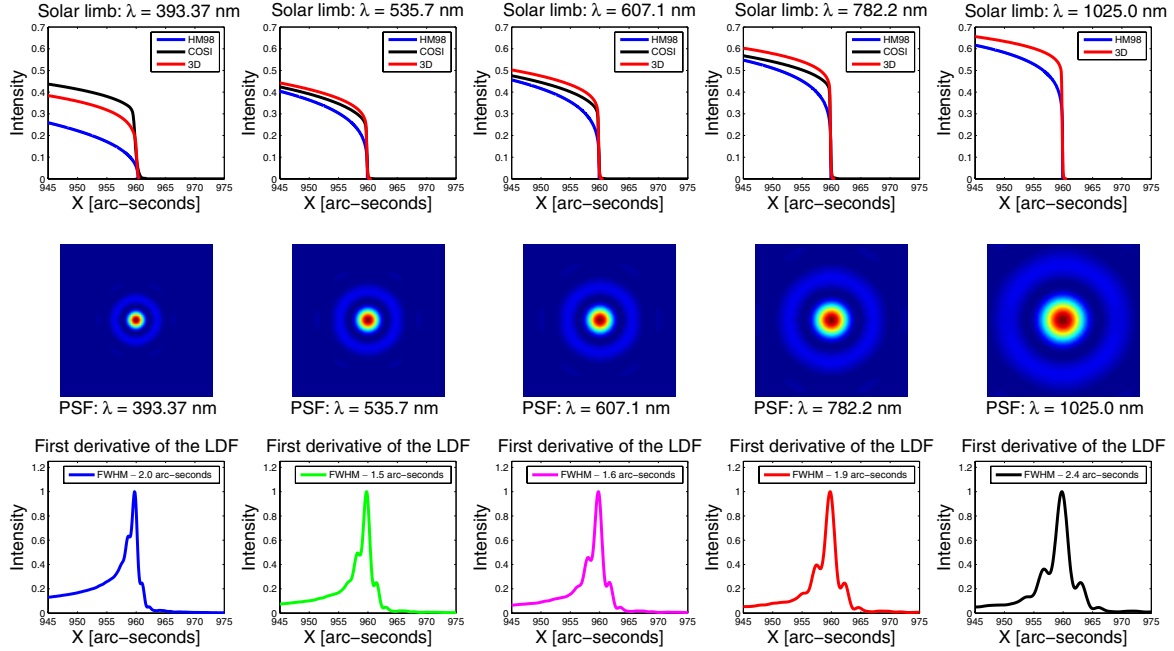


Fig. 12. Top: LDF at 393.37, 535.7, 607.1, 782.2 and 1025.0 nm, for the HM98 (empirical power-law model extrapolated to the limb), COSI models and 3D model. Their convolution with the nominal PSF of SODISM II is dominated by diffraction. Middle: SODISM II PSF for each wavelength. These PSF have been estimated by an optical model of SODISM II. Bottom: first derivative of the convolution between the two observables (LDF and PSF). It can be verified visually that the FWHM of the first derivative of the solar limb is about two arcsec.

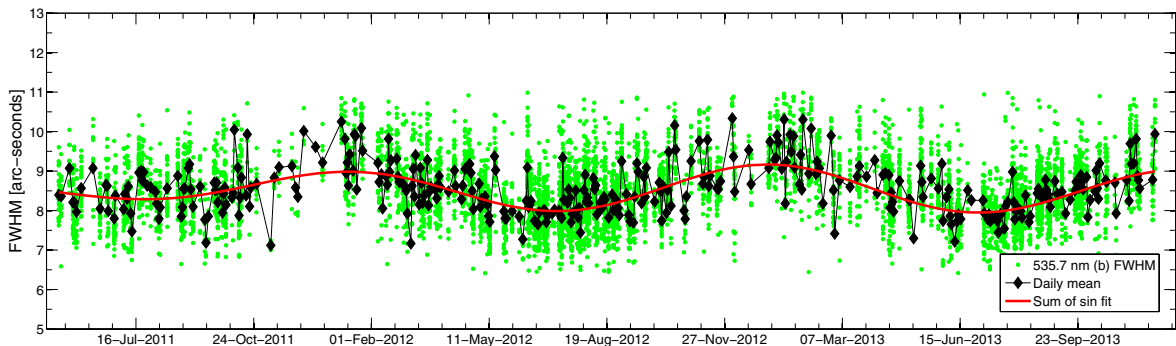


Fig. 13. Evolution of the solar limb first derivative FWHM at 535.7 nm (b) since the beginning of the mission (green dot). The black curve with diamond symbols corresponds to the FWHM of the daily mean at 535.7 nm (b).

however, which is probably related to the seasonal variations of the mean elevation of the Sun in the sky, which modulates both the influence of turbulence and the mean image contrast.

6.3. SODISM II uncertainty budget for determining the solar radius

Uncertainties for the absolute accuracy of the solar radius for different wavelengths are given in Table 5. Turbulence is a major source of uncertainty. The spatial and temporal variations of the refractive index change the path of light as it travels through the atmosphere, causing image motion and blurring. Turbulence limits the resolving power of the telescope. The Fried parameter, which qualifies the observations (seeing), is the dominant element in calculating the phase fluctuation variance. Considering a Kolmogorov model, the Fried parameter (r_0) is related to the angle of arrival fluctuation variance (σ_a^2) by

$$r_0 = 8.25 \times 10^5 \times D^{-\frac{1}{5}} \times \lambda^{\frac{6}{5}} \times (\sigma_a^2)^{-\frac{3}{5}}, \quad (2)$$

where D is the aperture of the telescope (m) and λ is the wavelength (m). This equation was used to compute the Fried parameter, and some results shown in the Table 4. It is predicted from the Kolmogorov theory of turbulence, and the known dispersion of air, that the Fried parameter varies with wavelength as $r_0 \propto \lambda^{\frac{6}{5}}$. As mentioned above, the average Fried parameter r_0 is 3.41 cm at 535 nm. Thus, from the proportional relationship, we can determine the different values of r_0 for SODISM II different wavelengths (3.97 cm at 607.1 nm, 5.38 cm at 782.2 nm and 7.44 cm at 1025.0 nm). Therefore, we know the bias and the associated uncertainty on solar radius measurement for each wavelength (540 ± 170 mas at 535.7 nm, 410 ± 160 mas at 607.1 nm, 160 ± 90 mas at 782.2 nm and 60 ± 50 mas at 1025.0 nm), and that from Fig. 5.

The SODISM II instrument is thermally controlled and appears to be robust against changes on the order of few microns or a few degrees of temperature (Meftah et al. 2014b). Temperatures of the instrument (housekeeping) are measured, and their variations (thermal effects) introduce an uncertainty

Table 5. SODISM II uncertainties for all wavelengths.

Uncertainty sources	535.7 (a)	607.1	782.2	1025.0	Type
Angular calibration	90	90	90	90	Random
Aerosols	–	–	–	–	D ^a
Calern-Sun distance	≤1	≤1	≤1	≤1	Random
Refraction	≤20	≤20	≤20	≤20	Random
Turbulence	170	160	90	50	Random
Optical distortion	–	–	–	–	C ^c
PSF	–	–	–	–	C ^c
Scattered light	–	–	–	–	N ^b
Pointing	–	–	–	–	D ^a
Thermal effects	≤10	≤10	≤10	≤10	Random

Notes. All values are in mas. ^(a) D: Data selection. ^(b) N: Negligible. ^(c) C: Calibration.

smaller than 10 mas on the determination of the solar radius (for each wavelength).

7. Results and discussion

7.1. Solar radius determination

7.1.1. Mean solar radii obtained after refraction correction

An evolution of the solar radius measurements obtained with SODISM II (SRPS reference) is shown in Fig. 14 as a function of time for different wavelengths and after refraction correction. From these corrected measurements, a mean solar radius for each wavelength is given in Table 6. The SODISM II mean radius of 959.237 arcsec (with $\sigma = 0.25$ arcsec) at 535.7 nm (a) is deduced from 20 300 measurements. This is our reference time-series (comparison with historical measurements made at Calern). The various evolutions indicate that with increasing wavelength (solar continuum) the mean solar radius increases. At 393.37 nm, chromospheric emissions are recorded. Given its location above the photosphere, the solar radius is larger than those measured by using photospheric emissions. There is a difference of 700 mas compared with our reference wavelength. Without turbulence and with a perfect instrument, this difference must be on the order of 400 mas. This channel requires a special analysis.

7.1.2. Mean solar radii obtained after turbulence correction

The final SODISM II results (solar continuum), after making all necessary corrections described in the previous sections, are listed in the Table 7. The value of the solar radius is found to be equal to 959.777 arcsec at 535.7 nm (a), while the estimated uncertainties of the measurements are typically smaller than 0.2 arcsec. At 1025.0 nm, the solar radius is smaller than those found at 607.1 nm and 782.2 nm.

7.2. Solar radius variability

The current solar cycle is probably going to be the weakest in 100 years, which is an unprecedented opportunity for studying the variability of the solar radius during this period. The SODISM II measurements we made are reproducible. We did not observe any significant degradation. The solar radius observed with SODISM II results from variations smaller than 50 mas that are out of phase with solar activity. Solar radius variations for SODISM II and different instruments are plotted in Fig. 2,

Table 6. SODISM II mean solar radius (R) for each wavelength and standard deviation (S at 1σ) of the daily mean values after refraction correction.

Wavelength [nm]	N	d	R	S
393.37	11 309	367	959.940''	0.106''
535.7 (a)	20 300	374	959.237''	0.125''
535.7 (b)	11 391	376	959.286''	0.103''
607.1	11 342	350	959.452''	0.126''
782.2	11 351	375	959.716''	0.099''
1025.0	11 759	375	959.772''	0.181''

Notes. N is the total number of measurements gathered between May 2011 and December 2013, and d is the number of observation days.

showing inconsistent results. Nevertheless, we can observe the measurement continuity between SODISM II and MDI.

7.3. Spectral dependence of solar continuum radius

One of the objectives of the PICARD mission is to deduce the spectral dependence of the solar limb profile. A study of the shape of the solar limb (models and observations) was carried out by Thuillier et al. (2011). Several kinds of solar atmosphere models were compared. Some models are constructed empirically for instance that of HM98, but contain no IPP. Others use theoretical models, such as VAL81 (Vernazza et al. 1981), FCH09 (Fontenla et al. 2009), and COSI, or are based on physical principles, such as SH09 (Short & Hauschmidt 2009). Finally, others use 3D numerical simulations. Table 8 compares the IPP for four wavelengths. The different solar models show the same trend and their predictions agree well. The differences (Δ IPP) of the inflection-point position at 607.1 nm, 782.2 nm and 1025.0 nm from the IPP reference at 535.7 nm are smaller than thirty mas for the different models, but numerous studies of solar radius variation at different wavelengths appear in the literature that show a higher wavelength dependence, but with conflicting results. These measurement differences are most likely dominated by a poor correction of the wavelength dependence of instrumental (plate-scale, PSF, etc.) and atmospheric effects and not on the weak wavelength dependence of the solar LDF itself in the photospheric continuum.

From a theoretical model, we analyzed the impact of an instrumental effect on the inflection-point position. Figure 15 highlights the impact of an optical aberration (astigmatism) on our fine metrology measurements. The trend we see with the instrument is real. Indeed, three interference filters are from the same fabrication batch (535.7, 607.1, and 782.2 nm). A more detailed laboratory measurement of the instrument PSF can help us to refine this result. At 1025.0 nm, the result is more delicate. For this wavelength, we manufactured the interference filter after all others. There may be a low deviation in the determination of the optical thickness. Moreover, for this wavelength the quantum efficiency of the CCD is poor and the difference between the mean corrections introduced for turbulence (Table 7) is 100 mas between 782.2 nm and 1025.0 nm. This is based on the theoretical $\lambda^{6/5}$ dependence of r_0 , but needs to be confirmed experimentally.

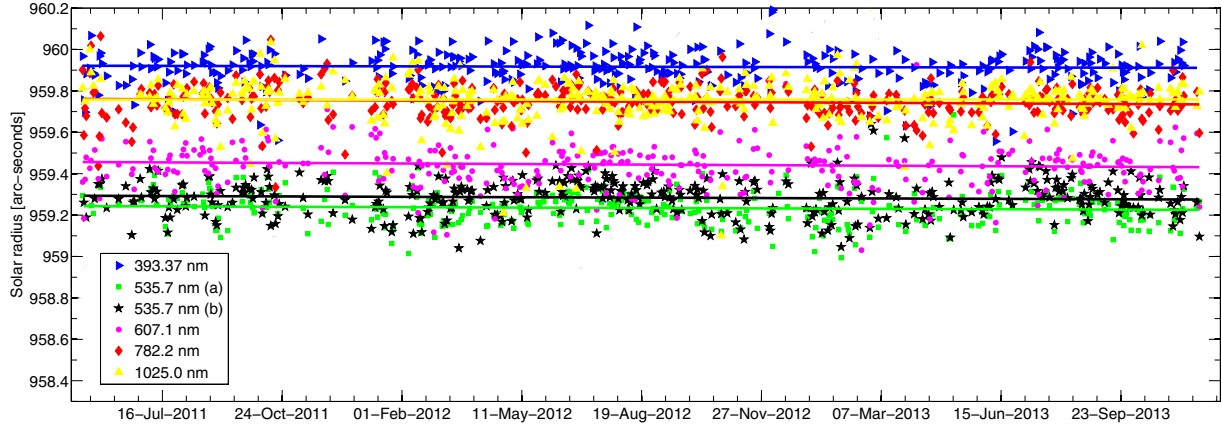


Fig. 14. Daily mean SODISM II observed solar radius with refraction correction as a function of time for different wavelengths. For all wavelengths, we obtained a negative slope of about 12 mas per year, which is not significant when compared with the 1σ uncertainty obtained on the mean radius (between 100 and 200 mas in Table 6). Any long-term instrumental degradation of the PSF or focus would lead to a slightly lower radius estimate.

Table 7. SODISM II mean solar radii and associated combined standard uncertainties after turbulence correction.

Wavelength [nm]	535.7 (a)	607.1	782.2	1025.0
Radius ^a ["]	959.237	959.452	959.716	959.772
Estimated r_0 [cm]	3.41	3.97	5.38	7.44
Turbulence bias ["]	0.54	0.41	0.16	0.06
Corrected radius ["]	959.777	959.862	959.876	959.832
Uncertainty – 1σ ["]	0.194	0.185	0.129	0.105

Notes. Results shown for each wavelength are obtained with quasi-identical exposure time. ^(a) Refraction correction only.

7.4. Discussion

The SODISM II mean radius value without turbulence correction (959.24 arcsec) obtained at 535.7 nm (a) is slightly lower than the mean value obtained by the two historic instruments (Solar Astrolabe and DORAYSOL) installed at Calern observatory (959.51 arcsec). Unfortunately, Solar Astrolabe and DORAYSOL are no longer in operation and simultaneous measurements could not be made to date. The SODISM II mean radius value obtained at 535.7 nm (b, 8.9 s) is slightly greater (50 mas) than 535.7 nm (a, 1.3 s), but the difference is within their uncertainties and they show the robustness of our instrumentation (almost equivalent results with two different interferential filters and with different exposure times). Thus, at 535.7 nm, we find a solar radius of 959.78 ± 0.19 arcsec, which is slightly higher but still compatible with the canonical solar radius (Auwers 1891).

For SODISM II at 607.1 nm, we found a solar radius of 959.86 ± 0.18 arcsec during the period 2011–2013. This result is also very similar to that obtained with the HMI instrument (959.90 ± 0.06 arcsec) during the last Venus transit. These results obtained with different instruments and methods highlight a probable underestimation of the solar radius canonical value (959.63 arcsec) or a slight evolution since the eighteenth century. On the other hand, our results at all wavelengths lead us to suspect an overestimation of the solar radius obtained with the MDI instrument (960.12 ± 0.09 arcsec). From radiative transfer simulations, we do not expect a variation of more than 20 mas between the measurements made at different wavelengths of the

Table 8. Difference (Δ IPP) of the inflection-point position at 607.1 nm, 782.2 nm, and 1025.0 nm from the IPP reference at 535.7 nm (a) for different solar models.

Wavelength (λ)	607.1 nm	782.2 nm	1025.0 nm
ΔIPP VAL81	11.9	30.2	–
ΔIPP FCH09	13.6	32.8	–
ΔIPP SH09	9.4	21.2	–
ΔIPP COSI	10.0	28.0	–
ΔIPP 3D	13.5	25.0	21.0
SODISM II ΔIPP	85.0	99.0	55.0

Notes. SODISM II ΔIPP represents the values obtained by measurement. All values are in mas.

photospheric continuum. We have shown, however, that chromatic effects of astigmatism can contribute significantly to establish such a wavelength dependence in the measurements. From the ground, the bias introduced by optical turbulence is also dependent on the wavelength, and an inappropriate correction would also lead to different results.

At 1025.0 nm, we initiated a new time-series and found a solar radius of 959.83 arcsec during the period 2011–2013. This wavelength is interesting because it is less sensitive to either optical turbulence and atmospheric absorption. Our detector performs less well in this spectral range, however, and we estimate that our best result in the present instrumental configuration is probably obtained at 782.2 nm (solar radius of 959.88 ± 0.13 arcsec).

The future work will be an even more detailed study of the instrumental and atmospheric turbulence effects and their uncertainty budget contribution. In addition, we have set up additional instrumentation to monitor various aspects of the instantaneous atmospheric conditions. A detailed analysis can also be conducted to verify the minor effects of aerosols on the solar radius measurements made by SODISM II. So far, we did not find any correlation between solar radius measurements and aerosol optical thickness or water vapor, which is less strong in winter. A seasonal effect still exists on the solar radius measurements after correction for refraction, but it is very likely related to the variation of the daily mean zenith distance, which enhances both the

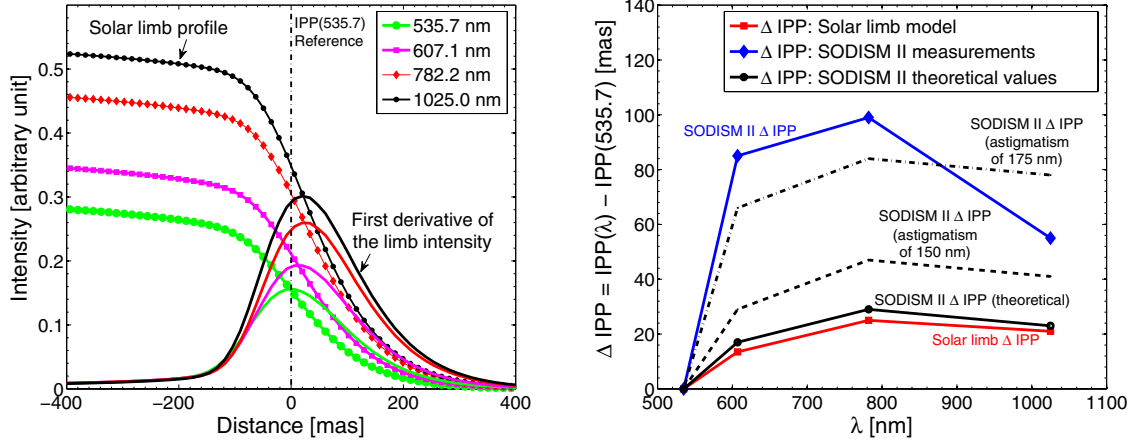


Fig. 15. *Left:* LDF at 535.7, 607.1, 782.2 and 1025.0 nm, for theoretical solar models. First derivative of the LDF for each wavelength. Location of the IPP(535.7) reference position. *Right:* the red curve with circle symbol represents ΔIPP as a function of wavelength for 3D solar model. The blue curve with diamond symbols represents ΔIPP as a function of wavelength for SODISM II measurements. The black curves represents ΔIPP as a function of wavelength for SODISM II theoretical results (convolution between LDF and PSF for three different cases).

effects of atmospheric extinction and turbulence. The most important parameters are the refraction and the optical turbulence. Scattering of the solar light by aerosols is not dominant.

Solar cycle 24 is particularly low, and as mentioned above, we find no significant correlation between solar activity or TSI and the variation of the solar radius. This finding is the same as that performed by SDS or MDI (Sofia et al. 2013; Bush et al. 2010). During the rising phase of cycle 24, however, we find much lower variations than those observed by SDS instrument over previous cycles. Only two and half years have been analyzed so far, but our first results show a remarkable stability at all wavelengths while the cycle was rising. This is consistent with the results obtained by MDI, which showed no significant variations of the solar radius in correlation or anticorrelation with activity over cycle 23.

8. Conclusion

At Calern (France), a set of instruments was installed to carry out solar radius measurements with the capability of distinguishing the atmospheric effect that might affect them. These effects are turbulence and aerosols scattering. The photometer provides a quality index of pictures taken by SODISM II (aerosol optical thickness and water vapor). The pyranometer measures the solar irradiance at ground level and provides another quality index for SODISM II measurements. A camera also contributes to data selection. These instruments allow us to discard contaminated data. Because turbulence effects cannot be avoided, an instrument is dedicated to measure this. SODISM II provides a nearly continuous record of the solar radius at different wavelengths since May 2011. MISOLFA measures the spatio-temporal parameters of the local turbulence since 2010. Currently, given the noise affecting its measurements, only monthly averages are used. The average Fried parameter r_0 is 3.41 cm for the period of observations reported here. We showed that it is possible to quantify the effect of aerosols through an associated modulation transfer function (MTF) that can be multiplied to the optical turbulence MTF to estimate the overall atmospheric MTF (e.g., Dror & Kopeika 1995). Therefore aerosols potentially have an impact on image spread, but it is expected to be small when

observing the Sun from the heated ground where most of the optical turbulence is generated. Our first results presented here confirm that to first order, the effect of aerosols is rather only extinction and that optical turbulence is the only significant effect that contributes to the image spread. A detailed analysis of the PAPS records will help us in the future to determine the potential minor effects caused by aerosols. In this work, data selection was made mainly with the PAPS, PPS, and CPS. We are still working to improve the MISOLFA signal-to-noise ratio and pipeline, however, to derive estimates of r_0 every minute. We have shown (Fig. 7 of Ikhslef et al. 2012) that at given moments the r_0 value can be as high as 8 cm, which is significantly higher than the monthly average value. From Fig. 5, we see that the bias introduced by turbulence is low and remains roughly constant for r_0 above 7 cm. Selecting these particular images would therefore effectively lead to a series with a lower bias introduced by turbulence and lower uncertainties associated with the estimated bias corrections. Main corrections to the observed radius of the Sun are (i) atmospheric refraction (at most ~ 1.0 arcsec); and (ii) seeing, which generates a bias lower than ~ 0.5 arcsec, which is wavelength dependent. The SODISM II solar radius at 535.7 nm, after making all necessary corrections, is close to 959.78 arcsec, while the estimated uncertainties of the measurements are typically smaller than 0.2 arcsec. For other wavelengths of the SODISM II instrument, the solar radii are close to 959.9 arcsec. The solar radius observed with SODISM II (during the period 2011–2013) results from variations smaller than 50 mas and it is out of phase with solar activity. A continuation of PICARD ground-based segment will allow us to confirm our observations about the variations of the solar radius.

Acknowledgements. This project is a collaboration between LATMOS, OCA, and CRAAG and is supported by CNES and CNRS. We thank CNES (Centre National d’Études Spatiales), CNRS (Centre National de la Recherche Scientifique), Laboratoire d’Optique Atmosphérique (University of Lille 1), and LESIA (Laboratoire d’Études Spatiales et d’Instrumentation en Astrophysique) for their support as well as all the participants who have devoted their expertise to this project. Numerous individuals have been involved in this project. They are all gratefully acknowledged for their respective contributions, although they cannot be listed here because many of them joined the development for only few months. The following institutes are acknowledged for providing the data: Solar Influences Data Center (Belgium), the “Physikalisch-Meteorologisches Observatorium Davos” (PMOD, Switzerland) and the Hansen Experimental Physics Laboratory (HEPL, Stanford University, United States). We especially

want to thank Rock Bush (HEPL team, Stanford University) who provided data from the MDI instrument. We also thank Alexander Shapiro and Werner Schmutz (PMOD) who provided COSI solar models at wavelengths associated with our instrument. We would like to thank Farrokh Vakili (Head of Côte d'Azur Observatory) for his support and provision of Calern site means. Finally, we thank the referee and the Editor for the constructive remarks and suggestions. This work is dedicated to the memory of Francis Laclare, who inspired a generation of astrophysicist to consider the measurement and interpretation of the solar diameter.

References

- Adassuriya, J., Gunasekera, S., & Samarasinha, N. 2011, Sun and Geosphere, 6, 17
- Assus, P., Borgnino, J., Martin, F., et al. 2002, in Astronomical Site Evaluation in the Visible and Radio Range, eds. J. Vernin, Z. Benkhaldoun, & C. Muñoz-Tuñón, ASP Conf. Ser., 266, 134
- Auwers, A. 1891, Astron. Nachr., 128, 361
- Badache-Damiani, C., Rozelot, J. P., Coughlin, K., & Kilifarska, N. 2007, MNRAS, 380, 609
- Ball, W. T., Unruh, Y. C., Krivova, N. A., et al. 2012, A&A, 541, A27
- BenMoussa, A., Gissot, S., Schühle, U., et al. 2013, Sol. Phys., 288, 389
- Braun, H., Christl, M., Rahmstorf, S., et al. 2005, Nature, 438, 208
- Brown, T. M. 1982, A&A, 116, 260
- Brown, T. M., & Christensen-Dalsgaard, J. 1998, ApJ, 500, L195
- Bush, R. I., Emilio, M., & Kuhn, J. R. 2010, ApJ, 716, 1381
- Corbard, T., Irbah, A., Assus, P., et al. 2010, Astron. Nachr., 331, P58
- Coulter, R. L., Kuhn, J. R., & Lin, H. 1996, in BAAS 28, 912
- Delache, P., & Kroll, R. J. 1994, Booktitle: The Solar Engine and its Influence on Terrestrial Atmosphere and Climate, ed. Nesme-Ribes, E. (Berlin, Heidelberg: Springer Verlag), 193
- Dror, I., & Kopeika, N. S. 1995, J. Opt. Soc. Am. A, 12, 970
- Duchon, C. E., & O'Malley, M. S. 1999, J. Appl. Meteorol., 38, 132
- Eddy, J. A., & Boornazian, A. A. 1979, in BAAS, 11, 437
- Emilio, M., Kuhn, J. R., Bush, R. I., & Scholl, I. F. 2012, ApJ, 750, 135
- Fontenla, J. M., Curdt, W., Haberreiter, M., Harder, J., & Tian, H. 2009, ApJ, 707, 482
- Foukal, P., Fröhlich, C., Spruit, H., & Wigley, T. M. L. 2006, Nature, 443, 161
- Gilliland, R. L. 1981, ApJ, 248, 1144
- Haberreiter, M., Schmutz, W., & Hubeny, I. 2008a, A&A, 492, 833
- Haberreiter, M., Schmutz, W., & Kosovichev, A. G. 2008b, ApJ, 675, L53
- Hauchecorne, A., Meftah, M., Irbah, A., et al. 2014, ApJ, 783, 127
- Hestroffer, D., & Magnan, C. 1998, A&A, 333, 338
- Hochedez, J.-F., Timmermans, C., Hauchecorne, A., & Meftah, M. 2014, A&A, 561, A17
- Holben, B. N., Tanré, D., Smirnov, A., et al. 2001, J. Geophys. Res., 106, 12067
- Ikhlef, R., Corbard, T., Irbah, A., et al. 2012, in SPIE Conf. Ser. 8444
- Irbah, A., Chibani, M., Lakhal, L., et al. 2001, in SF2A-2001: Semaine de l'Astrophysique Française, eds. F. Combes, D. Barret, & F. Thévenin, 59
- Irbah, A., Corbard, T., Assus, P., et al. 2010, in SPIE Conf. Ser., 7735
- Kuhn, J. R., Lin, H., & Loranz, D. 1991, PASP, 103, 1097
- Kuhn, J. R., Bush, R. I., Emilio, M., & Scherrer, P. H. 2004, ApJ, 613, 1241
- Kuhn, J. R., Bush, R., Emilio, M., & Scholl, I. F. 2012, Science, 337, 1638
- Laclare, F., Delmas, C., Coin, J. P., & Irbah, A. 1996, Sol. Phys., 166, 211
- Laclare, F., Delmas, C., Sinceac, V., & Chollet, F. 1999, Académie des Sciences Paris Comptes Rendus Série B Sciences Physiques, 327, 645
- Lakhal, L., Irbah, A., Bouzaria, M., et al. 1999, A&AS, 138, 155
- Meftah, M., Irbah, A., Corbard, T., et al. 2012, in SPIE Conf. Ser., 8446
- Meftah, M., Hauchecorne, A., Crepel, M., et al. 2014a, Sol. Phys., 289, 1
- Meftah, M., Hochedez, J.-F., Irbah, A., et al. 2014b, Sol. Phys., 289, 1043
- Morand, F., Delmas, C., Corbard, T., et al. 2010, C. R. Phys., 11, 660
- Parkinson, J. H., Morrison, L. V., & Stephenson, F. R. 1980, Nature, 288, 548
- Piau, L., Stein, R. F., Melo, S., et al. 2011, in SF2A-2011: Proc. Annual meeting of the French Society of Astronomy and Astrophysics, eds. G. Alecian, K. Belkacem, R. Samadi, & D. Valls-Gabaud, 407
- Ribes, E., Beardsley, B., Brown, T. M., et al. 1991, Booktitle: The Sun in Time, eds. C. P. Sonett, & M. S. Giampapa, & M. S. Matthews (Tucson: University of Arizona Press), 59
- Rozelot, J. P. 2001a, J. Atmos. Sol.-Terr. Phys., 63, 375
- Rozelot, J. P. 2001b, J. Atmos. Sol.-Terr. Phys., 63, 2005
- Rozelot, J. P., & Damiani, C. 2012, EPJH, 37, 709
- Scherrer, P. H., Schou, J., Bush, R. I., et al. 2012, Sol. Phys., 275, 207
- Schou, J., Scherrer, P. H., Bush, R. I., et al. 2012, Sol. Phys., 275, 229
- Schröder, W. 2001, J. Atmos. Sol.-Terr. Phys., 63, 2003
- Shapiro, A. I., Schmutz, W., Schoell, M., Haberreiter, M., & Rozanov, E. 2010, A&A, 517, A48
- Short, C. I., & Hauschildt, P. H. 2009, ApJ, 691, 1634
- Sofia, S., Chiu, H.-Y., Maier, E., et al. 1984, Appl. Opt., 23, 1235
- Sofia, S., Girard, T. M., Sofia, U. J., et al. 2013, MNRAS, 436, 2151
- Spruit, H. C. 1991, in The Sun in Time, eds. C. P. Sonett, M. S. Giampapa, & M. S. Matthews (Tucson: University of Arizona Press), 118
- Thuillier, G., Dewitte, S., & Schmutz, W. 2006, Adv. Space Res., 38, 1792
- Thuillier, G., Claudel, J., Djafer, D., et al. 2011, Sol. Phys., 268, 125
- Toulmonde, M. 1997, A&A, 325, 1174
- Vernazza, J. E., Avrett, E. H., & Loeser, R. 1981, ApJS, 45, 635
- Wittmann, A. 1977, A&A, 61, 225

II.5 Conclusions

En 2015 nous avons publié un nouvel article (Meftah, Hauchecorne, et al. 2015) qui analyse les mesures simultanées de PICARD/SODISM et SODISM-2 sur la période allant de 2011 (date de mise en service de SODISM-2) à 2013 (date de l'arrêt de la mission spatiale) et qui poursuit l'analyse des données SODISM-2 jusqu'en 2015 (Figure 30). Les variations de rayon observées avec l'instrument spatial SODISM sont inférieures à 20 mas sur la période 2010-2011. Pour SODISM-2, sur la période 2011-2014 les variations sont inférieures à ± 50 mas. Au-delà de 2011 l'instrument spatial se dégrade et la dispersion des résultats augmente jusqu'à dépasser celle obtenue au sol. Nous n'avons pas trouvé de corrélation significative entre l'activité et les variations du rayon sur cette période. Sur la période 2010-2011 les données spatiales de SODISM montrent une oscillation de période de 129.5 jours avec une amplitude de ± 6.5 mas. Cette variation n'est pas trouvée dans l'analyse des données de SODISM-2 qui n'a pas la sensibilité suffisante.

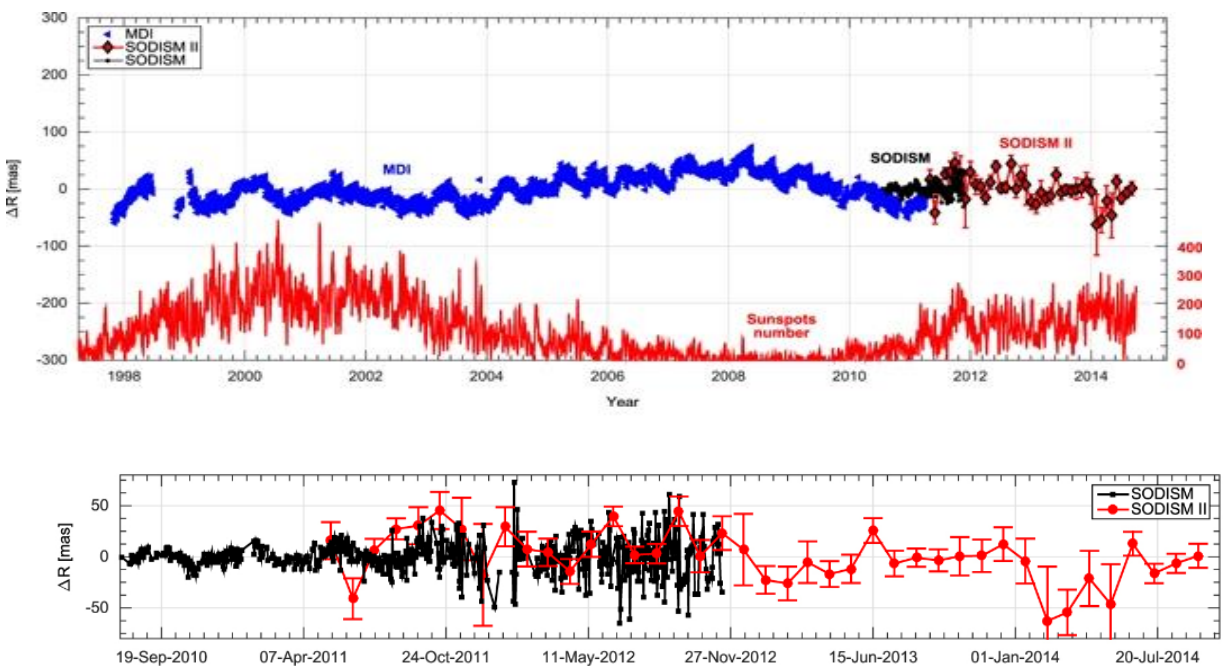


Figure 30 Haut : variations des mesures du rayon solaire au cours du temps avec SOHO/MDI (1996-2011), PICARD/SODISM (2010-2013) et PICARDSOL/SODISM-2 (2011-2015). Bas : zoom sur la période de recouvrement entre les données SODIM et SODISM-2. La variation du nombre de taches solaires est donnée sur la même période sur la figure du haut (Meftah, Hauchecorne, et al. 2015).

Le principal résultat de ces analyses sur la courte période de la phase ascendante du cycle 24 est que nous pouvons dire que l'instrumentation sol mise en place ainsi que la procédure d'analyse développée prenant en compte l'effet de la turbulence optique nous donne la capacité de détecter sans ambiguïté toute variation du rayon qui dépasserait significativement les 50 mas. Les 200 mas de variations détectées sur les cycles précédents par les mesures astrolabe couvrant 40 ans pourront donc à l'avenir être confirmées ou non si nous poursuivons ces observations sur le long terme. Cela suppose évidemment que nous continuons à surveiller la stabilité instrumentale, le vieillissement des filtres et à faire notamment des calibrations régulières du facteur d'échelle sur étoiles.

PARTIE III. Perspectives

III.1 La dynamo solaire profonde et aux pôles

Trois grands domaines restent à explorer pour pouvoir mieux contraindre les modèles de la dynamo solaire et comprendre le cycle d'activité de notre étoile : la circulation méridienne profonde jusqu'à la tachocline, la dynamique et le champ magnétique des zones polaires.

Une technique d'héliosismologie locale que je n'ai pas évoquée est celle de l'analyse temps-distance (Duvall, et al. 1993) dans laquelle nous cherchons les temps de parcours des ondes acoustiques individuelles. Il s'agit du temps que l'onde met, partant de la surface, pour aller au fond de sa cavité de propagation puis revenir à la surface à une certaine distance angulaire du point de départ. Le temps et la distance sont mesurés en cherchant le temps maximisant les fonctions de cross-corrélation pour chaque distance angulaire.

Cette méthode permet par la mesure des temps de parcours dans la direction Nord-Sud de remonter à la circulation méridienne. Comme pour l'analyse ring-diagram nous sommes cependant confinés dans les couches les plus superficielles. En augmentant la séparation angulaire entre les deux zones de la surface sur laquelle nous cherchons les corrélations, il est possible d'obtenir une information plus profonde. Cependant la technique habituelle repose sur une approximation en onde plane qui est alors mise à mal.

En collaboration avec S. Kholikov (GONG, NSO) j'ai pu mener une première analyse temps-distance multi instruments et obtenir les fonctions d'intercorrélation (Figure 31, gauche) qui permettent ensuite de déduire (par ajustement avec les fonctions de Gabor) les temps de parcours en fonction de la séparation angulaire sur le Soleil (Figure 31, droite). Cette première comparaison nous a permis de montrer une bonne cohérence entre les signaux de GONG HMI et PICARD alors que MDI semble significativement différent aux faibles distances. Les images MDI étant redimensionnées à bord, nous avons ensuite testé l'influence de la résolution sur ces analyses. L'objectif est ensuite d'inverser ces temps de corrélation obtenus pour les plus larges séparations angulaires afin de remonter à la circulation méridienne profonde.

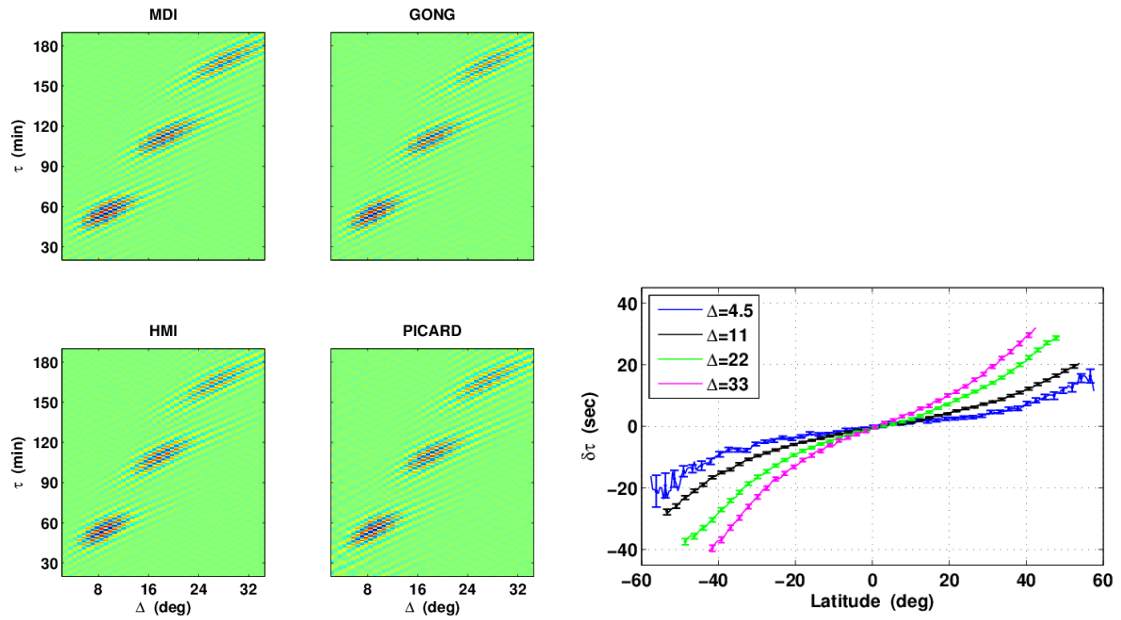


Figure 31 Gauche : Fonctions d'intercorrélation obtenues pour 4 instruments différents en vitesse (MDI, GONG et HMI) et en intensité (PICARD). Les 3 ‘paquets’ visibles sur chaque figure correspondent aux ondes qui se réfléchissent une, deux ou trois fois à la surface. Droite : Différences des temps de parcours mesurés dans la direction Nord-Sud en fonction de la latitude pour différentes séparations angulaires. Les points tournant pour ces distances sont approximativement 0.973, 0.933, 0.865, 0.79 R.

L'originalité de ce travail réside dans le fait que pour analyser les corrélations sur les larges séparations angulaires permettant d'atteindre la tachocline nous utilisons une décomposition en harmoniques sphériques des images. Les difficultés sont nombreuses mais nous espérons progresser dans la compréhension du signal observé et des différentes sources de bruits par la comparaison multi-instruments.

Ce type de techniques devrait aussi pouvoir être appliquée aux données Doppler de Solar Orbiter (2018-2026) mission ESA dont le lancement est prévu pour octobre 2018 (Müller, et al. 2013). Solar Orbiter sondera le Soleil en s'éloignant de l'écliptique (jusqu'à un maximum de 32°) permettant ainsi d'observer les zones plus proches des pôles. Cela permettra d'appliquer les techniques de l'héliosismologie locale sur des zones au-dessus de 60° de latitude pour lesquelles nous avons encore peu d'information. L'existence ou non d'une cellule de circulation méridienne à haute latitude pourra ainsi clairement être déterminée par exemple. L'évolution du champ magnétique polaire diffus pourra être étudiée conjointement. L'ensemble sera une avancée incontestable pour contraindre les modèles de la dynamo. De plus, en combinant ces données avec des images prises depuis une autre perspective (la terre un satellite en orbite terrestre comme SDO), il sera envisageable de calculer les fonctions d'intercorrélation entre les zones polaires observées par Solar Orbiter et des zones situées à grandes distances angulaires ouvrant la possibilité d'atteindre des zones aussi profondes que la tachocline (Figure 32).

Local helioseismology: near-polar regions

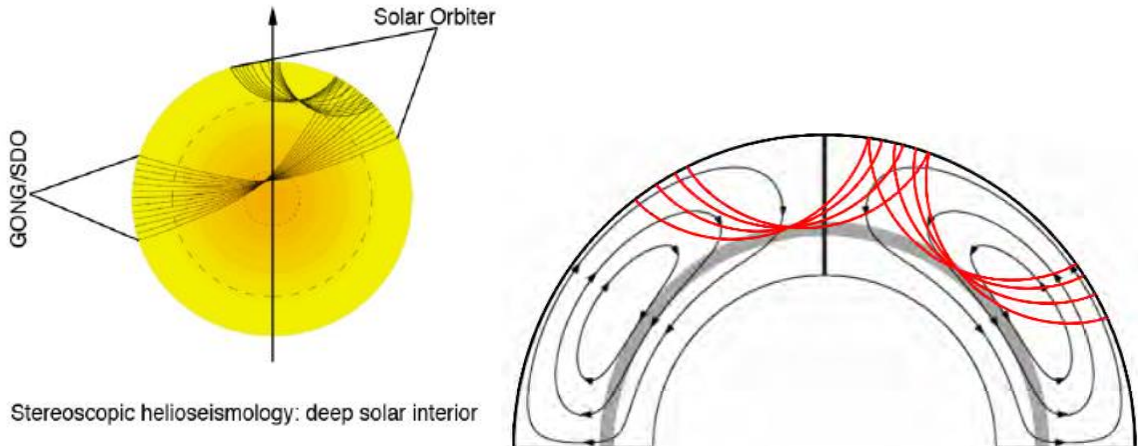


Figure 32 Illustration, à gauche de l'heliosismologie stéréoscopique envisagée avec Solar Orbiter (Müller, et al. 2013) et à droite, des possibilités de sondage profond des zones polaires qu'offrirait la mission POLARIS+ (Appourchaux et consortium 2016)

Les périodes en fin de mission pendant lesquelles Solar Orbiter sera significativement hors de l'écliptique seront cependant de relativement courtes durées et l'élévation au-dessus de l'écliptique ne dépassera pas les 32° ce qui ne permettra pas un suivi continu de la dynamique des pôles. Pour cette raison, T. Appourchaux et al. (2016) ont proposé qu'une autre mission POLARIS+ (POLAR Investigation of the Sun) soit ensuite envisagée dont l'objectif premier sera de déterminer les relations entre la dynamique, le magnétisme des pôles et le cycle solaire. Ce satellite serait propulsé par une voile solaire sur une orbite circulaire à 0.48 UA avec une inclinaison de 75° . Sur cette orbite d'une période de 4 mois, le satellite sera à haute latitude ($>60^\circ$) 29% du temps soit 35 jours lui permettant de réaliser pleinement un programme d'héliosismologie dédié à l'étude de la dynamique sub-polaire. Je suis associé à ce projet.

III.2 Le projet METEOSPACE

Nous avons vu l'importance d'observer le Soleil continûment sur des échelles allant du cycle de 11 ans jusqu'aux échelles permettant de chercher d'éventuelles évolutions séculaires. La surveillance de l'activité solaire en temps réel est également nécessaire pour la recherche sur les événements éruptifs et pour ses applications en météorologie de l'espace. En collaboration avec Jean-Marie Malherbe, j'ai commencé à m'impliquer directement dans ce domaine à travers le projet METEOSPACE d'installation d'une série de lunettes utiles pour la météorologie de l'espace sur le plateau de Calern.

La météorologie de l'espace s'attache à identifier et étudier les phénomènes susceptibles d'impacter directement les environnements planétaires. Pour l'environnement de la Terre, la première source de perturbation est le Soleil et ses éruptions. Le terme éruption regroupe en fait plusieurs types de phénomènes observés. Il y a principalement trois types d'éruptions solaires : celles qui sont associées à une variation locale et soudaine de luminosité (solar flare en anglais) et que l'on désigne souvent simplement par 'éruptions', celles qui sont associées aux éjections de masses coronales (que l'on désignera par leur acronyme anglais CME) et enfin les éruptions de filaments. Les CME étant souvent associées aux 'éruptions' les plus importantes, ces deux types d'éruptions sont parfois simultanés mais des CME ont été observées sans qu'une 'éruption' associée soit détectée et seules les 'éruptions' les plus violentes sont suivies de CME (Andrews 2003). Les deux phénomènes, même s'ils sont liés et représentent probablement deux aspects d'un même processus, sont en fait différents dans leurs émissions, la manière dont elles se propagent dans l'héliosphère et leurs impacts sur l'environnement terrestre.

Les 'éruptions' sont associées aux reconnexions de boucles de champ magnétique dans la chromosphère ou basse couronne, elles peuvent durer de quelques minutes à quelques heures et elles libèrent une énergie considérable (jusqu'à 10^{25} W) sous forme de rayonnement couvrant tout le spectre électromagnétique depuis les ondes radio jusqu'aux rayons X et gamma. Ce rayonnement voyage à la vitesse de la lumière et met donc huit minutes pour atteindre la Terre. Mais l'énergie libérée par ces 'éruptions' peut aussi accélérer des particules (protons, électrons) à très hautes énergies (Solar Energetic Particles, SEP) qui peuvent atteindre la Terre en quelques dizaines de minutes. L'énergie de ces 'éruptions' peut perturber l'ionosphère dans laquelle les ondes radio se propagent, dégradant les signaux de navigation et de communications.

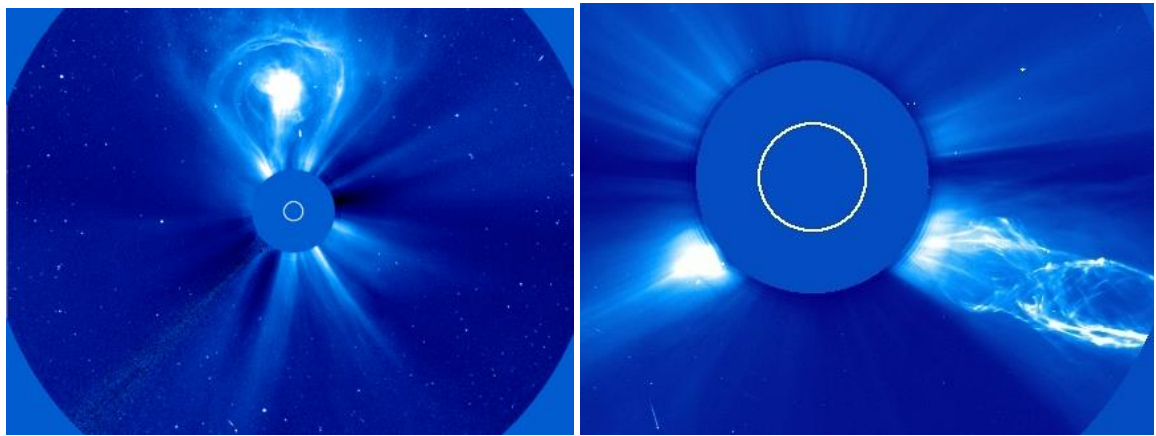


Figure 33 Deux exemples de CME observées par SOHO le 27 Février 2000 (gauche) et 2 juin 1998 (droite). L'image de gauche révèle la structure classique qui comporte trois parties : une boucle brillante surplombant une cavité coronale qui contient un cœur central de matière dense en provenance du filament éruptif. L'image de droite révèle une toute autre structure magnétique étroitement liée à la structure spiralée qu'avait le filament sous-jacent.

Les CME correspondent à l'expulsion d'un immense nuage de particules ionisées dans l'héliosphère. Elles sont observées directement avec les coronographes (Figure 33). A ces éjections peuvent être associées des ondes coronales globales (Chen 2016) visibles sur les images en extrême ultra-violet (EUV) et auxquelles sont liées les ondes chromosphériques de Moreton (Figure 34) observées pour la première fois dans la raie Halpha (Moreton 1960). En voyageant en moyenne à près de 500 de km par secondes, le plasma de la CME met trois jours et demi pour arriver dans l'environnement terrestre et affecter la magnétosphère. En fait les vitesses observées sont entre 300 et 2200 km/s correspondant à des temps de parcours vers la Terre allant de 19 heures à plus de 5 jours. Toutes les CME ne sont cependant pas dirigées vers la Terre. Celles qui le sont, sont appelées 'CME halo' parce que, sur les images des coronographes un halo se propage tout autour du disque solaire. Ces CME halo dirigées vers la Terre sont la cause des orages géomagnétiques qui induisent les aurores polaires mais peuvent aussi perturber les communications, affecter la précision des GPS, endommager les satellites, augmenter les doses de radiations subies par les astronautes ou par les passagers de lignes aériennes passant près des pôles ou même, dans les cas extrêmes, provoquer des perturbations sur les lignes hautes tension voir de mettre tout un réseau électrique hors service.

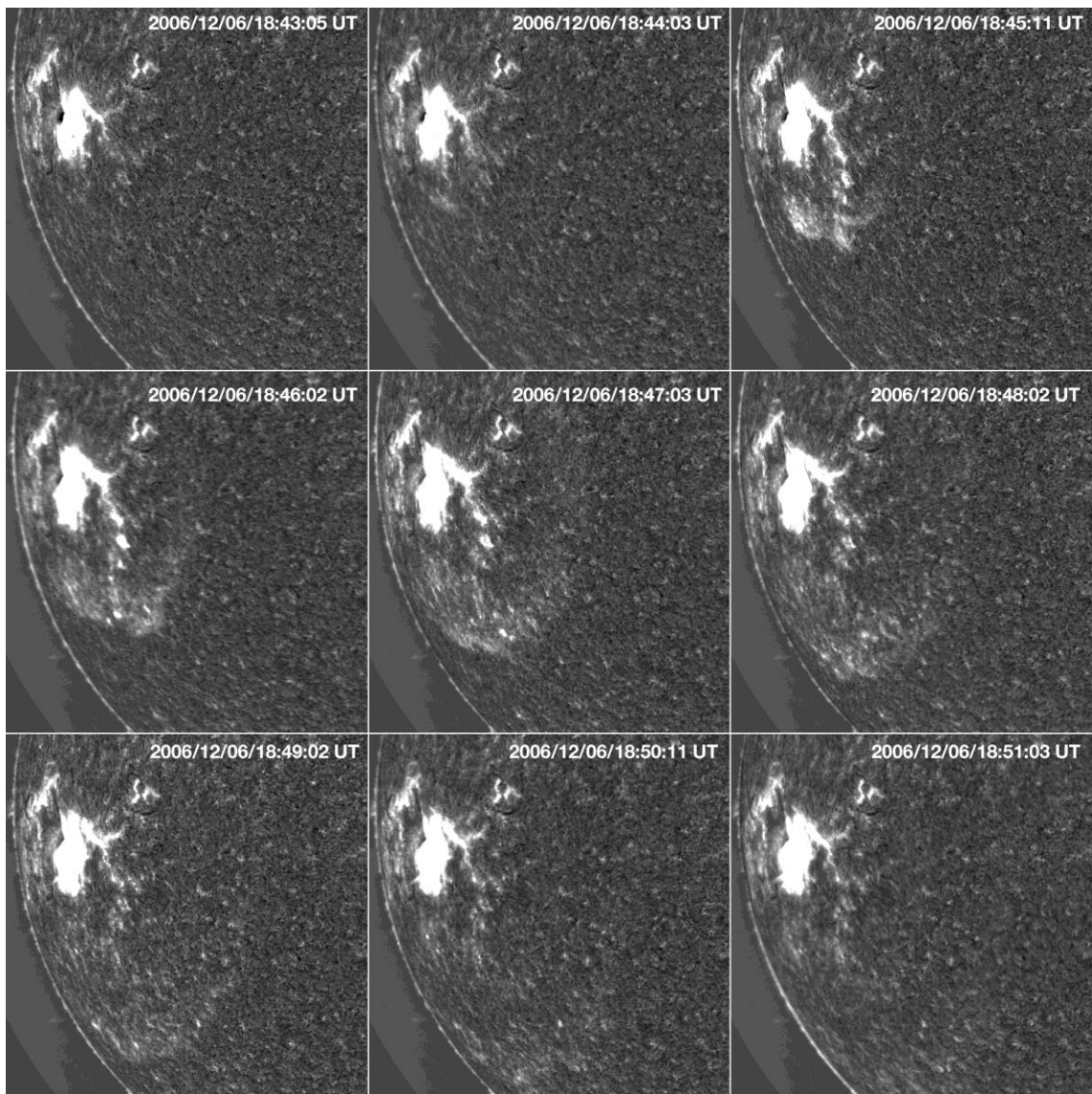


Figure 34 Exemple de propagation d'une onde chromosphérique de Moreton enregistrée dans la raie H-alpha le 6 Décembre 2006 par le Optical Solar Patrol Network (NSO/AURA/NSF and USAF Research Laboratory). L'onde se propage sur l'ensemble du disque solaire en une dizaine de minutes.

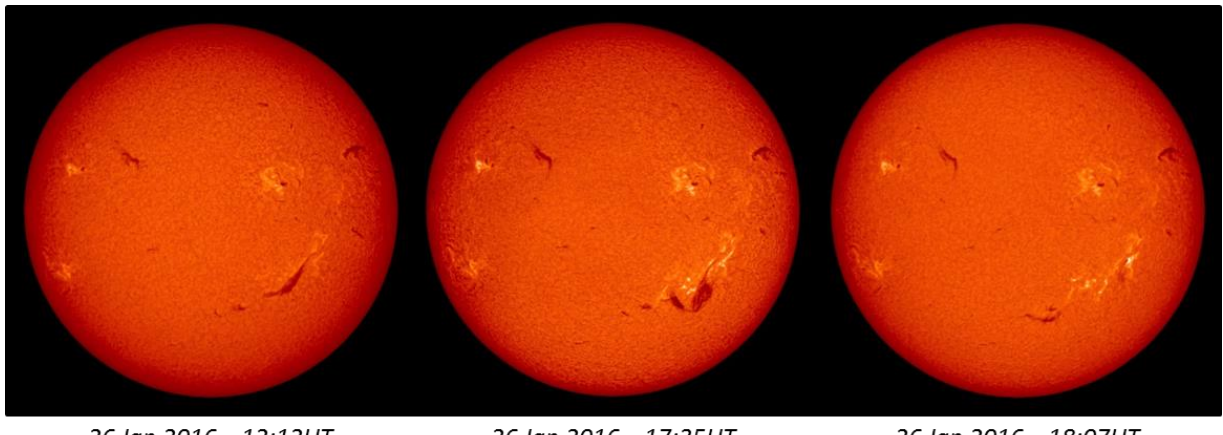


Figure 35 Eruption d'un filament enregistré par le réseau H-alpha GONG le 26 Janvier 2016. Une CME a été observée par SOHO juste après la disparition du filament.

Les filaments sont des nuages de plasma ancrés au niveau de la photosphère, qui s'élève jusque dans la chromosphère et la couronne et qui sont enserrés entre deux zones de polarités magnétiques différentes. Ces nuages sont plus denses et froids que le plasma environnant ce qui les fait apparaître comme des filaments sombres sur les images de la chromosphère et de la basse couronne. Lorsqu'ils sont observés aux limbes, sur le fond du ciel, ils prennent la dénomination de protubérances. Les filaments ont des durées de vie variables pouvant aller jusqu'à plusieurs semaines. Quand ils deviennent instables et disparaissent nous parlons d'éruption de filaments. Soit le plasma du filament retombe alors à la surface du Soleil soit il est éjecté tout ou partie et forme une CME (environ 70% des cas). Tout comme les CME associées aux 'éruptions', les CME provenant de l'éruption des filaments peuvent être géo-effectives c'est-à-dire produire un orage géomagnétique.

De nombreuses observations spatiales (SOHO puis SDO) sont menées dans la couronne ou en EUV dans la raie Hell à 304 Å sondant le domaine des températures de la transition chromosphère-couronne (80 000 K), mais la matière froide et dense y est invisible.

La raie H-alpha est la raie la plus adaptée pour surveiller les phénomènes solaires dès leur naissance, à la source de l'activité solaire, dans la chromosphère. Cependant aucune instrumentation spatiale n'utilise actuellement ce type de filtre.

Le projet METEOSPACE est une collaboration entre l'Observatoire de Paris, l'Observatoire de la Côte d'Azur et la DGA (Direction Générale de l'Armement). Il est né d'une part de la volonté d'obtenir sur un site ensoleillé des séquences à haute cadence en imagerie H-alpha qui permettent l'étude des phénomènes transitoires visibles dans la chromosphère et d'autre part de la volonté du responsable de FEDOME (Fédération des Données de Météorologie de l'Espace, L. Birée) d'acquérir de telles séquences en temps réel à partir d'un site institutionnel pour les besoins opérationnels de la défense aérienne.

La raie H-alpha permet en effet la détection depuis le sol des principaux phénomènes solaires rapides et transitoires qui peuvent être des signes précurseurs de CME:

- les instabilités des filaments solaires et les éruptions de filaments,
- les éruptions solaires,
- les ondes chromosphériques de Moreton.

Les ondes de Moreton H-alpha représentent la trace au niveau chromosphérique des ondes de choc coronales détectées en radio (sursauts de type II). Leur observation nécessite une cadence très rapide (10 s car elles se propagent à des vitesses de l'ordre de 1000 km/s et balaient le disque solaire en 10 minutes). Très peu d'événements ont pu être étudiés à ce jour conjointement avec des observations d'imagerie radio. Les observations conjointes Halpha et imagerie radio avec le Radiohéliographe de Nançay permettent de suivre spatialement et temporellement l'évolution de ces phénomènes. Pour mieux comprendre les liens entre 'éruptions', éruptions de filaments et CME ou encore les liens entre les ondes de choc coronales et les ondes de Moreton observées dans la chromosphère, il est en effet important d'avoir un ensemble d'observations continues permettant de voir la progression des phénomènes depuis la chromosphère vers la couronne.

METEOSPACE produira des données en continu au cours de la journée soit sur un mode routine à une image par minute soit sur un mode à haute cadence.

L'instrument automatique est constitué d'une monture unique assurant le suivi du Soleil et portant 3 lunettes de 100 mm d'ouverture, équipées chacune d'une caméra CCD et d'un filtre étroit permettant l'enregistrement d'images toutes les 10 secondes :

- une voie H-alpha haute cadence (0.4 Å FWHM)
- une voie imagerie des protubérances en CaII H (1.5 Å FWHM) avec lune artificielle de densité 1
- une voie à roue à filtres: CaII K (1.5 Å FWHM), bande CH dite G (8 Å FWHM), et peut être bande CN (7 Å FWHM).

Donc des raies atomiques ou bandes moléculaires dont certaines présentes sur Hinode (CH, CN, CaII H)

Le dispositif comprend par ailleurs :

- un pipeline automatique vers la base de données où l'intégralité des données apparaîtra en quasi temps réel et une interface sur le portail BASS2000,
- la mise en place d'un service de calcul axé sur l'aide à la prévision (qui utilisera aussi les données H-alpha du Pic du Midi et les données Radio de l'antenne ORFEES de la station de Nancay) dans le prolongement du projet FEDOME.

Les images H-alpha du Soleil étant potentiellement très utiles pour prédire les éruptions, les observatoires autour du monde observent le soleil à cette longueur d'onde à la fois pour les scientifiques et les militaires. Cela a conduit au réseau « Global High Resolution

H-alpha Network »⁷ auquel contribuent déjà Meudon et le pic du Midi mais qui rassemble des données assez disparates et non régulières venant d'instrumentations différentes. Il y a aussi le réseau GONG⁸ qui en plus de ses produits d'héliosismologie fournit depuis 2012, en temps réel, sur tout son réseau des images H-alpha pour les applications civiles et militaires (ces derniers ayant financé spécifiquement cette évolution du réseau). Nous avons prévu dès la conception du projet d'intégrer ces réseaux que nous viendrons compléter. Le filtre choisi est notamment identique à celui utilisés par les instruments du réseau GONG H-alpha.

MEUDON fournit des images H-alpha en basse cadence, et se positionne sur la cyclicité solaire à l'échelle du cycle de 11 ans, typiquement une seule image de chaque sorte par jour. Si ce site est parfait pour obtenir quelques images par jour, il ne permet pas (raison climatique) de suivre l'activité solaire en continu. L'imagerie H-alpha du Pic du Midi à également des capacités à haute cadence et des observations coronographiques et du champ magnétique sont également produites.

La seule station européenne réalisant des observations continues, avec une minute de cadence en H-alpha est GONG, aux Canaries. Nous avons estimé que la possibilité d'installer cette instrumentation à CALERN avec une équipe scientifique et technique locale sur une plateforme existante d'observations solaires est une opportunité unique à saisir qui viendra en complémentarité avec Meudon, le pic du Midi, Nançay pour la radioastronomie, les observations de SDO mais aussi celles in-situ à venir de Solar Orbiter. La lunette principale doit être installée à Calern courant 2017.

⁷ Global High Resolution H-alpha Network http://swrl.njit.edu/ghn_web/

⁸ Global Oscillation Network Group H Alpha Network Monitor <http://halpha.nso.edu/>

Bibliographie

- Ando, H., et Y. Osaki. «Nonadiabatic nonradial oscillations - an application to the five-minute oscillation of the sun.» *PASJ* 27 (1975): 581.
- Andrews, M. D. «A Search for CMEs Associated with Big Flares.» *Sol. Phys* 218 (2003): 261.
- Appourchaux, T., et the POLARIS+ consortium. «POLAR Investigation of the Sun / POLARIS+A.» Proposal for New Scientific Ideas for the Cosmic Vision programme, 2016.
- Assus, P., et al. «A generalized solar seeing monitor : MISOLFA (Moniteur d'Images Solaires Franco-Algérien).» Édité par Z. Benkhaldoun, C. Munoz-Tunon J. Vernin. *IAU Technical Workshop on "Astronomical Site Evaluation in the Visible and the Radio Range*. ASP Conference Proceedings, 2000.
- Babcock, H. W. «The Topology of the Sun's Magnetic Field and the 22-YEAR Cycle.» *ApJ* 133 (1961): 572.
- Ball, W. T., et al. «Reconstruction of total solar irradiance 1974-2009.» *A&A* 541 (2012): 27.
- Barekat, A., J. Schou, et L. Gizon. «The radial gradient of the near-surface shear layer of the Sun.» *A&A* 570 (2014): L12.
- Belucz, Bernadett, Mausumi Dikpati, et Emese Forgács-Dajka. «A Babcock-Leighton Solar Dynamo Model with Multi-cellular Meridional Circulation in Advection- and Diffusion-dominated Regimes.» *ApJ*. 806 (2015): 169.
- Berdja, A. «Effets de la Turbulence Atmosphérique lors de l'Observation du Soleil à Haute Résolution Angulaire.» Thèse de doctorat, Université de Nice Sophia-Antipolis, France, 2007.
- Brown, T.M. «Seeing-independent definitions of the solar limb position.» *A&A* 116 (1982): 260.
- Brown, Timothy M., D. F. Elmore, L. Lacey, et H. Hull. «Solar diameter monitor: an instrument to measure long-term changes.» *Ap. Opt.*, n° 21 (1982): 3588.
- Browning, M.K., M.S. Miesch, A.S. Brun, et J. Toomre. «Dynamo Action in the Solar Convection Zone and Tachocline: Pumping and Organization of Toroidal Fields.» *Astrophys. J.* 648 (2006): L157.
- Bruscaglioni, P., P. Donelli, A. Ismaelli, et G. Zaccanti. «"Monte Carlo calculations of the modulation transfer function of an optical system operating in a turbid medium.» *Appl. Optics* 32 (1993): 2813.
- Bush, R. I., M. Emilio, et J. R. Kuhn. «On the Constancy of the Solar Radius. III.» *ApJ* 716 (2010): 1381.
- Carroll, T. A., M. Kopf, I. Ilyin, et K. G. Strassmeier. «Zeeman-Doppler imaging of late-type stars: The surface magnetic field of II Peg.» *Astronomische Nachrichten* 328 (2007): 1043.

Charbonneau, P. «Dynamo Models of the Solar Cycle.» *Living Rev. Solar Phys.* 7 (2010): lrsp-2010-3.

Chen, P. F. *Global Coronal Waves*. Vol. 216, chap. 22 dans *Low-Frequency Waves in Space Plasmas, Geophysical Monograph Series*, édité par Dong-Hun Lee, Valery Nakariakov Andreas Keiling, 381-394. John Wiley & Sons, Inc, 2016.

Christensen-Dalsgaard. *Lecture Notes on Stellar Oscillations 5th edition*. Teoretisk Astrofysik Center: Institut for Fysik og Astronomi, Aarhus Universitet, 2014.

Corbard, T., et al. «Ring-Diagram Analysis with GONG++.» Édité par H. Sawaya-Lacoste. *Proceedings of SOHO 12 / GONG+ 2002. Local and global helioseismology: the present and future*. Big Bear Lake, CA, USA: ESA Publications Division, Noordwijk, Netherlands, 2003. 255 - 258.

Corbard, T. *Ring Diagram Analysis with GONG++*. Technical note, Tucson, Az: GONG, 2003, 1-22.

Corbard, T., et al. «Helioseismology with PICARD.» *Journal of Physics Conference Series* 440 (2013): id. 012025.

Corbard, T., et al. «MISOLFA solar monitor for the ground PICARD program.» *Astronomische Nachrichten* 351 (2010): P58 (CD volume).

Corbard, T., et M.J. Thompson. «The subsurface radial gradient of solar angular velocity from MDI f-mode observations.» *Sol. Phys.* 205 (2002): 211.

Corbard, T., F. Morand, F. Laclare, R. Ikhlef, et M. Meftah. «On the importance of astronomical refraction for modern Solar astrometric measurements.» Note technique, 2013.

Corbard, T., M. Dikpati, P.~A. Gilman, et M.~J. Thompson. «Effect of subsurface radial differential rotation on flux-transport solar dynamo.» Édité par A. Wilson. *SoHO 11 symposium, From Solar Min to Max: Half a Solar Cycle with SOHO*. Davos, Switzerland: ESA Special Publication, 2002. 75-78.

De Rosa, Marc L., Peter A. Gilman, et J. Toomre. «Solar Multiscale Convection and Rotation Gradients Studied in Shallow Spherical Shells.» *ApJ* 581 (2002): 1356.

Deubner, F.-L. «Observations of low wavenumber nonradial eigenmodes of the sun.» *A&A* 44 (1975): 371.

Dikpati, M., et P. Charbonneau. «A Babcock-Leighton Flux Transport Dynamo with Solar-like Differential Rotation.» *ApJ* 518 (1999): 508.

Dikpati, M., et P. Gilman. «Flux-Transport Dynamos with α -Effect from Global Instability of Tachocline Differential Rotation: A Solution for Magnetic Parity Selection in the Sun.» *ApJ* 559 (2001): 428.

Dikpati, M., T. Corbard, M.J. Thompson, et P.A. Gilman. «Flux Transport Solar Dynamos with Near-Surface Radial Shear.» *ApJ* 575 (2002): L41-L45.

- Dikpati, Mausumi, Giuliana de Toma, Peter A. Gilman, Charles N. Arge, et Oran R. White. «Diagnostics of Polar Field Reversal in Solar Cycle 23 Using a Flux Transport Dynamo Model.» *ApJ.* 601 (2004): 1136.
- Djafer, D., G. Thuillier, S. Sofia, et A. Egidi. «Processing Method Effects on Solar Diameter Measurements: Use of Data Gathered by the Solar Disk Sextant.» *Sol. Phys.* 247 (2008): 225.
- Domiciano de Souza, A., et al. «Beyond the diffraction limit of optical/IR interferometers. I. Angular diameter and rotation parameters of Achernar from differential phases.» *Astronomy & Astrophysics* 545 (2012): A130.
- Duvall, T. L., Jr., S. M. Jefferies, J. W. Harvey, et M. A. Pomerantz. «Time-distance helioseismology.» *Nature* 362 (1993): 430.
- Egidi, A., B. Caccin, S. Sofia, W. Heaps, W. Hoegy, et L. Twigg. «High-Precision Measurements of the Solar Diameter and Oblateness by the Solar Disk Sextant (SDS) Experiment.» *Sol. Phys.* 235 (2006): 407.
- Emilio, M., J. R. Kuhn, R. I. Bush, et P. Scherrer. «On the Constancy of the Solar Diameter.» *ApJ* 543 (2000): 1007.
- Fivian, Martin D., Hugh S. Hudson, Robert P. Lin, et H. Jabran Zahid. «A Large Excess in Apparent Solar Oblateness Due to Surface Magnetism.» *Science* 322 (2008): 560.
- Foukal, P., C. Fröhlich, H. Spruit, et T. M. L. Wigley. «Variations in solar luminosity and their effect on the Earth's climate.» *Nature* 443 (2006): 161.
- Fröhlich, C. «Evidence of a long-term trend in total solar irradiance.» *A&A* 501 (2009): L27.
- . «Total solar irradiance variability: What have we learned about its variability from the record of the last three solar cycles?» Édité par R. Fujii, K. Shibata, & M.A. Geller T. Tsuda. *Climate and Weather of the Sun-Earth System (CAWSES) Selected Papers from the 2007 Kyoto Symposium.* Kyoto: TERRAPUB, Tokyo, 2009. 217.
- Giles, P. M. «Time-distance measurements of large-scale flows in the solar convection zone.» Thèse de doctorat, Université de Stanford, 2000.
- González Hernández, I., R. Komm, F. Hill, R. Howe, T. Corbard, et D. A. Haber. «Meridional Circulation Variability from Large-Aperture Ring-Diagram Analysis of Global Oscillation Network Group and Michelson Doppler Imager Data.» *ApJ.* 638 (2006): 576-583.
- Gough, D. «How Oblate Is the Sun?» *Science* 337 (2012): 1611.
- . «On the seat of the solar cycle.» Édité par S. Sofia. *Variations of the Solar Constant.* NASA, 1981. 185.
- Gough, D. «Sizing up the Sun.» *Nature* 410 (2001): 313.

- Haber, Deborah A., Bradley W. Hindman, Juri Toomre, Richard S. Bogart, Rasmus M. Larsen, et Frank Hill. «Evolving Submerged Meridional Circulation Cells within the Upper Convection Zone Revealed by Ring-Diagram Analysis.» *ApJ* 570 (2002): 855.
- Harvey, J., R. Tucker, et L. Britanik. «High Resolution Upgrade of the GONG Instruments.» *Structure and Dynamics of the Interior of the Sun and Sun-like Stars SOHO 6/GONG 98 Workshop*. Boston, Massachusetts: ESA, 1998. 209.
- Hathaway, D. H., et al. «GONG Observations of Solar Surface Flows.» *Science* 272 (1996): 1306.
- Hill, F. «Rings and trumpets - Three-dimensional power spectra of solar oscillations.» *ApJ*. 333 (1988): 996.
- Hill, H. A., R. T. Stebbins, et J. R. Oleson. «The finite Fourier transform definition of an edge on the solar disk.» *ApJ* 200 (1975): 484.
- Hochedez, J.-F., C. Timmermans, A. Hauchecorne, et M. Meftah. «Dark signal correction for a lukecold frame-transfer CCD. New method and application to the solar imager of the PICARD space mission.» *A&A* 561 (2014): 17.
- Howard, R., et B. J Labonte. «Solar Cycles, Solar Oscillations, Solar Rotation, Flow Distribution, Periodic Variations, Plasma Oscillations, Stellar Mass, Stellar Structure.» *ApJ*. 239 (1980): L33.
- Howe, R., et al. «The High-latitude Branch of the Solar Torsional Oscillation in the Rising Phase of Cycle 24.» *ApJ*. 767 (2013): L20.
- Hoyt, et Schatten. *Sol. Phys.* 179 (1998): 189.
- Ikhlef, R., et al. «Atmospheric seeing measurements obtained with MISOLFA in the framework of the PICARD Mission.» *Ground-based and Airborne Telescopes IV*. Amsterdam: Proc. SPIE, 2012. 84446C.
- Ikhlef, R., et al. «MISOLFA: a generalized monitor for daytime spatio-temporal turbulence characterization.» *MNRAS* 458 (2016): 517.
- Ikhlef, R., et al. «MISOLFA: A Seeing Monitor for Daytime Turbulence Parameters Measurement.» Édité par M. Faurobert, C. Fang et T. Corbard. *EAS Publications Series* 55 (2012): 369.
- Irbah, A., et al. «MISOLFA: A Generalized Solar Seeing Monitor.» Édité par D. Barret, F. Thévenin F. Combes. *Société Française d'Astronomie et d'astrophysique, "Scientific Highlights 2001"*. Lyon, France: EDP Sciences, 2001. 59.
- . «The solar seeing monitor MISOLFA: presentation and first results.» *SPIE Conf Series*. 2010. 211.
- Irbah, A., F. Laclare, J. Borgnino, et G. Merlin. «Solar diameter measurements with Calern Observatory astrolabe and atmospheric turbulence effects.» *SOI. Phys.* 149 (1994): 231.

- Irbah, Abdanour, et al. «New Space Value of the Solar Oblateness Obtained with PICARD.» *ApJ* 785 (2014): 89.
- Jain, K., S. C. Tripathy, F. Hill, J. W. Leibacher, et A. A. Pevtsov. «Fifty Years of Seismology of the Sun and Stars.» *ASP Conference Proceedings*, 2013.
- Kitchatinov, L. L., V. V. Pipin, V. I. Makarov, et A. G. Tlatov. «Solar torsional oscillations and the grand activity cycle.» *Sol. Phys.* 189 (1999): 227.
- Komm, R. W., R. F. Howard, et J. W. Harvey. «Meridional Flow of Small Photospheric Magnetic Features.» *Sol. Phys.* 147 (1993): 207.
- Komm, R., et al. «Solar sub-surface fluid dynamics descriptors derived from Global Oscillation Network Group and Michelson Doppler Imager data.» *ApJ*. 605 (2004): 554.
- Komm, R., I. Gonzalez Hernandez, F. Hill, R. Bogart, M. C. Rabello-Soares, et D. Haber. «Subsurface Meridional Flow from HMI Using the Ring-Diagram Pipeline.» *Sol. Phys.* 287 (2013): 85.
- Komm, R., R. Howe, F. Hill, I. Gonzalez Hernandez, C. Toner, et T Corbard. «Ring Analysis of Solar Subsurface Flows and Their Relation to Surface Magnetic Activity.» *ApJ* 631 (2005): 636-646.
- Komm, R., R., Hill, F. Howe, I. Gonzalez Hernandez, et C. Toner. «Kinetic Helicity Density in Solar Subsurface Layers and Flare Activity of Active Regions.» *ApJ* 630 (2005): 1184.
- Komm, R., S. Morita, R. Howe, et F. Hill. «Emerging Active Regions Studied with Ring-Diagram Analysis.» *ApJ* 672 (2008): 1254.
- Kopeika, N.S., S. Solomon, et Y. Gencay. «"Wavelength variation of visible and near-infrared resolution through the atmosphere : dependence on aerosol and meteorological conditions.» *J. Opt. Soc. Am.* 71 (1981): 892.
- Kuhn, J. R., H. Lin, et D. Loranz. «Gain calibrating nonuniform image-array data using only the image data.» *PASP* 103 (1991): 1097.
- Kuhn, J. R., R. Bush, M. Emilio, et I. F. Scholl. «The Precise Solar Shape and Its Variability.» *Science* 337 (2012): 1638.
- Kuhn, J. R., R. I. Bush, M. Emilio, et P. H. Scherrer. «On the Constancy of the Solar Diameter. II.» *ApJ* 613 (2004): 1241.
- Lakhal, L., A. Irbah, M. Bouzaria, J. Borgnino, F. Laclare, et C. Delmas. «Error due to atmospheric turbulence effects on solar diameter measurements performed with an astrolabe.» *A&AS* 138 (1999): 155.
- Lean, J. L., Y.-M. Wang, et N. R. Sheeley. «The effect of increasing solar activity on the Sun's total and open magnetic flux during multiple cycles: Implications for solar forcing of climate.» *Geophysical Research Letters* 29 (2002): 2224.

- Lean, Judith. «Evolution of the Sun's Spectral Irradiance Since the Maunder Minimum.» *Geophysical Research Letters* 27 (2000): 2425.
- Lean, Judith, Juerg Beer, et Raymond Bradley. «Reconstruction of solar irradiance since 1610: Implications for climate change.» *Geophysical Research Letters* 22 (1995): 3195.
- Leibacher, J.W., et R.F. Stein. «A New Description of the Solar Five-Minute Oscillation.» *Astroph. Lett.* 7 (1971): 191.
- Leighton, R. B. «A Magneto-Kinematic Model of the Solar Cycle.» *ApJ* 156 (1969): 1.
- Leighton, R.B., R.W. Noyes, et G.W. Simon. «Velocity Fields in the Solar Atmosphere. I. Preliminary Report.» *ApJ* 135 (1962): 474.
- Lockwood, M., et C. Fröhlich. «Recent oppositely directed trends in solar climate forcings and the global mean surface air temperature.» *Proc. R. Soc. A.* 463 (2007): 2447.
- Lutomirski, R. F. «Atmospheric degradation of electrooptical system performance.» *Appl. Optics* 17 (1978): 3915.
- Meftah, M., et al. «Ground-based measurements of the solar diameter during the rising phase of solar cycle 24.» *A&A* 569 (2014): 60.
- Meftah, M., et al. «On the Constancy of the Diameter of the Sun during the Rising Phase of Solar Cycle 24.» *ApJ* 808 (2015): 4.
- Meftah, M., et al. «On the Determination and Constancy of the Solar Oblateness.» *Sol. Phys.* 290 (2015): 673.
- Meftah, M., et al. «Picard SODISM, a Space Telescope to Study the Sun from the Middle Ultraviolet to the Near Infrared.» *Sol. Phys.* 289 (2014): 1043.
- Meftah, M., et al. «PICARD SOL, a new ground-based facility for long-term solar radius measurements: first results.» *Journal of Physics Conference Series* 440 (2013): 012003.
- Meftah, M., et al. «SOVAP/ Picard, a Spaceborne Radiometer to Measure the Total Solar Irradiance.» *Sol. Phys.* 289 (2014): 1885.
- Morand, F., et al. «Mesures du rayon solaire avec l'instrument DORAYSOL (1999–2006) sur le site de Calern (observatoire de la Côte d'Azur).» *Comptes Rendus Physique* 11 (2010): 660–673.
- Morand, F., T., Irbah, A. Corbard, J.P. Marcovici, et G. Thuillier. «SODISM II : ADAPTATION DE L'INSTRUMENT SODISM AU SOL.» Document projet, 2009.
- Moreton, G. E. «H α Observations of Flare-Initiated Disturbances with Velocities \sim 1000 km/sec.» *AJ* 65 (1960): 494.
- Moreton, G. E., et H. E. Ramsey. «Recent Observations of Dynamical Phenomena Associated with Solar Flares.» *PASP* 72 (1960): 357.

- Müller, D., R. G. Marsden, O. C. St. Cyr, et H. R. Gilbert. «Solar Orbiter . Exploring the Sun-Heliosphere Connection.» *Sol. Phys.* 285 (2013): 25.
- Parker, E. «Hydromagnetic Dynamo Models.» *ApJ* 122 (1955): 293.
- Reinard, A. A., J. Henthorn, R. Komm, et F. Hill. «Evidence That Temporal Changes in Solar Subsurface Helicity Precede Active Region Flaring.» *ApJ* 710 (2010): L121.
- Rempel, M. «Flux-Transport Dynamos with Lorentz Force Feedback on Differential Rotation and Meridional Flow: Saturation Mechanism and Torsional Oscillations.» *ApJ* 647 (2006): 662.
- Rempel, M. «High-latitude Solar Torsional Oscillations during Phases of Changing Magnetic Cycle Amplitude.» *ApJ* 750 (2012): L8.
- Ribes, E., et al. «The variability of the solar diameter.» Dans *The Sun in Time*, édité par M. S. Giampapa, & M. S. Matthews C. P. Sonett, 59. University of Arizona Press, Tucson, AZ, 1991.
- Roddier, F. «The effect of atmospheric turbulence in optical astronomy.» Édité par E.Wolf. *Progress in Optics XIX* (1981).
- Sanchez, S. M., A. Fournier, K. J. R. Pinheiro, et J. Aubert. «A mean-field Babcock-Leighton solar dynamo model with long-term variability.» *An. Acad .Bras. Cienc.* 86 (2014): sous presse.
- Scafetta, N., et R. C. Willson. «ACRIM total solar irradiance satellite composite validation versus TSI proxy models.» *Astrophysics and Space Science* 350 (2014): 412.
- Scherrer, P. H., et al. «The Solar Oscillations Investigation - Michelson Doppler Imager.» *Solar Physics* 162 (1995): 129.
- Schou, J., et al. «Design and Ground Calibration of the Helioseismic and Magnetic Imager (HMI) Instrument on the Solar Dynamics Observatory (SDO).» *Solar Physics* 275 (2012): 229.
- Schussler, M. «The solar torsional oscillation and dynamo models of the solar cycle.» *A&A* 94 (1981): L17.
- Solanki, S. K., et Y. C. Unruh. «Solar irradiance variability.» *Astronomische Nachrichten* 334 (2013): 145.
- Spruit, H. C. «Origin of the torsional oscillation pattern of solar rotation.» *Sol. Phys.* 213 (2003): 1.
- . «Theory of luminosity and radius variations.» Édité par M. S. Giampapa, & M. S. Matthews C. P. Sonett. *The Sun in Time*. Tucson, AZ: University of Arizona Press, 1991. 118.
- Svalgaard, L., T.L. Jr. Duvall, et P.H. Scherrer. «The Strength of the Sun's Polar Fields.» *Solar Physics* 58 (1978): 225.
- Ulrich, R.K. «The Five-Minute Oscillations on the Solar Surface.» *ApJ* 162 (1970): 993.
- Wolf. «Mittheilungen über die Sonnenflecken. I.» *Astron. Mitt. Zurich* 1 (1859): 3.

Zaatri, A., Corbard T., M. Roth, et I., von der Lühe, O. Gonzalez Hernandez. «Comparison of geometrical mapping for ring diagram.» *Journal of Physics: Conference Series*, 2008: 012090.

Zaatri, A., R. Komm, I. Gonzalez Hernandez, R Howe, et T Corbard. «North-South Asymmetry of Zonal and Meridional Flows Determined From Ring Diagram Analysis of Gong++ Data.» *Sol. Phys.* 236 (2006): 227-244.

Zhao, M., et al. «Imaging and Modeling Rapidly Rotating Stars: α Cephei and α Ophiuchi.» *Astrophys J* 701 (2009): 209.

Annexe 1 Curriculum Vitae

Thierry Corbard
Astronome Adjoint

Né le 13 Août 1970 à Saint-Nazaire, Loire Atlantique (44)

Equipe Physique Solaire et Stellaire
Laboratoire Lagrange, UMR 7293 du CNRS
Observatoire de la Côte d'Azur

- **Thèmes de recherche**

Hélio / Astéroismologie - Activité solaire - Astrométrie solaire - Météorologie de l'espace - Problèmes inverses – Turbulence atmosphérique

Je m'intéresse principalement à la structure et la dynamique interne de notre étoile le Soleil. L'objectif est de mieux comprendre son fonctionnement et notamment l'interaction entre le champ magnétique interne et les processus dynamiques conduisant au cycle d'activité dont nous observons les manifestations en surface. J'utilise pour cela d'une part la modélisation numérique et d'autre part les méthodes de l'héliosismologie pour l'interprétation des observations obtenues à partir de satellites ou de réseaux de télescopes au sol. Les recherches en cours concernent principalement l'étude de l'interaction entre le magnétisme de surface et la dynamique sub-photosphérique 3D par le développement des techniques d'héliosismologie à haute résolution et la physique du cœur solaire par la recherche de l'identification des modes de gravité. Depuis 2008 je m'implique par ailleurs beaucoup dans un programme de métrologie solaire au sol, initié dans le cadre de la mission spatiale PICARD et dont l'objectif est le suivi à long terme des variations du diamètre solaire en liaison avec les variations d'éclairement total et spectral et leur lien avec le climat terrestre.

Les points forts et principaux résultats de mes activités de recherche sont :

I. Dynamique sub-photosphérique et héliosismologie locale

- ✓ Analyse des données GONG et SOHO/MDI, mesure de l'accélération du flux méridien jusqu'à 14 Mm sous la photosphère, mise en évidence de l'asymétrie N/S de la dynamique et de gradients radiaux de rotation sub-photosphériques corrélés avec l'activité magnétique. [10, 12, 15 + Thèse de A. Zaatri]

II. Astrométrie Solaire, PICARD-SOL (CO-PI)

- ✓ Développement, opération et exploitation d'un moniteur de turbulence et d'un télescope imageur régulé en température (SODISM-2) pour poursuivre les études de métrologie solaire au sol pendant la mission PICARD [1, 2, 4, 5, 8 + Thèse de R. Ikhlef en cours]

III. Structure interne, abondances et héliosismologie globale

- ✓ Démonstration que l'inconsistance entre les modèles déduits des nouveaux calculs d'abondances (C,N,O,Ne) et ceux déduits de l'héliosismologie existe aussi pour les observables sensibles au cœur [16]
- ✓ Développement de méthodes pour la recherche des modes g, préparation du programme d'heliosismologie de PICARD (CO-I), analyse des performances et premières analyses scientifiques [14, 40]

- **Enseignement**

Je donne à l'Université de Nice Sophia-Antipolis en moyenne 70 heures par an de travaux dirigés et travaux pratiques en:

- ✓ Méthodologie (Zététique) (L1)
- ✓ Thermodynamique (L2)
- ✓ Optique (L2)
- ✓ Analyse du signal (M2)
- ✓ Programmation (Langage C / PERL) (L1)

- **Encadrement**

- ✓ Co encadrement de deux thèses:
 - Amel Zaatri (2006-2010) "*Study of the dynamics of the subsurface layers of the sun using local helioseismology*"
Directeurs: G. Grec (OCA), & O. vd Lühe (Univ. of Freiburg, Germany) (co-tutelle)
 - Rabah Ikhlef (2013-2016, en cours) "*Effet de la turbulence optique sur l'astrométrie solaire par imagerie.*"
Directeurs: T. Corbard (OCA) & Hamadouch M'Hamed et Abdelatif Toufik (Algérie) (co-tutelle)
- ✓ J'ai encadré deux stages M2 (2002 et 2010) et quatre jeunes ingénieurs en contrat CDD (2007-2014).

- **Responsabilités nationales et internationales et administration de la recherche**

- ✓ Membre du Groupe B "Évolution des moyens actuels et analyse des nouveaux moyens à 5-10 ans" de la prospective 2014 en Astronomie-Astrophysique de l'INSU
- ✓ Membre du Comité des Utilisateurs du Multi Experiment Data & Operation Center (MEDOC) depuis 2012
- ✓ Membre du Comité Scientifique du Programme National Soleil-Terre (PNST) depuis 2010
- ✓ Responsable de l'équipe "Physique Solaire" du laboratoire Cassiopée de l'Observatoire de la Côte d'Azur entre 2008 et 2011
- ✓ CO-Investigateur de la mission spatiale Solar-Orbiter sélectionnée pour le programme COSMIC VISION de l'ESA

- ✓ Membre du Groupe d'Etude et de Validation des Performances PICARD (GEVP) (2011-2014)
- ✓ CO-Investigateur et membre du Comité Scientifique de la mission spatiale PICARD (CNES, 2008-2013)
- ✓ CO-Investigateur de l'instrument GOLF sur la sonde SoHO (NASA / ESA)
- ✓ Membre du Bureau et représentant pour la France de l'Action de Coordination Européenne (FP6) HELAS (HELIo and ASteroseismology network, 2006-2010)
- ✓ Membre du Comité des Utilisateurs du réseau américain Global Oscillation Network Group (GONG, 2003-2009)
- ✓ Membre du comité scientifique d'organisation de plusieurs conférences internationales (8 entre 2007 et 2014)
- ✓ Organisateur de deux conférences internationales à Nice (2008 et 2011)

- **Travaux d'expertise**

- ✓ 'Referee' d'articles pour le journal Solar Physics
- ✓ Membre du jury de thèse de 6 étudiants entre 2001 et 2011.

- **Parcours**

- ✓ **2003-** : Astronome Adjoint à l'Observatoire de la Côte d'Azur
- ✓ **2002:** Data Scientist, Global Oscillation Network Group of the National Solar Observatory, Tucson, Arizona, U.S.A.
- ✓ **2001:** Contrat Post-Doctoral au Collège Impérial de Londres et l'Institut d' Astronomie de Cambridge, U.K.
- ✓ **1999-2000:** Contrat Post-Doctoral au High Altitude Observatory, Boulder, Colorado, U.S.A.

- **Formation**

- ✓ **1995-1998:** Thèse à l'Observatoire de la Côte d'Azur "Inversion des Mesures Héliosismiques: La rotation Interne du Soleil"
- ✓ **1994-1995:** Service Militaire au Centre de Formation et d'Interprétation des Images Inter-armées (CF3I)
- ✓ **1993-1994:** Diplôme d'Études Approfondies "Imagerie en sciences de l'Univers", Université de Nice Sophia- Antipolis.
- ✓ **1990-1993:** Licence-Maîtrise de Physique, Université de Nantes
- 1988-1990:** Diplôme d'Études Universitaires Générales "Sciences de la matière", Université de Nantes.

Annexe 2 Liste de Publications

a) dans revues à comité de lecture

1. "MISOLFA: A generalized monitor for daytime spatio-temporal turbulence characterization", R. Ikhlef, **T. Corbard**, F. Morand, C. Renaud, M. Fodil, A. Ziad, J. Borgnino, M. Meftah, P. Assus, B. Chauvineau, A. Hauchecorne, P. Lesueur, G. Poiet, F. Ubaldi, M. Hamadouche, T. Abdelatif, **2016**, MNRAS 458, 517
2. *On the Constancy of the Diameter of the Sun during the Rising Phase of Solar Cycle 24*, M. Meftah, A. Hauchecorne, A. Irbah, **T. Corbard**, R. Ikhlef, F. Morand, C. Renaud, F. Riguet, F. Pradal, **2015**, ApJ 808, 4
3. *On the determination and constancy of the solar oblateness at 782.2nm*, M. Meftah, A. Irbah, A. Hauchecorne, **T. Corbard**, S. Turck-Chi'eze, J.-F. Hochedez, P. Boumier, A. Chevalier, S. Dewitte, D. Salabert, **2015**, Sol. Phys 290, 673
4. *New Space Value of the Solar Oblateness Obtained with PICARD*, A. Irbah, M. Meftah, A. Hauchecorne, D. Djafer, **T. Corbard**, M. Bocquier, E.M. Cisse, **2014**, ApJ 785, 89
5. *Ground-based measurements of the solar diameter during the rising phase of solar cycle 24*, M. Meftah, **T. Corbard**, A. Irbah, R. Ikhlef, F. Morand, C. Renaud, A. Hauchecorne, P. Assus, J. Borgnino, B. Chauvineau, M. Crepel, F. Dalaudier, L. Damé, D. Djafer, M. Fodil, P. Lesueur, G. Poiet, M. Rouzé, A. Sarkissian, A. Ziad, F. Laclare, **2014**, A&A 569, 60
6. *Picard SODISM, a Space Telescope to Study the Sun from the Middle Ultraviolet to the Near Infrared*, M. Meftah, J.F. Hochedez, A. Irbah, A. Hauchecorne, P. Boumier, **T. Corbard**, S. Turck-Chi'eze, S. Abbaki, P. Assus, E. Bertran, P. Bourget, F. Buisson, M. Chaigneau, L. Damé, D. Djafer, C. Dufour, P. Etcheto, P. Ferrero, M. Hers e, J.P. Marcovici, M. Meissonnier, F. Morand, G. Poiet, J.Y. Prado, C. Renaud, N. Rouanet, M. Rouzé, D. Salabert, A.J. Vieau, **2014**, Sol. Phys. 289, 1043
7. *The Plate Scale of the SODISM Instrument and the Determination of the Solar Radius at 607.1 nm*, M. Meftah, A. Hauchecorne, M. Crepel, A. Irbah, **T. Corbard**, D. Djafer, J.F. Hochedez, **2014**, Sol. Phys. 289, 1
8. "Solar radius measurements with the DORAY SOL instrument (1999-2006) at the Calern site of the observatoire de la Côte d'Azur" F. Morand, C. Delmas, **T. Corbard**, B. Chauvineau, A. Irbah, M. Fodil, F. Laclare, **2011**, Comptes Rendus Physique 11, 660
9. "MISOLFA solar monitor for the ground PICARD program", **T. Corbard**, A. Irbah, P. Assus, C. Dufour, M. Fodil, F. Morand, C. Renaud, E. Simon, **2010**, Atron. Nach. 331, 58
10. "Solar radius measurements with the SODISM instrument: methods and algorithm developments for the PICARD Payload Data Center", A. Irbah, C. Dufour, M. Meftah, M. Meissonnier, G. Thuillier, P. Assus, **T. Corbard**, G. Pradels, **2010**, Atron. Nach. 331, 59
11. "Sensitivity of the sub-photospheric flow fields inferred from ring-diagram analysis to the change on the solar model", A. Zaatri, J. Provost, **T. Corbard**, M. Roth, **2010**, Astrophysics and Space Science 328, 135
12. "POLAR investigation of the Sun—POLARIS", T. Appourchaux, P. Liewer, M. Watt, D. Alexander, V. Andretta, F. Auchre, P. d'Arrigo, J. Ayon, **T. Corbard**, S. Fineschi, W. Finsterle, L. Floyd, G. Garbe, L. Gizon, D. Hassler, L. Harra, A. Kosovichev, J. Leibacher, M. Leipold, N. Murphy, M. Maksimovic, V. Martinez-Pillet, B.S.A. Matthews, R. Mewaldt, D. Moses, J. Newmark, S. Régnier, W. Schmutz, D. Socker, D. Spadaro, M. Stuttard, C. Trosseille, R. Ulrich, M. Velli, A. Vourlidas, C.R. Wimmer-Schweingruber, T. Zurbuchen, **2010**, Experimental Astronomy 23, 1079

13. “Comparison of the sidereal angular velocity of subphotospheric layers and small bright coronal structures during the declining phase of solar cycle 23”, A. Zaatri, H. Whl, M. Roth, **T. Corbard**, R. Brajsa, **2010**, A&A 504, 589
14. “Monitoring the scale factor of the PICARD SODISM instrument”, P. Assus, A. Irbah, P. Bourget, **T. Corbard**, **2008**, Atron. Nach. 329, 517
15. “Helioseismology program for PICARD satellite”, **T. Corbard**, P. boumier, T. Appourchaux, S.J. Jiménez-Reyes, B. Gelly, **2008**, Atron. Nach. 329, 508
16. “Comparison of geometrical mapping for ring diagram analysis”, A. Zaatri, T. Corbard, M. Roth, I. González-Hernández, O. von der Lühe, **2008**, Journal of Physics Conference Series 118, 2090
17. “Sensitivity of low degree oscillations to the change in solar abundances”, A. Zaatri, J. Provost, G. Berthomieu, P. Morel, **T. Corbard**, **2007**, A&A 469, 1145
18. “North-South asymmetry of zonal and meridional flows determined from ring diagram analysis of GONG data”, A. Zaatri, R. Komm, I. González-Hernández, R. Howe, **T. Corbard**, **2006**, Sol. Phys. 236, 227
19. “Meridional Circulation Variability from Large-Aperture Ring Diagram Analysis of GONG and MDI Data”, I. González-Hernández, R. Komm, F. Hill, R. Howe, **T. Corbard**, D. A. Haber, **2006**, ApJ 638, 576
20. “Ring Analysis of Solar Subsurface Flows and Their Relation to Surface Magnetic Activity”, R. Komm, R. Howe, F. Hill, I. González-Hernández, C. Toner, **T. Corbard**, **2005**, ApJ 631, 636
21. “About the solar radiative rotation”, R.A. García, **T. Corbard**, W.J. Chaplin, S. Couvidat, A. Eff-Darwich, S.J. Jiménez Reyes, S.G. Korzennik, J. Ballot, P. Boumier, E. Fossat, C.J. Henney, R. Howe, M. Lazreck, J. Leibacher, P.L. Pallé, S. Turck-Chièze, **2004**, Sol. Phys. 220, 269
22. “Solar sub-surface fluid dynamics descriptors derived from Global Oscillation Network Group and Michelson Doppler Imager data”, R. Komm, **T. Corbard**, B. R. Durney, I. González-Hernández, F. Hill, R. Howe, C. Toner, **2004**, ApJ. 605, 554
23. “The rotation of the deep solar layers”, S. Couvidat, R. A. García, S. Turck-Chièze, **T. Corbard**, C. J. Henney, S. J. Jiménez-Reyes, **2003**, ApJ 597, L77
24. “IRIS++ database: Merging of IRIS + Mark-1 + LOWL”, D. Salabert, E. Fossat, B. Gelly, S. Tomczyk, P. Pallé, S. J. Jiménez-Reyes, A. Cacciani, **T. Corbard**, S. Ehgamberdiev, G. Grec, J. T. Hoeksema, S. Kholikov, M. Lazrek, F. X. Schmieder, **2002**, A&A 390, 717
25. “Flux-transport solar dynamos with near-surface radial shear”, M. Dikpati, **T. Corbard**, M.J. Thompson, P. Gilman, **2002**, ApJ 575, L41
26. “The subsurface radial gradients of solar angular velocity from MDI f-modes observations” **T. Corbard**, M.J. Thompson, **2002**, Sol. Phys. 205, 211
27. “A comparison of solar p mode parameters from MDI and GONG: splitting coefficients and rotation inversions”, J. Schou, R. Howe, S. Basu, J. Christensen Dalsgaard, **T. Corbard**, F. Hill, R. Komm, R.M. Larsen, M.C. Raballo-Soares, M.J. Thompson, **2002**, ApJ 567, 1234
28. “Analysis of the solar cycle and core rotation using 15 years of Mark-I observations: 1984-1999. I. The Solar Cycle”, S.J. Jiménez-Reyes, **T. Corbard**, P.L. Pallé, S. Tomczyk, **2001**, A&A 379, 622
29. “Structure of the core: Effect of asymmetry of peak profiles”, S. Basu, S. Turck-Chièze, G. Berthomieu, A.S. Brun, **T. Corbard**, G. Gonczi, J. Christensen-Dalsgaard, J. Provost, S. Thiery, A.H. Gabriel, P. Boumier, **2000**, ApJ 535, 1078
30. “Non linear regularization for helioseismic inversions”, **T. Corbard**, L. Blanc-Féraud, G. Berthomieu, J. Provost, **1999**, A&A 344, 696
31. “Inferring the equatorial solar tachocline from frequency splittings”, **T. Corbard**, G. Berthomieu, J. Provost, P. Morel, **1998**, A&A 330, 1149
32. “Solar internal rotation from LOWL data : A 2D regularized least-squares inversion using B-splines”, **T. Corbard**, G. Berthomieu, P. Morel, J. Provost, J. Schou, S. Tomczyk, **1997**, A&A 324, 298

33. "Differential Rotation and Dynamics of the Solar Interior", M.J. Thompson, J. Toomre, E.R. Anderson, H.M. Antia, G. Berthomieu, D. Burtonclay, S.M. Chitre, J. Christensen-Dalsgaard, **T. Corbard**, M. DeRosa, C.R. Genovese, D.O. Gough, D.A. Haber, J.W. Harvey, F. Hill, R. Howe, S.G. Korzennik, A.G. Kosovichev, J.W. Leibacher, F.P. Pijpers, J. Provost, E.J. Rhodes Jr., J. Schou, T. Sekii, P.B. Stark, P.R. Wilson, **1996**, Science 272, 1300

b) cours publié d'une école du CNRS

34. "La rotation interne du Soleil déduite de l'héliosismologie", **T. Corbard**, **1998**, E. Schatzman (ed) Cours de Structure interne d'Aussois, Observatoire de Paris, Meudon (61 pages).

c) communications dans des colloques internationaux

Actes de colloques avec comité de lecture / Revues invitées

35. *PICARD SOL, a new ground-based facility for long-term solar radius measurements: first results*, M. Meftah, T. Corbard, A. Irbah, F. Morand, R. Ikhlef, C. Renaud, A. Hauchecorne, P. Assus, B. Chauvineau, M. Crepel, F. Dalaudier, D. Djafer, M. Fodil, F. Laclare, P. Lesueur, M. Lin, G. Poiet, **2013**, Journal of Physics Conference Series 440, id. 012003
36. *Helioseismology with PICARD*, **T. Corbard**, D. Salabert, P. Boumier, T. Appourchaux, A. Hauchecorne, P. Journoud, A. Nunge, B. Gelly, J.F. Hochedez, A. Irbah, M. Meftah, C. Renaud, S. Turck-Chièze, **2013**, Journal of Physics Conference Series 440, id. 012025
37. "The solar tachocline and its variation (?) ", Revue Invitée **T. Corbard**, S.J. Jiménez-Reyes, S. Tomczyk, M. Dikpati, P. Gilman, **2001**, SOHO 10 / GONG 2000 meeting, Helio- and Asteroseismology at the Dawn of the Millennium, ESA SP-464, p. 265.
38. "Internal Rotation and Dynamics of the Sun from GONG Data", S.G. Korzennik, M.J. Thompson, J. Toomre, H.M. Antia, G. Berthomieu, D. Burtonclay, S.M. Chitre, J. Christensen-Dalsgaard, **T. Corbard**, A. Eff-Darwich, D.O. Gough, R. Howe, F.P. Pijpers, J. Provost, J. Schou, T. Sekii, M.J. Thompson, P.R. Wilson, Li Yan ,**1997**, Proceedings of IAU 181 Symposium: Sounding Solar and Stellar Interiors, J. Provost & F.X. Schmider (eds), Kluwer, Dordrecht, p. 211

Actes de colloques sans comité de lecture

39. "Main results of the PICARD mission", M. Meftah, **T. Corbard**, A. Hauchecorne, A. Irbah, P. Boumier, A. Chevalier, W. Schmutz, R. Ikhlef, F. Morand, C. Renaud, J.-F. Hochedez, G. Cessateur, S. Turck-Chièze, D. Salabert, M. Rouzé, M. van Ruymbeke, P. Zhu, S. Kholikov, S. Koller, C. Conscience, S. Dewitte, L. Damé, D. Djafer, **2016**, Proc. SPIE 9904, Space Telescopes and Instrumentation 2016: Optical, Infrared, and Millimeter Wave, 99040Z (July 29, 2016); doi:10.1117/12.2232027
40. "Picard, a solar mission dedicated to the study of the Sun: current results", M. Meftah, J. F. Hochedez, S. Dewitte, A. Hauchecorne, A. Irbah, P. Boumier, **T. Corbard**, S. Turck-Chièze, P. Zhu, **2014**, 40th COSPAR Scientific Assembly, Moscow, Russia, 2 - 10 August 2014, Abstract D2.2-20-14
41. *The PICARD Scientific Mission: status of the program*, M. Rouzé, A. Hauchecorne, J.F. Hochedez, A. Irbah, M. Meftah, **T. Corbard**, S. Turck-Chièze, P. Boumier, S. Dewitte, W. Schmutz, **2014**, 13th International Conference on Space Operations 2014, Pasadena, CA, 5-9 May 2014, American Institute of Aeronautics and Astronautics, SapceOps 2014 Conference, p. 1705
42. *Helioseismology from SODISM and HMI Intensity Images*, **T. Corbard**, D. Salabert, P. Boumier, the PICARD team, **2013**, National Solar Observatory Workshop 27, Fifty Years of Seismology of the Sun and Stars, eds. Jain, K., Tripathy, S.C., Hill, F., Leibacher, J. W. and Pevtsov, A. A., Astronomical Society of the Pacific Conference Series, vol. 478, p. 151

43. “*PICARD SOL mission, a ground-based facility for long-term solar radius measurement*” M. Meftah, A. Irbah, **T. Corbard**, F. Morand, G. Thuillier, A. Hauchecorne, R. Ikhlef, M. Rouze, C. Renaud, D. Djafer, S. Abbaki, P. Assus, B. Chauvineau, E.M. Cissé, F. Dalaudier, E. D’Almeida, M. Fodil, F. Laclare, P. Lesueur, M. Lin, J.P. Marcovici, G. Poiet, **2012**, Ground-based and Airborne Instrumentation for Astronomy IV. Proceedings of the SPIE, Vol. 8446, 844676
44. “*Atmospheric seeing measurements obtained with MISOLFA in the framework of the PICARD Mission*”, R. Ikhlef, **T. Corbard**, A. Irbah, F. Morand, M. Fodil, B. Chauvineau, P. Assus, C. Renaud, M. Meftah, S. Abbaki, J. Borgnino, E.M. Cissé, E. D’Almeida, A. Hauchecorne, F. Laclare, P. Lesueur, M. Lin, F. Martin, G. Poiet, M. Rouzé, G. Thuillier, A. Ziad, **2012**, Ground-based and Airborne Telescopes IV. Proceedings of the SPIE, Vol. 8444, 84446C
45. “*MISOLFA : a seeing monitor for daytime turbulence parameters measurement*”, R. Ikhlef, **T. Corbard**, A. Irbah, M. Meftah, F. Morand, M. Fodil, P. Assus, C. Renaud, B. Chauvineau, **2012**, 4th french-chinese meeting on Solar Physics: Understanding solar activity: Advances and Challenges, Nice, Nov. 15-18, 2011 , eds. Faurobert, M., Fang, C. and Corbard, T., European Astronomical Society Publications Series, vol. 55, p. 369
46. “*Ground-based solar astrometric measurements during the PICARD mission*”, A. Irbah, M. Meftah, **T. Corbard**, R. Ikhlef, F. Morand, P. Assus, M. Fodil, M. Lin, E. Ducourt, P. Lesueur, G. Poiet, C. Renaud, M. Rouze, **2011**, Optics in Atmospheric Propagation and Adaptive Systems XIV, eds. Stein, K. and Ginglewski, J.D., Proceedings of the SPIE (Prague, 09/2011), vol. 8178, p. 81780A
47. “*The solar seeing monitor MISOLFA: presentation and first results*”, A. Irbah, **T. Corbard**, P. Assus, J. Borgnino, C. Dufour, R. Ikhlef, F. Martin, M. Meftah, F. Morand, C., Renaud, E. Simon, **2010**, Society of Photo-Optical Instrumentation Engineers (SPIE) Conference Series 7735, p. 211
48. “*Sensitivity of ring analysis to near-surface magnetism*”, **T. Corbard**, **2009**, HELAS Workshop NA3-4 The Acoustic Solar Cycle, eds. Elsworth, Y.P. and Thompson, M.J., University of Birmingham, 6-8 January 2009, CD Volume
49. “*CoRot observations of active giants: preliminary results*”, P. Gondoin, M. Fridlund, M.J. Goupil, F. Baudin, R. Samadi, C. Barban, K. Belkacem, **T. Corbard**, M.A., Dupret, B. Foing, R. den Hartog, Y. Lebreton, J. Lochard, P. Mathias, E. Michel, P. Morel, A. Moya, A. Palacios, J.P Zahn, **2009**, American Institute of Physics Conference Series 1094, p. 864
50. “*The Solar Subsurface Radial Gradient of Angular Velocity as Revealed by Ring Diagram Analysis*”, A. Zaatri, **T. Corbard**, **2009**, Astronomical Society of the Pacific Conf. Series 416, p. 99
51. “*Rotation inversions of artificial solarFLAG Sun-as-a-star data*”, W.J. Chaplin, T. Sekii, T. Appourchaux, F. Baudin, P. Boumier, **T. Corbard** T, Y. Elsworth, S.T. Fletcher, R.A. García, S.J. Jiménez-Reyes, M. Lazrek, R. New, D. Salabert, T. Toutain, R. Wachter, **2006**, Proceedings of SOHO 18/GONG 2006/HELAS I, Beyond the spherical, K. Fletcher & M.J. Thompson, ESA SP-624, p. 82
52. “*European helio- and asteroseismology network HELAS*”, M. Roth, O. v.d. Luhe, P. Palle, M.J. Thompson, J. Christensen-Dalsgaard, M.J.P.F.G. Monteiro, L. Gizon, M.P. Di Mauro, C. Aerts, J. Daszynska-Daszkiewicz, **T. Corbard**, **2006**, Proceedings of SOHO 18/GONG 2006/HELAS I, Beyond the spherical Sun, K. Fletcher & M.J. Thompson (eds), ESA SP-624, p. 130
53. “*How does the change on solar abundances affect low degree modes?*”, A. Zaatri, J. Provost, G. Berthomieu, P. Morel, **T. Corbard**, **2006**, Proceedings of SOHO 18/GONG 2006/HELAS I, Beyond the spherical Sun, K. Fletcher & M.J. Thompson, ESA SP-624, p. 92
54. “*B0-angle effect on zonal and meridional flow determinations from 3 years ring diagram analysis of GONG++ data*”, **2006**, A. zaatri, R. Komm, I. González Hernández, R. Howe, **T. Corbard**, **2006**, Proceedings of SOHO 18/GONG 2006/HELAS I, Beyond the spherical Sun, K. Fletcher & M.J. Thompson (eds), ESA SP-624, p. 55
55. “*The internal structure of the Sun inferred from g modes and low frequency p modes*”, Y. Elsworth, F. Baudin, W. Chaplin, B. Andersen, T. Appourchaux, P. Boumier, A.M. Broomhall, **T. Corbard**, W. Finsterle, C. Frhlich, A. Gabriel, R.A. Garcia, D.O. Gough, G. Grec, A. Jimenez, A. Kosovichev, J. Provost, T. Sekii, T. Toutain, S. Turck-Chièze, **2006**, Proceedings of SOHO 18/GONG 2006/HELAS I, Beyond the spherical Sun, K. Fletcher & M.J. Thompson (eds), ESA SP-624, p. 22

56. "The *DynaMICS* project", S. Turck chièze, W. Schmutz, G. Thuillier, A. Cacciani, P. pallé, V. Domingo, J. Ballot, G. Berthomieu, A. Bonanno, A.S. Brun, J. christensen-Dalsgaard, **T. Corbard**, S. Couvidat, A.M. Darwich, B. dintrans, W. finsterle, E. Fossat, R.A. García, B. Gelly, D. Gough, J. Guzik, A.J. Jiménez, S. Jiménez-Reyes, A. Kosovichev, P. Lambert, S. Lefebvre, I. Lopes, M. Matric, S. Mathis, S. Mathur, P.A.P. Nghiem, L. Piau, J. Provost, M. Rieutord, J.M. Robillot, T. Rogers, T. Roudier, I. Roxburgh, J.P. Rozelot, S. Talon, M. Thompson, S. Vauclair., J.P. Zahn, **2006**, SOHO-17. 10 Years of SOHO and Beyond, H. Lacoste and L. Ouwehand. (eds), ESA SP-617, p. 162
57. "HELAS - European Helio- and Asteroseismology Network", M. Roth, O. von der Luhe , Pere Palle , M. Thompson, J. Christensen- Dalsgaard, M. Monteiro , L. Gizon, M. P. Di Mauro, C. Aerts, J. Daszynska-Daszkiewicz, **T. Corbard**, **2006**, SOHO-17. 10 Years of SOHO and Beyond, H. Lacoste & L. Ouwehand (eds), ESA SP-617, p. 157
58. "Recent progress on G- mode search", T. Appourchaux, B. Andersen, A.M. Barlow, F. Baudin, P. Boumier, W. Chaplin, **T. Corbard**, Y. Elsworth, W. Finsterle, C. Frhlich, A. Gabriel, D.O. Gough, R.A. Garcia, G. Grec, A. Kosovichev, A. Jimenez, J. Provost, T. Toutain, S. Turck-Chièze, T. Sekii, **2006**, SOHO-17. 10 Years of SOHO and Beyond, H. Lacoste & L. Ouwehand (eds), ESA SP-617, p. 2
59. "The Magnetism of the Solar Interior for a Complete MHD Solar Vision" S. Turck-Chièze, T. Appourchaux, J. Ballot, G. Berthomieu, P. Boumier, A. S. Brun, A. Cacciani, J. Christensen-Dalsgaard, **T. Corbard**, S. Couvidat, A. Eff-Darwich, B. Dintrans, E. Fossat, R. A. Garcia, B. Gelly, L. Gizon, D. Gough, A. Jimenez, S. Jiménez-Reyes, A. Kosovichev, P. Lambert, I. Lopes, M. Martic, S. Mathis, N. Meunier, P. A. Nghiem, P. Palle, L. Piau, J. Provost, M. Rieutord, J. M. Robillot, T. Rodier, I. Roxburgh, J. P., Rozelot, S. Solanki, S. Talon, M. Thompson, G. Thuillier, S. Vauclair, J. P. Zahn, **2006**, 2005 ESLAB Symposium Trends in Space Science and Cosmic Vision 2020, ESA SP-588, p. 193
60. "The ESTER project", M. Rieutord, **T. Corbard**, B. Pichon, B. Dintrans, F. Lignières, **2005**, SF2A-2005: Semaine de l'Astrophysique Francaise, F. Casoli, T. contini, J.M. Hameury, L. Pagani (eds), p. 759
61. "2 Years of Meridional Circulation from GONG Ring Diagrams", I. González Hernández, R. Komm, **T. Corbard**, F. Hill, R. Howe, D. A. Haber, **2005**, Eos Trans. AGU, 86(18), Jt. Assem. Suppl., Abstract SP32A-01
62. "Jets in the Solar Tachocline as Diagnostics of Global MHD Processes", J. Christensen Dalsgaard, **T. Corbard**, M. Dikpati, P. A. Gilman, M.J. Thompson, **2005**, Large scale Structures and their Role in Solar Activity, ASP conf. Ser. 346, p. 115
63. "Detection of Jets and Associated Toroidal Fields in the Solar Tachocline", J. Christensen Dalsgaard, **T. Corbard**, M. Dikpati, P. A. Gilman, M. J. Thompson, **2004**, SOHO 14 Helio- and Asteroseismology: Towards a Golden Future, ESA SP-559, p. 376
64. "Meridional Variability from Large-Aperture Ring Diagrams", I. González Hernández, R. Komm, F. Hill, R. Howe, **T. Corbard**, **2004**, SOHO 14 Helio- and Asteroseismology: Towards a Golden Future, ESA SP-559, p. 444
65. "Solar Subsurface Flows and Vorticity", R. Komm, R. Howe, I. González Hernández, F. Hill, D. A. Haber, B. Hindman, **T. Corbard**, **2004**, SOHO 14 Helio- and Asteroseismology: Towards a Golden Future, ESA SP-559, p. 520
66. "Vorticity of Solar Subsurface Flows and Torsional Oscillations", R. Komm, R. Howe, I. González-Hernández, F. Hill, D. Haber, B. hindman, **T. Corbard**, **2004**, 204th AAS meeting, Denver, BAAS 36, p. 757.
67. "The Role of Time Varying Meridional Flow Pattern During Past 20 years In Influencing Upcoming Solar Cycle Features", M. Dikpati, G. de Toma, P. A. Gilman, **T. Corbard**, E. J. Rhodes, D. A. Haber, R. S. Bogart, P. J. Rose, **2004**, 204th AAS meeting, Denver, BAAS 36, p. 756.
68. "Meridional Circulation Variability from Large-Aperture Ring Diagrams", I. Gonzalez-Hernandez, R. Komm, **T. Corbard**, F. Hill, R. Howe, **2004**, 204th AAS meeting, Denver, BAAS 36, p. 756.
69. "New Constraints on the dynamics of the solar sub-photospheric layers from high resolution helioseismology", **T. Corbard**, F. Hill, J. Leibacher, C. Toner, **2003**, EGS-AGU-EUG, Nice, 07-11 April 2003, Geophysical Research Abstracts, Vol. 5, #07761

70. "The LoHCo Project. 1 – Comparison of Ring-Diagram Local Helioseismology on GONG++, MDI and Mt. Wilson Data Sets", R. S. Bogart, J. Schou, S. Basu, J. Bolding, F. Hill, R. Howe, R. W. Komm, J. W. Leibacher, C. G. Toner, **T. Corbard**, D. A. Haber, B. W. Hindman, J. Toomre, E. J. Rhodes, P. J. Rose, and LoHCo Project Team, **2003**, 34th SPD Meeting, BAAS 35, p. 822.
71. "Flow maps from GONG+ ring diagrams", R. Komm, J. Bolding, **T. Corbard**, F. Hill, R. Howe, C. Toner, **2003**, 34th SPD Meeting, BASS 35, p. 823.
72. "Localized Frequency Shifts from GONG+", R. Howe, R. W. Komm, F. Hill, J. Bolding, C. Toner, **T. Corbard**, **2003**, 34th SPD Meeting, BAAS 35, p. 822.
73. "Ring Diagram Analysis with GONG++", **T. Corbard**, C. Toner, F. Hill, K. Hanna, D. Haber, B. Hindman, R. Bogart **2003**, SOHO 12 / GONG+ 2002: Local and Global Helioseismology: The Present and Future, ESA Publication Division, ESA-SP-517, p. 255.
74. "An Image Merge for GONG+", C. G. Toner, D. Haber, **T. Corbard**, R. Bogart, **2003**, SOHO 12 / GONG+ 2002: Local and Global Helioseismology: The Present and Future, ESA Publication Division, ESA-SP-517, p. 405.
75. "The GONG++ Data Processing Pipeline", F. Hill, J. Bolding, C. Toner, **T. Corbard**, S. Wampler, B. Goodrich, **2003**, SOHO 12 / GONG+ 2002: Local and Global Helioseismology: The Present and Future, ESA Publication Division, ESA-SP-517, p. 295
76. "The Search for the solar core dynamics with SOHO / GOLF", S. Couvidat, S. Turck-Chieze, R. A. García, **T. Corbard**, **2003**, 3D Stellar Evolution Conference, Livermore, Eds.: S. Turcotte, S. Keller, R. Cavallo, ASP Conf. Ser. 293, p. 276
77. "The Dynamics of the solar core with SOHO/GOLF", S. Couvidat, S. Turck-Chieze, R. A. García, **T. Corbard**, **2002**, SF2A Scientific Highlights 2002, F. Combes, D. Barret (eds), EDP Sciences, p. 441.
78. "Enhanced facilities for local helioseismology with GONG+ images", **T. Corbard**, C. Toner, F. Hill, **2002**, 200th AAS Meeting, BAAS 34, p. 644.
79. "Effect Of the Subsurface Radial Differential Rotation On Flux-Transport Solar Dynamos", **T. Corbard**, M. Dikpati, P. Gilman, M.J. Thompson, **2002** SOHO-11: From Solar Minimum to Maximum, ESA SP-508, p. 75.
80. "Global acoustic low frequency domain after half a cycle aboard SOHO", S. Turck-Chieze, R. A. Garcia, S. Couvidat, S. Kosovichev, L. Bertello, **T. Corbard**, G. Berthomieu, J. Provost, A. Darwish, **2002** SOHO-11: From Solar Minimum to Maximum, ESA SP-508, p. 593.
81. "Variations of the solar interior with the cycle, theoretical and observational aspects.", **T. Corbard**, S.J. Jiménez-Reyes, **2001**, SF2A-2001, Scientific Highlights, EDP sciences, p. 109.
82. "Comparing Global Solar Rotation Results from MDI and GONG", R. Howe, R. W. Komm, F. Hill, J. Christensen-Dalsgaard, J. Schou, M.J. Thompson, **T. Corbard**, **2001**, American Geophysical Union, Spring Meeting 2001, abstract #SP31A-14
83. "LOWL p-mode frequencies and their variation with solar activity ", S.J. Jiménez-Reyes, **T. Corbard**, P.L. Pallé, S. Tomczyk, **2001**, SOHO 10 / GONG 2000 meeting: Helio- and Asteroseismology at the Dawn of the Millennium, ESA SP-464, p. 107.
84. "Signature of the solar cycle in the low degree p-modes using MARK-I ", S.J. Jiménez-Reyes, **T. Corbard**, P.L. Pallé, **2001**, SOHO 10 / GONG 2000 meeting: Helio- and Asteroseismology at the Dawn of the Millennium, ESA SP-464, p. 103.
85. "About structure inversion sof simulated COROT data for a solar like star ", G. Berthomieu, T. Toutain, G. Gonczi, **T. Corbard**, J. Provost, P. Morel, **2001**, SOHO 10 / GONG 2000 meeting: Helio- and Asteroseismology at the Dawn of the Millennium, ESA SP-464, p. 411.
86. "The solar cycle and the tachocline: Theories and Observations", **T. Corbard**, S.J. Jiménez-Reyes, S. Tomczyk, M. Dikpati, P.Gilman, **2001**, I SOLSPA Euroconference: The solar cycle and terrestrial climate, ESA SP-463, p. 21.
87. "P-mode frequency shift as solar activity index ", S.J. Jiménez-Reyes, **T. Corbard**, P.L. Palle, S. Tomczyk, **2001**, I SOLSPA Euroconference: The solar cycle and terrestrial climate, ESA SP-463, p. 341.

88. "Solar rotation from GOLF/LOWL", **T. Corbard**, S.J. Jiménez-Reyes, S. Tomczyk, and the GOLF team, **2000**, 31st SPD meeting, BAAS 32, p. 801.
89. "Solar cycle variations of oscillation mode parameters from LOWL and MARK-I instruments", S.J. Jiménez Reyes, **T. Corbard**, S. Tomczyk, P. L. Pallé, **2000**, 31st SPD meeting, BAAS 32, p. 1289.
90. "Inversion of IRIS helioseismic data and the solar structure ", G. Berthomieu, G. Gonczi, **T. Corbard**, , J. Provost, **1999**, Proceedings of the Xth IRIS/TON Workshop, Taschkent September 1998, Eds S. Emgamberdiev, p. 24.
91. "On the use of non-linear regularization in inverse methods for the solar tachocline profile determination ", **T. Corbard**, G. Berthomieu, J. Provost, L. Blanc-Féraud, **1998**, Proceedings of the SOHO6/GONG98 workshop, ESA SP-418, p. 747.
92. "The solar internal rotation from GOLF splittings", **T. Corbard**, M.P. Di Mauro, T. Sekii, and the GOLF team, **1998**, Proceedings of the SOHO6/GONG98 workshop, ESA SP-418, p. 741.
93. "Solar sound speed inferred from SOHO helioseismic data", G. Gonczi, G. Berthomieu, **T. Corbard**, J. Provost, P. Morel, and the GOLF team, **1998**, Proceedings of the SOHO6/GONG98 workshop, ESA SP-418, p. 461.
94. "The solar core rotation from LOWL and IRIS or BiSON data ", **T. Corbard**, G. Berthomieu, J. Provost, E. Fossat **1998**, Proceedings of IAU 181 Symposium (poster volume), OCA & UNSA, Nice, p. 79.
95. "The solar rotation rate from inversion of the first GONG datasets", **T. Corbard**, G. Berthomieu, J. Provost, **1998**, Proceedings of IAU 181 Symposium (poster volume), OCA & UNSA, Nice, p. 77.
96. "Solar rotation from 2D inversion", **T. Corbard**, G. Berthomieu, G. Gonczi, J. Provost, P. Morel, **1995**, Fourth SoHO Workshop: Helioseismology, ESA SP-376 vol. 2, p. 289.

d) autres publications

97. 'On the importance of astronomical refraction for modern Solar astrometric measurements", **T. Corbard**, F. Morand, F. Laclare, R. Ikhlef, M. Meftah, **2013**, Research note, arXiv:1304.0147v2 [astro-ph.SR]
98. "Foreword", M. Faurobert, C. Fang, **T. Corbard**, **2012**, 4th french-chinese meeting on Solar Physics: Understanding solar activity: Advances and Challenges, Nice, Nov. 15-18, 2011 , eds. Faurobert, M., Fang, C. and Corbard, T., EAS Publications Series, Volume 55, 2012, p. 1
99. "Four years of HELAS", M. Roth, O. v.d. Lühe, C. Aerts, J. Christensen-Dalsgaard, **T. Corbard**, J. Daszyńska-Daszkiewicz, M.P. Di Mauro, L. Gizon, S. Jiménez-Reyes, M.J.P.F.G. Monteiro, P.L. Pallé, M.J. Thompson, **2010**, Astronomische Nachrichten, Vol.331, Issue 9/10, p. 1084
100. "European Helio- and Asteroseismology Network HELAS", M. Roth, O. von der Luhe , Pere Palle , M. Thompson, J. Christensen- Dalsgaard, M. Monteiro , L. Gizon, M. P. Di Mauro, C. Aerts, J. Daszynska-Daszkiewicz, **T. Corbard**, **2006**, Proceedings of SOHO 18/GONG 2006/HELAS I, Beyond the spherical Sun (ESA SP-624). 7-11 August 2006, Sheffield, UK. Editor: Karen Fletcher. Scientific Editor: Michael Thompson, Published on CDROM, p. 130.1
101. "Ring-Diagram Analysis with GONG++, **T. Corbard**, Technical note (22 pages), **2003**
102. "Inversion des mesures héliosismiques: La rotation interne du Soleil", **T. Corbard**, **1998**, Thèse de doctorat, Université de Nice-Sophia-Antipolis.

Titre	Héliosismologie et Astrométrie solaire à haute résolution
Résumé	<p>La recherche en physique solaire et stellaire a été très largement influencée ces dernières décennies par l'application des techniques de sismologie permettant pour la première fois de sonder l'intérieur des étoiles. Pour le Soleil, il est possible d'aller encore plus loin avec l'imagerie à haute résolution et haute cadence. Ainsi depuis les années 2000 s'est développée une branche particulière de l'héliosismologie appelée « héliosismologie locale » permettant de sonder en détails et en temps quasi-réel notamment les couches les plus superficielles de la photosphère.</p> <p>La première partie de ce manuscrit concerne mes activités dans le domaine de l'héliosismologie à haute résolution. Je montre comment j'ai contribué activement au développement des outils nécessaires à l'exploitation des nouvelles observations à haute résolution des réseaux américains GONG et sonde spatiale SOHO. Avec ces outils, j'ai ensuite cherché à apporter des contraintes aux modèles cinématiques de la dynamo en étudiant notamment la circulation méridienne, la dynamique autour des zones actives et les oscillations de torsion. J'ai ainsi pu contribuer aussi au débat sur le siège possible de la dynamo et la caractérisation de ses composantes.</p> <p>Dans la seconde partie, je présente ma contribution aux développements de la base instrumentale PICARD-SOL développée sur le site de Calern (OCA) dans le cadre de la mission spatiale PICARD pour la mesure et le suivi à long terme du rayon solaire. L'astrométrie solaire par imagerie directe est venue se substituer aux techniques d'astrolabe utilisées auparavant en posant de nouveaux challenges pour la prise en compte des effets de turbulence et de réfraction. La poursuite de ces travaux est placée ensuite en perspective dans le cadre des projets instrumentaux actuels et le développement de la météorologie de l'espace.</p>
Mots-clés	Physique Solaire – Héliosismologie - Astrométrie
Title	High resolution Helioseismology and solar Astrometry
Abstract	<p>Research in solar and stellar physics has been tremendously influenced these past decades by the use of seismic techniques that allowed us for the first time to explore the interior of stars. For the Sun, it is possible to go even further with high resolution and high cadence imaging. Thus, since the years 2000 a new field has emerged called “local helioseismology” that gives us the ability to probe in details and in quasi real time the most superficial layers beneath the solar photosphere.</p> <p>The first part of this document reports my activities and contribution in the field of local helioseismology. I show how I actively contributed to the development of the numerical tools that were needed to analyze the new high resolution images provided by the American ground-based network GONG and the NASA/ESA SOHO spacecraft. Then, I worked to set new constraints on the Kinematic flux transport solar dynamo models by studying the meridional circulation, active zones dynamics or the torsional oscillations of the rotation rate. This led me to contribute to the debate on the seat of the solar dynamo and the various characteristics of its main components.</p> <p>In the second part, I present my contribution to the development of the new solar astrometry facility PICARD-SOL that was set up at Calern observatory (OCA) in the framework of the space mission PICARD dedicated to the measurement and monitoring of the solar diameter. Solar astrometry from direct high resolution imaging has replaced the traditional astrolabe technics and has raised new challenges in order to take into account turbulence and astronomical refraction effects in ground based data analysis.</p> <p>My future work is then placed in perspective within the framework of the new instrumental projects and the development of space weather.</p>
Keywords	Solar Physics – Helioseismology - Astrometry